Studies to reduce greenhouse gases emissions from particles detectors operation at the CERN LHC experiments

Gianluca Rigoletti

To cite this version:

Gianluca Rigoletti. Studies to reduce greenhouse gases emissions from particles detectors operation at the CERN LHC experiments. Physics [physics]. Université de Lyon, 2022. English. NNT : 2022LYSE1051 . tel-04050232

HAL Id: tel-04050232
https://theses.hal.science/tel-04050232

Submitted on 29 Mar 2023

N° d'ordre NNT: 2022LYSE1051

THÈSE DE DOCTORAT DE L'UNIVERSITÉ DE LYON
opérée au sein de
l'Université Claude Bernard Lyon 1

École Doctorale N° 52
PHYSIQUE ET ASTROPHYSIQUE DE LYON (PHAST)

Spécialité de doctorat : physique

Soutenue publiquement le 25/03/2022, par:
Gianluca Rigoletti

Studies to reduce greenhouse gases emissions from particles detectors operation at the CERN LHC experiments

---

Devant le jury composé de:

Laktineh Imad, Professeur, Université Claude Bernard Lyon	Président
Paganoni Marco, Professeur, Università degli Studi Milano-Bicocca	Rapporteur
Nom, prénom, grade/qualité, établissement/entreprise	Rapporteur.e
Carloganu Cristina, Directrice de Recherche CNRS, Université Clermont Auvergne	Examinatrice
Nom, prénom, grade/qualité, établissement/entreprise	Examinateur.rice
Nom, prénom, grade/qualité, établissement/entreprise	Directeur de thèse
Guida Roberto, Staff, European Organization for Nuclear Research (CERN)	Co-directeur de thèse
Mandelli Beatrice, Staff, European Organization for Nuclear Research (CERN)	Invitée

DOCTORAL THESIS

Studies to reduce greenhouse gases emissions from particles detectors operation at the CERN LHC experiments

Author:
Gianluca RIGOLETTI

Supervisor:
Prof. Patrick NEDELEC
Dr. Roberto GUIDA

A thesis submitted in fulfillment of the requirements
for the degree of Doctor of Philosophy

CERN, Experimental Physics
Detector Technologies
École doctorale de physique, PHAST
Université de Lyon 1

"In theory there is no difference between theory and practice. In practice there is."

Benjamin Brewster

Abstract

Gianluca RIGOLETTI

Studies to reduce greenhouse gases emissions from particles detectors operation at the CERN LHC experiments

A wide range of gas mixtures is used to operate different gaseous detectors at the CERN LHC experiments. Some of these gases, namely $C_2H_2F_4$, CF_4, SF_6, C_4F_{10}, are classified as Greenhouse Gases (GHG) with a high Global Warming Potential, therefore subjected to a phase-down policy affecting their price and market availability. These gases are responsible for 70% of CERN particle detector operation's direct greenhouse gas emissions. The Organisation's objective is to reduce such emissions by 28% by the end of 2024 (baseline year: 2018). The present work shows the development of two main research strategies delineated by the CERN gas group to reduce GHG emissions. Wherever suitable, large detector volumes are operated with recirculating gas systems. The first part of this thesis focuses on optimizing existing gas system technologies to improve operating performances and further reduce gas consumption. In particular, dedicated monitoring infrastructures were designed to properly tune the active control parts of the different gas modules. Furthermore, specific data analysis pipelines were developed to evaluate a gas system's performance and monitor gas consumption. A second research line examined in this work consisted of studying the performance of RPC detectors operated with eco-friendly gases. RPCs at ATLAS and CMS experiments are operated with a three-component gas mixture mainly based on $C_2H_2F_4$ (R-134a, GWP_{100} = 1430), around 5% of i-C_4H_{10}, and a minor fraction of 0.3% of SF_6 (GWP_{100} = 22800). Due to the presence of leaks at the detector level, $C_2H_2F_4$ dominates the overall CERN GHG emissions. Alternatives to $C_2H_2F_4$ were identified in R-1234ze, a molecule in the family of HydroFluoroOlefins with a GWP_{100} = 7, while SF_6 alternatives were found in the Novec family (Novec™ 4710 and Novec™ 5110), C_4F_8O, CF_3I, and Amolea™ 1224yd. RPC performance with gas mixtures based on alternative gases was firstly evaluated in laboratory conditions by studying the detector's efficiency, currents, streamer probability, prompt charge, cluster size, and time resolution. Few selected gas mixtures were then tested at the Gamma Irradiation Facility, which provides muon beam and gamma background radiation, allowing to emulate the High Luminosity LHC background conditions. Few gas mixtures showed similar rate capability performance with respect to the standard gas mixture. Long-term performance studies were started, and preliminary studies on impurities productions for HFO-based gas mixtures are presented, showing the R-1234ze molecule produces an order of magnitude more F^- ions than the $C_2H_2F_4$ one.

Résumé

Gianluca RIGOLETTI

Études visant à réduire les émissions de gaz à effet serre émis par les détecteurs de particules des expériences LHC du CERN

Une large gamme de mélanges gazeux est utilisée pour le fonctionnement de différents détecteurs à gaz dans les expériences LHC du CERN. Certains de ces gaz, notamment $C_2H_2F_4$, CF_4, SF_6 et C_4F_{10}, sont classifiés parmi les gaz à effet de serre (GHG) à fort potentiel de réchauffement planétaire (GWP) et soumis donc à une politique de réduction progressive de leurs prix et de leur disponibilité sur le marché. Ces gaz sont responsables de 70% des émissions GHG directes provenant du fonctionnement du CERN. L'objectif de l'Organisation est de réduire ces émissions de 28% d'ici à la fin de 2024 (année de référence : 2018). Le présent travail montre le développement de deux stratégies de recherche définies par le groupe gaz du CERN pour réduire les émissions GHG. Dans la mesure du possible, les détecteurs de grand volume sont exploités avec des systèmes de recirculation des gaz, reutilisant jusqu'à 90 % de ceux-ci. Ce travail de thèse se concentre sur l'optimisation des technologies de système à gaz existantes afin d'améliorer les performances d'exploitation et de permettre une réduction supplémentaire de la consommation. En particulier, des logiciels de surveillance ont été spécialement conçues pour régler correctement les parties de contrôle des différents modules des systèmes à gaz. En outre, des pipelines d'analyse de données spécifiques ont été développés pour évaluer la performance d'un système à gaz et pour surveiller les consommations. Un deuxième axe de recherche examiné dans ce travail consiste en l'étude des performances des détecteurs RPC avec l'utilisation de gaz alternatifs. Les RPCs des expériences ATLAS et CMS fonctionnent actuellement avec un mélange gazeux à trois composants, principalement basé sur le $C_2H_2F_4$ (GWP_{100} = 1430), environ 5 % de i-C_4H_{10}, et de 0,3 % de SF_6 (GWP_{100} = 22800). En raison de la présence de fuites au niveau des détecteurs, le $C_2H_2F_4$ domine l'ensemble des émissions GHG du CERN. Une alternative à ce gaz pourrait-être le R-1234ze, une molécule appartenant à la famille des Hydro-Fluoro-Olefins (HFO) avec un GWP_{100} de 7, tandis que des alternatives au SF_6 ont été trouvées parmi les gaz de la famille Novec (Novec™ 4710 et Novec™ 5110), C_4F_8O, CF_3I et Amolea™ 1224yd. Les performances des RPC avec des mélanges de gaz basés sur des gaz alternatifs ont d'abord été évaluées en laboratoire en étudiant l'efficacité du détecteur, les courants, la probabilité de formation de streamers, la charge, la cluster size et la résolution temporelle. Quelques mélanges de gaz sélectionnés ont ensuite été testés dans la Gamma Irradiation Facility du CERN qui fournit un faisceau de muons et un rayonnement gamma de fond, permettant de simuler les conditions de rayonnement du HL-LHC. Quelques mélanges gazeux ont montré des performances similaires en termes de rate de détection par rapport au mélange standard. Des études de performance à long terme ont été lancées et des études préliminaires sur la production d'impuretés dans les mélanges gazeux à base de HFO sont présentées dans ce travail, mettant en évidence que la molécule R-1234ze produit environ dix fois plus d'ions F- que la molécule $C_2H_2F_4$.

Summary

Studies to reduce greenhouse gases emissions from particles detectors operation at the CERN LHC experiments

CERN is an international organization founded in 1954 with the aim of performing world-class research in particle physics, pushing the frontiers of current instrumentations and technologies for the benefit of all. Among several experiments and facilities, the Large Hadron Collider (LHC) accelerator and its experiments ALICE, ATLAS, CMS, LHCb, were designed to explore the physics of the Standard Model by studying the collision of hadrons at the energy scale of the TeV in a controlled environment.

Although each experiment was designed to probe different aspects of the Standard Model, they share some particle detector technologies. Muons, which provide a clean signature of most interesting collision events, are detected by LHC experiments through several different gaseous particle detectors. Each gaseous detector at LHC is operated with a gas mixture and has specific needs in terms of gas quality, input flow rate, operating pressure, and safety. To meet each detector's requirements, dedicated gas systems were designed. Each gas system is organized in blocks of different modules interoperating with each other. The modular approach was chosen in the early design phases to ease operation across different detectors and reduce building times and costs. Furthermore, large volume detectors are mostly operated with up to 90% of gas recirculation for environmental, technological, and economic reasons.

Some of the gases used for LHC gaseous detectors are nowadays identified as Greenhouse Gases (GHG). A GHG is a gas responsible for the Greenhouse effect, which consists of the absorption by the atmosphere of infrared radiation emitted by the Earth's surface with the consequent increase of the atmospheric temperature. To measure the strength of the Greenhouse effect, Global Warming Potential (GWP_{100}) is typically used. It is defined as the heat that one gas can absorb in the atmosphere with respect to the heat absorbed by the same mass of CO_2 over a fixed period. The 2019-2020 CERN Environment Report reported that particle detectors account for the largest GHGs emissions due to the fluorinated gases used to operate the detectors. In particular, $C_2H_2F_4$ (R-134a) is responsible for 73% of total tons of CO_2 equivalent (tCO_2 e) emissions from detector operation, CF_4 for 20% and SF_6 for about 7%.

The Fourth Assessment Report of the Intergovernmental Panel on Climate Change stated that, based on existing scientific data, developed countries would need to reduce greenhouse gas emissions by 80% to 95% below 1990 levels by 2050 to limit global climate change to a temperature increase of 2 °C and thus prevent undesirable climate effects. The European Commission adopted a roadmap to reduce the GHGs emission from fluorinated gases with

the target of reducing their emissions to one-fifth from 2014 to 2030. The regulation, written in 2014, defines several different strategies to reduce emissions by requiring regular checks on equipment, containing, recover or destroying GHGs where possible, restricting the placing on the market of equipment working with GHG where suitable alternatives are present and gradually reducing the amount of HydroFluoroCarbons (HFC) that can be placed on the market by allocating distribution quotas to individual manufacturers.

CERN has internally adopted different strategies to align with the latest environmental requirements. In particular, for gas systems, four initial research branches were foreseen:

- Optimization of current gas system technologies to improve gas system performance in terms of recirculation fraction, operation stability, and gas mixture quality;
- Research, development, construction of gas recuperating systems that recover a specific gas component exhausted from the system and store it in containers to be reused as a fresh supply;
- Studies on detector performance operated in LHC environments with low GWP_{100} gas mixtures;
- Abatement and disposal plants where GHGs cannot be recovered;

The work presented in this thesis mainly focused on the strategies to optimize the gas system, and on the use of alternative gases for Resistive Plate Chamber (RPC) detectors.

The optimization of gas systems covers a broad range of mechanical and software upgrade interventions performed during Long Shutdown 2 (LS2). New additional distribution racks were installed at different cavern levels in the ATLAS RPC gas system to allow a finer control on the pressure of the detector, thus reducing possible gas waste from leaking chambers. For each distribution rack in the ATLAS, ALICE, CMS RPC systems, a mechanical volume emulating a chamber volume, namely reference chamber, was installed. The volume was designed to be accessible and leak-tight so that its pressure could be used as feedback for distribution regulation. In the CMS RPC gas systems, new control valves were recently installed for precise regulation of the detector's pressures. From the software point of view, gas systems are operated with CERN's UNified COntrol System framework (UNICOS), which integrates a Supervised Control And Data Acquisition (SCADA) application with low-level functions for Programmable Logic Controllers (PLC) machines used to interface with plant's field objects. Gas Control Systems (GCS) are used to set the gas system to a desired operational state and retrieve archived sensor data to spot eventual anomalies. The automatic regulation performed on a field object such as a valve using an analog sensor as feedback is ensured by the industrial standard Proportional Integral Derivative (PID) controller implemented in the UNICOS framework. A set of tunable parameters define the PID response to the change of the system's dynamics. PIDs are largely employed in gas systems to ensure that the correct flow is sent from the mixer using Mass Flow Controllers and to ensure a stable detector chamber pressure through regulation valves.

During LS2, the startup phase of the ALICE TOF gas system was generating interlock alarms that caused the stop of the gas system. After investigating the issue, it was found out that the alarms were generated due to the input pressure of the pump module crossing safety tresholds. A systematic PID study was conducted to understand the effect of the change of the PID parameters of the pump regulation valve in relation to the ones in distribution regulation valves of the gas system. After several configurations were tested, proper PIDs parameters allowing a correct startup phase of the system were found.

During LS2, the ATLAS MDT system behaved differently from the Run 2 period. In particular, chamber pressures were found to have an overshoot of 30-40 millibars during the system's startup, a value considerably higher than 2-3 millibars present during Run 2. A dedicated PID tuning campaign took place to improve the regulation during the startup phase of the system by leveraging the newly-added UNICOS startup parameters feature. Several different thresholds and hysteresis values were set to control the transition between the two operational states of the distribution rack. For the two operational states, namely RunReady and RunNotReady, two sets of proportional and integral gains were adjusted to minimize the initial chamber pressure overshoot and the subsequent undershoot in the first hours of startup of the gas system.

The optimization of gas systems was also performed by improving the available monitoring tools for both gas system experts and detector users. The Human Machine Interface (HMI) provided by GCSs to operators is designed according to the UNICOS standard. Such standards were designed several years ago to produce homogeneous panels that allowed minimal effort for operators to understand different control systems. However, the standards imposed several limitations to the operator experience in terms of monitoring the system. In particular, it was observed that for large systems comprising several distribution racks, the monitoring tools provided by SCADA were not sufficient. Furthermore, the modular organization of a gas system could result in a deeply nested tree navigation structure, making it slow and somewhat cumbersome the navigation between different modules. Two monitoring solutions were conceived and designed to address the mentioned issues. The first one consisted of designing a web-based dashboard using Grafana to visualize a limited set of sensor data in a single page, such as distribution pressure and regulation valves. The Grafana web dashboard allowed both operator and detector users to easily access relevant time-series data from any device with minimal navigation effort. A second solution consisted of implementing an HMI SCADA panel displaying selected device values from different gas system modules. Together with the current value, each device showed the minimum and maximum value over the last weekly data, allowing to spot gas system anomalies without the need to open trending tools for each device.

Data analysis pipelines were developed to improve the performance of a few gas systems and understand their behavior during Run periods. The investigation consisted of the retrieval of time series data and the analysis of their behavior over time. The analysis was run on CERN Service for Web-based ANalysis (SWAN), a Jupyter notebook connected to the CERN NeXt Accelerator Logging Service (NXCALS) cluster, where all gas system data is continuously stored. In particular, few analyses were conducted on flow cells data of RPC gas systems to understand possible time-related or rack-related leak developments.

A second strategy to reduce GHG emissions consisted of studying the performance of RPC detectors operated with alternative gases. High Pressure Laminate (HPL) RPCs in the ALICE, ATLAS, and CMS experiments are operated with a gas mixture of about 90-95% of R-134a and a around 0.3% of SF_6. The presence of leaks at the detector level made the

RPCs accountable for the highest GHG emissions from particle detectors at CERN. Alternative gases to R-134a were identified in R-1234ze, a gas in the family of HydroFluoroOlefins (HFO) with a GWP_{100} of 7, largely employed in automotive refrigerants. Alternatives to SF_6 were mainly identified in gases of the Novec™family, in particular Novec™ 4710 and Novec™ 5110, and in other fluorinated gases such as C_4F_8O, CF_3I, and Amolea™ 1224yd. A dedicated laboratory setup was built to study the performance of 2 mm, single gap RPCs performance to find a suitable eco-friendly gas mixture that required no change in the current RPC systems installed at LHC. The RPCs performances were evaluated regarding efficiency, currents, streamer probability, prompt charge, cluster size, and time resolution. The standard R-134a-based gas mixture was initially characterized and used as a baseline reference. The addition of Helium (He) or Carbon Dyoxide (CO_2) up to 50% in the standard gas mixture was then studied. It was found out that the addition of around 40% of He or CO_2 to the mixture resulted in a lower GWP_{100}, stable RPCs performance, and a lower working point. Few gas mixtures based on the addition of R-1234ze and He or CO_2 were tested. Results showed that an amount of R-134a is needed to stabilize performance in terms of streamer contaminations. It was also observed that the addition of He to HFO-based gas mixtures helped lowering the working point, matching the standard gas mixture one without significant performance losses. However, there are concerns about the use of He in the LHC cavern due to the Photomultiplier Tubes (PMT) on calorimeters. Alternative gases to SF_6 were studied by replacing SF_6 in the standard gas mixture with the candidate gas and varying its concentration in steps of 0.1%. Novec™ 5110 was firstly tested due to its excellent environmental properties ($GWP_{100} = 1$). Results showed discrete performance, requiring it to be operated at concentrations of 2% to achieve sufficient streamer suppressions. The main difficulty faced with the gas was a high boiling point of 26 °C, making it difficult to operate at high flows and ambient temperature. Although Novec™ 4710 has a higher GWP_{100}, it showed excellent performance, matching the ones of the standard gas mixture when used in concentrations of 0.1%. Investigations are currently being carried on to understand the effects of its usage in the presence of water vapor. C_4F_8O has a GWP_{100} of around 8000. The required amount to match standard gas mixture performance was about 2%, making its effective GWP_{100} contribution higher than SF_6, thus not eco-friendly. CF_3I has a low GWP_{100} of 1, almost zero Ozone Depletion Potential (ODP), and showed similar performance to SF_6 in the standard gas mixture. However, the gas may not be used in the LHC cavern for safety reasons due to its mutagenic toxicity levels being higher than the currently accepted ones. Finally, Amolea™ 1224yd, a gas in the family of the Hydro-Chloro-Fluoro-Olefins, was tested. Results showed similar performance to the standard gas mixture when used in a 0.3-0.5% concentration. The gas also has a $GWP_{100} < 1$ and ODP = 0, making it a valuable eco-friendly alternative to SF_6. However, its relatively high boiling point of 15 °C makes the gas difficult to be used at high flows.

Few selected gas mixtures were then tested in a dedicated RPC setup built at the CERN Gamma Irradiation Facility (GIF++), located in the North Area on the H4 beamline. The setup consisted of three 2 mm single gap RPC detectors installed in the GIF++ irradiation area, where a 12.5 TBq ^{137}Cs source and the presence of muon beam allowed to test RPCs performance in LHC and HL-LHC environments. The RPCs' performances were evaluated during muon beam time at different irradiation conditions. The foremost RPCs parameters were then interpolated at the working point for the different gamma rates, and a study on the behavior of the currents, efficiency, working point, cluster size, and time resolution

was conducted. Preliminary results showed similar performance between the standard gas mixture and He-based gas mixtures. CO_2-based gas mixtures showed a higher current and slightly higher efficiency drop at rates of 500 Hz/cm^2. The use of R-1234ze without R-134a required higher concentrations of CO_2, leading to a higher drop of efficiency for expected HL-LHC background rates. R-1234ze and R-134a with the addition of CO_2 or He were found to be a good compromise between RPCs performance and GWP_{100}. Novec™ 4710 and Amolea 1224 yd were tested, confirming the results obtained in laboratory conditions that could be used as suitable replacements for SF_6. Furthermore, Amolea 1224 yd was also tested in place of i-C_4H_{10} to understand possible quenching properties of the gas to help reduce streamer suppression. Finally, impurities studies produced by RPCs in the presence of background radiation were studied. RPCs were operated at full efficiency with the standard gas mixture and with a five-component R-1234ze/R-134a/CO_2/i-C_4H_{10}/SF_6 27.25/27.25/40/4.5/0.3 gas mixture. The production of HF from the output of the chambers was measured by means of Ion Selective Electrodes. It was found out that when operated in at the same efficiency and background conditions, the R-1234ze based gas mixture produced around four times more HF than the standard gas mixtures, indicating that the R-1234ze could produce around an order of magnitude more HF with respect to R-134a. Long-term performance studies on the RPCs operated in LHC-like environments were started.

Études visant à réduire les émissions de gaz à effet serre émis par les détecteurs de particules des expériences LHC du CERN

Le Conseil Européen pour la Recherche Nucléaire (CERN) est une organisation internationale fondée en 1954 dont l'objectif est de mener des recherches en physique des particules au niveau international, en repoussant les limites des instruments et des technologies actuels, dans l'intérêt de tous. Parmi plusieurs expériences et installations, l'accélérateur Large Hadron Collider (LHC) et ses expériences ALICE, ATLAS, CMS, LHCb, ont été conçus pour explorer la physique du modèle standard en étudiant la collision des hadrons à l'échelle d'énergie du TeV, dans un environnement contrôlé.

Bien que chaque expérience ait été conçue pour sonder des aspects différents du modèle standard, elles partagent certaines des technologies de détection de particules. Les muons, qui fournissent une signature propre de la plupart des événements de collision intéressants, sont détectés par les expériences du LHC au moyen de plusieurs détecteurs de particules gazeux différents. Chaque détecteur gazeux du LHC fonctionne avec un mélange gazeux et a des besoins spécifiques en termes de qualité de gaz, de débit d'entrée, de pression de fonctionnement et de sécurité. Pour répondre aux exigences de chaque détecteur, des systèmes à gaz dédiés ont été conçus. Chaque système est organisé en blocs de différents modules qui interagissent les uns avec les autres. L'approche modulaire a été choisie dès les premières phases de conception pour faciliter l'utilisation des différents détecteurs et réduire les délais et les coûts de construction. En outre, pour des raisons environnementales, technologiques et économiques, les détecteurs à grand volume sont généralement exploités avec une recirculation des gaz qui peut atteindre jusqu'à 90%.

Certains des gaz utilisés dans les détecteurs gazeux du LHC sont aujourd'hui identifiés comme des gaz à effet de serre (GHG). L'effet de serre consiste en l'absorption par l'atmosphère du rayonnement infrarouge émis par la surface de la Terre. Pour mesurer l'intensité de l'effet de serre, on utilise généralement le potentiel de réchauffement global (GWP_{100}). Il est défini comme la chaleur qu'un gaz peut absorber dans l'atmosphère par rapport à la chaleur absorbée par la même masse de CO2 sur une période de temps donné. Le rapport sur l'environnement 2019-2020 du CERN, indique que les détecteurs de particules sont à l'origine des plus importantes émissions de GHG, en raison des gaz fluorés utilisés pour les faire fonctionner. En particulier, le $C_2H_2F_4$ (R-134a) est responsable de 73% des émissions totales de CO_2 (tCO_2 e) liées au fonctionnement des détecteurs, le CF_4 de 20% et le SF_6 d'environ 7%.

Le quatrième rapport d'évaluation du Groupe d'experts intergouvernemental sur l'évolution du climat a indiqué que, sur la base des données scientifiques existantes, les pays développés devraient réduire leurs émissions de gaz à effet de serre de 80% à 95% par rapport aux niveaux de 1990 d'ici à 2050 pour limiter le changement climatique mondial à une augmentation de température de 2 °C et prévenir ainsi les effets climatiques indésirables. La Commission européenne a adopté une feuille de route pour réduire l'émission de GHG des gaz fluorés, avec pour objectif de réduire leur émission d'un cinquième entre 2014 et 2030. Le règlement, rédigé en 2014, définit plusieurs stratégies différentes pour réduire les émissions en exigeant des contrôles réguliers des équipements, la contention, la récupération ou la destruction des GHG lorsque cela est possible, ainsi que la restriction de la mise sur le marché d'équipements fonctionnant avec des GHG lorsque des alternatives appropriées sont présentes et la réduction progressive de la quantité d'HydroFluoroCarbures (HFC) pouvant être mise sur le marché en attribuant des quotas de distribution aux fabricants individuels.

Le CERN a adopté en interne plusieurs stratégies différentes pour s'aligner sur les dernières exigences environnementales. En particulier, pour les systèmes à gaz, quatre branches de recherche initiales ont été prévues :

- Optimisation des technologies actuelles des systèmes à gaz afin d'améliorer leurs performances en termes de fraction de recirculation, de stabilité du fonctionnement et de qualité du mélange gazeux;
- Recherche, développement, construction de systèmes de récupération de gaz qui récupèrent un composant gazeux spécifique évacué du système et le stockent dans des conteneurs pour être réutilisé comme un nouvel approvisionnement;
- Études sur les performances des détecteurs employés dans les environnements LHC avec des mélanges gazeux à faible GWP_{100};
- Destruction et élimination des gaz à effet de serre qui ne peuvent être récupérés.

Le travail présenté dans cette thèse s'est principalement concentré sur les stratégies d'optimisation des systèmes à gaz et sur l'utilisation de gaz alternatifs dans les détecteurs Resistive Plate Chambers (RPC).

L'optimisation des systèmes à gaz couvre un large éventail d'interventions de mise à niveau mécanique et logicielle effectuées pendant le LS2. Des nouveaux racks de distribution supplémentaires ont été installés à différents niveaux de caverne dans le système à gaz ATLAS RPC pour permettre un contrôle plus fin de la pression du détecteur, réduisant ainsi le gaspillage possible de gaz dans les chambres non étanches. Pour chaque rack de distribution dans les systèmes ATLAS, ALICE, CMS RPC, un volume mécanique simulant le volume du détecteur a été installé. Ce volume a été conçu pour être accessible et étanche, de telle sorte que sa pression puisse être utilisée pour la régulation de la distribution. Dans les systèmes à gaz CMS RPC, de nouvelles vannes de contrôle ont été récemment installées pour une régulation précise de la pression des détecteurs. Du point de vue du logiciel, les systèmes à gaz sont exploités avec UNified COntrol System du CERN (UNICOS), qui intègre une application de contrôle et d'acquisition de données (SCADA) avec des fonctions de bas niveau pour les automates programmables (PLC) utilisés pour communiquer avec les objets physique du système à gaz. Les Gas Control Systems (GCS) sont utilisés pour régler le système à gaz dans un état opérationnel souhaité, ainsi que pour récupérer les données archivées des capteurs afin de repérer d'éventuelles anomalies. La régulation automatique effectuée sur un objet de terrain tel qu'une vanne en utilisant un capteur analogique comme feedback est assurée par le contrôleur standard industriel Proportionnel Intégral Dérivé (PID) présent dans UNICOS. Un ensemble de paramètres réglables définit la réponse du PID au changement de la dynamique du système. Les PID sont largement utilisés dans les systèmes à gaz pour garantir l'envoi d'un débit de gaz correct par le mélangeur à l'aide de régulateurs de débit massique, ainsi que pour assurer une pression stable dans la chambre du détecteur à l'aide de vannes de régulation.

Pendant le LS2, le système à gaz ATLAS MDT s'est comporté différemment de la période Run 2. En particulier, les pressions de la chambre ont eu un dépassement de 30-40 millibars pendant le démarrage du système, une valeur considérablement plus élevée que les 2-3 millibars présents pendant le Run 2. Une campagne de réglage du PID a été menée pour améliorer la régulation pendant la phase de démarrage du système en utilisant la nouvelle fonction de paramètres de démarrage d'UNICOS. Plusieurs seuils et valeurs d'hystérésis différents ont été définis pour contrôler la transition entre deux états opérationnels du rack de distribution. Pour les deux états opérationnels, à savoir RunReady et RunNotReady, deux ensembles de gains proportionnels et intégraux ont été ajustés pour minimiser le dépassement initial de la pression de la chambre et le dépassement ultérieur dans les premières heures du démarrage du système de gaz.

Pendant le LS2, la phase de démarrage du système de gaz ALICE TOF générait des alarmes de verrouillage qui provoquaient l'arrêt du système de gaz. Après avoir étudié le problème, il a été découvert que les alarmes étaient générées par la pression d'entrée du module de pompe franchissant les seuils de sécurité. Une étude systématique a été menée pour comprendre l'effet de la modification du paramètre PID de la vanne de régulation de la pompe en relation avec ceux de la vanne de régulation présente dans les deux racks de distribution du système à gaz. Après avoir testé plusieurs configurations, des paramètres PIDs appropriés permettant une phase de démarrage correcte du système ont été trouvés.

L'optimisation des systèmes à gaz a également été réalisée en améliorant les outils de surveillance disponibles, tant pour les experts en systèmes à gaz que pour les utilisateurs de détecteurs. L'interface homme-machine (HMI) fournie aux opérateurs pour le GCS est conçue selon la norme UNICOS. Ces normes ont été pensées il y a plusieurs années dans le but de produire des panneaux homogènes permettant aux opérateurs de comprendre les différents systèmes de contrôle avec un minimum d'effort. Cependant, ces normes imposent plusieurs limites à l'expérience de l'opérateur en termes de contrôle du système. En particulier, il a été observé que pour les grands systèmes comprenant plusieurs racks de distribution, les outils de surveillance fournis par le SCADA n'étaient pas suffisants. En outre, l'organisation modulaire d'un système à gaz pouvait donner lieu à une structure de navigation profondément imbriquée, rendant la navigation entre les différents modules lente et quelque peu encombrée. Deux solutions de surveillance ont été conçues pour résoudre les problèmes mentionnés. La première consistait à concevoir un tableau de visualisation web utilisant Grafana pour visualiser un ensemble limité de données de capteurs, comme la pression de distribution et les vannes de régulation, sur une seule page. Le dashboard web de Grafana a permis aux utilisateurs des détecteurs d'accéder facilement aux données de séries temporelles pertinentes à partir de n'importe quel appareil avec un effort de navigation minimal. Une deuxième solution a consisté à mettre en œuvre un panneau HMI SCADA affichant des valeurs de dispositifs sélectionnés provenant de différents modules du système à gaz. En plus de la valeur actuelle, chaque dispositif affichait la valeur minimale et maximale des dernières données hebdomadaires, ce qui permettait de repérer les anomalies du système à gaz sans avoir à ouvrir des outils de tendance pour chaque dispositif. Pour améliorer les performances de quelques systèmes à gaz et comprendre leur comportement pendant les périodes de fonctionnement, des pipelines d'analyse de données ont été développés. L'analyse a été effectuée sur CERN Service for Web based ANalysis (SWAN), un ordinateur portable jupyter connecté au cluster CERN NeXt Accelerator Logging Service

(NXCALS), où toutes les données du système à gaz étaient stockées. L'analyse consistait à la récupération de données de séries temporelles et au calcul de leur comportement dans le temps. En particulier, des analyses ont été menées sur les données des cellules qui mesure le débit des systèmes à gaz RPC afin de comprendre les éventuels développements de fuites pendant le fonctionnement du système.

Une deuxième stratégie pour réduire les émissions de GHG a consisté à étudier les performances des détecteurs RPC fonctionnant avec des gaz alternatifs. Les RPC en bakélite des expériences ALICE, ATLAS et CMS fonctionnent avec un mélange gazeux composé d'environ 90 à 95% de R-134a et d'une fraction plus faible de 0,3% de SF_6. En raison de la présence de fuites au niveau des détecteurs, les RPC sont responsables des plus grandes émissions de GHG des détecteurs de particules du CERN. Des gaz alternatifs au R-134a ont été identifiés dans le R-1234ze, un gaz de la famille des hydro fluoro oléfines (HFO) avec un GWP_{100} de 7, largement utilisé dans les réfrigérants automobiles. Les alternatives au SF6 ont été principalement identifiées dans les gaz de la famille NovecTM, en particulier le Novec™ 4710 et le Novec™ 5110, ainsi que le C_4F_8O, le CF_3I et l'Amolea™ 1224yd. Une installation de laboratoire dédiée a été construite pour étudier les performances des RPCs de 2 mm, single-gap, dans le but de trouver un mélange de gaz écologique approprié qui ne nécessite aucun changement dans les systèmes RPC actuels installés au LHC. Les performances des RPC ont été évaluées en termes d'efficacité, de courants, de probabilité de streamer, de charge prompte, de taille de cluster et de résolution temporelle. Dans un premier temps, le mélange gazeux standard à base de R-134a a été caractérisé et utilisé comme référence de base. L'ajout d'hélium et de CO_2 jusqu'à 50% dans les mélanges gazeux standard a été étudié. Il s'est avéré que l'ajout d'environ 40% d'hélium ou de CO_2 au mélange permettait d'obtenir un GWP100 inférieur, des performances stables des RPCs et un point de fonctionnement plus bas. Quelques mélanges de gaz basés sur l'addition de R-1234ze et d'Hélium ou de CO_2 ont été testés. Les résultats ont montré qu'une quantité de R-134a devait être conservée pour stabiliser les performances en termes de contamination des streamers. Il a été observé que l'ajout d'hélium aux mélanges gazeux à base de HFO permettait d'abaisser le point de fonctionnement et pouvait correspondre à celui du mélange gazeux standard sans perte de performance significative. Cependant, l'utilisation d'Hélium dans la caverne du LHC pourrait endommager les tubes photomultiplicateurs (PMT) présents sur les calorimètres.

Des gaz alternatifs au SF_6 ont été étudiés en remplaçant le SF_6 dans le mélange de gaz standard par le gaz candidat et en faisant varier sa concentration par pas de 0,1%. Le Novec™ 5110 a été testé en premier lieu, en raison de ses excellentes propriétés environnementales (GWP_{100} = 1). Les résultats ont montré une performance discrète, nécessitant de l'utiliser à des concentrations de 2% pour obtenir des suppressions de streamers suffisantes. Les principales difficultés rencontrées avec ce gaz étaient un point d'ébullition élevé de 26 °C, rendant difficile son exploitation à des débits élevés et à température ambiante. Bien que le Novec™ 4710 ait un GWP_{100} plus élevé, il a montré d'excellentes performances, égalant celles du mélange gazeux standard lorsqu'il est utilisé à des concentrations de 0,1%. Des recherches sont actuellement menées pour comprendre les effets de son utilisation en présence de vapeur d'eau. Le CF_4 8O a un GWP_{100} d'environ 8000. La quantité requise pour atteindre les performances du mélange gazeux standard est d'environ 2%, ce qui rend sa contribution au GWP100 effectif plus élevée que celle du SF_6, et donc non écologique. Le CF_3I a un bas

GWP_{100} de 1, un potentiel d'appauvrissement de l'ozone (ODP) presque nul et a montré des performances similaires à celles du SF_6 dans le mélange de gaz standard. Cependant, ce gaz n'a pas pu être utilisé dans la caverne du LHC pour des raisons de sécurité en raison de ses niveaux de toxicité mutagène supérieurs à ceux actuellement acceptés. Enfin, Amolea™ 1224yd, un gaz de la famille des Hydro-Chloro-Fluoro-Oléfines a été testé. Les résultats ont montré une performance similaire à celle du mélange gazeux standard lorsqu'il est utilisé à une concentration de 0,3-0,5%. Le gaz a également un $GWP_{100} < 1$ et ODP = 0, ce qui en fait une alternative écologique précieuse au SF_6. Cependant, son point d'ébullition relativement élevé de 15 °C rend le gaz difficile à utiliser à des débits élevés.

Quelques mélanges gazeux sélectionnés ont ensuite été testés dans un dispositif RPC dédié construit à la Gamma Irradiation Facility (GIF++), située dans la zone nord sur la ligne de faisceau H4. Le system s'est composé de trois détecteurs RPCs single gap de 2 mm installés dans la zone d'irradiation GIF++, où une source de 137Cs de 13,4 TBq et la présence d'un faisceau de muons nous ont permis de tester les performances des RPC dans les environnements similaires à LHC et HL-LHC. Les performances des RPC ont été évaluées pendant la durée du faisceau de muons en effectuant plusieurs prises de données à tension et conditions d'irradiation differents. Les principaux paramètres des RPC ont ensuite été interpolés au point de fonctionnement pour les différents taux gamma et une étude sur le comportement des courants, l'efficacité, le point de fonctionnement, la cluster size et la résolution temporelle a été menée. Les résultats préliminaires ont montré une performance similaire entre le mélange de gaz standard et les mélanges de gaz à base d'hélium. Les mélanges gazeux à base de CO_2 ont montré au contraire un courant plus élevé et une baisse d'efficacité légèrement supérieure pour des taux de 500 Hz/cm^2. L'utilisation du R-1234ze sans R-134a nécessité des concentrations plus élevées de CO_2, conduisant à une plus grande chute d'efficacité pour les taux de fond attendus du HL-LHC. R-1234ze et R-134a avec l'ajout de CO_2 ou d'hélium se sont avérés être un bon compromis entre les performances des RPC et le GWP_{100}. Novec™ 4710 et Amolea 1224 yd ont été testés, confirmant les résultats obtenus dans des conditions de laboratoire et pouvant être utilisés comme substituts appropriés du SF_6. En outre, l'Amolea 1224 yd a également été testé à la place de l'i-C_4H_{10} afin de comprendre les éventuelles propriétés d'extinction du gaz pour aider à réduire la suppression des streamers. Enfin, des études sur les impuretés produites par les RPCs en présence du rayonnement de fond ont été lancées. Les RPCs ont été exploité à pleine efficacité avec le mélange gazeux standard et avec un mélange gazeux à cinq composants R-1234ze/R-134a/CO_2/i-C_4H_{10}/SF_6 27,25/27,25/40/4,5/0,3. La production de HF à la sortie des chambres a été mesurée avec des électrodes sélectives d'ions. Il a été constaté que lorsqu'il fonctionnait avec le même rendement et dans les mêmes conditions de base, le mélange gazeux à base de R-1234ze produisait environ 4 fois plus de HF que les mélanges gazeux standard, ce qui indique que le R-1234ze pourrait produire environ un ordre de grandeur de HF de plus que le R-134a. Des études sur les performances à long terme des RPCs exploités dans des environnements similaires à ceux du LHC ont été lancées. Les performances du système gazeux en termes de distribution du gaz et d'efficacité de l'épurateur dans l'élimination du HF sont actuellement étudiées.

Quelques mélanges gazeux sélectionnés ont ensuite été testés dans un dispositif RPC dédié construit à la Gamma Irradiation Facility (GIF++), située dans la zone nord sur la ligne de

faisceau H4. Le system s'est composé de trois détecteurs RPCs single gap de 2 mm installés dans la zone d'irradiation GIF++, où une source de 137Cs de 12,5 TBq et la présence d'un faisceau de muons nous ont permis de tester les performances des RPC dans les environnements similaires à LHC et HL-LHC. Les performances des RPC ont été évaluées pendant la durée du faisceau de muons en effectuant plusieurs prises de données à tension et conditions d'irradiation differents. Les principaux paramètres des RPC ont ensuite été interpolés au point de fonctionnement pour les différents taux gamma et une étude sur le comportement des courants, l'efficacité, le point de fonctionnement, la cluster size et la résolution temporelle a été menée. Les résultats préliminaires ont montré une performance similaire entre le mélange de gaz standard et les mélanges de gaz à base d'hélium. Les mélanges gazeux à base de CO_2 ont montré au contraire un courant plus élevé et une plus grande chute d'efficacité pour des taux de 500 Hz/cm2. L'utilisation du R-1234ze sans R-134a nécessité des concentrations plus élevées de CO_2, conduisant à une plus grande chute d'efficacité pour les taux de fond attendus du HL-LHC. R-1234ze et R-134a avec l'ajout de CO_2 ou d'hélium se sont avérés être un bon compromis entre les performances des RPC et le GWP100. Novec™ 4710 et Amolea™ 1224yd ont été testés, confirmant les résultats obtenus dans des conditions de laboratoire et pouvant être utilisés comme substituts appropriés du SF_6. En outre, l'Amolea™ 1224yd a également été testé à la place de l'i-C_4H_{10} afin de comprendre les éventuelles propriétés du quenching du gaz pour réduire les streamers. Enfin, des études sur les impuretés produites par les RPCs en présence du rayonnement de fond ont été lancées. Les RPCs ont été exploité à pleine efficacité avec le mélange gazeux standard et avec un mélange gazeux à cinq composants R-1234ze/R-134a/CO_2/i-C_4H_{10}/SF_6 27,25/27,25/40/4,5/0,3. La production de HF à la sortie des chambres a été mesurée avec des électrodes sélectives d'ions. Il a été constaté que lorsqu'il fonctionnait avec le même rendement et dans les mêmes conditions de base, le mélange gazeux à base de R-1234ze produisait environ 4 fois plus de HF que les mélanges gazeux standard, ce qui indique que le R-1234ze pourrait produire environ dix fois plus de HF que le R-134a. Des études sur les performances à long terme des RPCs exploités dans des environnements similaires à ceux du LHC ont été lancées.

Contents

List of Figures

List of Tables

List of Abbreviations

CERN	**C**onseil **E**uropéen **R**echerche **N**ucléaire
LHC	**L**arge **H**adron **C**ollider
ALICE	**A** **L**arge **I**on **C**ollider **E**xperiment
ATLAS	**A** **T**oroidal **L**HC **A**apparatu**S**
CMS	**C**ompact **M**uon **S**olenoid
LHC	**L**arge **H**adron **C**ollider **b**eauty
MIP	**M**inimum **I**onizing **P**article
GHG	**G**reen **H**ouse **G**as
GWP	**G**lobal **W**arming **P**otential
RPC	**R**esistive **P**late **C**hamber
MFC	**M**ass **F**low **C**ontroller
GCS	**G**as **C**ontrol **S**ystem
HMI	**H**uman **M**achine **I**interface
SCADA	**S**upervised **C**ontrol **A**nd **D**ata **A**cquisition
UNICOS	**UN**ified **I**ndustrial **CO**ntrol **S**ystems
PLC	**P**rogrammable **L**ogic **C**ontroller
PCO	**P**rocess **C**ontrol **O**bject
PID	**P**roportional **I**ntegrative **D**erivative

1 High Energy Physics at CERN

The *Conseil Européen pour la Recherche Nucléaire* (CERN) is an international organization founded in 1954 with the current main activity set to fundamental research in particle physics. CERN's mission is to provide a unique set of particle accelerator facilities to enable research at the forefront of human knowledge, perform world-class research in fundamental physics and unite people from all over the world to push the frontiers of current technologies for the benefit of humankind. Among the several accelerator facilities, the Large Hadron Collider (LHC) accelerator complex and its experiments were designed to explore the physics of the Standard Model (SM) by studying the collision of high energy hadrons in a controlled environment. Predictions of the SM theory, such as the Higgs mechanism, were successfully tested by the discovery of the Higgs boson during the past run activities of LHC. However, the SM is incomplete as it raises some unanswered questions that require the study of physics beyond the model. The current LHC program and its future High Luminosity phase (HL-LHC) are designed to consolidate the SM predictions, observe rare events, and investigate the physics beyond the SM [1]. The present Chapter illustrates the design of the LHC complex and its accelerators, together with the physics studied at LHC and the foreseen infrastructure upgrades.

1.1 The Large Hadron Collider

The Large Hadron Collider is the world's largest and most powerful particle accelerator and collider that allows scientists to probe matter's structure at the tiniest possible dimension. It consists of two circular, 26.7 km, superconducting rings located 100 meters below the ground, located on the Franco-Swiss border near Geneva, Switzerland. LHC was installed in the tunnel constructed between 1984 and 1989 for the CERN Large Electron-Positron (LEP) collider. The first LHC beam was delivered in 2008, with the first collisions produced around 2009. LHC is initially supplied with pre-accelerated protons from the Injection chain. Negative Hydrogen ions H^- are initially supplied to the linear accelerator, initially LINAC2 and currently replaced by LINAC4, providing H^- with energies up to 160 MeV. The ions reach then the Proton Synchrotron Booster (PSB), made up of four superimposed synchrotron rings that strip out the electrons from the protons, which are then accelerated up to 2 GeV for injection to the Proton Synchrotron (PS). A further acceleration stage is ensured by the Super Proton Synchrotron (SPS), a 7 km circumference accelerator where protons are brought up to 450 GeV. The SPS provides beam then to the LHC and other North Area (NA) experiments, such as NA61/Shine, NA62, COMPASS and many test facilities. A schematic representation of the accelerator complex is reported in Figure 1.1

Inside the LHC, two-particle beams travel in opposite directions in separate beam pipes kept at ultra-high vacuum. The particles are guided around the accelerator and squeezed

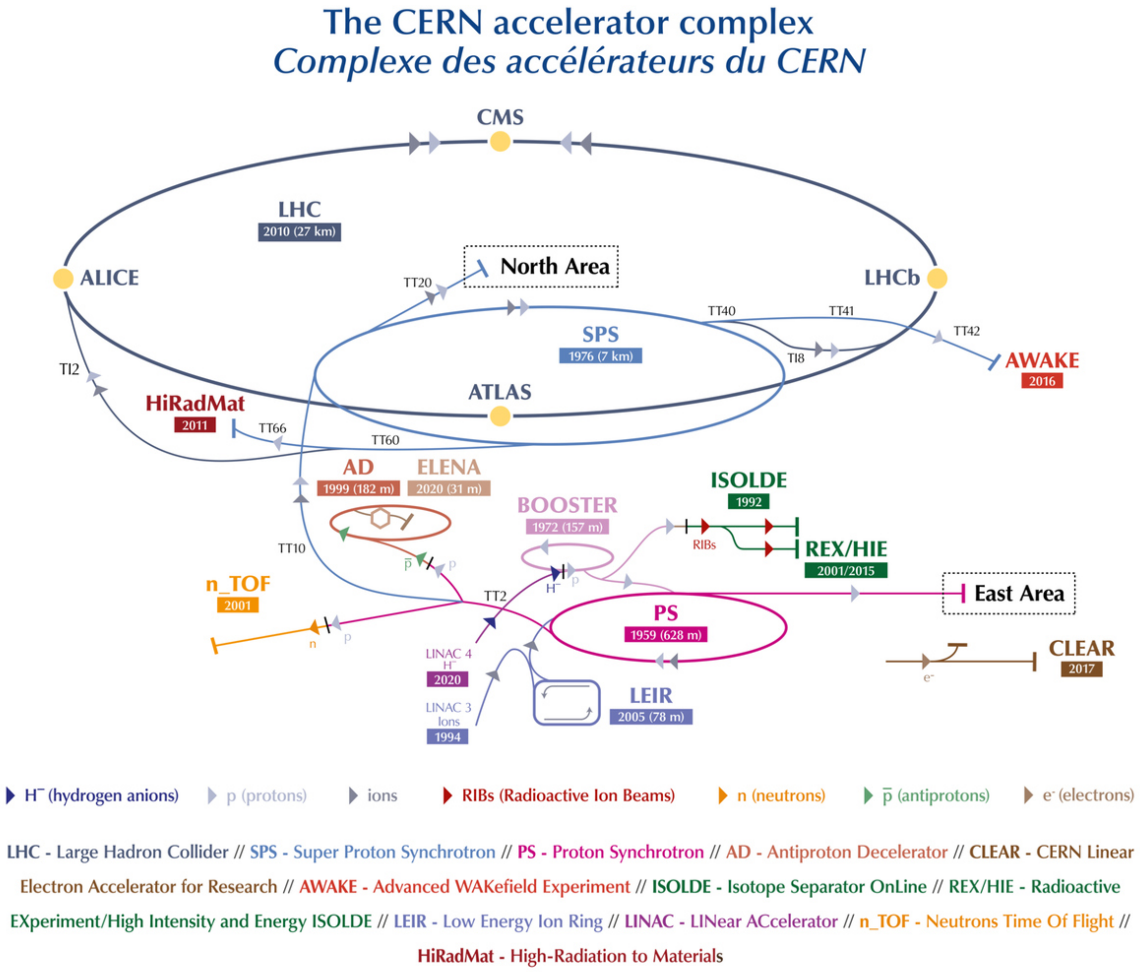

FIGURE 1.1 – the CERN accelerator and experiments complex [2].

into bunches using a set of 1232 superconducting dipoles and 474 quadrupoles. At the nominal energy of 7 TeV, a magnetic field of around 8.4 T in the magnets is generated, with a current of 11.7 kA flowing in the superconducting elements made of Niobium-Titanium (NbTi) material cooled down at the temperature of 1.9 K with superfluid Helium. The LHC can nominally provide center-of-mass energy of 14 TeV for proton-proton collisions and 1045 TeV for Pb-Pb ones, created by 2556 bunches containing 1.15×10^{11} protons each, with a bunch spacing of 25 ns and contained in a beam size of 2.5 μm. The LHC baseline program aimed to produce results with an initial luminosity of at least one fb^{-1} by the end of 2011 and 4-8 fb^{-1} by the end of 2012. During the first run period in 2011-2012, LHC delivered proton collisions at 7 and 8 TeV center-of-mass energies, accumulating around 26 fb^{-1} of luminosity, a value beyond the expectations initially set culminated with the announced discovery of the Higgs boson on July 4th, 2012.

1.2 Overview of experiments at LHC

The fundamental purpose of LHC is to understand the present content of the Universe and its evolution since the Big Bang by exploring the inner structure of matter and the forces that govern its behavior. The high center-of-mass energy allows the production of massive particles predicted by the SM, while a high luminosity provides access to rare events. In order to better study these phenomena, LHC was designed to have four interaction points where collisions happen. Four different experiments around each interaction point, namely ALICE, ATLAS, CMS, LHCb, were built [3].

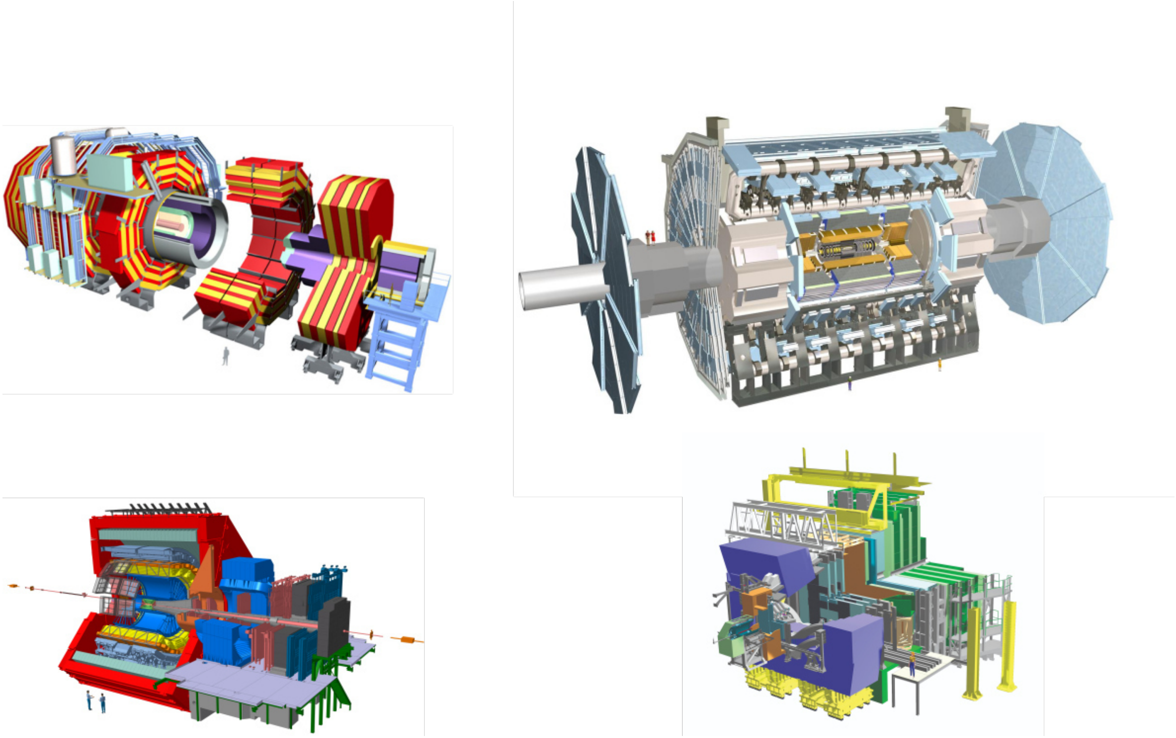

FIGURE 1.2 – The four LHC experiments, CMS, ATLAS, ALICE and LHCb [4, 5, 6, 7]

A Large Ion Collider Experiment (ALICE) is an experiment optimized for studies of quark-gluon plasma physics at high energy density values in nuclei collisions. Quark-gluon plasma

	ALICE	**ATLAS**	**CMS**	**LHCb**
Total weight [10^3 kg]	10000	7000	12500	5600
Length [m]	26	46	20	21
Diameter [m]	22	15	16	
Magnet	Solenoid/dipole	Toroid + Solenoid	Solenoid	Dipole

TABLE 1.1 – Main design parameters of the four LHC experiments

is of particular interest for SM physics as it is thought to be the primordial state of the Universe during the first Big Bang phases before quark and gluons bounded together to form protons and neutrons. ALICE focuses on physics close to region $\eta \approx 0$ and on the region -4.0 < η < -2.5. The region with midrapidity orthogonal to the beamline is equipped with a central barrel detector, while the forward region was designed to have a single-arm muon spectrometer to study the complete spectrum of heavy quarkonia via the $\mu^+\mu^-$ channel decay.

A Toroidal LHC ApparatuS (ATLAS) and Compact Muon Solenoid (CMS) are general-purpose experiments with extensive physics goals. They consists of a cylindrical barrel region with two end-cap sections. The main difference between ATLAS and CMS lies in their lever arm size and magnetic configuration. As the muon momentum resolution $\Delta p_T/p_T$ of the LHC experiments is proportional to $B^{-1}L^{-2}$ should be better than 10% for muons energy up to 1 TeV, ATLAS has a longer lever arm while CMS has a compact lever arm but a stronger magnetic field: CMS is equipped with a solenoidal magnetic field of 3.8 T in the barrel region, while ATLAS uses an extended combination of a toroidal magnetic field of 1 T in the muon system and an additional 2 T solenoid surrounding the inner region.

The Large Hadron Collider beauty (LHCb) experiment measures heavy-flavor physics by studying CP violations and rare decays of beauty and charm hadrons. It is a single-arm forward spectrometer that exploits the fact that bb$^-$ pairs are mainly produced in the forward direction. The first sub-detector is mounted close to the collision point, with the others following one behind the other over a length of 20 meters.

Different experiments have different physics goals and design layouts, but common design principles were adopted to detect particles in collision events. Each experiment measures neutral and charged particles with a proper momentum resolution and high granularity. All experiments were designed to be efficient after years of operation in the harsh LHC environment. Several different sub-detectors are employed in the experiments for different purposes:

Inner tracking detectors

Tracking detectors are the first detectors encountered by particles emerging from the collisions at the interaction point. Tracking detectors are typically composed of different layers in which different technologies are employed. In particular, high-precision pixel detectors are typically employed in the innermost layers, while tracking silicon or gaseous detectors are used in the outermost regions.

Calorimeters

Electromagnetic and hadronic calorimeters are used to measure the energy and momentum of hadrons, electrons, and photons produced at the interaction points or as decay products of other unstable particles. The calorimeters' size was designed so that most of the showers are entirely contained in the volume of the detecting elements to optimize the energy resolution. Another essential feature of LHC calorimeters is the generation of fast trigger signals response, which decides if a collision event is interesting enough to be recorded for further data analysis.

Muon spectrometers

The LHC physics performance depends on the trigger efficiency and momentum resolution muons up to the TeV scale of p_T. Dedicated sub-detectors are needed as muons escape calorimeters. Muon spectrometers are typically installed in the outer regions of the experiment's detector. Gaseous particle detector technologies are employed, which have the advantage of having a large radiation length X_0 and can cover large areas for relatively lower prices than other detector technologies.

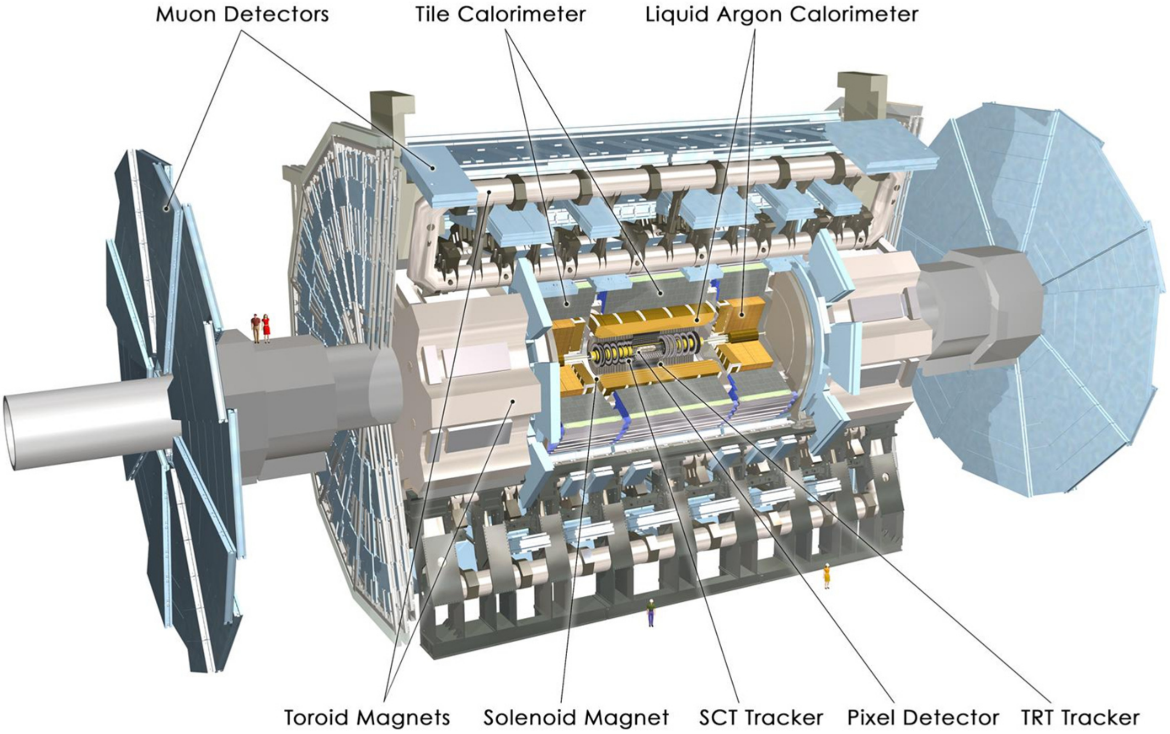

FIGURE 1.3 – schema of the sub-detectors of the ATLAS apparatus.

1.3 The High Luminosity LHC project and future upgrades

After the Long Shutdown (LS) 1 period, LHC underwent a series of upgrades that enabled it to operate from 2015 at center-of-mass energies of 13 TeV. However, after the Run 2 period ended in 2018, the statistical gain in running the accelerator without a considerable luminosity increase beyond its design value would have become marginal. In May 2013

CERN council adopted the European Strategy for Particle Physics that stated that «[...] Europe's top priority should be the exploitation of the full potential of the LHC, including the high-luminosity upgrade of the machine and detectors with a view to collecting ten times more data than in the initial design, by around 2030 [...]». The High Luminosity LHC (HL-LHC) project was defined to allow LHC to deliver an increased instantaneous luminosity around five times beyond the original design value and about ten times more the integrated luminosity over the LHC lifetime. The HL-LHC project will provide more accurate measurements of new particles and enable the observation of rare processes below the current sensitivity level. The project was approved as a priority project in the EU Strategy Report for High Energy Physics and the approval of its budget by the CERN Council (Medium Term Plan 2015). This major upgrade is now in full swing of implementation together with its companion upgrade programs of the LHC injectors upgrade (LIU) and detectors (ALICE, ATLAS, CMS, LHCb).

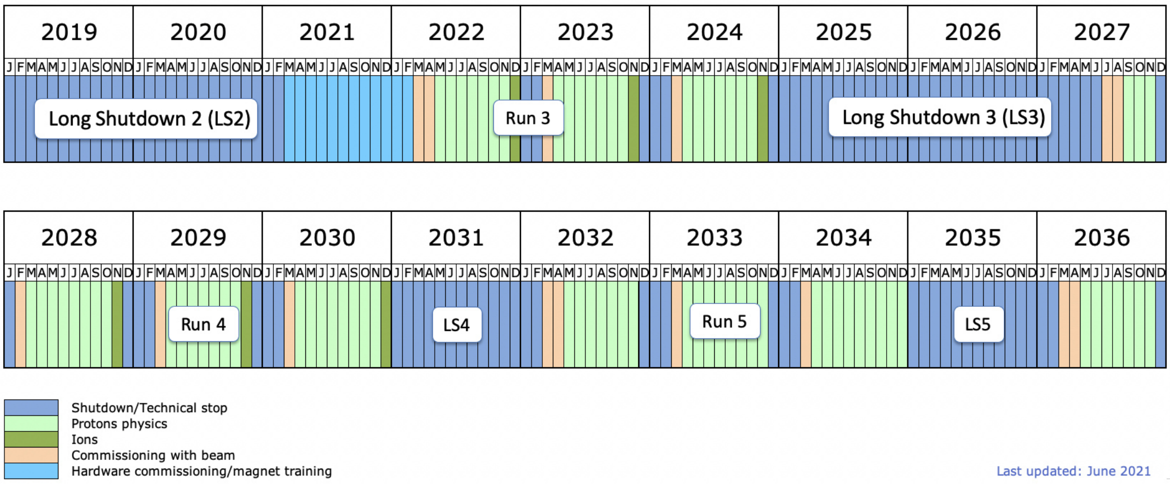

FIGURE 1.4 – LHC baseline schedule as of June 2021

The upgrade of the accelerator complex will pose several technological challenges, requiring significant upgrades for the accelerator: [8]:

- *Inner Tripler Magnets*: After one year of HL-LHC operation, some components of the low-beta quadrupoles magnets will integrate a dose entering the region of radiation damage that may result in electric breakdowns. The low-beta triplet will be replaced, though the intervention will require around two years of shutdown.
- *Cryogenic system*: The cryogenic system will undergo several upgrades aiming at separating the magnet cooling from the Superconducting Radio Frequency system.
- *Collimator and dipoles*: The current LHC dipoles will be replaced with shorter ones, providing a more intense magnetic field. The gained space will allow the installation of special collimators.
- *Quench Protection System*: new improved protection mechanism based on a modern design will be employed to avoid the QPS becoming the bottleneck along with the ageing of the machines.

Together with the accelerator, the LHC experiments foresee significant upgrades to their detectors:

ALICE[9]

The complete characterization of the properties of the quark-gluon plasma requires precise measurements of light and heavy flavor over a wide momentum range. Major upgrades will be reported to the experimental apparatus during Run 3 and Run 4, consisting of improving track reconstruction performance for low momentum particles, both in terms of spatial resolution and efficiency. The upgraded system will allow a more effective selection of the decay vertices of heavy-flavor mesons and baryons. The readout rate will be increased to rates up to 50 kHz for Pb-Pb collisions in continuous readout mode, enabling to record a sample of minimum-bias collisions around two orders of magnitude larger than the one collected during Run 2. In order to reach the desired goals, the detector will be equipped with a new Inner Tracking System (ITS) of seven layers made with Monolithic Active Pixel Sensors (MAPS). The hit resolution of the detector will be about 5 μm, and the material budget of the three innermost layers will be reduced from the present 1.1% to 0.3% of the radiation length. The new performance of the ITS is expected to provide an improvement of factor three for the track impact parameter resolution. A new Muon Forward Tracker (MFT) placed along the beam axis between -460 mm and -768 mm from the interaction point will be instrumented with the same MAPS used in the ITS to provide precise tracking and secondary vertex reconstruction for muon tracks in the region $-3.6 < \eta < -2.5$. In order to enable continuous Pb-Pb readout at a rate of 50 KHz while keeping the same transverse momentum resolution, new readout chambers for the Time Projection Chamber (TPC) based on the Gas Electron Multiplier (GEM) technologies were installed. Also, a significant upgrade of the readout electronics of the Time Of Flight TOF, MUON, and ZDC detectors is expected to enable recording to the foreseen Pb-Pb rate of 50 kHz.

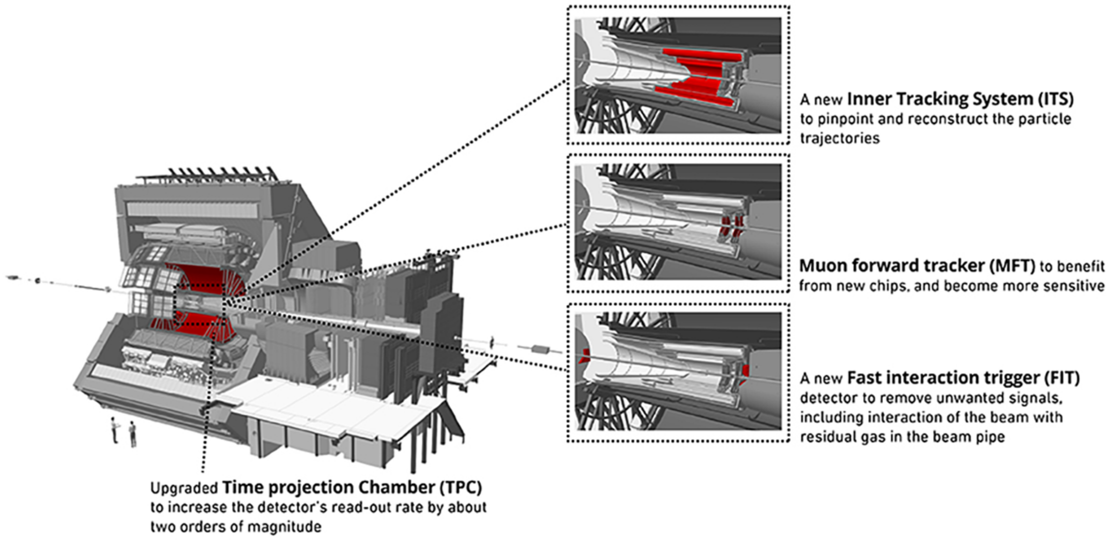

FIGURE 1.5 – Schematic drawing showing the upgraded sub-detectors of the ALICE apparatus.

ATLAS[10]

An upgrade of the Trigger and Data Acquisition system (TDAQ) will be necessary to enable more complex triggering and improve the bandwidth, increasing acceptance for many physics processes. The experiment is expected to process regional tracking at rates of 40 MHz, while global tracking rates will be around 100-200 KHz. A new silicon Inner Tracking detector (ITk), consisting of an inner pixel and outer strip detector, will replace the current one. The total surface area of silicon in the new pixel system will measure about 13 m^2. The strip detector will comprise 165 m^2 of silicon. A High Granularity Timing Detector (HGTD), based on a low-gain avalanche silicon sensor, will be installed in the region $2.4 < \eta < 4$, covering an area of about 6.4 m^2. The detector timing performance is expected to be around 30-50 ps, allowing the mitigation of pile-up effects and improving the track-to-vertex resolution. The Liquid Argon (LAr) and Tile calorimeters electronics will be upgraded to improve radiation tolerance limits. The Muon Spectrometer will also undergo several upgrades, detailed in the next Chapter of this thesis.

CMS[11]

Similar to the ATLAS experiments, new tracking detectors will be installed. The inner tracker will feature a small pixel sensor, while the outer tracker will be equipped with a strip and macro pixel sensor instead. A high granularity calorimeter (HGCAL) will be installed to cover the region $1.4 < |\eta| < 3$ based on silicon sensors. New muon detectors will be installed to complement the existing ones, extend the coverage, improve the acceptance and increase the redundancy. A dedicated minimum ionizing particle (MIP) timing detector (MTD) will be used to record time-of-flight information to help distinguish particles originating from interesting vertices. A new luminometer based on forward pixel rings will provide a more accurate luminosity measurement and additional redundancy.

LHCb[12]

The LHCb detector will be upgraded to overcome the hardware-based trigger limiting the amount of data taken and to allow the sub-detectors systems to withstand the increased radiation-induced damage. Most components will be unchanged during the upgrade, except for a new pixel vertex detector replacing the current VErtex LOcator (VELO) detector. The Trigger Tracker (TT) stations will be replaced by new silicon microstrip Upstream Tracker (UT) stations and the straw outer chamber were recently replaced with scintillating fibers detector (SciFi). A new trigger-less frontend electronic system capable of reading out the detector at the LHC clock frequency will be installed in the next LHC runs, with new and novel chips redesigned for pixel sensors, UT, and RICH detectors. The hardware-based trigger will be replaced to efficiently run the detector at higher luminosity, with event selection happening by the software-based High-Level Trigger (HLT). The increased event rate will be handled by an upgrade on the software trigger network that enables the handling of a multi-terabyte data stream.

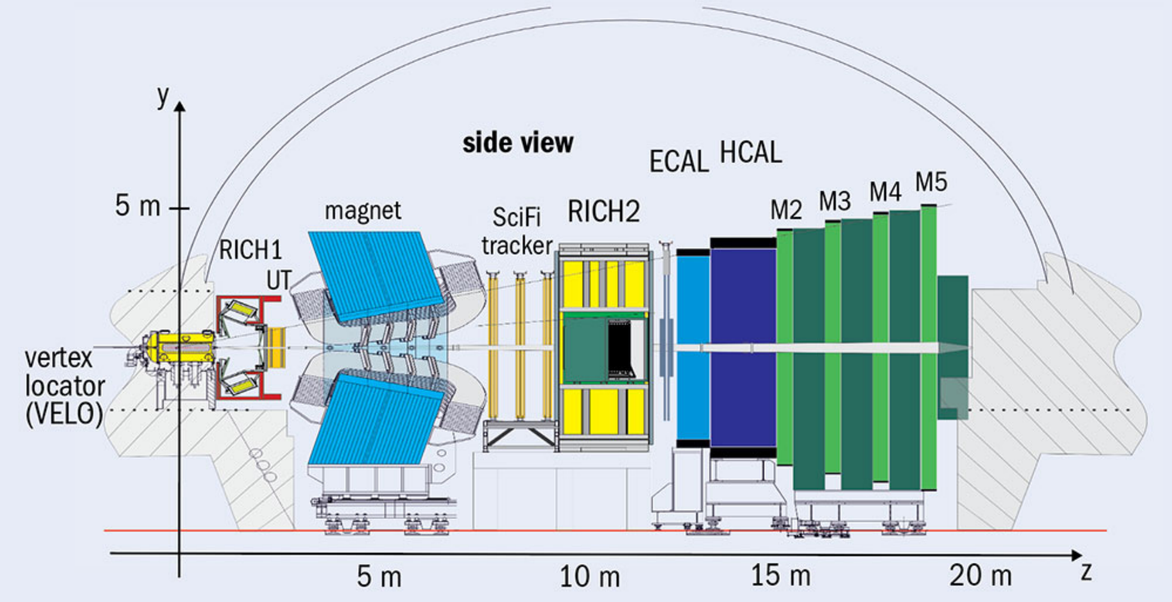

FIGURE 1.6 – Cross-section of the LHCb detector elements. Credit: LHCb

2 Muon systems at LHC

Muons can easily escape the electromagnetic and hadronic calorimeters. The detection of muons is a fundamental process in the framework of the LHC physics program, as they provide clean probes on many events of interest. The four main LHC experiments are equipped with muon spectrometers based on gasesous detector technologies used for event trigger, veto selection, and tracking purposes. Each Experiment's muon detection system is specifically designed for the Experiment's physics program, vastly differing in terms of physical layout and performance from the other Experiments' muon systems. The present Chapter aims at providing an overview of the currently installed muon systems at the LHC experiments. The first part is dedicated to gaseous detectors and their working principle. The different layouts and performance are discussed. Next, an overview of the current LHC muon systems is given regarding their technical requirements, design, and layout. The LHC gas systems are discussed in Chapter 3. Lastly, the different gas mixtures employed for the muon sub-detectors are discussed, focusing on the performance requirements, safety, and environmental concerns.

2.1 Gaseous Detectors

When a charged particle crosses a gas medium, it can interact with the gas molecules. If the energy left by the charged particle is high enough, it can ionize the gas molecule and create a set of ion-electron pairs along its track. When an electrical field is applied, such pairs start to accelerate. Electrons have a mobility around three order of magnitude higher than ions, so they are the main ones responsible for initiating new ionization processes along the gas volume. The accelerating electrons that are not lost by recapture processes may gain sufficient energy to ionize as well other gas molecules. This chain process is typically referred to as avalanche multiplication and largely depends on several factors, such as the gas itself, the gas volume geometry, and the electric field magnitude and geometry. The region where the applied electric field is proportional to the developed charge is typically the region of interest for most modern gaseous detectors as it depends on the Minimum Ionizing Particle (MIP) momentum. When further increasing the electric field, the proportionality between with the collected charge is broken: such region, oftern referred to as the Geiger region, is typically employed by radiation detectors as it allows to detect ionizing particles without the need for sophisticated readout electronics. After the Geiger region, a discharge in the gas-filled volume may happen, leading to a plasma region between the electrodes known as Corona discharge.

The dynamics of the avalanche mechanism were studied by John Sealy Townsend at the beginning of 1900. It was observed that the process depended on the ratio between the intensity of the electric field E and the density of the gas n. An electron moving along the

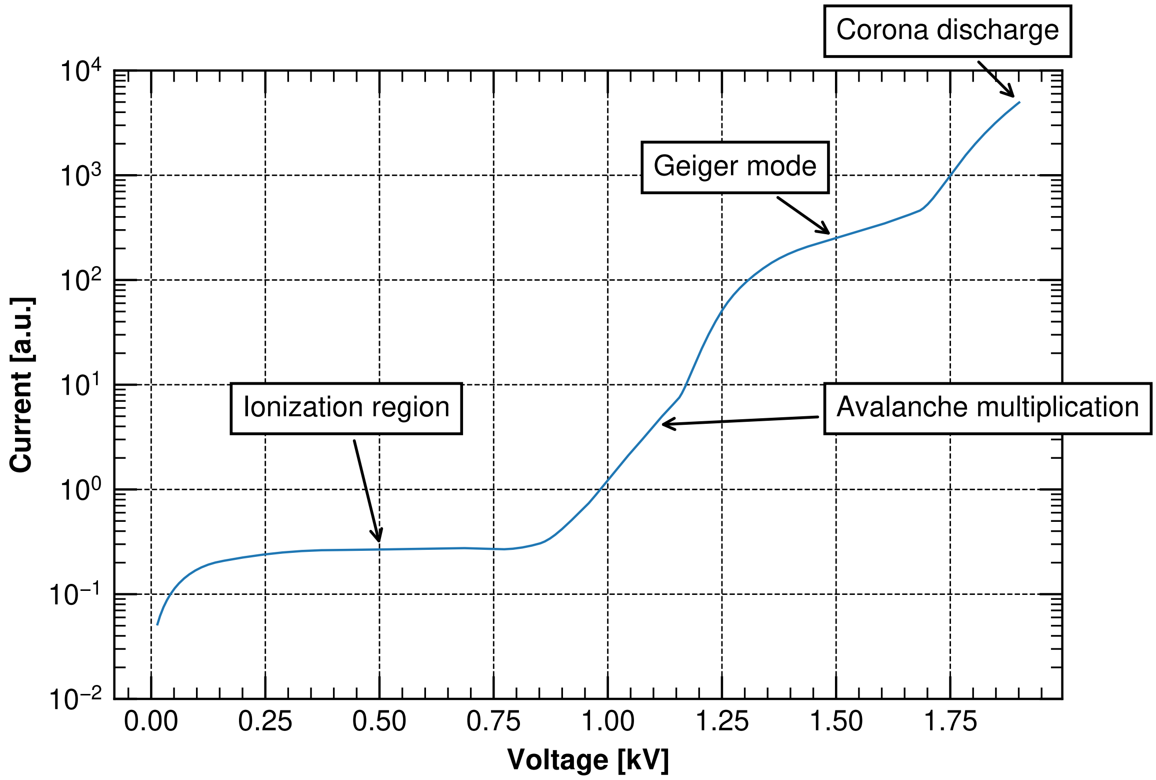

FIGURE 2.1 – Ionization regions: current gain versus applied voltage.

gas-filled volume experiences both elastic collisions that change the direction of its motion but do not change its energy, and elastic collision, where the electron can transfer part of its energy to another molecule in the gas. In the simplest case of an electric field parallel to the x axis, the increase of free electrons $\mathrm{d}n_e$ in an avalanche process can be described by the number of free electrons present n_e starting an avalanche in the infinitesimal space $\mathrm{d}x$ by:

$$\mathrm{d}n_e = \alpha n_e \,\mathrm{d}x \tag{2.1}$$

Where α is the so-called Townsend first coefficient, expressing the number of free electrons created per unit length. If n_0 free electrons are initially present at x=0, then the number ne of avalanche-created electrons at x=d is:

$$n_e = n_0 \exp(\alpha d) \tag{2.2}$$

with $\exp(\alpha d)$ often referred to as the gas gain. The development of the avalanches depends on their size. When sufficiently large, space-charge effects may lead to the modification of the local electrical field, thus changing the dynamic of the development of the avalanche itself. The charge development mechanism was initially exploited in the 1950s by constructing pulsed parallel spark detectors, operated by applying a short (in the order of microseconds) high electric field to a gas-filled volume whenever an external trigger was provided to the detector. The devices were operated in pulsed mode as an applied continuous electric field was somewhat unstable due to the breakdowns happening in the presence of a large number of primary electrons, imperfections on the surface of the electrodes, and after pulses observed following the primary avalanches. Together with parallel geometry, the development of cylindrical configuration detectors, based on anode wires, was largely studied. In particular, Single Wire Proportional Chambers (SWPC) were designed as cylinders acting as a cathode with a wired centered along the z axis used as the anode. The radial electrical of a SWPC chamber field can be described by:

$$E(r) = \frac{V}{r \ln(b/a)} \tag{2.3}$$

where r is the distance from the center, b is the radius of the anode wire and a is the cathode radius. The avalanche process only begins when the electric field is high enough, thus only when free electrons are close enough to the anode wire. It is important to note that, differently from parallel field geometry detectors, the ionization region of cylindrical detectors may not correspond to the ionization one. The electron drift times before starting an ionization may significantly differ between each other, depending on the distance from the center where the primary ion-electron pair was created. In 1968, Multi Wire Proportional Chambers (MWPC) were invented. They consisted of two cathode parallel planes, organized in a strip layout with a pitch of a few millimeters. Within the two cathode planes, an array of anode wires was inserted. The overall charge development process was very similar to an array of SWPC. MWPCs set the basis for modern gaseous detectors, such as Drift Tubes, Time Projection Chambers, and Ringing Imaging Cherenkov Detectors, thanks to their triggering and tracking performance. The recent advance in the development of micro-mesh structures allowed the construction of the so-called Micro Pattern Gaseous Detectors (MPGD). MPGDs detectors were initially designed to overcome the main rate and tracking limitations of MWPCs. Typically, the multiplication region is separated from the drift region, and sub-mm meshes are employed to create multiplication regions with high gains. Remarkable detectors in the MPGD family include Micro-mesh gaseous structures (Micromegas) and Gas Electron Multipliers (GEM). MPGDs were more resistant to radiation damage to MWPCs and could achieve higher rate capability. Recently, the MPGDs were also installed at CERN LHC experiments. In particular, GEMs at the LHCb experiments were employed during Run 1 and Run 2, while Micromegas was installed on the ATLAS New Small Wheel (NSW) during the LS2 phase, and CMS was equipped with GEM detectors for the next LHC Runs.

2.2 Muon spectrometers at LHC

In the present section, a short overview of the currently installed muon sub detectors at the different LHC experiments is discussed, focusing on the requirements of each experiment and the detectors systems upgrade performed during the LS2 phase.

ALICE[13]

The ALICE Muon Spectrometer's primary goal is to study measurements of heavy quarks in Pb-Pb, Pb-A, A-A collisions via the muonic channel. The muon spectrometer allows for measuring muons and quarkonia production in an intermediate rapidity range $-4.0 < y < -2.5$, and it is located downstream of the ALICE detector covering the angular range $171^\circ <$

$\theta < 178°$, consisting of 3 absorbers, a muon magnet, a trigger system, and a tracking system. The absorber reduces the main particle flux originated by the nuclei collisions by a factor of 100 and protects detectors from low-energy particles created by secondary interactions. A magnet is installed downstream of the absorber, and it generates a magnetic field of 0.7 T perpendicular to the beam axis that is used to measure muons momenta by tracking their path along the field. The trigger system is located between 16 m and 17 m downstream of the interaction point and consists of 4 planes of 18 Resistive Plate Chambers (RPCs) operated in saturated avalanche mode with an R-134a/i-C_4H_{10}/SF_6 89.7/10/0.3 gas mixture. The time resolution with the current detector and front-end electronics is around 2 ns, suitable for LHC bunch crossing identification. Starting from Run 3, the RPCs will be operated in continuous readout mode (as opposed to the previous trigger operated mode), and the information from the four trigger detection planes will be processed locally to determine the type of event (low p_T or high p_T). The information will be later sent to the ALICE central trigger processor to generate a level 0 trigger. The muon tracking system uses muon tracking chambers (MCH) to measure the transverse muon momenta in the bending plane p_{zy}. The tracking system comprises five stations with two detection planes consisting of 5 mm Drift Multi Wire Proportional chambers with bi-Cathode Pad read-out, providing a spatial resolution better than 100 μm.

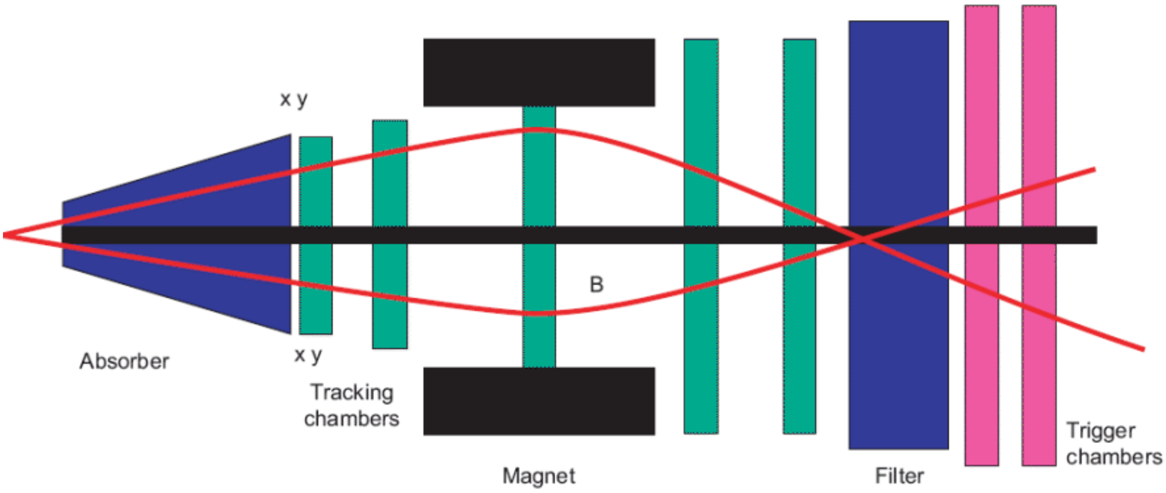

FIGURE 2.2 – Schema of the ALICE Muon Spectrometer

ATLAS[14]

The ATLAS muon spectrometer is the world's largest muon spectrometer. It comprises three stations in the barrel and endcap regions (inner, middle, and outer), designed to detect charged particles exiting the calorimeters. Monitored Drift Tubes (MDT) are used as precision-tracking chambers in the full angular acceptance, with the exception of the End-cap Inner region $2 < |\eta| < 2.7$, where Cathode Strip Chambers were initially employed and currently replaced with the New Small Wheel containing Micromegas and small Thin Gap Chambers (TGC) detectors. The trigger system is achieved using RPCs and TGCs in the barrel ($|\eta| < 1.05$) and endcap ($1.05 < |\eta| < 2.4$) regions, respectively, thanks to their excellent time resolution.

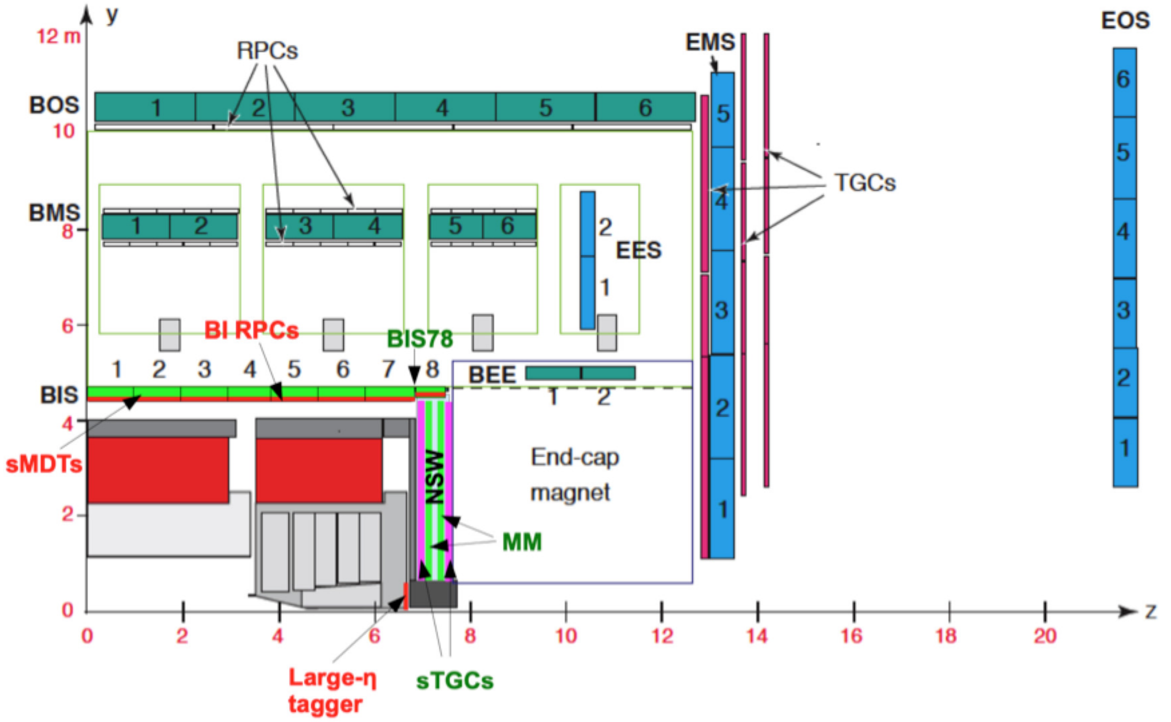

FIGURE 2.3 – y-z view of the Phase II upgrade for the ATLAS muon spectrometer for the Large sector[15]

Given the HL-LHC physics program, the muon spectrometer needs to cope with a foreseen rate of 1 MHz for muon momenta of 20 GeV, which is currently not possible with the installed electronics. A two-phase upgrade program for the muon spectrometer was designed to enhance the rate capability of the spectrometer. The phase I upgrade was successfully performed during the LS2 period and included the installation of two NSW on side A and side C of the ATLAS detector. Also, the installation of RPC triplets for the BIS78 project was done to perform measurements in the $1 < |\eta| < 1.3$ region. The phase II upgrade foresees the installation of new RPCs and TGCs trigger layers both in the barrel and endcap regions, the reduction of fake trigger muons combining the information from the NSWs and TGCs, and the use of MDTs as a trigger to improve muon momenta resolution. In the inner region of the barrel, new 1 mm gap RPCs triplets will be installed to enlarge the acceptance and the efficiency of the trigger.

CMS[16]

Muons are part of many analyses performed within the CMS physics program. For this reason, the CMS experiment is equipped with a large superconducting coil generating a solenoidal magnetic field of around 4 T and by an iron yoke. The yoke is divided into five wheel sections in the barrel region and a group of four endcap disks at each end side of the detector. The iron yoke is equipped with a robust and redundant muon system that provides standalone trigger capabilities, muons identification, and momenta measurement. The pseudorapidity region $|\eta| < 1.2$ is covered by four stations of drift tubes chambers installed in the barrel. In the endcap section Cathode Strip Chambers (CSC) cover the range $0.9 < |\eta| < 2.4$. The stations are used as tracking detectors and participate in the trigger. Additionally, a set of RPCs is installed in each barrel and endcap station to improve the trigger robustness, covering up to $|\eta| < 1.6$.

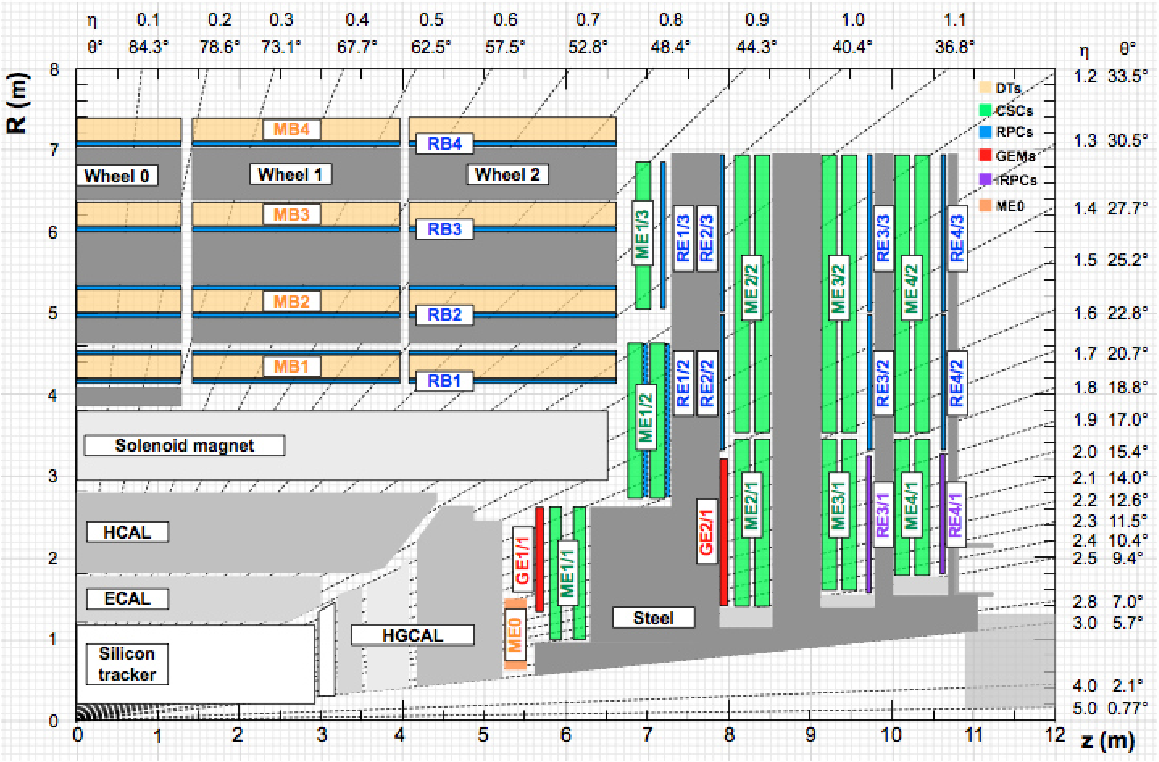

FIGURE 2.4 – r-z view of the muon stations foreseen to be installed in the CMS experiment[17]

The forward region will be instrumented with additional layers of new detectors based on triple-GEM technology to cope with the HL-LHC program's foreseen luminosity and trigger rate increase. The choice of the triple-GEM technology was driven by the detector's rate capability of up to tens of kHz/cm^2, a time resolution of $\approx$7 ns, and spatial resolution of $\approx$200 μm, which make them suitable for the purposes of the upcoming CMS operation. Two layers of GEM detectors named GE1/1 were successfully installed during the LS2 phase and will participate in CMS's Run 3 data-taking campaign. Two additional layers, named GE2/1 will be installed in 2023/2024, and six additional layers named ME0 are foreseen to be installed during the Long Shutdown 3 period expected to take place in 2025-2027. Figure 2.4 shows the final configuration of the muon stations that will be installed for HL-LHC run.

LHCb[7]

The LHCb experiment's main purpose is the study of CP violation and rare decays of beauty and charm hadrons. Muons are present in the final state of many CP-sensitive B decays. Muon identification is assured by five multi-layer stations along the beam axis designed to trigger with high efficiency on high p_T muon tracks within the 25 ns LHC bunch crossing window. Each muon station is equipped with 276, 5 mm gap MWPCs chambers. During Run 1 and Run 2, the high rate region was covered by 12 double layers of triple GEM detectors, removed then during the LS2 period. Electronics and detectors upgrades are foreseen in phase II upgrade [18]. New, highly radiation tolerant, Off Detector Electronics will replace the currently installed one and new, higher readout granularity and detectors will be installed in the central regions of the first stations to overcome the efficiency losses due to the increase of detector deadtime caused by the higher luminosities. A strong R&D campaign is currently ongoing on the micro-Resistive WELL (μWELL) detectors, a family of multi-pattern gaseous detectors that were designed to fulfill rate capability performance up to 3 MHz/cm2, an efficiency better than 95% in the time window defined by the bunch crossing (25 ns) and stability up to 6 C/cm^2 integrated charge in 10 years at G=4000.

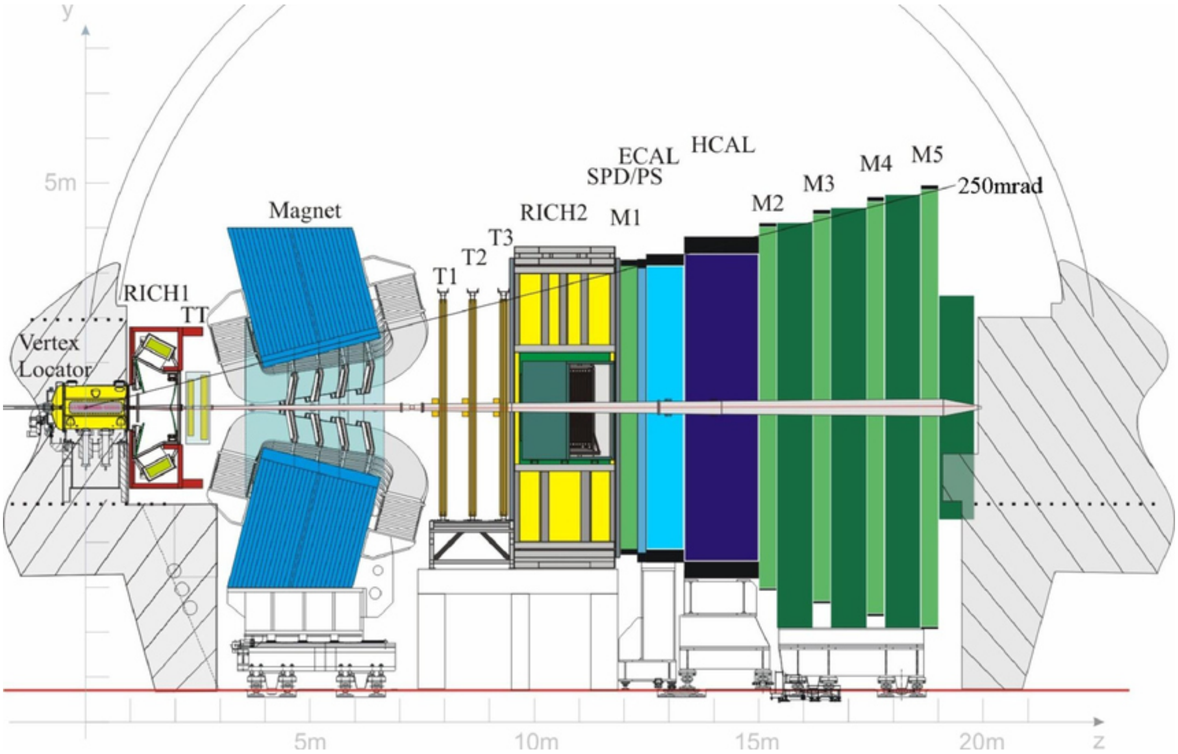

FIGURE 2.5 – Schema of the LHCb detector along the z axis. The muon system is identified by the M1-M5 stations[19].

2.3 Gas mixtures for LHC gaseous detectors

The previous sections show that muon detectors at LHC are gaseous detectors. Most gaseous detectors are operated with a well-defined gas mixture, depending on the type, geometry, and performance requirements. The gas mixtures used for the different gaseous detectors are reported in Table 2.1

Although each detector has a different gas mixture, few common gases can be identified. In particular, Argon is used by tracking chambers and MPGDs as it provides large amounts of ion-electron clusters, thus significant gains with high voltage. CO_2 is added to the tracking detectors thanks to its quenching properties to suppress streamers and reduce photon-feedback signals. Transition radiation trackers are operated with Xenon-based gas mixtures due to its high Z number. The high number of nucleons in Xenon leads to a higher cross-section for the photoelectric effect used to convert the transition radiation photons to a signal. Bakelite-based RPCs are operated with a three-component-based gas mixture with the addition of some water vapor. A main fraction of R-134a ($C_2H_2F_4$) is present in the mixture as it provides a high number of primary clusters, and at the same time, the presence of

Experiment	Detector	Gas Mixture
ALICE	MID	89.7/10/0.3 R-134a/i-C_4H_{10}/SF_6 + 40% RH
	TRD	85/15 Xe/CO_2
	TPC	∼85/10/5 Ne/CO_2/N_2
	TOF	93/7 R-134a/SF_6
	HMPID	CH_4
	CPV	80/20 Ar/CO_2
	MCH	80/20 Ar/CO_2
ATLAS	MDT	93/7 Ar/CO_2 + 700 ppm H_2O
	MicroMegas	93/5/2 Ar/CO_2/i-C_4H_{10}
	RPC	94.7/5/0.3 R-134a/i-C_4H_{10}/SF_6 + 40% RH
	TGC	55/45 n-C_5H_{12}/CO_2
	TRT	Xe or Ar + CO_2 based
	CSC	40/50/10 Ar/CO_2/CF_4
	DT	85/15 Ar/CO_2
	RPC	95.2/4.5/0.3 R-134a/i-C_4H_{10}/SF_6 + 40% RH
LHCb	RICH1	C_4F_{10}
	RICH2	CF_4
	MWPC	40/55/5 Ar/CO_2/CF_4

TABLE 2.1 – Gas mixtures used by the different LHC detectors.

fluorine atoms increases the electronegativity of the molecule, slowing down free electrons. i-C_4H_{10} is used as a quencher to suppress undesired photon-feedback effects originating from avalanche development, and a small concentration of SF_6 is further added to suppress streamer contamination. The addition of water vapor is required to maintain a constant resistivity of the electrodes and stabilize the detectors' performance. The ALICE MID gas mixture is flammable, while the ATLAS and CMS RPC gas mixtures are classified as non-flammable. Glass-based RPCs, mainly used in the ALICE TOF experiments, are instead operated without i-C_4H_{10} but with a considerable amount of SF_6 as its electronegativity improves the detector's time resolution. In wire-based detectors such as CSCs and MWPCs, some amount of CF_4 is used as an anti-aging additive which prevents wire deposit and polymerization. Fluorocarbon gases at room temperature and pressure are used as Cherenkov radiators; C_4F_{10} in LHCb RICH 1 and CF_4 in LHCb RICH 2 were chosen for their low dispersion. The refractive index is respectively 1.0014 and 1.0005 at 0 °C, 101.325 kPa and 400 nm. About 5% CO_2 is added in the gas mixture of RICH 1 to quench scintillation in the gas. A highly quenching gas mixture of n-C_5H_{12} and CO_2 is used in Thin Gap Chambers (TGC) to enable the detector to operate in saturated avalanche mode without streamers and to reduce the dependence of the signal from the incident angle of the impinging particle. The HMPID detector is operated with pure CH_4 gas since it is transparent to Vacuum Ultra Violet (VUV) radiation down to 130 nm, and it allows the chambers to be operated at a stable gas gain with no deterioration of quantum efficiency for the required rates.

2.4 Gas systems for particle detectors at LHC

Gas systems are responsible for providing a stable and controller gas mixture to the detectors in the experiments [20, 21]. A correct and stable gas mixture is fundamental for the detector's operation, as a slight variation of the gas in terms of pressure, composition, and quality may significantly affect the detector's performance. Thus, proper gas systems maintenance and operation constitutes a critical activity in the correct operation of muon systems. More than 30 gas systems were built across different LHC and non-LHC experiments. In order to simplify the design, construction, and operation, gas systems were built using a modularized approach. Each gas system module shares common traits and functionalities between different gas systems and is independent of other modules. Such modularity allows the reduction of human resources and minimization of maintenance and operation costs.

2.4.1 Gas system modules

The following gas modules are currently employed in LHC gas systems:

Mixer

The mixer unit takes individual gases from the primary gas supply lines and creates the required gas mixture and flow using a set of Mass Flow Controllers (MFC). Mixers can be set to operate at a constant injection flow or by injecting gas only when specific conditions are met, such as a drop of pressure in the loop system. Typical mixers consist of a rack installed in the surface's service building.

Distribution

Distribution modules are responsible for providing the gas mixture to the chambers. The flow is split into one or more channels, and it is measured by a set of individual input and output flowmeters, often referred to as flow cells. One or more distribution racks may be present for each gas system to allow a fine regulation of the gas to different areas of the detector complex. When multiple racks are present, the flow to each rack is regulated using a downstream pressure regulation placed at the module's input, and the flow of each channel is regulated using adjustable impedances. Distribution racks are often provided with a pressure transmitter to measure the pressure at the input of the module, at the detector level, and the return of the detector (the output of the module). Pneumatic control valves may be present to regulate the pressure of the detectors, typically in the order of a few millibars relative to the atmospheric pressure. The distribution racks are often installed in the proximity of the detector in the underground experimental cavern. During unforeseen stops or planned maintenance of the distribution module, the pressure of the detector is ensured by a mechanical backup system that sends one gas component directly from the primary supply lines.

Pump

A compressor is installed in the underground service cavern to collect the returning gas from the distribution racks. A loop bypass control valve is installed on the compressor, and a controller is used to ensure that the pump module operates at constant input pressure, allowing a stable extraction of gas flow from the distribution and minimizing perturbations on the chambers. In general, more than one compressor is present on the module in case of failure or need for increased flow rate.

Exhaust

The gas returning from the pump module is collected by the exhaust module, where it can be reinjected to the recirculating loop or sent to the atmosphere. Furthermore, the exhaust is typically equipped with an MFC that allows the high pressure region of the closed-loop to be kept at a fixed pressure by exhausting gas when required.

Purifier

The purifier module is responsible for eliminating some of the impurities collected by the gas along the loop. The main impurities accumulated by the detectors include Air, water vapor, and molecules originating from the breaking gas components in the gas gaps during avalanche multiplication. O_2 and H_2O can be efficiently removed by the purifiers, while no technologies are currently available to remove N_2. More than one purifier module can be installed in a gas system, depending on the requirements. Two columns containing absorber material are installed in a purifier module. The gas entering the purifier input passes through the column containing absorber material that traps the specific impurity. After some time, the absorber material starts losing its absorption efficiency, so the column is switched to the second one. During this period, the inactive column undergoes a regeneration process: the column is heated up, flushed with a gas (Argon or Ar/H_2, depending on the absorber material) and the impurities are extracted via a vacuum pump. The column is later reconditioned by purging it with some system's gas mixture to avoid undesired trapping of gas components during the column run.

Analysis

Gas analysis modules were developed to monitor the quality of the gas mixture from different sampling points of the gas system. Typically, O_2 and H_2O are continuously monitored with the precision of part-per-million (ppm) using dedicated devices. Additionally, infrared monitoring devices are employed to monitor concentration levels of CO_2, CF_4, SF_6, or flammable gases such as i-C_4H_{10}. In some cases, the module has a Gas Chromatograph device used to obtain high precision measurements of the concentration of different gas components along the system lines.

Gas system's active mechanical and electronic parts are regulated and controlled using industrial control systems technologies, mainly based on Programmable Logic Controllers (PLCs) and Supervised Control and Data Acquisition (SCADA) frameworks. Some gas systems are operated in the so-called open mode, with the gas returning from the chamber exhausted to the atmosphere. Some others, especially in the presence of large detector volumes or expensive gas components, were instead designed to be operated in a closed-loop mode. Each gas system downtime is expected to be 0% during LHC Run periods and must comply with industrial and CERN's safety standards. Each gas module containing flammable gas components is built by respecting the European directives for equipment with a potentially explosive atmosphere (ATEX). Where possible, gas system modules foresee a purge mode used to remove the process gas from the system during long shutdown periods.

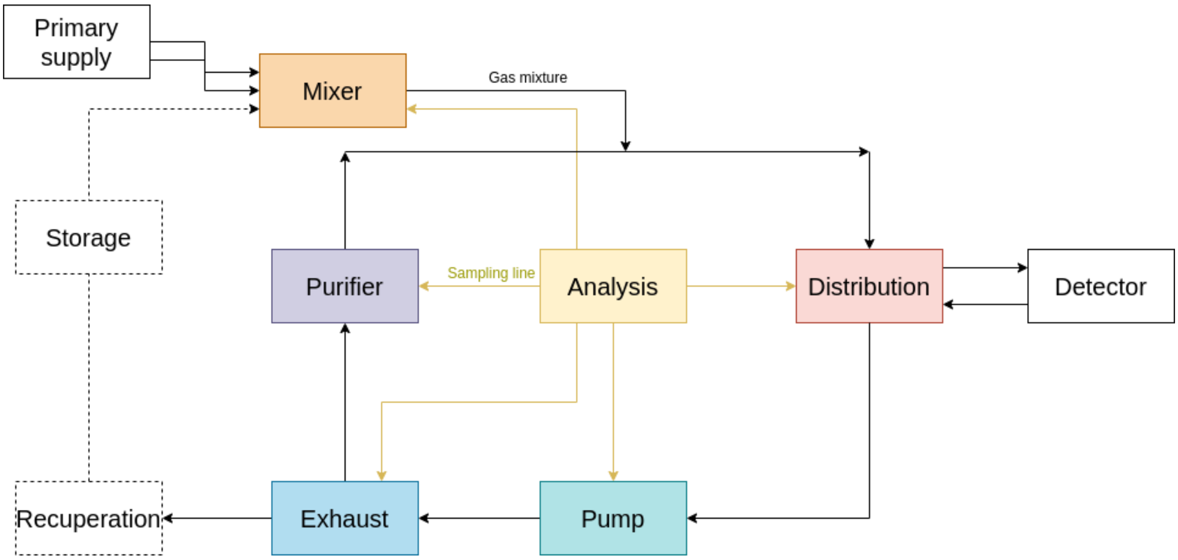

FIGURE 2.6 – Simplified schema of a gas system and the connection between its modules

2.4.2 Gas Control Systems

Gas Control Systems (GCS) are essential elements for the operation of gas systems. They allow operators to act on the gas system by controlling a set of actuators, such as On/Off valves or regulation valves. They also allow monitoring the system by reading and archiving values of several hundreds of sensors installed within different modules. GCS are also responsible for coordinating the operational states of the different modules by orchestrating them with user-defined logic. GCSs were developed using the CERN-made Unified Industrial Control System (UNICOS) framework, based on the standard ISA-88 for batch control systems. The monitoring and control of a gas system are performed by accessing a WinCC-OA SCADA application connected to a PLC device that acts on the field instruments installed on the gas system itself. Each GCS project is independent of other projects, meaning that its running conditions are not affected by the operating condition of other systems. The code used to run a GCS project is generated using a spreadsheet file, named specification file, that describes all the physical and virtual devices, such as their names, address, range of measurement, and other metadata relevant to the targeted device. The specification file is used as an input for the Unicos Application Builder (UAB) that generates both the code for the PLC machine and for the SCADA computer. Further custom application logic can be added to the generated PLC project if required. Once the GCS is appropriately configured, it can be accessed through a terminal server hosted on the CERN Technical Network. The project is accessed by launching the WinCC-OA application. As a result, a window application window showing the overview of the gas system is displayed. The application allows users to navigate through different panels containing the relative information for each gas system module. In addition to the monitoring access of live values, the users are provided with a trending tool that allows them to inspect the time series of up to 8 different devices on the same plot. The system's control happens by sending commands through the main Process Control Objects (PCO), where the running state of the gas system or a module can be changed. Gas systems are also provided with the possibility of changing parameters related to the running state of the PCO. For instance, the pressure or flow setpoint can be changed

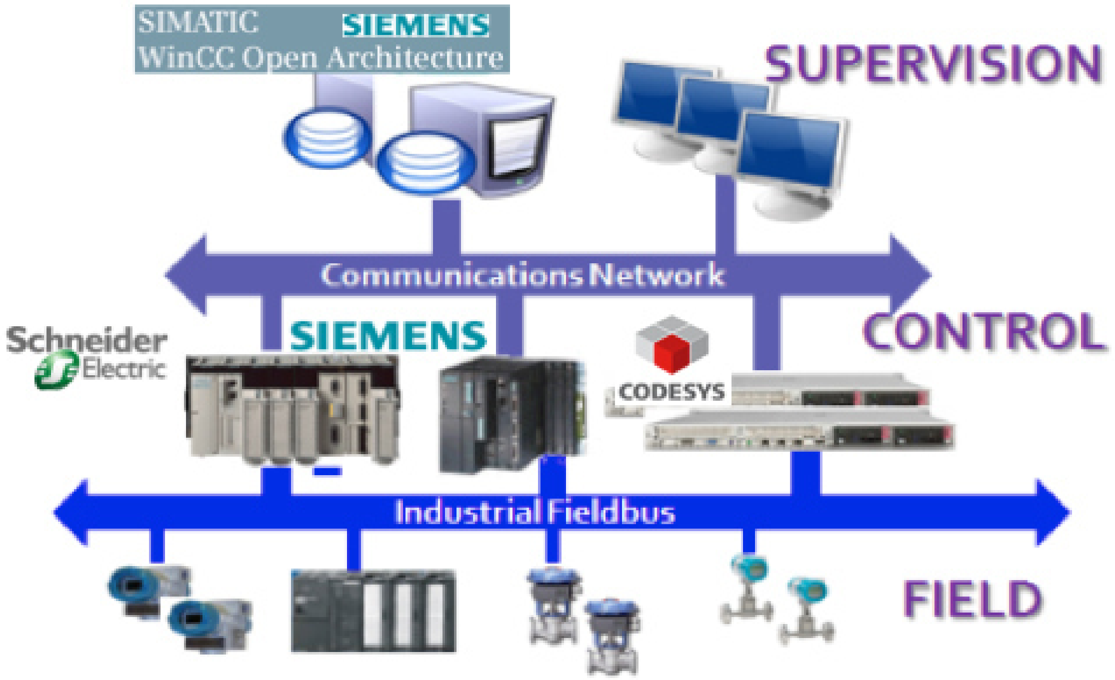

FIGURE 2.7 – CERN's UNICOS architecture [22].

during the Run operation of the Mixer or Distribution module. The communication from the operator to PLC happens through a set of parameters called recipes that are stored first on SCADA and then sent to the PLC without interrupting its running cycle. Alarms are vastly used in GCS projects: they are employed for warning purposes by setting thresholds that allow the expert to intervene before a possible switch of the gas system to a critical running state. An alarm can be triggered on a binary digital value or a set of thresholds in the case of an analog value. If needed, they can generate an interlock signal acting on the operational status of the gas system. When an alarm condition is met, a notification is sent through SMS and email channels.

2.5 Greenhouse gases emissions from particle detectors at LHC

Few gases employed in LHC gaseous particle detectors are known to be greenhouse gases (GHG). The greenhouse effect is a process happening at Earth's atmospheric level: about two-thirds of the Sun's radiation reaching the terrestrial surface is absorbed. Since Earth's surface temperature is much lower than the Sun's one, the absorbed radiation is re-emitted in space at much lower wavelengths, typically in the infrared region. The presence of GHG in the atmosphere is such that the GHGs themselves trap part of the Earth's emitted radiation. The GHG molecules absorb the infrared radiation in the form of excited roto-vibrational states, with a consequent increase in the gas temperature. Earth's atmosphere is naturally provided with GHGs, the most common one being water vapor and the second one CO_2. The absence of such gas would cause the average Earth's surface to drop from 14 °C to -18 °C. In such cases, water would freeze, and life forms would be significantly impacted. GHGs are mixed in the atmosphere and travel around the globe, making the

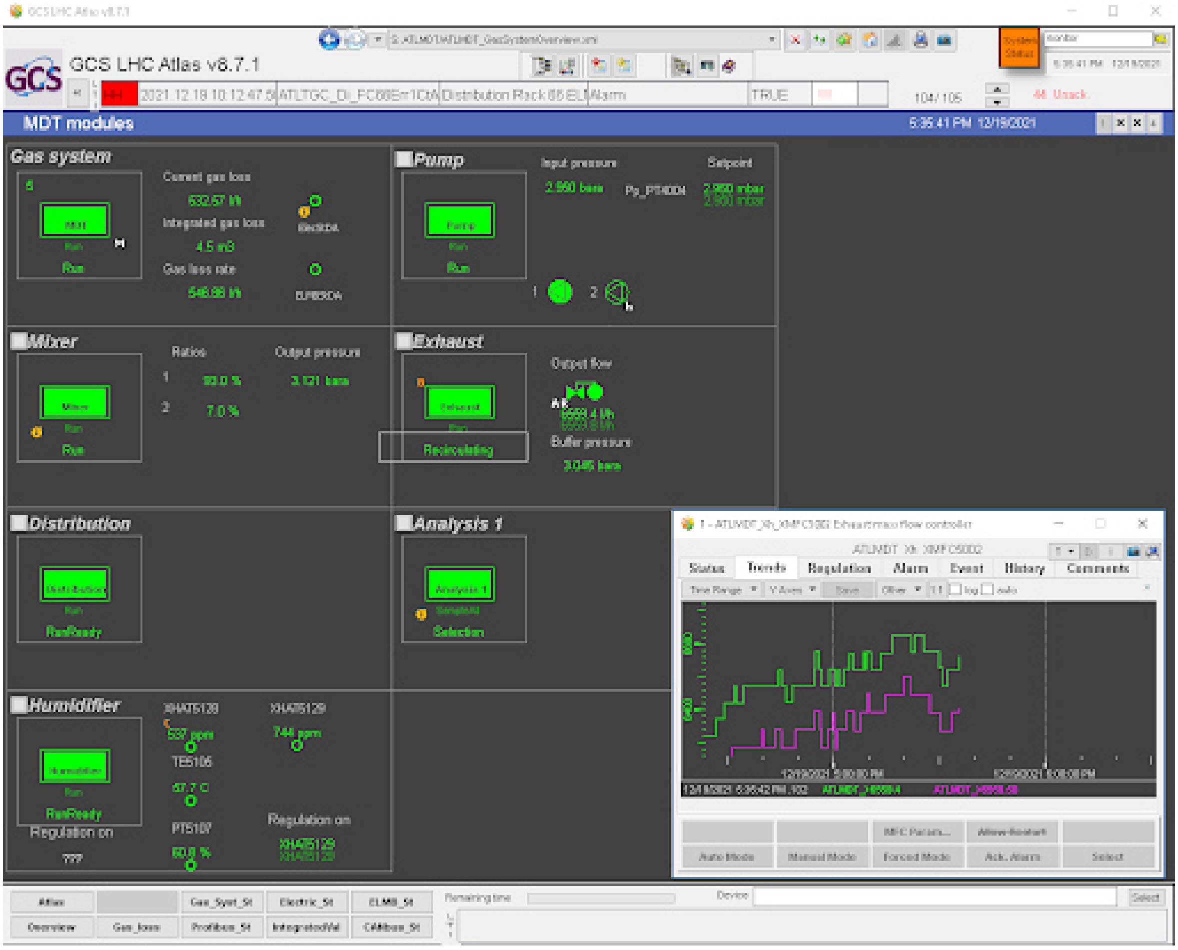

FIGURE 2.8 – Overview of a GCS SCADA application. Each project consists of several PCOs, typically one for each gas system module, running with a custom configured logic.

Gas	**Family**	**Atmospheric lifetime**	**GWP$_{100}$**
CO_2		50-200 years	1
CH_4	Hydrocarbons	12 years	25
i-C_4H_{10}	Hydrocarbons	7 days	3.3
n-C_5H_{12}	Hydrocarbons	$\sim$weeks	5
$C_2H_2F_4$	Hydrofluorocarbons	14 years	1430
Tetrafluoromethane/CF4	Perfluorocarbons	50 000 years	7390
SF_6	Perfluorocarbons	3200 years	22800

TABLE 2.2 – GHGs used by CERN LHC particle detectors and their main greenhouse properties.

greenhouse effect a global process. Among natural GHGs emitted from life forms, a significant amount of CO_2 and CH_4 has been emitted by human activity since the beginning of the industrial revolution, contributing to a steady rise of the Earth's average temperature. The measure of a GHG contribution to the greenhouse effect is typically performed using the Global Warming Potential (GWP), defined as the amount of heat that one ton of gas can absorb with respect to one ton of CO_2 over a time range. Since GWP is an integrated measure over a time range, its value may significantly differ depending on the considered period, as the dynamics of the radiative absorption depend on the gas's chemistry in the atmosphere. For instance, a gas compound may have a higher absorption power with respect to CO_2 but a significantly short atmospheric lifetime, making it a low GWP gas. In this context, whenever not specified, GWP is considered to be measured over a time period of 100 years (GWP$_{100}$). Several artificial gases created by human activity are nowadays classified as GHGs. In particular, ChloroFluoroCarbons (CFC), HydroFluoroCarbons (HFC), and Perfluorocarbons (PFC) are the families with the highest known GWP gases. The main employed GHGs for particle detectors at CERN LHC experiments are reported in Table 2.2

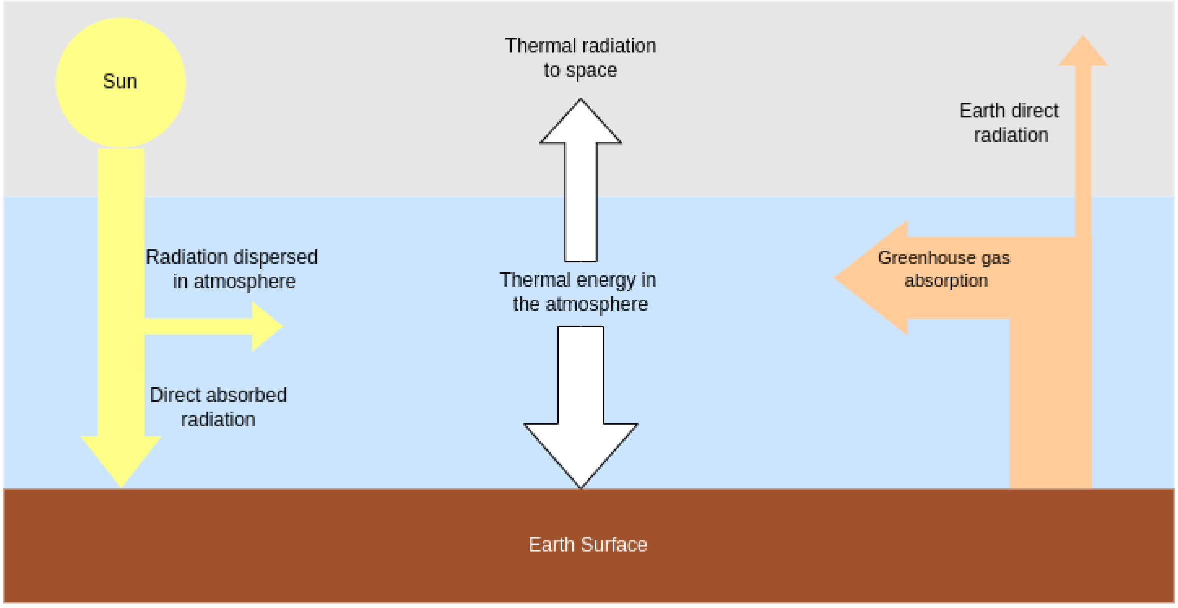

FIGURE 2.9 – Simplified energy balance of the greenhouse effect

The Fourth Assessment Report of the Intergovernmental Panel on Climate Change stated that, on the basis of existing scientific data, developed countries would need to reduce greenhouse gas emissions by 80% to 95% below 1990 levels by 2050 to limit global climate change to a temperature increase of 2 °C and thus prevent undesirable climate effects [23]. The European Commission adopted a roadmap to reduce the GHGs emission from fluorinated gases with the target of reducing their emission to one-fifth from 2014 to 2030 [24]. The regulation, written in 2014, defines several different strategies that can be summarised as:

- Prevent the emission of fluorinated GHGs by requiring regular leak checks on the equipment
- Contain, recover, destroy GHGs where possible
- Restrict the placing on the market of equipment based on fluorinated GHGs where suitable alternatives are present
- Gradually reduce the amount of HFCs that can be placed on the market by allocating quotas to the individual manufacturers

To align with the latest environmental standard, the European Strategy for Particle Physics update formalized in 2020 [25] stated that: «The environmental impact of particle physics activities should continue to be carefully studied and minimised. A detailed plan for the minimisation of environmental impact and for the saving and re-use of energy should be part of the approval process for any major project. Alternatives to travel should be explored and encouraged.» As reported in the 2019-2020 CERN Environment Report, particle detectors account for the largest GHGs emissions due to the fluorinated gases used to operate the detectors. When looking at the emissions from different detectors, ATLAS RPC and

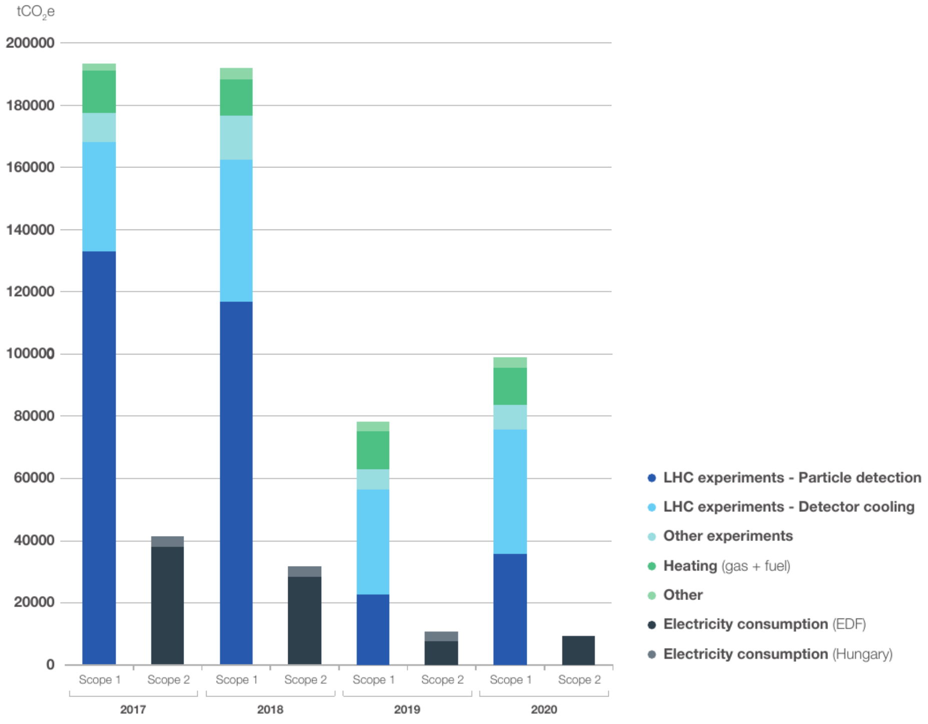

FIGURE 2.10 – CERN GHG emissions for direct emissions (Scope 1) and energy indirect emission (Scope 2) [26]

CMS RPC systems had the highest CO_2 e emissions. Most of the RPC emissions are due to the presence of leaks at the chamber level. RPCs operated with around 95% of R-134a, making it the primary GHG from particle detectors. CF_4 accounts for the second-highest emissions. The reason is due to the detector volumes operating with such gases (CMS CSC, LHCb RICH2, LHCb MWPC) and its considerably high GWP_{100} of 7900. As it can be noticed from Figure2.12 CO_2 equivalent SF_6 emissions are lower than CF_4. Although used in small concentrations of 0.3% in RPC systems (except for TOF, where it is used with a concentration of 7%), the total CO_2 equivalent emissions from SF_6 are non-neglectable due to its extremely high GWP_{100} of 22800, weighing around 16 times more than the same released quantity of R-134a. CERN has defined a set of different strategies to reduce the GHG emissions from particle detectors:

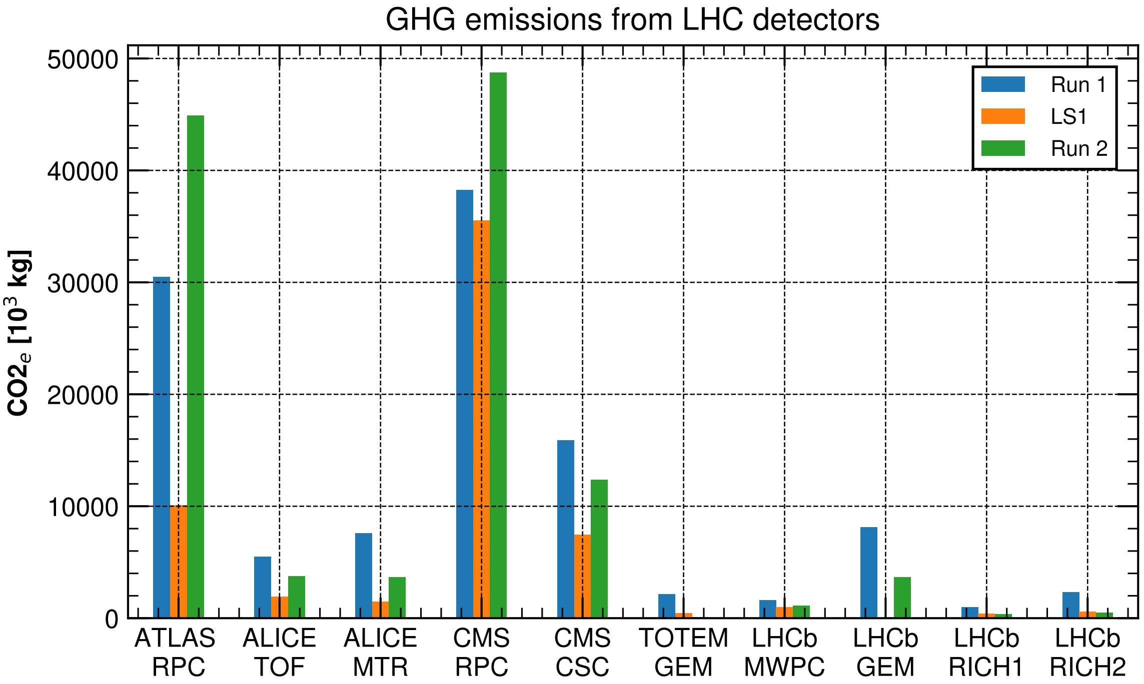

FIGURE 2.11 – Tonnes of CO_2 equivalent emissions from LHC detectors systems during Run1, LS1, and Run 2 periods

Optimization of current technologies

The optimization of gas systems allows them to operate with performances beyond their original requirements, in order to improve operation and reduce gas consumption. Both hardware and software interventions were performed during the LS2 upgrade period of LHC for selected gas systems. For instance, the ATLAS RPC gas system was upgraded by installing a new distribution rack to reduce hydrostatic pressure on the detectors and operate them at lower pressure, thus reducing the effective leak rate. A set of pressure regulation valves was installed on the CMS RPC gas system to allow precise and optimal tuning of the detector's pressure and reduce gas emissions. Gas Control Systems (GCS) were upgraded with several features to improve the monitoring and control of gas systems. New modern monitoring tools and data analysis infrastructure were designed to investigate the gas

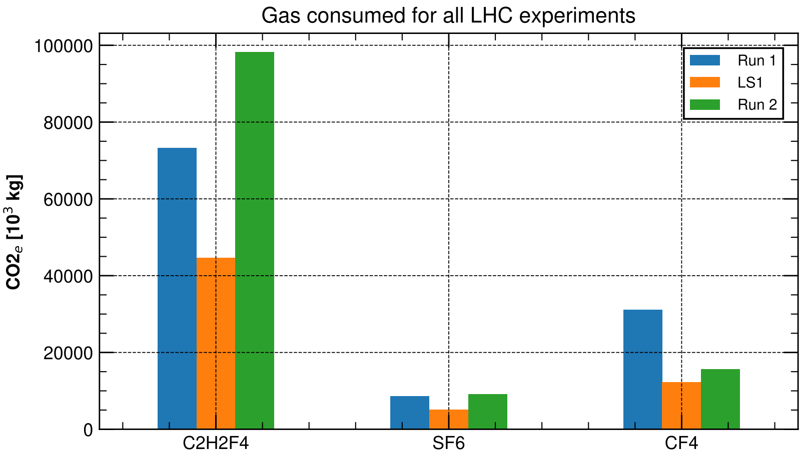

FIGURE 2.12 – Total tonnes of equivalent CO_2 (tCO2e) consumption from LHC particle detectors during Run 1, LS 1, Run 2 period for R-134a, CF_4 and SF_6

consumption and spot possible gas system-related issues. A detailed set of the mentioned optimizations is detailed in Chapter 3 of this work.

Gas recuperation systems

Gas recuperation aims at recuperating an expensive or GHG component from the gas that would be otherwise exhausted from the gas system. In particular, gas recuperation plants consist of recuperating the gas mixture that is exhausted from the system, letting it undergo a purification process, separating the target gas component from the mixture, storing it into containers, and reusing the component as a fresh supply. Gas recuperation plants introduce a considerably higher complexity in the system as they need to be specifically designed for the gas systems themselves. Different recuperation plants were designed for LHC gas systems. In ALICE and ATLAS, the Xenon from the transition radiation detectors is recuperated from the exhausted purifier module and reinjected in the closed-loop system. In ATLAS, the n-C_5H_{12} is recuperated from TGCs using a cryogenic distillation process by cooling down the gas mixture and separating the n-pentane from the CO_2. In CMS and LHCb, CF_4 is recuperated from CSC and RICH 1 exhausts using selective membrane absorbers. Finally, an R-134a recuperation plant for RPC systems plant is currently being designed and tested [27].

Alternative gases

An R&D research branch is dedicated to searching for eco-friendly alternatives to GHGs that can be employed to operate gas detectors without affecting their performance and without changing the current detector technology. CF_4 alternatives are currently being researched for wire chambers such as CSCs and MPGDs such as triple-GEMs. This research line is also particularly active for RPCs detectors, being R-134a the main responsible for GHG emissions. Studies on the performance of RPCs operated with eco-friendly gas mixtures are discussed in Chapter 4 of this work.

3 Optimization of Gas Systems technologies

As described in the previous Chapter, gas systems provide required gas conditions for various LHC and non-LHC gaseous detectors. Although they are designed in modules, each gas system may present its own complexity due to the detector requirements or specific implementation of the gas system itself. The optimization of gas systems is a set of interventions performed during LHC maintenance and upgrade periods such as LS2. The upgrades aim to improve the gas system's performance and control to allow a better, safer, and more stable operation. The optimizations can be made at the hardware level - such as new components installation - or at the software level, such as an improved stepping sequence for startup phases. The optimization can also be coupled at both hardware and software sides. For instance, the installation of an additional pressure regulation valve is accompanied by the presence of different controller objects in the GCS. The optimization of gas systems could also improve the reduction of gas consumption, especially for closed-loop systems, by acting on the tuning of the several controllers present in the loop chain. Also, the settings of the different sophisticated level of warnings and alarms on the system allow for operator interventions based on the criticality of the detected issues. Gas systems could also be optimized for start-up phases, where the operating conditions are possibly less stable than the run conditions. A set of software-level optimizations that were performed on the current LHC gas systems is described in the present Chapter. The first part is dedicated to describing the software developments and upgrades made during the LS2 phase to improve specific gas systems for detectors at LHC experiments. The second part is dedicated to the tools used to retrieve online and offline data from gas systems, focusing on CERN monitoring tools and logging services. The last part is focused on the description of the Proportional-Integrative-Derivative (PID) controller and the tuning process for few GCSs. A detailed analysis of gas system-specific cases is presented.

3.1 Software development and upgrades for Gas Control Systems

As described in the previous Chapter, the GCS can be thought of as a service interfacing two areas: from one side the field instrumentation devices employing PLCs. From the other side, the SCADA interface allowing the operator to monitor and control the instrumentation devices. Multiple GCS upgrades can be performed in different parts of the software infrastructure. For instance, at the SCADA level, periodic upgrades are made to the WinCC-OA software, applying patches on the JCOP framework and on the UNICOS framework. Minor or major upgrades can be applied, depending on the effects of the patches to the PLC control system. Some significant upgrades are usually related to adding new features specifically targeted for the gas system or to the modification and bug fixing of present issues in the code.

Due to the complexity of the systems and the need to interface a SCADA tool with field bus devices, the development of new features happens following the flow documented in the UNICOS framework. The process is usually called software generation, and the steps can be summarized as:

1. The set of controlled devices, such as analog input sensor, analog output for actuators, process controller objects, mass flow controllers, etc., is defined in a .xlsx or .xml specification file. Each device is uniquely identified by a name and is assigned a set of parameters, such as the range, unit of measurement and other dependent device meta-data.
2. The specification file is supplied to the UNICOS Application Builder (UAB) program, which parses the specification for each device and can create the necessary files to be installed in the PLC machine and on the SCADA server.
3. The software is loaded in the PLC, and eventual custom logic is added in the dedicated templated files. The PLC is also configured for proper connection to the SCADA server via the MODBUS protocol on the Ethernet layer.
4. The SCADA server is loaded with the WinCC-OA application and the UNICOS framework. The UAB generated files for the SCADA side are loaded into the server, and the communication with the PLC is set.

A few minor upgrades can also happen without generating the project by modifying the production code of the PLC without stopping it. These interventions are usually done when the gas system cannot be stopped, and the modification is required for proper operation. The software upgrades made by LS2 shipped a few critical features for improved gas system control:

Startup PID parameters

PID parameters for a controller object were usually expressed in terms of fixed Kc, Ti, Td, Tds. The GCS software upgrade adds a new set of PID parameters that could be employed during the start-up phase of the gas system. The condition for the start-up phase could be time-dependent, using a timer to discriminate between start-up and run-ready conditions, or value-dependent, where the start-up phase is activated when the process variable is above or below a configurable threshold.

Pressure sensor selection for regulation valve controller

In closed-loop distribution racks, it is often required to regulate the pressure on the detector using a control valve. The valve is controlled using the UNICOS PID controller object, allowing the user to select the valve opening as the output variable (OV) and read the chamber pressure sensor as the process variable (PV). In the case of a faulty pressure sensor or a leaky chamber where the pressure sensor is present, the regulation of the valve could lead to undesired effects in terms of pressure and flow stability in the detector. In such cases, it could be preferred to regulate using the pressure sensor installed at the output of the detector, inside the distribution rack, or the pressure sensor installed in a verified leak-tight volume, referred to as a dummy chamber. The GCS upgrade allows setting the process variable to a pivot variable that can assume the values of either the chamber or the output sensor, depending on the activated recipe. This feature is crucial for operating large gas systems such as the ATLAS and CMS RPC ones, where a pressure transmitter on the detector side cannot be easily replaced or leaks at detector level cannot be easily repaired.

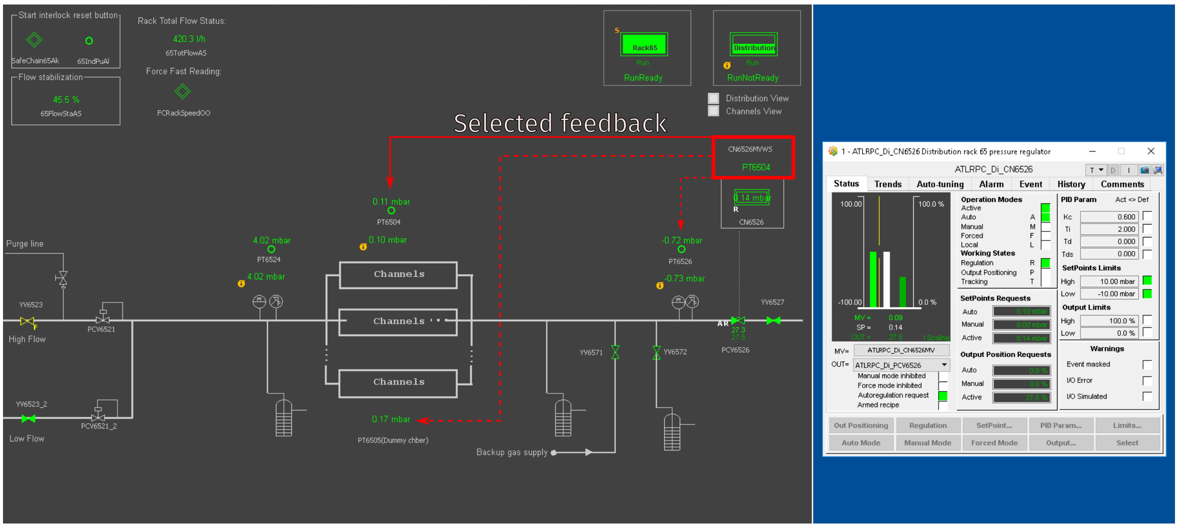

1 - ATLRPC_Di_CN6526 Distribution rack 65 pressure regulator

ATLRPC_Di_CN6526

MV = 0.09
SP = 0.14
OUT = 27.5

MV= ATLRPC_Di_CN6526MV
OUT= ATLRPC_Di_PCV6526

Manual mode inhibited ☐
Force mode inhibited ☐
Autoregulation request 🟩
Armed recipe ☐

Operation Modes
Active 🟩
Auto A 🟩
Manual M ☐
Forced F ☐
Local L ☐

Working States
Regulation R 🟩
Output Positioning P ☐
Tracking T ☐

SetPoints Requests
Auto 0.10 mbar
Manual 0.00 mbar
Active 0.14 mbar

Output Position Requests
Auto 0.0 %
Manual 0.0 %
Active 27.5 %

PID Param Act <> Def
Kc 0.600 ☐
Ti 2.000 ☐
Td 0.000 ☐
Tds 0.000 ☐

SetPoints Limits
High 10.00 mbar 🟩
Low -10.00 mbar 🟩

Output Limits
High 100.0 % ☐
Low 0.0 % ☐

Warnings
Event masked ☐
I/O Error ☐
I/O Simulated ☐

FIGURE 3.1 – Distribution monitoring (on the left) and faceplate PID controller on the right. The PID controller feedback is selected to the chamber pressure (red line), but can optionally be switched to other pressure sensors (dashed red lines).

Recipes archiving

Previous to the LS2 GCS upgrades, only the process values were stored in the LHC logging database. With the recent upgrades also the values of the recipe are stored in the central archiving database, allowing one to correlate the operation of the gas system with the changes made in the regulation, such as setpoints, device selection, or PID parameters. This feature is particularly useful when trying to tune PID parameters as the setpoint could be used to analyze the step response of the controller object to guess the optimal PID gains set.

Profibus and CAN-bus monitoring

Different field communication protocols are employed by the gas systems installations, depending on the instrumentation devices' environmental conditions and requirements. In particular, the Profibus protocol is used for communication between the PLC and different devices, such as regulation valve controllers, mass flow controllers, and Wago I/O cards, while the CANbus network is used for flow cells reading due to its multiplexing capabilities. Due to the complexity of the networks and the harsh environment under which the devices operate, bits of information in the communication may be lost or incorrectly transmitted. Both CAN bus, and Profibus protocols feature error handling on the communication between devices and can set an error flag on the nodes when the communication packets are incorrectly transmitted. The monitoring of the nodes on the Fieldbus networks is therefore helpful to detect possible communication errors with single devices or with the whole network. Counter variables are added to the PLC to monitor the Profibus and CAN-bus networks. Their counter values are displayed on a dedicated WinCC-OA panel, grouping the information per node and showing the total number of detected error flags together with the error counting over the last 24 hour period.

GasSystem

7	0	○	◇
Wago1ErrCt	Wago1ErrDtCt	Wg1ErrCtAA	Wago1ErrRst
13	0	○	◇
Wago2ErrCt	Wago2ErrDtCt	Wg2ErrCtAA	Wago2ErrRst

☐ Mixer

11	0	○	◇
Wago1ErrCt	Wago1ErrDtCt	Wg1ErrCtAA	Wago1ErrRst
11	0	○	◇
FestoErrCt	FestoErrDtCt	FestoErrCtAA	FestoErrRst

Gas Line1

15	0	○	◇
X1106ErrCt	X1106ErrDtCt	X1106ErrCtAA	X1106ErrRst
7	0	○	◇
X1109ErrCt	X1109ErrDtCt	X1109ErrCtAA	X1109ErrRst

Gas Line2

9	0	○	◇
X1206ErrCt	X1206ErrDtCt	X1206ErrCtAA	X1206ErrRst
8	0	○	◇
X1209ErrCt	X1209ErrDtCt	X1209ErrCtAA	X1209ErrRst

Gas Line3

9	0	○	◇
X1306ErrCt	X1306ErrDtCt	X1306ErrCtAA	X1306ErrRst
9	0	○	◇
X1309ErrCt	X1309ErrDtCt	X1309ErrCtAA	X1309ErrRst

☐ Distribution

13	0	○	◇
Wago1ErrCt	Wago1ErrDtCt	Wg1ErrCtAA	Wago1ErrRst
13	0	○	◇
Wago2ErrCt	Wago2ErrDtCt	Wg2ErrCtAA	Wago2ErrRst
13	0	○	◇
Wago3ErrCt	Wago3ErrDtCt	Wg3ErrCtAA	Wago3ErrRst

Racks

0	0	○	◇
PCV6126ErrCt	PCV6126ErDtCt	PCV6126ErrCtAA	PCV6126ErrRst
25	0	○	◇
PCV6226ErrCt	PCV6226ErDtCt	PCV6226ErrCtAA	PCV6226ErrRst
28	0	○	◇
PCV6326ErrCt	PCV6326ErDtCt	PCV6326ErrCtAA	PCV6326ErrRst
15	0	○	◇
PCV6426ErrCt	PCV6426ErDtCt	PCV6426ErrCtAA	PCV6426ErrRst
14	0	○	◇
PCV6526ErrCt	PCV6526ErDtCt	PCV6526ErrCtAA	PCV6526ErrRst
14	0	○	◇
PCV6626ErrCt	PCV6626ErDtCt	PCV6626ErrCtAA	PCV6626ErrRst
13	0	○	◇
PCV6726ErrCt	PCV6726ErDtCt	PCV6726ErrCtAA	PCV6726ErrRst
13	0	○	◇
PCV6826ErrCt	PCV6826ErDtCt	PCV6826ErrCtAA	PCV6826ErrRst
13	0	○	◇
PCV6926ErrCt	PCV6926ErDtCt	PCV6926ErrCtAA	PCV6926ErrRst
15	0	○	◇
PCV6624ErrCt	PCV6624ErDtCt	PCV6624ErrCtAA	PCV6624ErrRst
13	0	○	◇
PCV6724ErrCt	PCV6724ErDtCt	PCV6724ErrCtAA	PCV6724ErrRst
13	0	○	◇
PCV6824ErrCt	PCV6824ErDtCt	PCV6824ErrCtAA	PCV6824ErrRst
13	0	○	◇
PCV6924ErrCt	PCV6924ErDtCt	PCV6924ErrCtAA	PCV6924ErrRst

☐ Humidifier

11	0	○	◇
Wago1ErrCt	Wago1ErrDtCt	Wg1ErrCtAA	Wago1ErrRst
11	0	○	◇
X5121ErrCt	X5121ErrDtCt	X5121ErrCtAA	X5121ErrRst

☐ Pump

13	0	○	◇
Wago1ErrCt	Wago1ErrDtCt	Wg1ErrCtAA	Wago1ErrRst
13	0	○	◇
ZC4003ErrCt	ZC4003ErrDtCt	ZC4003ErrCtAA	ZC4003ErrRst

☐ Purifier1

11	0	○	◇
Wg1ErrCt	Wg1ErrDtCt	Wg1ErrCtAA	Wg1ErrRst
10	0	○	◇
X2020ErrCt	X2020ErrDtCt	X2020ErrCtAA	X2020ErrRst

☐ Purifier2

11	0	○	◇
Wg1ErrCt	Wg1ErrDtCt	Wg1ErrCtAA	Wg1ErrRst
10	0	○	◇
X2020ErrCt	X2020ErrDtCt	X2020ErrCtAA	X2020ErrRst

☐ Purifier3

11	0	○	◇
Wg1ErrCt	Wg1ErrDtCt	Wg1ErrCtAA	Wg1ErrRst
0	0	○	◇
X2020ErrCt	X2020ErrDtCt	X2020ErrCtAA	X2020ErrRst

☐ Exhaust

11	0	○	◇
Wago1ErrCt	Wago1ErrDtCt	Wg1ErrCtAA	Wago1ErrRst
11	0	○	◇
X5002ErrCt	X5002ErrDtCt	X5002ErrCtAA	X5002ErrRst
11	0	○	◇
FestoErrCt	FestoErrDtCt	FestoErrCtAA	FestoErrRst

☐ Analysis 1

11	0	○	◇
Wago1ErrCt	Wago1ErrDtCt	Wg1ErrCtAA	Wago1ErrRst

☐ Analysis 2

13	0	○	◇
Wago2ErrCt	Wago2ErrDtCt	Wg2ErrCtAA	Wago2ErrRst

FIGURE 3.2 – Profibus monitoring panel.

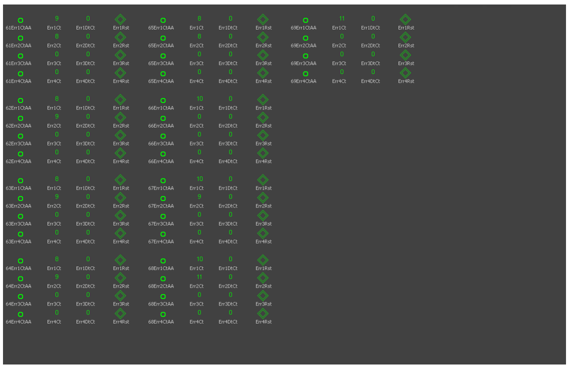

○	9	0	◇	○	8	0	◇	○	11	0	◇
61Err1CtAA	Err1Ct	Err1DtCt	Err1Rst	65Err1CtAA	Err1Ct	Err1DtCt	Err1Rst	69Err1CtAA	Err1Ct	Err1DtCt	Err1Rst
○	8	0	◇	○	8	0	◇	○	0	0	◇
61Err2CtAA	Err2Ct	Err2DtCt	Err2Rst	65Err2CtAA	Err2Ct	Err2DtCt	Err2Rst	69Err2CtAA	Err2Ct	Err2DtCt	Err2Rst
○	0	0	◇	○	0	0	◇	○	0	0	◇
61Err3CtAA	Err3Ct	Err3DtCt	Err3Rst	65Err3CtAA	Err3Ct	Err3DtCt	Err3Rst	69Err3CtAA	Err3Ct	Err3DtCt	Err3Rst
○	0	0	◇	○	0	0	◇	○	0	0	◇
61Err4CtAA	Err4Ct	Err4DtCt	Err4Rst	65Err4CtAA	Err4Ct	Err4DtCt	Err4Rst	69Err4CtAA	Err4Ct	Err4DtCt	Err4Rst
○	8	0	◇	○	10	0	◇				
62Err1CtAA	Err1Ct	Err1DtCt	Err1Rst	66Err1CtAA	Err1Ct	Err1DtCt	Err1Rst				
○	9	0	◇	○	0	0	◇				
62Err2CtAA	Err2Ct	Err2DtCt	Err2Rst	66Err2CtAA	Err2Ct	Err2DtCt	Err2Rst				
○	0	0	◇	○	0	0	◇				
62Err3CtAA	Err3Ct	Err3DtCt	Err3Rst	66Err3CtAA	Err3Ct	Err3DtCt	Err3Rst				
○	0	0	◇	○	0	0	◇				
62Err4CtAA	Err4Ct	Err4DtCt	Err4Rst	66Err4CtAA	Err4Ct	Err4DtCt	Err4Rst				
○	8	0	◇	○	10	0	◇				
63Err1CtAA	Err1Ct	Err1DtCt	Err1Rst	67Err1CtAA	Err1Ct	Err1DtCt	Err1Rst				
○	9	0	◇	○	9	0	◇				
63Err2CtAA	Err2Ct	Err2DtCt	Err2Rst	67Err2CtAA	Err2Ct	Err2DtCt	Err2Rst				
○	0	0	◇	○	0	0	◇				
63Err3CtAA	Err3Ct	Err3DtCt	Err3Rst	67Err3CtAA	Err3Ct	Err3DtCt	Err3Rst				
○	0	0	◇	○	0	0	◇				
63Err4CtAA	Err4Ct	Err4DtCt	Err4Rst	67Err4CtAA	Err4Ct	Err4DtCt	Err4Rst				
○	8	0	◇	○	10	0	◇				
64Err1CtAA	Err1Ct	Err1DtCt	Err1Rst	68Err1CtAA	Err1Ct	Err1DtCt	Err1Rst				
○	9	0	◇	○	11	0	◇				
64Err2CtAA	Err2Ct	Err2DtCt	Err2Rst	68Err2CtAA	Err2Ct	Err2DtCt	Err2Rst				
○	0	0	◇	○	0	0	◇				
64Err3CtAA	Err3Ct	Err3DtCt	Err3Rst	68Err3CtAA	Err3Ct	Err3DtCt	Err3Rst				
○	0	0	◇	○	0	0	◇				
64Err4CtAA	Err4Ct	Err4DtCt	Err4Rst	68Err4CtAA	Err4Ct	Err4DtCt	Err4Rst				

FIGURE 3.3 – AN-bus monitoring panel.

3.2 Large scale, real time data visualization monitoring tools

The number of devices installed for each GCS is mainly dependent on the requirements of the gas system. However, even the simplest gas systems can feature hundreds of devices, each stored and available for the supervising tools. When dealing with large installations, it is often needed to monitor the temporal evolution of different devices. The WinCC-OA supervision program is mainly designed for control purposes, although it provides a trend widget that allows the operator to display up to 8 devices on the same trend. The trending tool is notably useful for quick visualization as it is relatively simple to visualize a device from the Human Machine Interface (HMI) panels. The trending widgets also allow setting different y-axis scales independently for each device. It is then possible to adjust the scale and have each device with a diverse range and offset. Furthermore, the data is retrieved dynamically based on the time window requested by the operator. The WinCC-OA application retrieves data from an Oracle database configured for device archiving. However, most of the data regarding the position status of analog devices and On/Off status for digital devices is available through the CERN Data Interchange Protocol (DIP). DIP is a communication protocol that allows real-time data exchange over different, heterogeneous systems. The service itself is a publisher/subscriber system, with an intermediate name server acting as a service provider. From the publisher's point of view, a publication is pushed to the name server, making it available for the consumers to read. Each publication belongs to only one publisher, and it is expected that the subscriber knows a priori the path of the desired publications. The DIP service is primarily employed in all control systems at CERN. For instance, a Detector Control System (DCS) may subscribe to a set of relevant environmental parameters made available by the Heating, Ventilation, and Air Conditioning (HVAC) control system. Several DIP publications are made available by the GCS: analog values related to field sensor and transmitter, On/Off status of valves and digital switches, enumerable values associated with the status of the process control objects. The availability of Gas Systems values

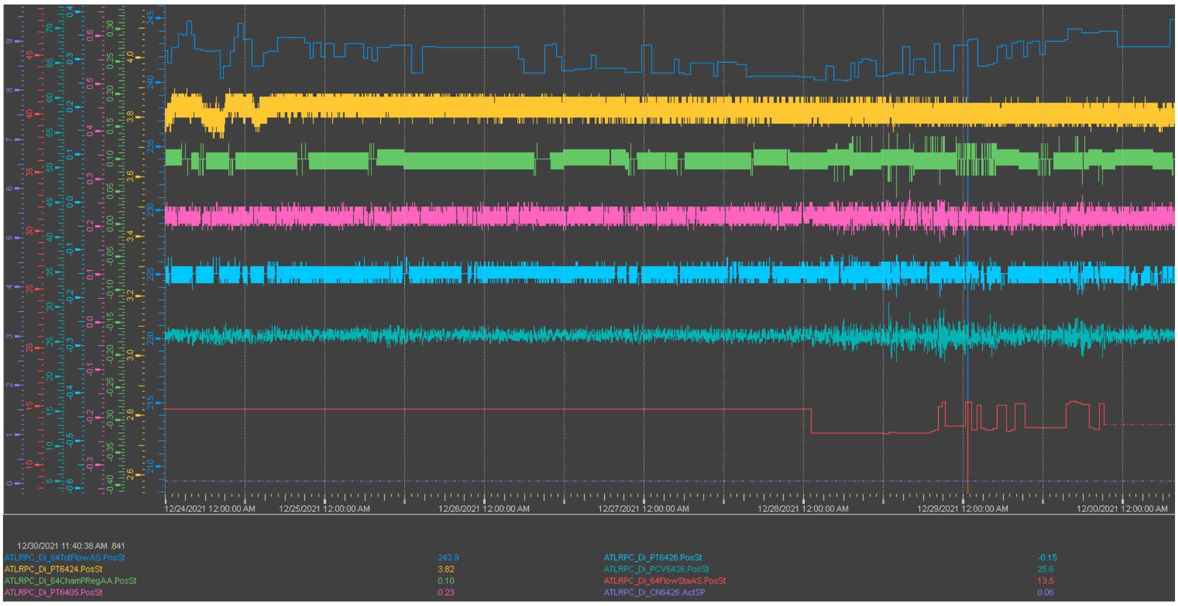

```
12/30/2021 11:40:38 AM .841
ATLRPC_Di_64TotFlowAS.PosSt      243.9    ATLRPC_Di_PT6426.PosSt         -0.15
ATLRPC_Di_PT6424.PosSt           3.82     ATLRPC_Di_PCV6426.PosSt        25.6
ATLRPC_Di_64ChamPRegAA.PosSt     0.10     ATLRPC_Di_64FlowStaAS.PosSt    13.5
ATLRPC_Di_PT6405.PosSt           0.23     ATLRPC_Di_CN6426.ActSP         0.06
```

FIGURE 3.4 – WinCC-OA trending tool

through DIP allows designing monitoring applications independent of the GCS. Few modern monitoring architectures were tested and are currently being examined. For the GCS DIP publications, a highly optimized time-series database was deployed through the CERN Database On-Demand (DBOD) service. The time-series database was chosen to be InfluxDB thanks to the deploy and provisioning support offered by the DBOD service. Since the DIP APIs are written in Java or C++, a Python program interfacing with the C++ APIs was designed to retrieve desired publication values and store them on the InfluxDB database [1]. The application was designed to continuously fetch the available publications and regularly store them with a configurable polling time. The reasons for choosing a database instance different from the one used by the WinCC-OA application are multiple. First, the oracle database is mainly designed for WinCC-OA-only access. Also, the database architecture is not particularly optimized for time series data, sometimes making access to aggregated data difficult. The InfluxDB instance provided more flexibility as the instance was managed directly, and no accidental data loss could impact the supervision layer. The Grafana web application provided the visualization of the InfluxDB data. Grafana is a modern monitoring system that allows the creation and organization of dashboards for time series data. The dashboards can be created, modified, and deleted through intuitive user interfaces without any programming steps required. The Grafana web app was mainly used to aggregate the visualization of several sensors into a single web page so that the user could visualize and detect possible issues in the easiest and fastest possible way. A few examples of dashboards and their use are presented.

---

[1] `Dip to influx` codebase: `https://gitlab.cern.ch/grigolet/dip-to-influx`.

3.2.1 CMS RPC and HVAC tests

During LS2, the control software for the Heating, Ventilation, and Air Conditioning (HVAC) systems for CMS and ATLAS was upgraded. The ventilation systems provided new operation modes with different injection and extraction Air speeds in the UX cavern. A recommissioning phase was necessary to ensure the upgraded control system would operate as designed. However, RPCs chambers in the cavern could be affected by the variation of the UX environmental pressure during the HVAC tests in case of a mismatch of the speed between the injected Air and the extracted one. A Grafana dashboard was designed to visualize the detector and reference chamber pressure values for each distribution rack in the CMS UX cavern. Together with the pressure sensors, the Air speed injection and extraction trend and the US and UX environmental pressures were added. A screenshot of the dashboard is shown in Figure 3.5 The first panel represents the differential pressures measured by the GCS sensors. The second panel shows the Air speed and pressure for the injection and extraction part. It can be observed that several different ramp-ups and downs are present, depending on the operating mode of the HVAC system. The panels from the second row show the chamber pressure PTxx04 and the dummy chamber pressure PTxx05. The visualization of all the chamber pressures allowed us to investigate the pressure drop observed at around 11:00 and correlate it with the spike in the UX environmental pressure due to a failure of the selected HVAC mode during that period.

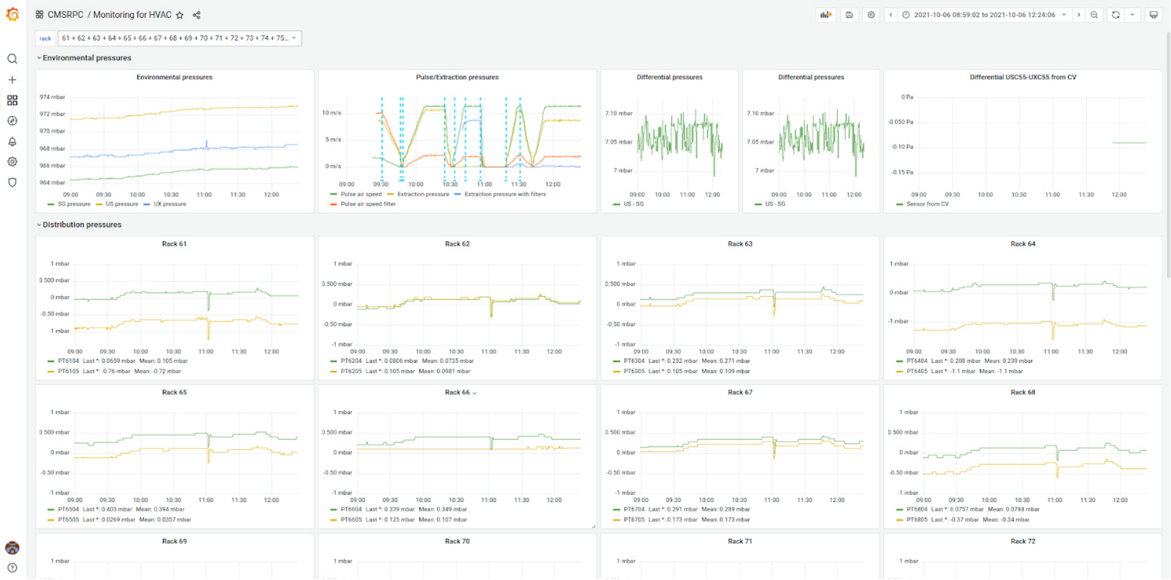

FIGURE 3.5 – Screenshot of the Grafana dashboard for HVAC tests and CMS RPC detector pressure monitoring

3.2.2 ATLAS MDT distribution pressure monitoring

After the LS2 upgrade of the software for the ATLAS MDT gas system, a pressure overshoot at the detector's output of each distribution rack was observed every time the gas system was restarted. No clear reasons were known about the possible causes at the time. A dedicated PID tuning campaign was then set up to adjust the response of the control valve at the output of the distribution racks to minimize the pressure overshoots during the startup phases of the system. A detailed analysis of the tuning campaign is presented in Section3.4

A dedicated Grafana dashboard was built. For each rack, the input and output pressure was monitored. Furthermore, for each output pressure, a panel displaying the pressure difference to the setpoint was made available on a separate page and reported in Figure 3.6. The main panel displayed the output pressure overshoot and undershoot over the first 24 hours of the period from the start-up phase of the system t_0. The overshoot and undershoot were defined as the $p_{overshoot} = max(p(t) - p_{setpoint}),\ t \in [t_0, t_0 + 24\ \texttt{hours}]$. A color map was used to help the user identify which racks required better tuning. The trend panels from the second rows displayed instead of the value $\Delta p = p(t) - p_{setpoint}$ over time, giving useful information about the required time for each rack to reach the desired pressure setpoint after the initial oscillations.

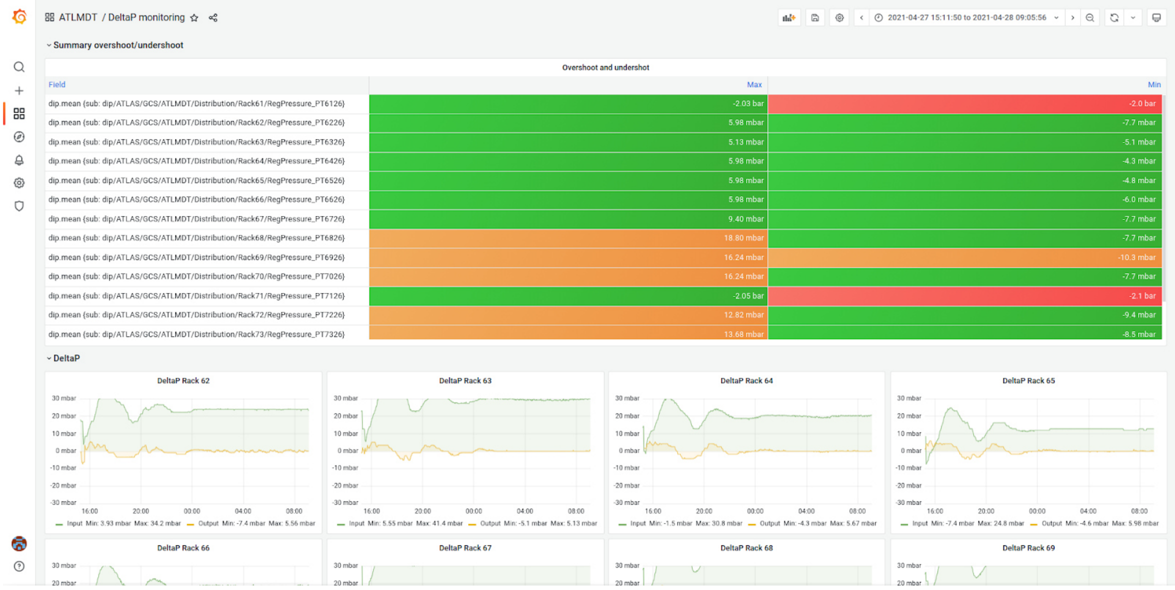

Overshoot and undershoot

Field	Max	Min
dip.mean {sub: dip/ATLAS/GCS/ATLMDT/Distribution/Rack61/RegPressure_PT6126}	-2.03 bar	-2.0 bar
dip.mean {sub: dip/ATLAS/GCS/ATLMDT/Distribution/Rack62/RegPressure_PT6226}	5.98 mbar	-7.7 mbar
dip.mean {sub: dip/ATLAS/GCS/ATLMDT/Distribution/Rack63/RegPressure_PT6326}	5.13 mbar	-5.1 mbar
dip.mean {sub: dip/ATLAS/GCS/ATLMDT/Distribution/Rack64/RegPressure_PT6426}	5.98 mbar	-4.3 mbar
dip.mean {sub: dip/ATLAS/GCS/ATLMDT/Distribution/Rack65/RegPressure_PT6526}	5.98 mbar	-4.8 mbar
dip.mean {sub: dip/ATLAS/GCS/ATLMDT/Distribution/Rack66/RegPressure_PT6626}	5.98 mbar	-6.0 mbar
dip.mean {sub: dip/ATLAS/GCS/ATLMDT/Distribution/Rack67/RegPressure_PT6726}	9.40 mbar	-7.7 mbar
dip.mean {sub: dip/ATLAS/GCS/ATLMDT/Distribution/Rack68/RegPressure_PT6826}	18.80 mbar	-7.7 mbar
dip.mean {sub: dip/ATLAS/GCS/ATLMDT/Distribution/Rack69/RegPressure_PT6926}	16.24 mbar	-10.3 mbar
dip.mean {sub: dip/ATLAS/GCS/ATLMDT/Distribution/Rack70/RegPressure_PT7026}	16.24 mbar	-7.7 mbar
dip.mean {sub: dip/ATLAS/GCS/ATLMDT/Distribution/Rack71/RegPressure_PT7126}	-2.05 bar	-2.1 bar
dip.mean {sub: dip/ATLAS/GCS/ATLMDT/Distribution/Rack72/RegPressure_PT7226}	12.82 mbar	-9.4 mbar
dip.mean {sub: dip/ATLAS/GCS/ATLMDT/Distribution/Rack73/RegPressure_PT7326}	13.68 mbar	-8.5 mbar

FIGURE 3.6 – Grafana dashboard for the PID tuning campaign conducted for the distribution pressure regulation for the ATLAS MDT gas system.

3.2.3 ATLAS TGC and MicroMegas flow monitoring

During LS2 activities on the ATLAS TGC and MicroMegas (MMG) gas systems, several different interventions were performed. Among them, the adjustment of the flow for each channel connected to each distribution rack was required. Due to the difficult access to the TGC UX distribution racks mounted on different levels of the ATLAS Big Wheels, a solution to monitor the flow without the usage of a laptop computer was crucial. A dashboard was then designed to visualize all the channel flows for a select rack. Each channel flow was displayed in a trend panel. Their live values were organized in a histogram form to allow the operator to easily catch the channels requiring additional adjustment. A similar dashboard was also designed for the MMG gas systems due to the ease of access for external users to the flow cells data without the need of the GCS SCADA application. The dashboards for the TGC and MMG systems were designed so that the user could easily select the distribution rack from a dropdown menu on the top left corner of the page. The input and output flow cells are then grouped into two histograms displaying the latest available values. A set of user-defined thresholds were added to help the user understand whether each channel flow

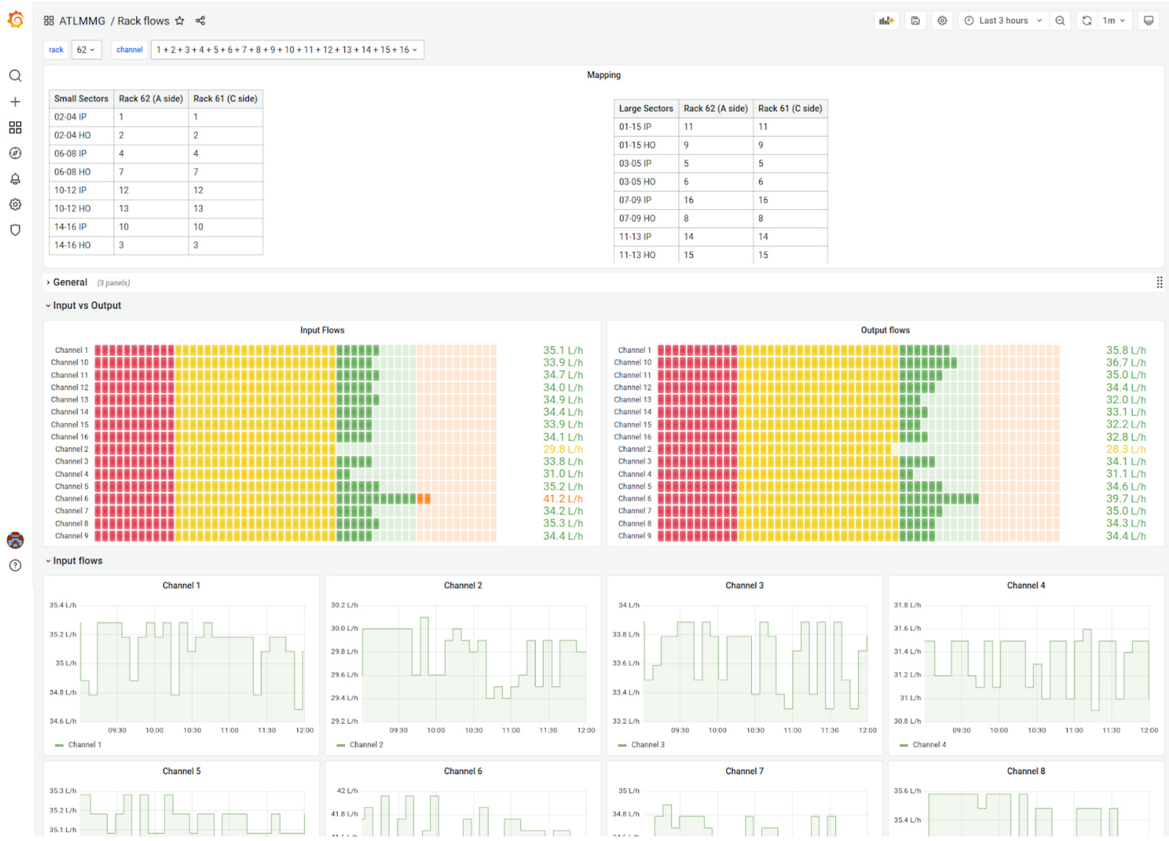

Mapping

Small Sectors	Rack 62 (A side)	Rack 61 (C side)
02-04 IP	1	1
02-04 HO	2	2
06-08 IP	4	4
06-08 HO	7	7
10-12 IP	12	12
10-12 HO	13	13
14-16 IP	10	10
14-16 HO	3	3

Large Sectors	Rack 62 (A side)	Rack 61 (C side)
01-15 IP	11	11
01-15 HO	9	9
03-05 IP	5	5
03-05 HO	6	6
07-09 IP	16	16
07-09 HO	8	8
11-13 IP	14	14
11-13 HO	15	15

	Input Flows	Output flows
Channel 1	35.1 L/h	35.8 L/h
Channel 10	33.9 L/h	36.7 L/h
Channel 11	34.7 L/h	35.0 L/h
Channel 12	34.0 L/h	34.4 L/h
Channel 13	34.9 L/h	32.0 L/h
Channel 14	34.4 L/h	33.1 L/h
Channel 15	33.9 L/h	32.2 L/h
Channel 16	34.1 L/h	32.8 L/h
Channel 2	29.8 L/h	28.3 L/h
Channel 3	33.8 L/h	34.1 L/h
Channel 4	31.0 L/h	31.1 L/h
Channel 5	35.2 L/h	34.6 L/h
Channel 6	41.2 L/h	39.7 L/h
Channel 7	34.2 L/h	35.0 L/h
Channel 8	35.3 L/h	34.3 L/h
Channel 9	34.4 L/h	34.4 L/h

FIGURE 3.7 – The ATLAS MMG grafana dashboard flow monitoring.

corresponded to the desired range. A trend panel for each flow cell was made available on the bottom rows.

3.2.4 An overview panel for GCS applications

The supervision layer of a GCS application is organized in HMI panels. Each panel was designed to resemble the different modules of the gas systems. For instance, one panel is usually generated for the mixer module, one for the humidifier, one for the pump, etc. For the distribution module, one panel was added for each rack. The high number of panels in a GCS application may affect the capability of the supervision layer to provide an overview of the whole gas system. In particular, the most relevant parameters for each module may require several navigation steps to be accessed. Furthermore, each panel provides only information about the current status of the gas system and doesn't provide any statistics about the performance of a sensor unless the sensor's data is inspected using the trending widget. The increasing complexity and granularity of gas systems required a solution to allow the gas experts to investigate the system's general status in the easiest and fastest possible way. The issue was addressed by designing an overview HMI panel. The panel was built with the idea of displaying the most relevant data from transmitters and sensors, gathered from different modules, under a unified point of access. Such a panel allowed the operator to perform regular gas systems routine checks. In case of issues spotted from the overview panel, a navigation link to each gas module was made available to allow a thorough inspection of the affected module. Although it was integrated into the SCADA application, the overview panel was deployed as an application independent from the GCS. The project was built as a Soft Front-End project, meaning that no interaction and control of physical instrumentation was required. The specification file included one line for each device that had to be included in the overview panel. For each device, it was then possible to specify two types of statistics: time-based or device-based. The time-based statistics consisted in retrieving simple aggregated values, such as max, min, average over a rolling time window. This statistic was added for most devices, such as loop flow, loop input pressure, pump regulation valve, etc. The device-based statistics allowed instead to perform simple aggregations between different devices, designed with the idea of checking minimum, maximum, and average pressures when multiple distribution racks are present. A panel prototype was built for the ATLAS MDT gas system, shown in Figure 3.8. The panel was built by drawing a simplified schema of the closed-loop system and by placing each relevant sensor value in the place reflecting the actual position in the gas system. For each sensor value, its appropriate or time or device-based statistics were also displayed. The value was calculated every hour for time-based statistics by taking a moving window of a week in the past, allowing the operator to get insightful information about a possible drop or spikes of the sensor when performing a weekly check on the system without opening the trend widgets for each sensor.

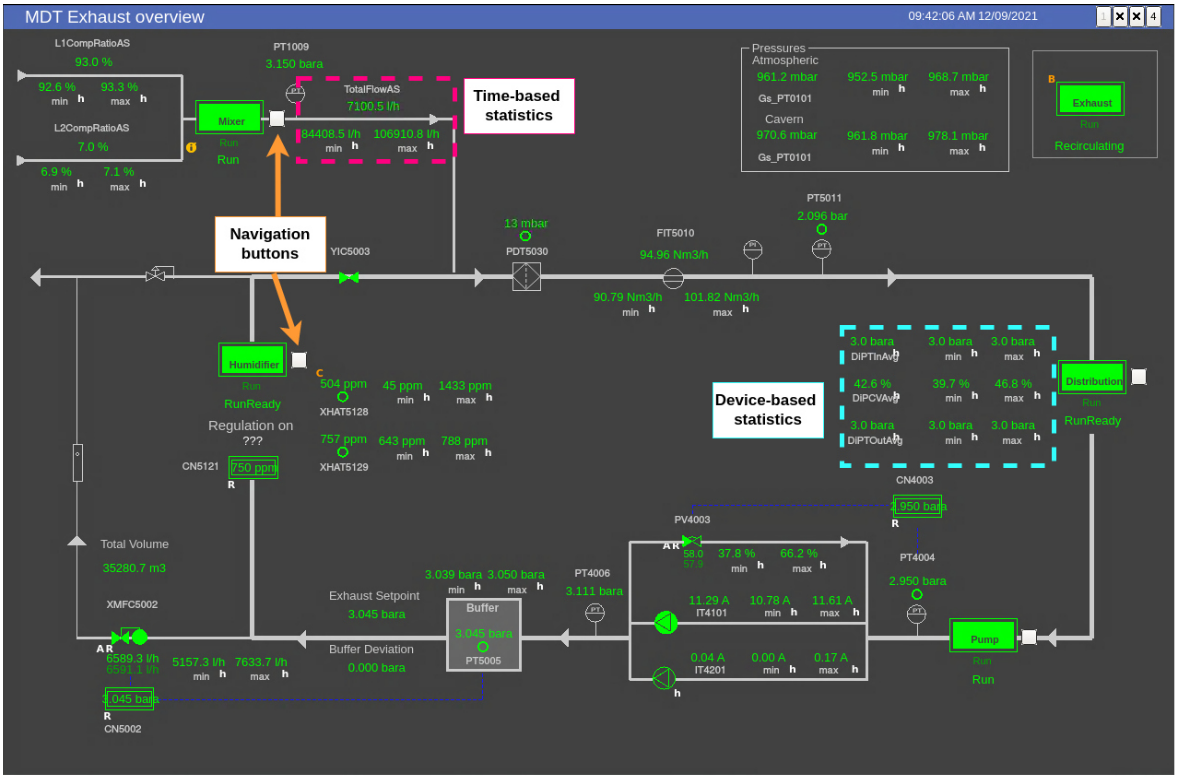

FIGURE 3.8 – Overview panel designed for the ATLAS MDT gas system. The panel shows a simplified schema of the closed-loop system, with the different sensors placed in their relative position to the gas system.

3.3 Offline data analysis of gas system data

The present section describes the available tools to retrieve gas system data and how the data was used to conduct tests, anomaly detection, and optimizations on the gas systems. As previously mentioned, most of the SCADA data points elements are archived on an Oracle

Experiment	Number of devices	Mean data pointsday
ALICE	19706	3240000
ATLAS	6156	6660000
CMS	36609	3830000
LHCb	17002	3530000

TABLE 3.1 – Archiving statistics for the different Gas Control Systems for the LHC experiments.

database, mainly accessible by the SCADA application only. A second layer of archiving was provided by the CERN accelerator logging system (CALS), an Oracle database system that made available most of the data sensors from all CERN accelerator infrastructures and beam-related applications. The service was running from 2003 to 2021, where it was then replaced with the Next CERN's Accelerator Logging Service (NXCALS), based on Big Data technologies and able to cope with the increasing data I/O throughput demand [28]. The NXCALS service is based on the Apache Hadoop technology for data storage and provides APIs on top of the Apache Spark analytics solution. The service is production-ready and includes Java and Python programming languages support.

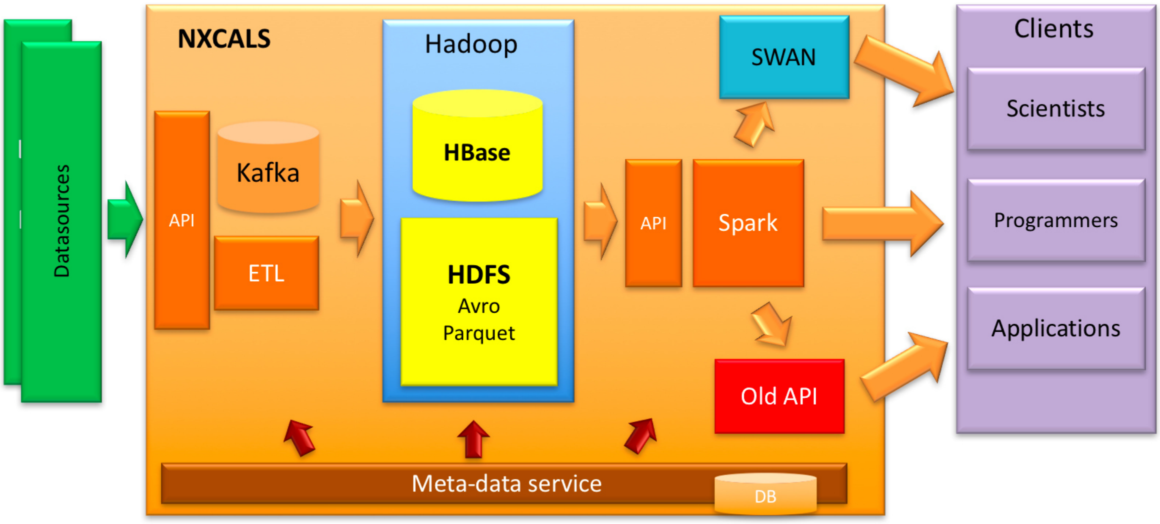

FIGURE 3.9 – NXCALS architecture diagram, as shown from NXCALS website documentation.[2]

Most gas systems archived data is stored in the NXCALS Hadoop file system. The data can be accessed by setting the connection to the NXCALS cluster and querying the device name over a desired time window. The CERN's Service for Web-based ANalysis (SWAN) provides a ready-to-use Python's Jupyter environment to use NXCALS APIs. Also, the recently developed Timber web application[3] provides easy access to all the NXCALS data without requiring the use of a programming language. The archiving rate for each device depends on several factors. In the first instance, the WinCC-OA archiving settings allow different deadband algorithms to lower the number of stored data points without losing much information. The deadband configuration is particularly useful for analog sensors whose reading

---

[3] `http://timber.cern.ch/`

may be affected by electrical noise. The default deadband configuration for the analog sensors in most of GCS was chosen to be "Deadband AND Time": whenever the process value changes more than the value set in the deadband the data point is stored into the database. If no change above the threshold is encountered, the data point is stored when a configurable amount of time has passed. A schema of the deadband and archiving settings for two different archiving algorithms is reported in Figure 3.10 The archiving for digital devices such as On/Off valves or step sequences of a controller object are usually stored using an Old/New comparison mechanism, meaning that a data point is archived whenever the current value is different from the last stored one. Each device is archived with its name. The naming convention for the device follows the one established during the design phases of the LHC gas systems. The first three letters uniquely identify the experiment, while the second three indicate the detector system. The gas system module follows, characterized by two letters and separated from the detector name with an underscore. A trailing underscore separates the gas system name from the device type, indicated by two or more characters. Following the device name, four digits indicate the module type and the device's position with respect to the gas system module. The consistency of the naming convention for gas systems allows the gas system experts to locate the device by looking at its name quickly, and on the opposite: it easily lets the operator find the name for the device given its position and scope in the gas system.

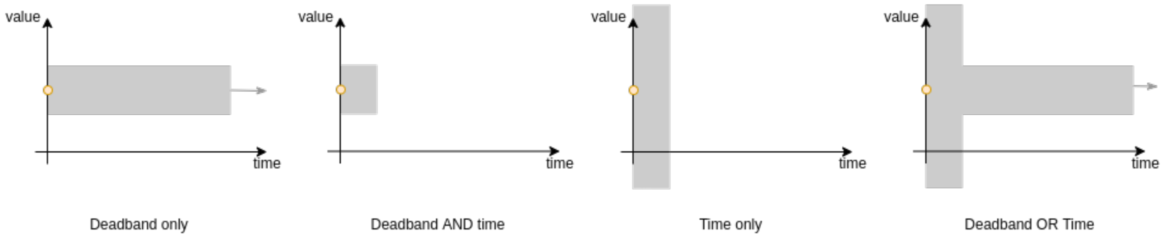

FIGURE 3.10 – Different archiving mechanisms for time or tolerance dependent values. The default GCS settings for analog devices are set to be "Tolerance AND Time" based.

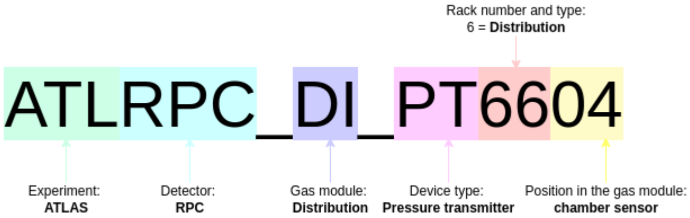

FIGURE 3.11 – Schema of the naming convention applied for a device on the ATLAS RPC gas system

3.3.1 Data aggregation and visualization for anomalies detection

The storage of gas systems data allows one to perform different gas system optimizations. In the first instance, the historical data could be used to detect anomalies in the functioning of a gas component. Identification of anomalies is sometimes referred to as anomaly detection, and it is a field that found an extensive application in sensor data and industrial control systems [29, 30, 31, 32, 33]. Assessments of automated anomaly detection systems for gas systems are currently being performed. A simplified approach to anomaly detection can be made by retrieving historical data and performing simple statistics on the whole time series or on rolling time windows. Few examples are reported in this Section. A second use for historical data is the optimization of controllers for regulating objects. In particular, tuning of PID controller gains is an operation-critical procedure for the correct operation of gas systems. The details about PID controllers are presented later in this Chapter.

Gas flow analysis for the ATLAS RPC system

The flow-related data for the ATLAS RPC gas system was used to understand and monitor the evolution of leaks at the detector level. Input and output flow cell data were analyzed for different selected periods, and the gas loss rate, defined as $\Delta_{GasLossRate} = (\phi_{input} - \phi_{output})/\phi_{input}$, was used to compare data between different periods with different gas mixtures flowing in the detector. The selected periods were used to compare the gas system performance during Run 2 with the detector working with a 94.7/5/0.3 R-134a/i-C_4H_{10}/SF_6 gas mixture against the LS2 period, where the RPC system was working with a gas mixture of 97/3 N_2/R-134a. The historical trend was retrieved for each distribution rack channel, as shown in Figure 3.12

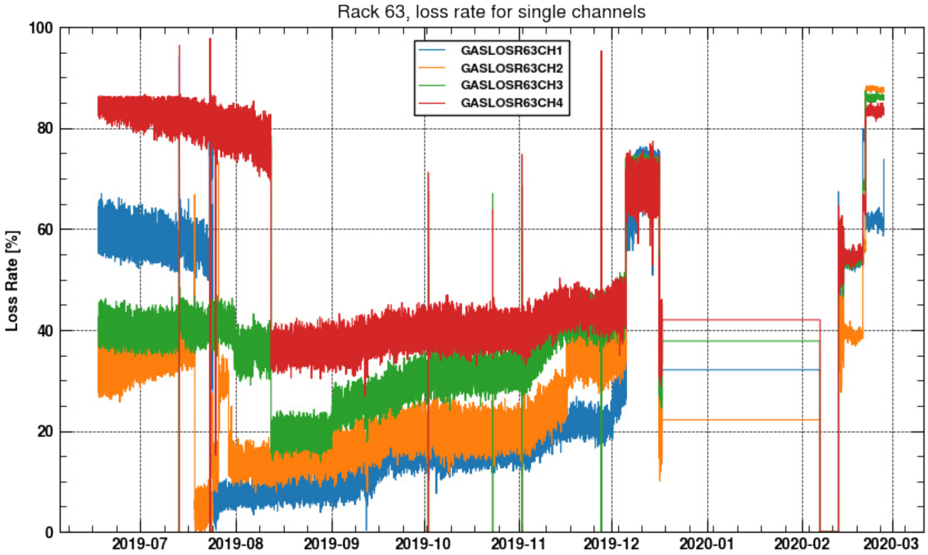

FIGURE 3.12 – Gas loss rate for a few channels of a distribution rack in the ATLAS RPC system during the LS2 phase

The mean gas loss rate for different selected periods was added to a bar plot as shown in Figure 3.13, allowing us to understand which of the chosen periods was the one to look for possible anomalies in the gas system. A second analysis consisted in retrieving the historical loss rate data for each channel for the 2018 year, corresponding to the last Run2 period for LHC. The Python ruptures library was employed for offline change point detection [34]. Each channel loss rate was tested with different change point detection algorithms to determine the dates when the library detected a change in the trend. In particular, the Pruned Exact Linear Time (PELT) model [35] was used thanks to its simplicity and linear computational cost.

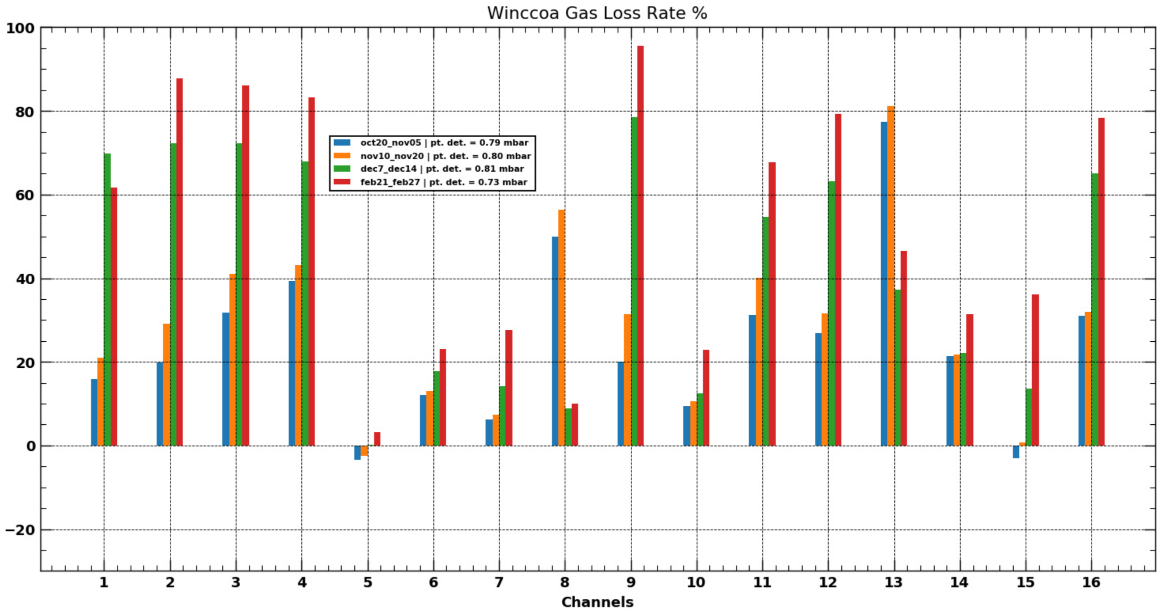

FIGURE 3.13 – Mean Gas loss rate data for rack 63 of ATLAS RPC system measured during different periods of 2019

The PELT model was used together with an $L1$ cost function, particularly robust to identify a change in the mean, mode, median values of the time series [36]. Given an interval I and the relative signal y_{t_t}, the $L1$ cost function for the interval I can be defined as:

$$c(y_I) = \sum_{t \in I} \|y_t - \hat{y}\|_1 \tag{3.1}$$

where $\hat{y}$ is the median of y_t over the interval I. Few other parameters for the change point estimation were adjusted to avoid overfitting the time series data and to avoid the detection of eventual spikes in the signal as potentially dependent on a different class of anomalies and easily detectable with peak finding algorithms.

Once a suitable set of parameters was found, the change point detection was applied to each channel in each distribution rack, as shown in Figure 3.14. The dates detected by the algorithm were collected and later aggregated in a time histogram as shown in Figure 3.15 The dates with the highest count in change points were then identified using the Python peakutils library [37]. Such information was then used to investigate possible changes in the RPC gas system operation on the selected dates. No clear correlations with other gas systems values were found, suggesting external causes may cause the development of the leak in the considered periods.

Change of gas mixture in the ATLAS TGC detector

The ATLAS TGC detector is operated during LHC runs with a gas mixture of 45/55 CO_2/n-C_5H_{12}. The gas mixture is known to be highly flammable due to the presence of n-pentane. As such, several safety risk assessments must be taken every time a human intervention must be performed in the proximity of the chamber installations. During the LHC pilot beam period in October 2021, the New Small Wheel (NSW) installed on side A of the ATLAS experiment was operated with the nominal, n-pentane based gas mixture. After the pilot

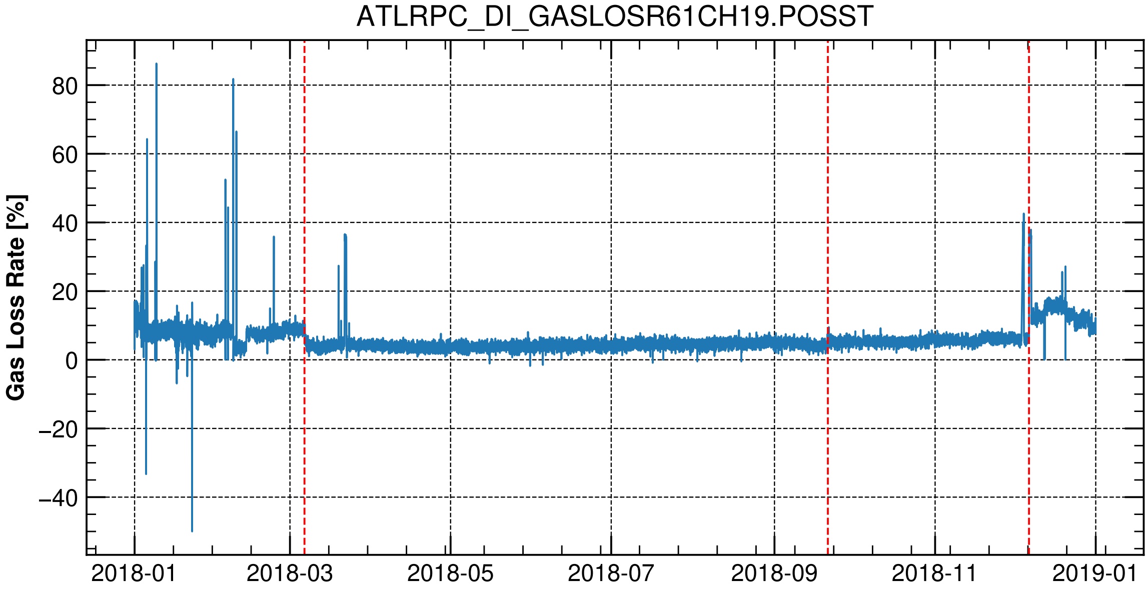

FIGURE 3.14 – Detected change points (in dashed red vertical lines) for the gas loss of a single channel. The algorithm was tuned to detect mostly change points in the mean and median value, discarding spikes that could represent a different class of anomalies.

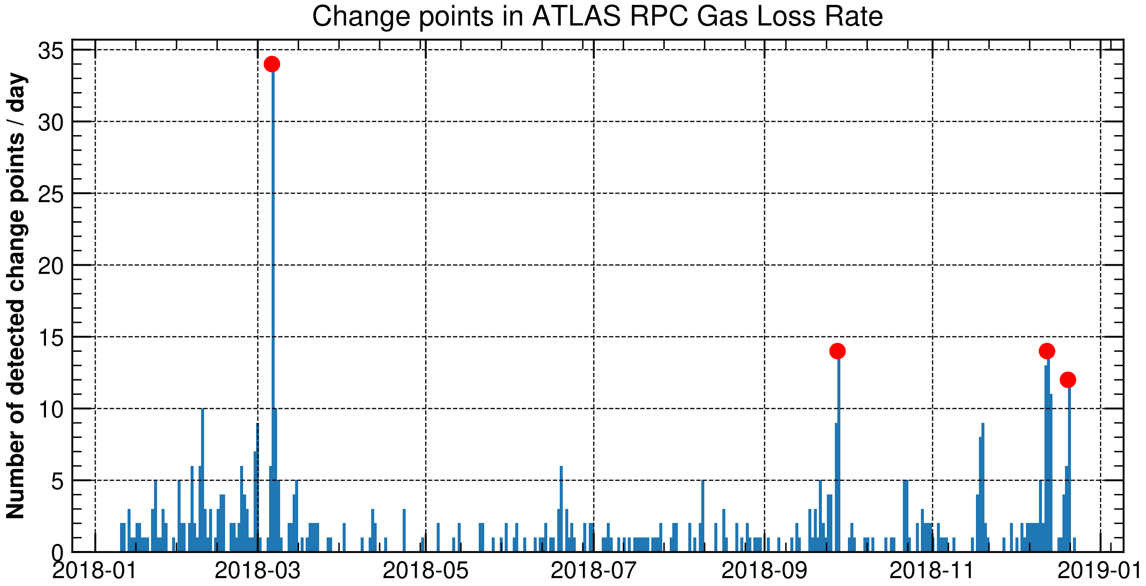

FIGURE 3.15 – Number of detect change points in the ATLAS RPC system during 2018 for all the gas loss rate signals. Few dates can be easily identified by their relatively higher number of change point counts.

beam period, the NSW sector needed to be flushed again with pure CO_2 to remove every presence on n-pentane from the gap volume of the chamber and allow a safe operation in the UX cavern. The flow cell readout working principle was exploited to estimate the time required to flush away n-pentane from the chamber volumes. Flow cells for the TGC gas system were calibrated in laboratory conditions for pure CO_2 gas. The addition of n-pentane to the gas mixture changes the thermal conductivity of the gas mixture itself. Consequently, the temperature slope curve used by the internal flow cell resistance to determine flow varies whether pure CO_2 or TGC gas mixtures are flushed.

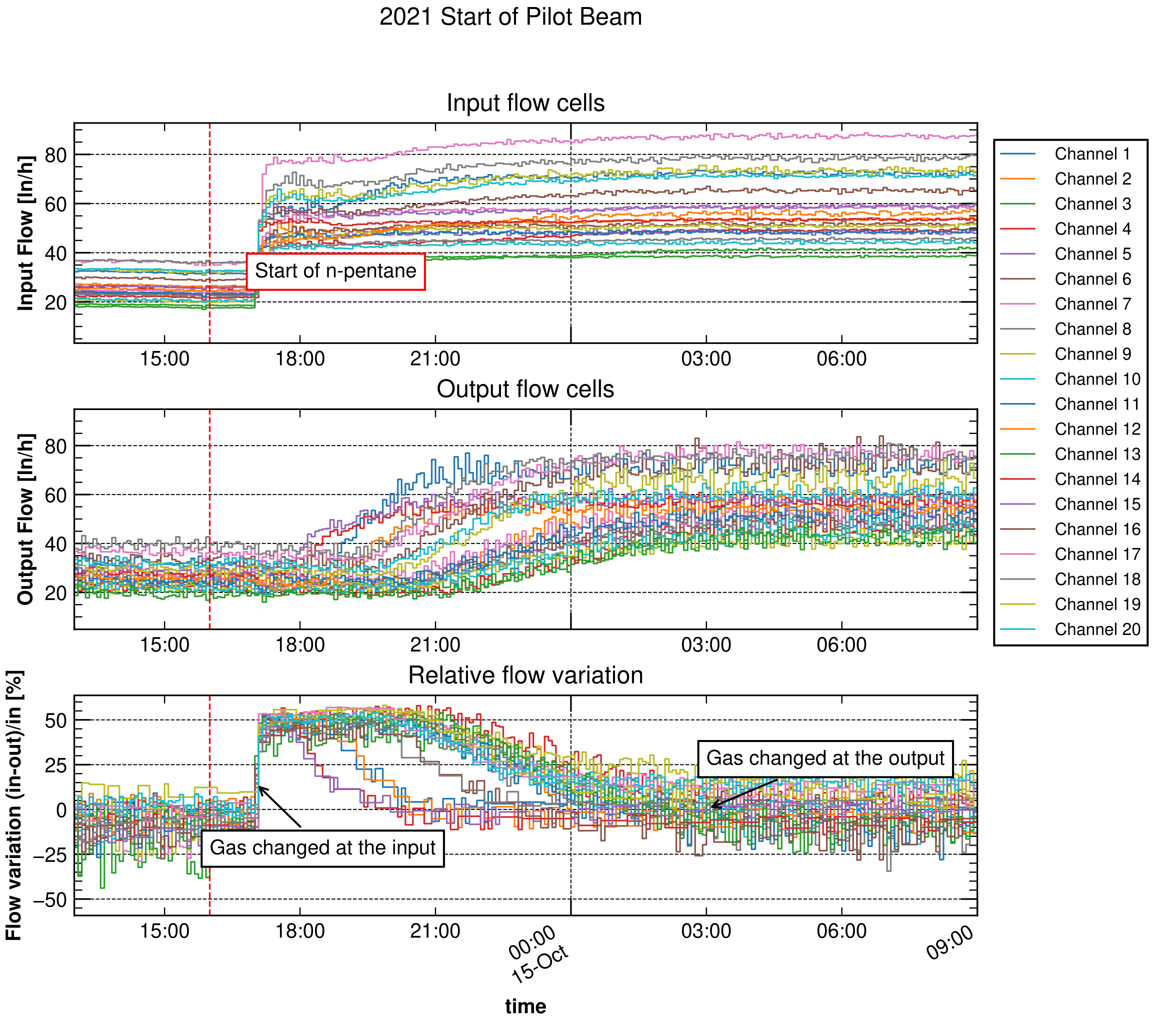

FIGURE 3.16 – Input, output and gas loss rate for the new small wheel gas channels during the start of the TGC gas system for 2021 LHC Pilot beam. The vertical red dashed line corresponds to the start of the injection of n-pentane from the mixer module.

The estimated arrival time was then used as a reference value for the opposite process, i.e., the minimum amount of time required for the n-pentane to be removed from the chambers. The time was estimated to be around 12 hours, accounting for an additional safety interval of 2 hours. The data relative to the removal of n-pentane is shown in Figure 3.17. It can be observed that the time required for the n-pentane to be removed from the detector corresponded to around 11 hours, a value compatible with the one previously calculated.

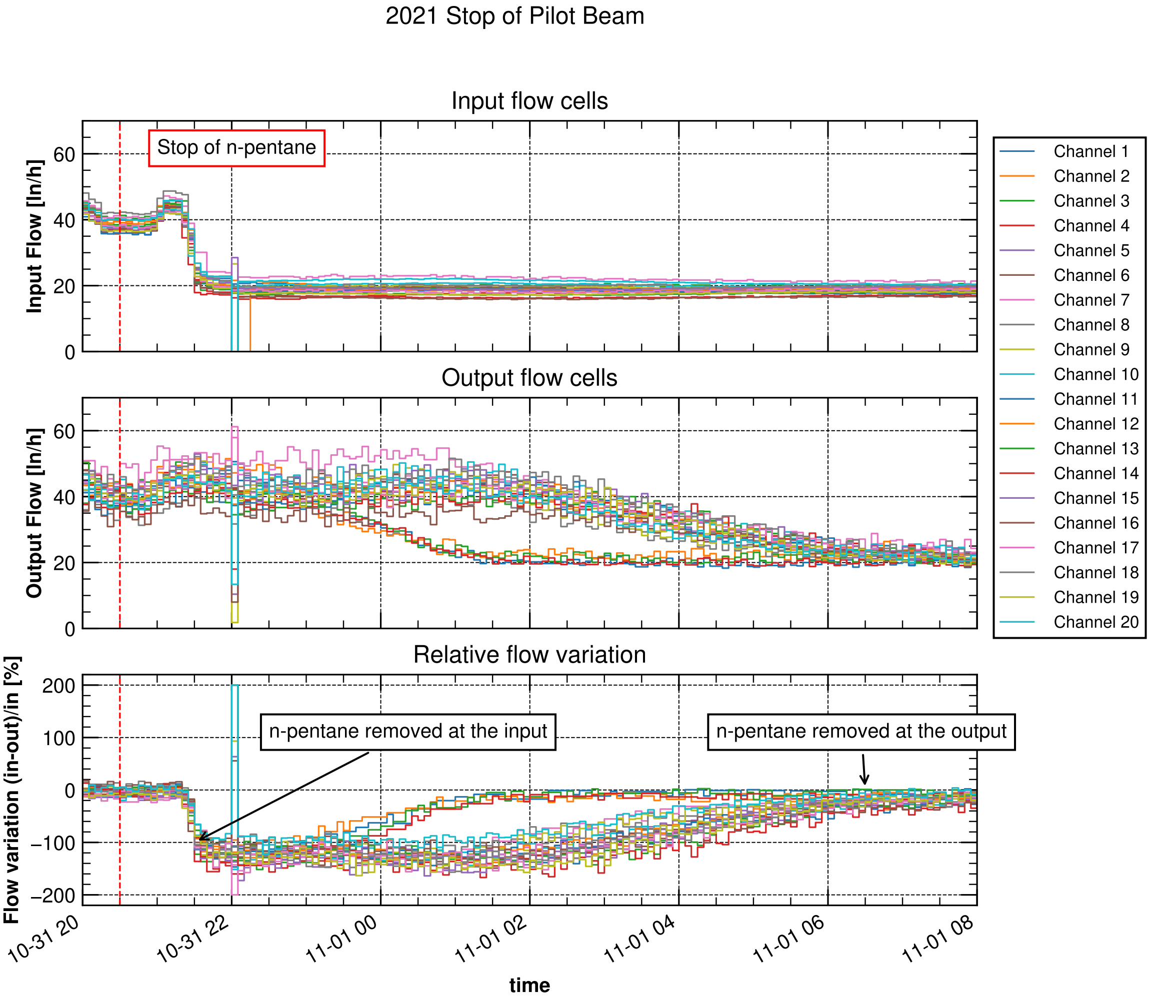

FIGURE 3.17 – input, output and gas loss rate for the new small wheel gas channels during the stop of the TGC gas system for the 2021 LHC Pilot beam. The vertical red dashed line corresponds to the stop of the injection of n-pentane from the mixer module.

3.4 Tuning of PID gains for auto-regulating controllers

Gas systems are responsible for providing gas mixtures to detectors under stable and controlled conditions. The stability of the gas can be described in terms of its quality, flow rate, and pressure in different parts of the system. Several LHC gas systems use regulating objects to ensure the proper operation of the gas system. Two controller objects are mainly used at the software level: the Process Control Object (PCO) and the Proportional-Integral-Derivative Controller (PID). The PCO is used to program the logic of a set of plant actuators, such as On/Off valves, heaters, and pumps. Instead, the PID controller is a general control loop mechanism that ensures a selected process variable reaches the desired setpoint by acting on an actuator. PID controllers are primarily employed in several modules of gas systems. The PID controller provides a set of parameters that needs to be appropriately tuned to ensure the operating condition of the devices, therefore of the gas system itself. A brief introduction to control theory and PID controllers is given in the present Section. Later, a few examples of PID gains for different LHC gas systems are discussed.

3.4.1 The Proportional-Integral-Derivative controller

Control theory is the discipline that deals with the control of dynamic systems. Control theory aims to develop models that describe how a set of inputs should be governed to lead the dynamic system to the desired state. Suppose we have a system with a command input $u(t)$ and output $y(t)$. The system is transformed by a process P that transforms $u(t)$ into $y(t)$. Let us define the reference state of the system $r(t)$. Two main categories of control loops can be distinguished: the open-loop or feedforward and the closed-loop or feedback. The open-loop process depends only on the input $u(t)$ to produce $y(t)$. Closed-loop processes, however, compare $y(t)$ with the reference $r(t)$. Typically, for closed-loop systems the error $e(t)$ is defined as $e(t) = r(t) - y(t)$. The error is then used as an input, and the system tracks the target reference by minimizing the error itself. Feedback systems have the advantage of being able to correct even when the dynamics of the process are unknown, which is the case for most real-life systems.

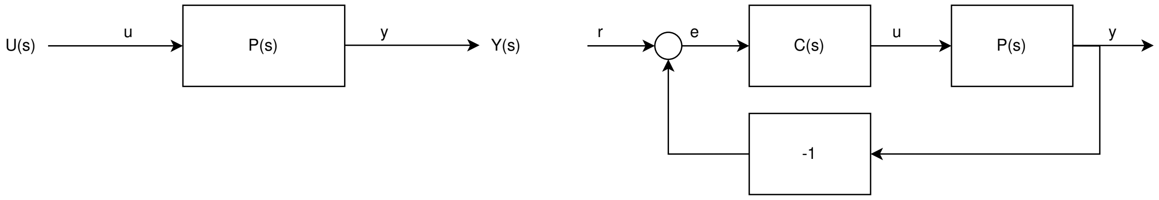

FIGURE 3.18 – Open and closed loop processes.

A controller C is a process that modulates the system dynamics. The Proportional-Integral-Derivative (PID) controller is one of the most employed feedback controllers in industrial systems. As the name suggests, the PID controller takes the error e(t) input and applies three linearly combined outputs: proportional, integral, and derivative. One of the most common for the PID controller is the expression:

$$u(t) = K_p e(t) + K_i \int e(t)\,\mathrm{d}t + K_p \frac{\mathrm{d}e(t)}{\mathrm{d}t} \tag{3.2}$$

Where K_p is often referred to as the proportional gain, K_i the integral gain, K_d the derivative gain. It should be noted that the three terms are linearly combined and independent from each other. This allows one to understand the effect of each term in the formula.

If we take a proportional only controller in the form $u(t) = K_p e(t)$, we can observe that the output response is driven only by the error at time t. For this reason, the proportional part is often referred to as the "present" part, as the proportional controller is only concerned with the value of the error at the present time t. The proportional-only controller works well with integrating systems, i.e., systems for which the output $y(t)$ depends on $\int u(t)dt$. An intuitive example of an integrating process is a liquid tank whose level is regulated by a valve with values on ($u = 1$) or off ($u = 0$). The measured output, in this case, is the level of the tank $y(t)$. When the valve is opened, the output y starts to increase until the valve is closed. Once the valve is closed, the level remains fixed over time. A simple description of the process can be expressed in the form:

$$y(t) = a + b \int u(t)\,\mathrm{d}t \tag{3.3}$$

where a is the initial water level, and b is a coefficient determining the flow passing through the valve when opened. If a leak is present on the water in the tank, the output $y(t)$ won't depend on the amount of liquid passed through the valve and the leak rate. The system is said to be non-integrating or short-time integrating as the output of the process does not depend only on the accumulated inputs $u(t)$. P-only controllers are not suitable for non-integrating processes as they lead to a steady-state error for which the output $y(t)$ would never reach the setpoint. This counterintuitive effect is due to the fact that the calculated value of $u(t)$ becomes smaller when the error $e(t)$ decreases, i.e., when the value of $y(t)$ gets closer to the setpoint. However, if $y(t)$ reaches the desired setpoint, $e(t)$ becomes zero, and the controller output $u(t)$ becomes 0, which leads to a decrease of the output $y(t)$ for non-integrating processes.

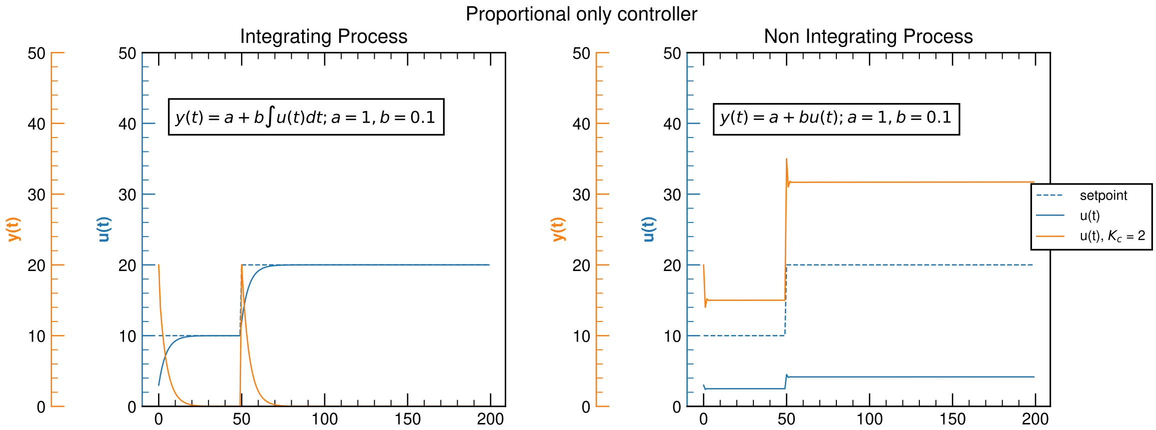

FIGURE 3.19 – On the left, an integrating process with a P-only controller. The change of setpoint is used to show the response of the controller. It can be observed that after a certain amount of time the y(t) reaches the desired setpoint. On the right, a P-only controller with a non-integrating process. After a relatively small amount of time the system reaches a steady state without reaching the setpoint.

For this reason, PI or PID controllers are often used for most non-integrating, real-life systems. PI controllers are often preferred over PIDs as the derivative controller may lead to regulation instabilities in the presence of noise from the measured variable. The integral part in the PI controller produces an output that depends on the integral of the error $e(t)$, solving the problem of steady-state error as the integral error would be accumulated during the steady-state phase, leading to an increased response of the controller. The derivative part acts on the time derivative of the process variable. The derivative part is often used to avoid overshoots in the presence of setpoint changes as its response is proportional to the gradient of $e(t)$. However, in the form expressed by Formula 3.2, the derivative part may increase significantly in an instantaneous setpoint change or in the presence of noise in the measured variable as shown in Figure 3.20.

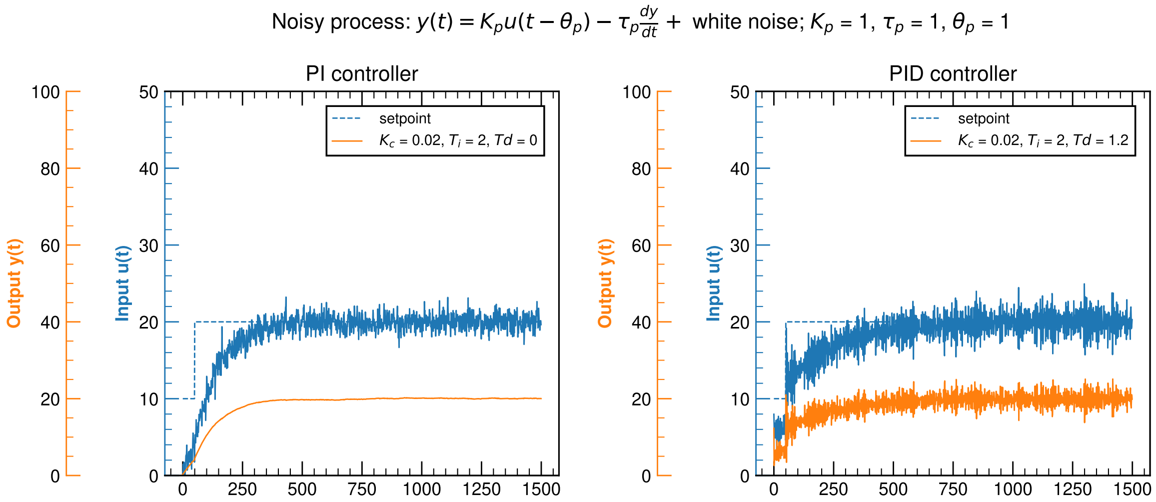

FIGURE 3.20 – Simulation of a setpoint change for a First Order Plus Dead Time (FOPDT) process. On the left, a PI controller is used. On the right, a full PID controller is used. The increase of noise is due to the derivative part that increases the output due to the derivative of the fast frequency signals induced by the noise.

Several commercial implementations of the PID controllers introduce an additional parameter that acts as a low pass filter. In gas systems, PI controllers are usually preferred as sufficient to fulfill the regulation performance requirements. Although more straightforward, the choice of the Kc and Ti gains dramatically affects the system's dynamics: a poorly set of parameters may lead to sustained instabilities in the presence of change in the process input or the setpoint. An example of different fluctuations arising by choice of different combinations of PID parameters is reported in Figure 3.21

The choice of the gains Kc and Ti largely depends on the dynamic of the process and the requirements in terms of performance and stability of the controller. High gains may lead to faster response time but also increased instabilities of the controller. Several tuning rules have been studied in the past 70 years [38]. Classical tuning methods found in the literature include the Ziegler-Nichols frequency response method, the Choen-Coon method, and the Internal Model Control method. However, most models assume that the transfer function modeling the plant is known. This condition is not always met, especially in large and complex plants. Some simple tuning rules required knowledge of the process's transfer function in the frequency domain. However, modeling is not always available in large and

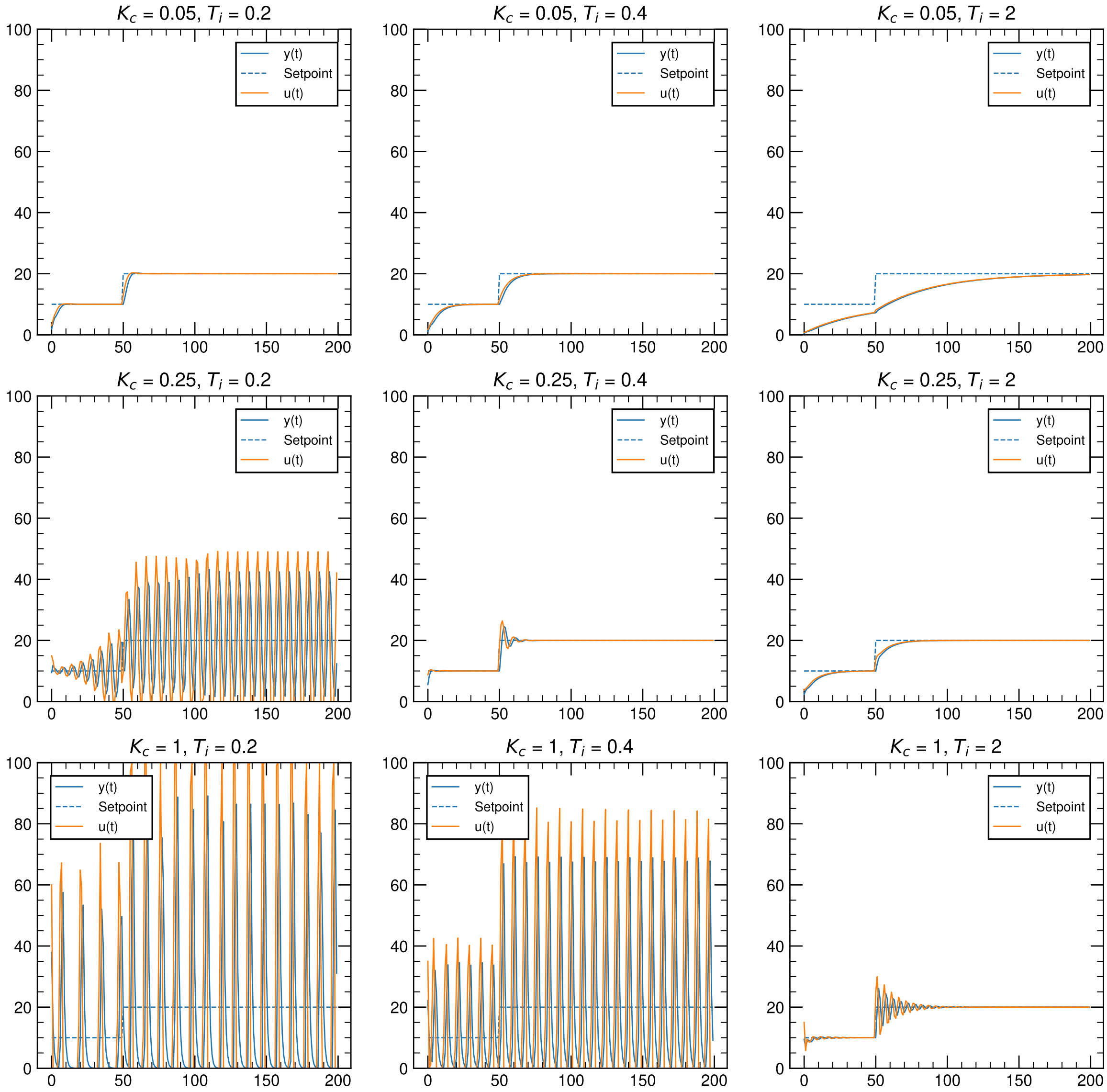

FIGURE 3.21 – Simulation of the response of a PI controller with different choice of the Kc and Ti gains. Several different responses can be observed. Undertuned or overturned gains may lead to slow reaction of the controller to setpoint changes or to sustained instabilities.

complex industrial plants. Most of the works are then based on heuristic rules, aiming at different goals (such as fast setpoint tracking and disturbance rejection) and might be required to perform open or closed-loop step response tests. Open and closed-loop step tests may be dangerous for controllers LHC gas systems regulating detector's pressure, as a change of setpoint may induce a force that could apply mechanical stress on the surface of the detectors themselves. For these reasons, the tuning procedure is often performed by gas system experts who supervise the process and change the value of the gains of the PI controller accordingly. The International Society of Automation (ISA) standard form, also used by the UNICOS CPC framework, thus in the LHC gas system, has a different definition from Formula 3.2:

$$PID = K_c(1 + \frac{1}{T_i s} + \frac{T_d s}{1 + \frac{T_d}{T_{ds} s}}) \tag{3.4}$$

It is important to note that, with respect to Formula3.2, the UNICOS PID definition is expressed using the Laplace form in the frequency domain. Also, K_c is a proportional gain dominating all the proportional, integral, and derivative parts. The integral gain is reported to the denominator, and a fourth parameter, T_{ds}, is introduced to eliminate the controller's response to high-frequency signals, often due to electronics noise in the measured sensor.

3.4.2 Regulation of chamber pressure for the ATLAS MDT gas systems

The ATLAS MDT gas system is one of the biggest recirculating gas systems, composed of 15 distribution racks providing a total flow of around 100 m^3/h of gas to the chambers. The MDT detectors are operated with a gas mixture of 93/7 % Ar/CO_2 and a few hundreds of ppm of H_2O. Each distribution rack has an input and output valve that is opened when the system is switched on and closed when the rack is stopped. Furthermore, a pressure transmitter PTxx24 is installed together with a manual regulation valve at the input of the distribution rack to regulate the flow sent to the chambers. An output pressure transmitter PTxx26 is then installed on the common return lines before a pneumatic control valve to ensure the detectors are operated at the desired pressure setpoint of usually 3 bar absolute (bara). A controller object is used to regulate the output pressure using the control valve at the software level. In this context, the control valve is the Manipulated Variable (MV), while the setpoint (SP) is fixed at 3 mbar, and the Process Variable (PV) is identified by the opening position of the valve expressed in the range [0, 100]%. A simplified schema of a distribution rack is reported in Figure 3.22.

Since February 2020, it was observed that whenever the gas system was restarted after a short period, the output pressure PTxx26 was overshooting and undershooting a few tens of millibars around the setpoint for most of the racks in the first hours of the system restart. After an equilibration time of 10 to 24 hours, the output pressure was observed to stabilize around the setpoint. Figure 3.23 shows all the distribution output pressures evolution during the first few hours of the system restart before and after February 2020. While investigations were ongoing to understand possible reasons, a PID tuning campaign was set up to enhance the performance of the regulation. The campaign consisted in stopping the gas system for around 30 minutes, changing the PID gains, restarting the gas system, and monitoring the output pressure for the relevant racks. The GCS upgrade made during LS2

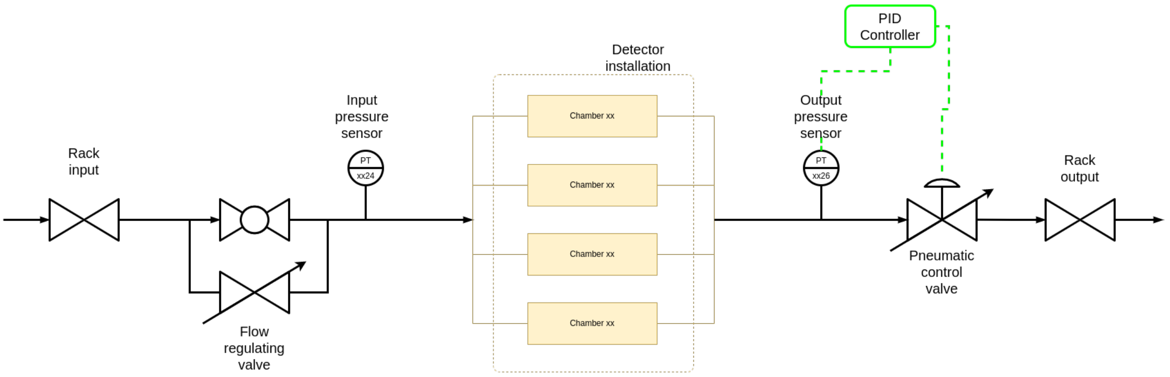

FIGURE 3.22 – Simplified process and instrumentation drawing for the distribution rack of the MDT gas system. The pneumatic control valve is regulated by a PID controller using PTxx26 as a process variable.

introduced an additional set of PID gains, namely StartUp parameters, that could be activated in place of the nominal Run parameters, depending on the status of the rack. Such a feature allowed us to use two sets of PIDs. The condition to switch between one set to another depended on the value of the output pressure and on a hysteresis parameter that could be configured through the activation of dedicated recipes. For each rack, it was possible to select the lower and higher values for the output pressure to trigger the switch between PID gains. The hysteresis parameter was instead introduced to avoid a continuous change of gains in the case of noisy sensors or small oscillations around one of the thresholds. The StartUp proportional gain was chosen to be higher than the Run one to allow the regulation valve to cope with the higher flow variations expected during the first hours of the gas system startup phase.

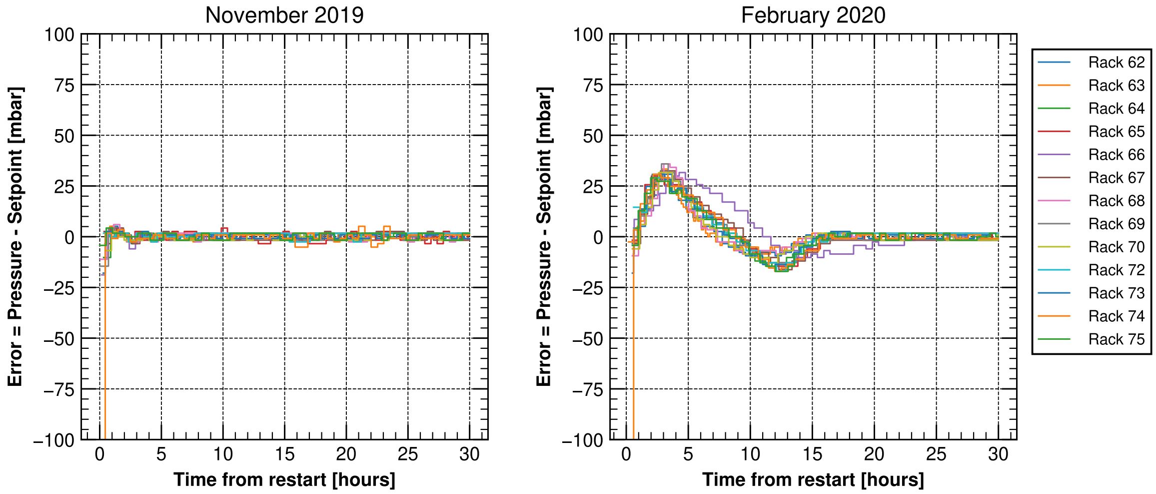

FIGURE 3.23 – Pressure deviation from setpoint after MDT gas system restart before and after 2020. A clear overshoot of around 25 mbars for most racks output is visible on the right plot.

Several trials and errors tests were conducted. For each startup, either the gains, the thresholds, or the hysteresis parameters were changed. The gains tested differed between each distribution rack due to the different detector volume, thus input flow that each rack had to provide. On average, the StartUp Kc gain was set two times higher with respect to the

Test number	**Run** K_c	 T_i	**Startup** Kc	 T_i	**Hysteresis**	**Run/St.up lower threshold [bara]**	**Run/St.up upper threshold [bara]**
0	0.2	1	0.3	2	0.05	3.05	2.9
1	1	2.5	2	2	0.003	3.005	2.995
2	1	2.5	2	2	0.002	3.003	2.997
3	1	2.5	4	1	0.002	3.003	2.997

TABLE 3.2 – Summary of a few conducted PID tuning tests for Rack 70. Test 0 refers to the system's initial conditions before performing optimizations.

Run one. Instead, the StartUp Ti was set to be around 20% lower than the Run one, leading to a higher integral response during the startup phase due to the PID controller definition in Formula 3.4. Few different upper and lower threshold limits for the Run/StartUp mode of distribution racks were tested. In particular, it was found that the valves could regulate well enough with narrow ranges of 3 mbar for the upper and lower thresholds since during the Run phase, the pressure stability is better than 3 mbar. The optimal hysteresis parameter was found to be 2 mbar, avoiding possible continuous changes in the applied PID gains. Figure 3.24 report the pressure oscillations and valve response of rack 70, chosen as an indicative example, for a few selected tests. Test 0 corresponds to the initial verification of the process dynamics, without any PID tuning performed. Test 1, 2, and 3 corresponds to different tuned parameters, for which a summary is reported in Table 3.2.

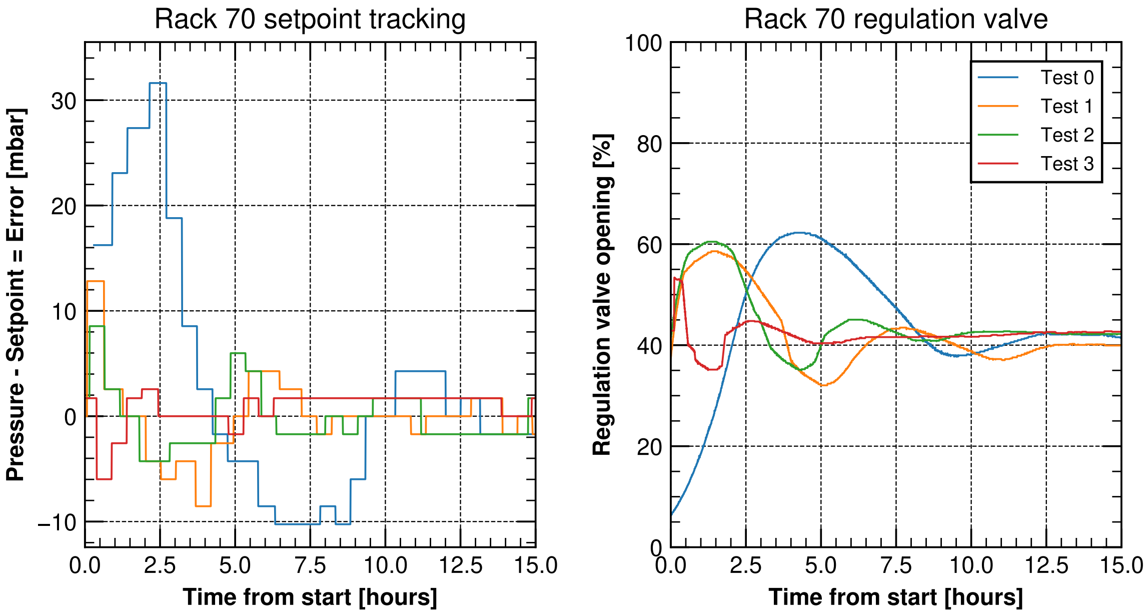

FIGURE 3.24 – On the left, pressure deviation from the setpoint for MDT Rack 70 for different conducted tests. On the right, the response of the regulation valve for the same tests.

It can be observed that for test 3, the valve response had a pretty fast response during the initial hours of startup of the system, with some change in slope due to the transition of the rack from the run to startup phase and vice-versa.

By looking at the pressure oscillations, it is possible to observe that the lowest overshoot and undershoot was obtained in test 3, for which Startup PID gains were considerably more aggressive than the ones of previous tests. More aggressive PID gains were applied to most distribution racks, and the overall performances were measured by taking the overshoot and undershoot value for each test and rack. Figure 3.25 shows an overview of the regulation performance for all the MDT distribution racks. A significant improvement was observed between the initial state (Test 0) and the first tuning process made with Test 1, where the PID gains were generally increased. In Test 4 the startup gains were increased 3-4 times more. Test 4 showed a general improvement with overshoots and undershoot being less than 5 mbar, confirming that the hypothesis formulated by the observation of Test 3. No clear improvements were observed by acting only on the hysteresis parameter and lower/upper state thresholds, suggesting that the issue could be in the startup response of the valve being too low for the system.

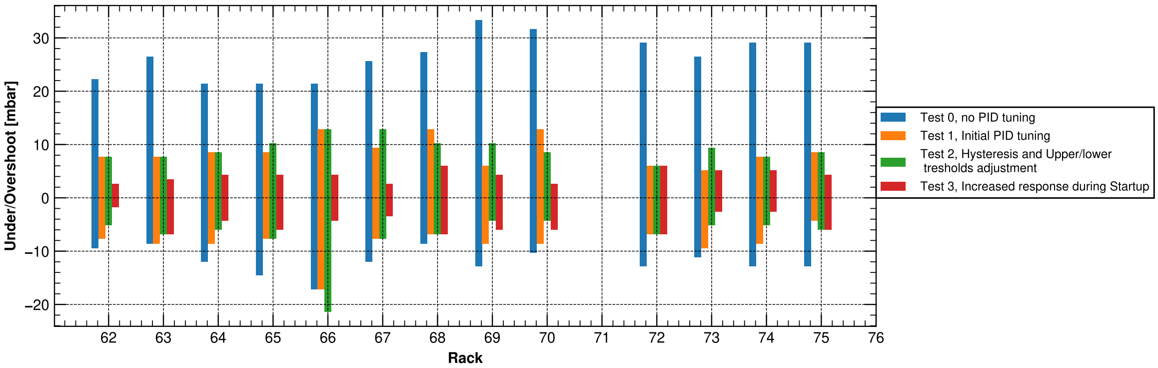

FIGURE 3.25 – Overshoot and undershoot for selected tuning tests for all the MDT distribution racks

3.4.3 Optimization of the startup phase for the ALICE TOF gas system

The ALICE TOF gas system is a closed-loop gas system responsible for providing a 93/7 % R-134a/SF_6 gas mixture to the Time Of Flight detector installed in the ALICE experiment. The gas system has two distribution racks providing each around 450 nl/h of flow to chambers. Like most LHC closed-loop gas systems, a regulation valve is installed on the pump module to allow the system to operate at a constant input pressure of a few millibars below the atmospheric pressure. This design enables the pump to suck the gas returning from the chambers. The setpoint for the TOF gas system is a value ranging from -8 to -10 mbarg, depending on the running conditions.

During LS2, it was observed that the system could not be restarted automatically by the control system, and the manual intervention of an operator was required. The reason was due to the PT4004 pressure sensor's interlock condition deviating too much from the desired setpoint.

Hence, proper PID tuning was required to allow the system to restart without any manual intervention. The tuning procedure was performed both on the pump Kc and Ti gains and in the distribution rack ones since the dynamics of the process is a chain of two controllers: the gas is first arriving at the output of the distribution where the PCV6126 and PCV6226 valves are present. However, the gas is also sucked by the pump, regulated by the PV4003

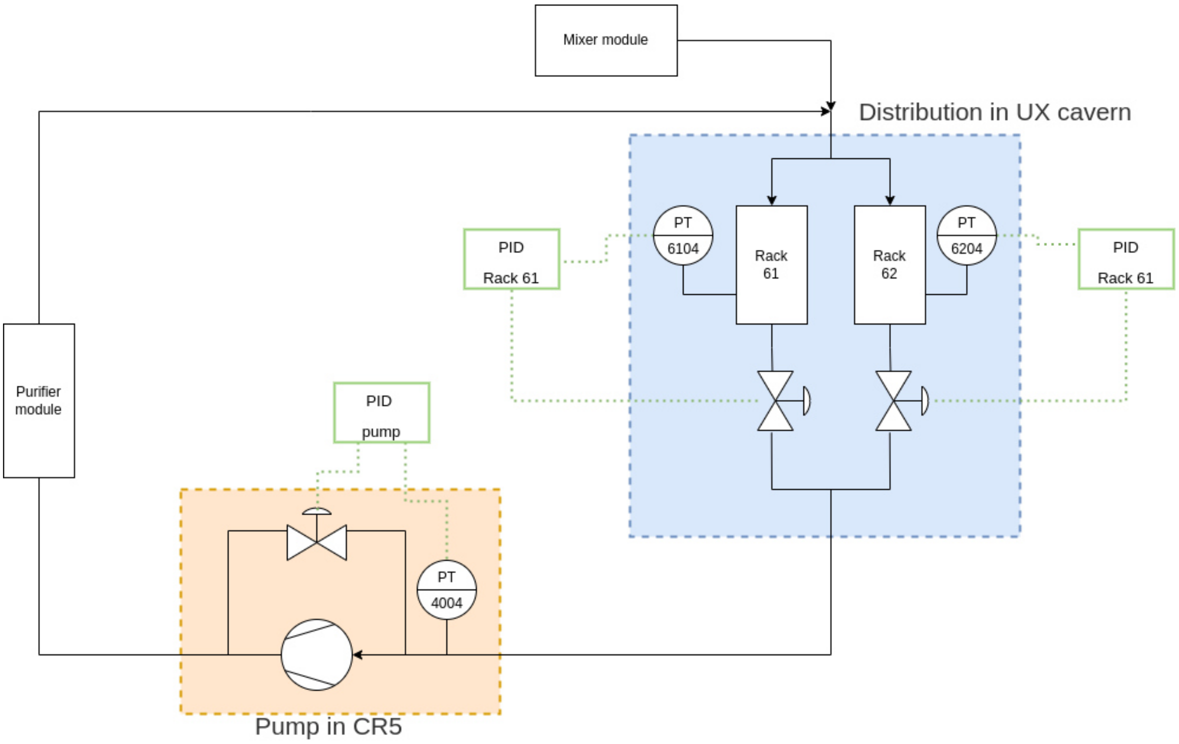

FIGURE 3.26 – Simplified schema of the TOF gas system with the position of the installed regulating valves and their controllers.

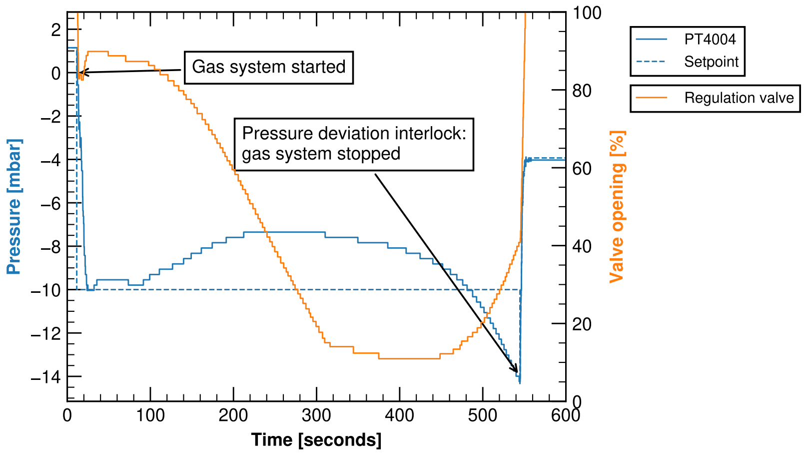

FIGURE 3.27 – Interlock condition observed during the startup of the TOF gas system. The deviation of the pump input pressure PT4004 from the setpoint generated a full stop interlock condition.

valve. A significant change in the pump regulation may affect the distribution regulation, such as saturating the valves' output.

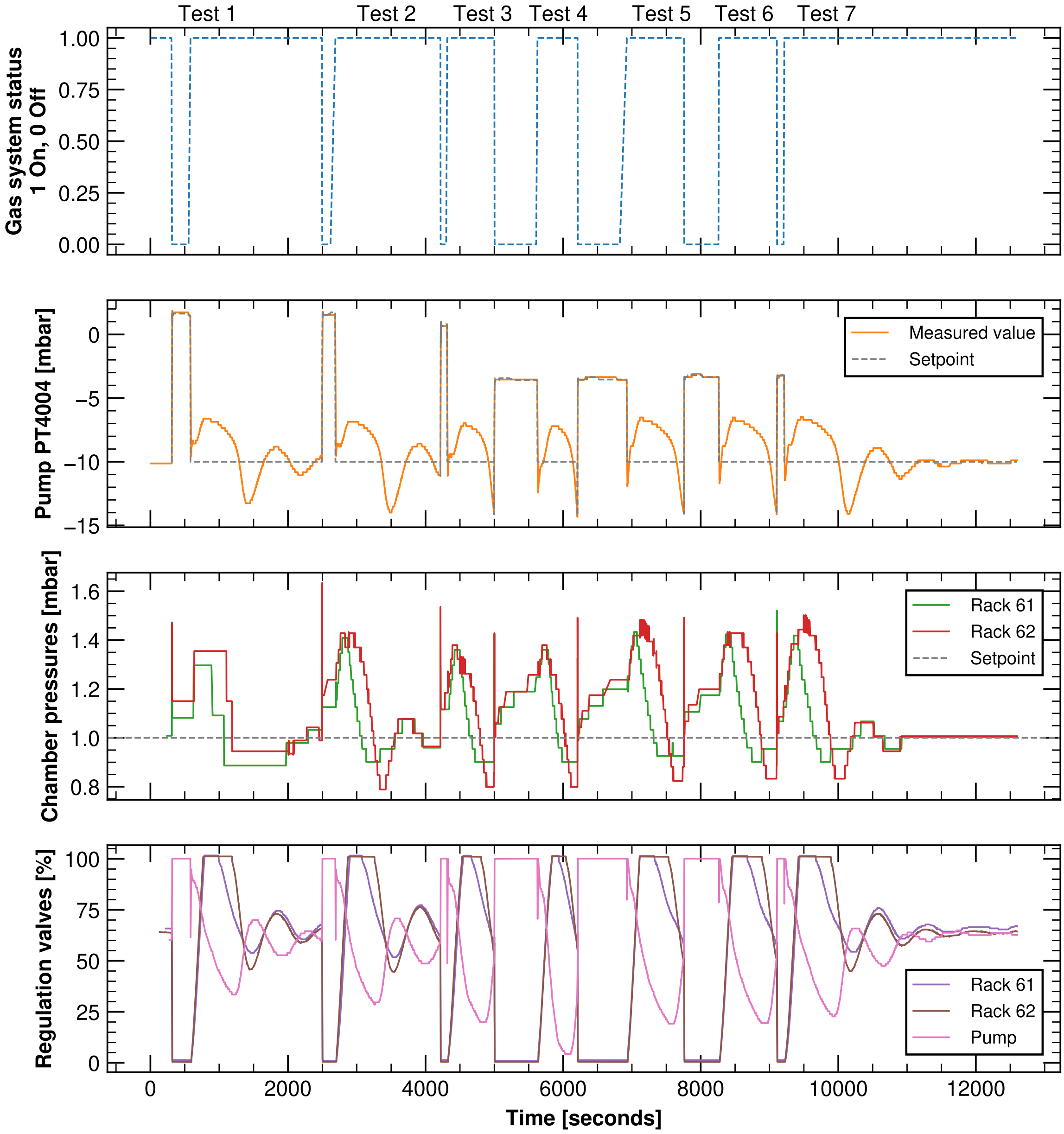

FIGURE 3.28 – Time series of the foremost monitored parameters during the turning procedure for the TOF gas system. a) Gas system status. b) Pump input pressure PT4004, c) Chamber pressure of the two distribution racks 61, 62. c) Regulation valve opening of the distribution racks 61, 62 and of the pump module.

Figure 3.28 shows the temporal evolution of the different parameters monitored during the tuning campaign. A summary of the tested PID gains with the obtained results is reported in Table 3.3. With respect to the initial conditions in Test 0, the startup K_c gain was increased from 3 to 10, and the integral action was reduced by increasing T_i from 10 to 140. The system was observed to start correctly, although few oscillations of 0.5 mbars were observed at the level of the detector pressure. The integral action was increased by reducing T_i from 140 to 100, showing a faster controller response. However, results in Test 2 showed that the distribution valves output saturated at 100% for 5 to 8 minutes, with an overall variation

Test nr.	**Pump** **Kc St.Up Pump**	**Ti St.Up Pump**	**Distribution** **Kc St.Up Distribution**	**Ti St.Up Distribution**	**Remarks**
0	3	10	0.6	2.1	System could not start
1	10	140	0.6	2.1	System started ok
2	10	100	0.6	2.1	System started, distribution valves at 100% for few minutes
3	15	100	3	10	System could not start
4	20	100	3	10	System could not start
5	10	100	3	10	System could not start
6	10	100	0.6	2.1	System could not start
7	10	140	0.6	2.1	System started ok

TABLE 3.3 – Summary table of the performed PID tuning tests on the ALICE TOF gas system. The set of PID parameters accepted were the ones that allowed the gas system to start without the generation of interlocks.

of 0.6 mbars on the output pressures. The distribution PID gains were then increased in Test 3, 4, 5, but the system could not restart due to the pressure deviation of the pump from the setpoint. The system was then brought back to the conditions of Test 1 to validate the settings and choose them as parameters to use for regulation of the pump and distribution during the startup. The settings found were not optimal as the output of the distribution valves saturates at 100%, and the pressure of the chambers increase by around 0.5 mbar. However, due to the complex non-linearity of the system, proper tuning may require the identification of the system in terms of its transfer function. Ongoing studies are being carried on to understand how the system could be modeled from real data to optimize the tuning of the startup parameters.

4 Performance studies of RPC detectors operated with eco-friendly gas mixtures

The present chapter describes the experimental campaign conducted on RPCs operated with eco-friendly gas mixtures. The tests were conducted first in laboratory conditions with cosmic muons and later under LHC-like conditions, with gamma background and muon beam. The study was carried on to find a replacement to the current ALICE, ATLAS, and CMS RPC gas mixture, having a volume-equivalent GWP_{100} of around 3380, with an alternative, lower GWP, gas mixture that requires no change in currently installed front-end electronics, power supply, and gas systems. The tests were conducted on single gap, 2 mm, High-Pressure Laminate (HPL)[1], RPCs with active detection surface dimensions in the same magnitude order as the RPC installed in LHC experiments. The choice of the gap size was dictated by the fact that most of the ALICE, ATLAS, and CMS RPC detectors have a gap of 2 mm. However, future upgrades foresee the installation of thinner gap RPCs [39]. The study consisted first in a commissioning phase of the setup with the detector operated with the standard CMS gas mixture. The performances were evaluated in terms of currents, detection efficiency, streamer probability, cluster size, and time resolution. Later, the search for lower GWP gas mixtures was conducted by understanding the effects of adding a component into the standard gas mixture such as He or CO_2 and replacing R-134a with R-1234ze. Several gas mixtures with different gases were tested by changing the concentration of one component at a time, allowing us to map the detector's performance to the single gas component of the mixture. Once a few gas mixtures were selected as suitable alternatives to the standard gas mixture, a setup was built at the Gamma Irradiation Facility (GIF++) to characterize the RPC performance with LHC-like conditions. The performance of the detectors for different gas mixtures was evaluated with muon beam and different gamma background rates. In addition, a dedicated experimental campaign was conducted to quantify the production of fluoride impurities of the detector through the Ion Selective Electrodes (ISE) technique. The goal was to understand the rate production of F^- ions produced by the RPC when operated at full efficiency under different background conditions and with different gas mixtures. The first part of this Chapter is dedicated to the historical setups and developments of the Resistive Plate Chamber detector. In particular, a focus is made on the modern RPC detector used in the present LHC experiments and on the physics of signal development. The second part describes the experimental setup used to conduct the tests presented in this work. The third and fourth parts describe the development of the data acquisition system and analysis

---

[1] HPL RPCs are also improperly referred to as Bakelite RPCs

library specifically developed for the experimental campaign. The last two parts are dedicated to the performance characterization of RPC operated with eco-friendly gas mixtures, first in laboratory conditions and later in LHC-like conditions.

4.1 The Resistive Plate Chamber detector

The Resistive Plate Chambers detector belongs to the family of parallel plate gaseous geometry detectors. The development of the parallel plate chambers dates back to the end of 1940, when the first parallel plate counters works were published. The initial prototypes were chambers operated in spark mode with metallic electrodes. As such, the signal from an ionizing particle could generate a drop of 100 V on a 50 Ohm terminated plate. Furthermore, the detectors were not operated in continuous mode but rather in pulsed mode, where an electric field was generated for a few hundreds of nanoseconds, and the track of the ionizing particle was recorded. Around the beginning of 1970, resistive electrodes were used to build spark-operated parallel counters. A great part of the work on these detectors was carried on by Yu. Pestov [40].

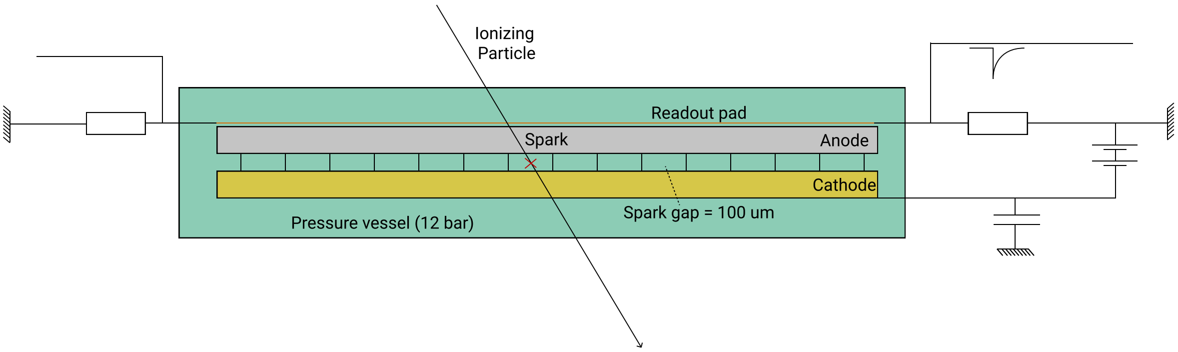

FIGURE 4.1 – Schematics of the working principle of a spark chamber. The signal was read out by reading the voltage drop across a resistor connected to the plate.

Around 1980, Rinaldo Santonico and Roberto Cardarelli built the prototypes of the modern RPCs, using compressed phenolic resin laminate material for the electrodes [41]. The advantage of the built detectors was that they did not require a complex process as those used to build Pestov counters. The detectors were easy to assemble, making them suitable to cover large surfaces. The voltage was distributed using a thin layer of conductive painting material applied to one electrode side. The electrodes were treated by coating them with a layer of linseed oil to ensure a better smoothness of the inner surface of the electrodes and avoid possible local non-uniformities of the electric field inside the gap. The signal takeout was accomplished using a set of copper strips terminated from one side and installed between the mechanical frame and the electrode, separated from the conductive layer with a 0.2-0.3 mm Mylar sheet. The first results showed almost full detection efficiency and time resolutions of around one nanosecond. RPCs did not require particular current amplifiers for signal detection as they were initially operated in streamer or spark mode. Sometime after their invention, the interest of operating them in avalanche mode arose, mainly due to the requirement of operating them with higher rates in large experiments such as the ones at LHC. The reduction of the induced charge had the advantage of increasing the rate capability of the detector. However, as the signal becomes smaller, a pre-amplification stage driven by front-end electronics was required to ensure proper processing of the signal. RPCs were initially operated at atmospheric pressure with a gas mixture based on 60-70% of Argon, 30-40% of butane, and 3-5% of CF_3Br. The addition of an electronegative gas was found to improve charge localization and suppress transversal spatial charge effects [42]. The operation of RPCs in pure avalanche mode was studied around 1993 in the works of Duerdoth et al. [43] Crotty et al. [44], Anderson et al. [45]. As mentioned in the previous chapters, the bakelite RPCs installed at the ALICE, ATLAS, and CMS experiments are operated in avalanche mode with a gas mixture based on a main fraction of a Freon gas, R-134a, known to be electronegative. An amount of 5-10 % of i-C_4H_{10} is added to absorb UV photons and reduce possible photon feedback effects. A small amount of 0.3% of SF_6 is added to the mixture: streamers are further suppressed thanks to its high electronegativity. In addition to the three components, the gas mixture is humidified by adding water vapor to the gas to have 30-40% relative humidity. The humidification of the gas is necessary as Bakelite electrodes contain some amount of water. The surface contact with a dry gas mixture would make the bakelite dry, with the consequent increase of its resistivity [46].

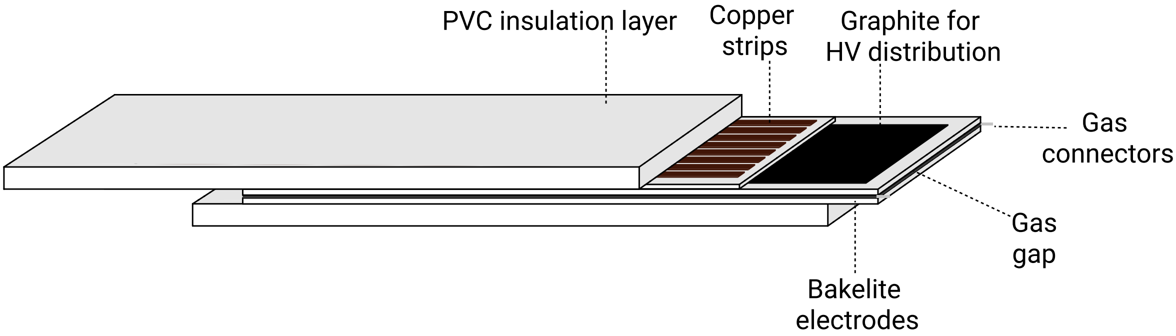

FIGURE 4.2 – Frame layour of a modern Reistive Plate Chamber detector

4.1.1 Signal formation

A simplified model describing the induced charge inside the gap of an RPC can be given by the statistics of avalanche development due to the primary ion-electron clusters generated by an MIP. The following considerations are valid for the development of the avalanche signal from somewhere in the gas gap and up to the surface of the anode [47]. Space charge effects are neglected in the first instance. Let us denote n_{cl} the number of primary ion-electron clusters generated by an ionizing particle crossing the gas gap. This number also includes the pairs generated by primary electrons with ionizing other atoms if their energy is high enough. n_{cl} is a stochastic variable that follows an exponential distribution. Given the gas gap g, it is helpful to define λ as the quantity $\lambda = n_{cl}/g$, indicating the cluster number per unit length. The probability of observing k cluster within a gap is described by a Poisson distribution and can be expressed as:

$$P_{cl}(n_{cl} = k) = \frac{(g\lambda_{eff})^k}{k!} e^{-g\lambda_{eff}} \tag{4.1}$$

It is worth noting that the expected value from the distribution is $g\lambda$, indicating that, on average, a MIP creates $g\lambda$ clusters. This formula allows calculating the maximum intrinsic efficiency an RPC can have given its gap thickness. The value can be calculated from the probability of observing zero clusters in the gap:

$$P_{cl}(n_{cl} = 0) = e^{-g\lambda_{eff}} \tag{4.2}$$

It can be noticed P_{cl} increases that for decreasing values of g. This intuitively means that the detection efficiency for a narrower gap is smaller than for a wide gap. Let us now consider the application of an electric field. In particular, only the electronic dynamics is initially taken into account as their mobility is about three order of magnitudes higher than ions; hence they are responsible for the signal development in the first nanoseconds from the ionizing events. The electric field properties can be described in terms of the effective Townsend coefficient α^*, describing the number of electrons produced by one electron per unit length in the direction of the electric field. Under the assumption that the probability of generating secondary ionizations is constant along the gas gap, the avalanche charge at position x from the cathode can be described as the sum of the avalanche charges developed by primary clusters:

$$q(x) = \sum_{j=1}^{n_{cl}} q_e n_0^j M_j e^{\alpha^*(x - x_o^j)} \quad x_0^{n_{cl}} < x \leq g \tag{4.3}$$

Where q_e is the elementary electron charge, n_0^j is a stochastic variable describing the number of primary pairs for cluster j, M_j is a stochastic variable taking into account fluctuations in avalanche development, and x_0^j is the initial position of j-th cluster. The formula is valid for the $x \leq g$, i.e., for the development of the avalanche before reaching the cathode. A time description of the charge can be given by assuming a constant drift velocity of the electrons in the electric field:

$$q(t) = \sum_{j=1}^{n_{cl}} q_e n_0^j M_j e^{\alpha^* v_d t} \sum_{j=1}^{n_{cl}} n_0^j M_j \quad 0 < t \leq \frac{g - x_0^{n_{cl}}}{v_d} \tag{4.4}$$

Similarly to Formula 4.3, the equation holds for the values of t before the avalanche reaches the cathode. A description of the induced charge on the readout strips can be given by using the Shockley-Ramo theorem, which express the induced current due to a charge moving in the proximity of an electrode:

$$i_{ind} = q\mathbf{v_d} \cdot \mathbf{E_w} \tag{4.5}$$

Where $\mathbf{v_d}$ is the drift velocity and $\mathbf{E_w}$ is the weighting field, assumed perpendicular to the drift velocity. $\mathbf{E_w}$ can be expressed in terms of the electrode plate thickness d and its relative dielectric permittivity ϵ_r:

$$E_w = \frac{\epsilon_r}{\epsilon_r g + 2d} = \frac{1}{g + 2d/\epsilon_r} \tag{4.6}$$

The current can then be calculated by using Formulas 4.4 and 4.5:

$$i_{ind}(t) = \mathbf{v_d} \cdot \mathbf{E_w} q_e e^{\alpha^* v_d t} \sum_{j=1}^{n_{cl}} n_0^j M_j \tag{4.7}$$

The induced charge can be derived by integrating the current over the time development of the avalanche:

$$q_{ind} = \frac{\epsilon_r g}{\epsilon_r g + 2d} \frac{q_e}{\alpha^* g} \sum_{j=1}^{n_{cl}} n_0^j M_j [e^{\alpha^*(g - x_0^j)} - 1] \tag{4.8}$$

4.1.2 Foremost parameters of RPCs

Formula 4.8 gives approximate but valuable information about the RPC detectors parameters. A derivation of the detector's efficiency can be modeled by describing the efficiency as the fraction of events crossing a certain electronic threshold q_{thr}. By neglecting the statistical fluctuations of the avalanche development and setting n_0^j to 1, it can be shown that the efficiency ϵ can be computed as[48]:

$$\epsilon = 1 - e^{1-\eta/\alpha} g\lambda [a + \Delta V_w \frac{\alpha - \eta}{q_e} q_{thr}]^{\lambda/\alpha} \tag{4.9}$$

where η is the Townsend attachment coefficient and ΔV_w is the voltage drop across the electrodes due to the induced charge, that can be expressed as:

$$\Delta V_w = \frac{\epsilon_r g}{\epsilon_r g + 2d} = \frac{g}{g + 2d/\epsilon_r} \tag{4.10}$$

Using the same model, it is also possible to describe the charge distribution in terms of gap size. By neglecting stochastic avalanche fluctuations, the charge distribution follows a probability density functions that can be expressed in terms of λ and α^*:

$$P(q_{ind} = q) = S_n q^{\lambda/\alpha^* - 1} \tag{4.11}$$

It is worth noting that the distribution follows different asymptotic behaviors for $q \to 0$, depending on the ratio λ/α^*. In particular, if $\lambda/\alpha^* < 1$ the distribution diverges. This case is typical for RPC used in LHC experiments having a gap of 2 mm or less and operated with the standard gas mixture. The typical values of λ are around 5.5 clusters / mm and α^* around 9 / mm.

When the ratio $\lambda/\alpha^* > 1$ the distribution tends to 0 for values of $q \implies 0$. This is the typical situation for wide gap RPC. The different behavior can be intuitively understood if we consider that λ rules the cluster generation process in Formula4.11 and α^* determines the avalanche multiplication described by the Townsend mechanism. A wider gap has "more space" or useful gas length where an ionizing particle can start a multiplication, leading to higher intrinsic efficiency of the detector. On the opposite side, for narrow-gap RPCs, only a small region of the gap close to the cathode is available for the ionizing particle to start an avalanche that the readout system can detect. Another important parameter in an RPC

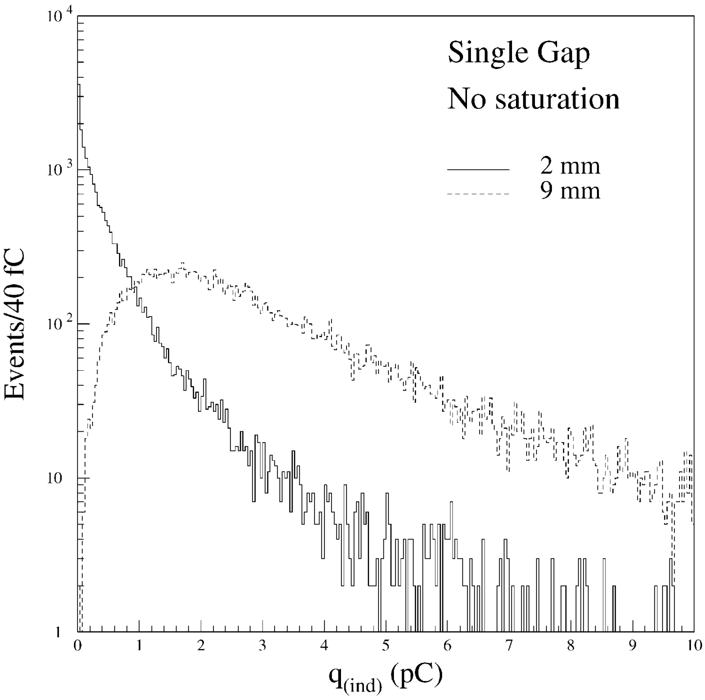

FIGURE 4.3 – Simulation of charge distribution for narrow and wide gap[49]

detector is the time resolution. Similarly, for efficiency, it is possible to compute the time at which the induced currents cross a certain threshold $\mathrm{I}_t hr$ and deduce the standard deviation of the statistical distribution. The induced current can be expressed as:

$$i_{ind}(t) = I_s e^{\alpha^* v_d t} \tag{4.12}$$

Where I_s is the signal amplitude, exponentially distributed around some average amplitude. The time at which the signal crosses I_{thr} threshold is:

$$t = \frac{1}{\alpha^* v_d} ln \frac{I_{thr}}{I_s} \tag{4.13}$$

And by making the corresponding calculation for the distribution, the standard deviation can be expressed as:

$$\sigma_t = \frac{1.28}{\alpha^* v_d} \tag{4.14}$$

It is important to note that the following results are the intrinsic time resolution of the detector and do not depend on I_{thr}. The typical value for a 2 mm gap RPC operated with Freon-based gas mixture gives $\sigma_t \approx 1$ ns. Several corrections might be applied to the formula by considering the space charge effects and the electronegativity of the gas, which affects the average number of initiated avalanches.

When the electric field is high enough, an avalanche may lead to the creation of a plasma filament between the anode and the cathode, known as a streamer. Streamers start to be more present as the electric field is increased. This phenomenon was studied in detail by

Raether [50]. It was shown that sparks appear when the total prompt charge reaches the values of 10^8 electrons and with a characteristical time ranging from few dozens to hundreds of nanoseconds. In the work of Cardarelli [51] the avalanche was studied, indicating that it acts as a precursor of streamer signals and that with increasing electric fields, the time between the avalanche and the streamer tends to decrease, up to the point that the avalanche is not distinguishable from the rise time of the streamer. Initially, RPCs were operated in streamer mode, as detecting a signal did not require a pre-amplification stage. However, some interest in running them in avalanche-only mode arose to maximize the rate capability. Such a feature is critical in high-rate environments such as LHC experiments, for which a particular effort is made by looking for new gas mixtures presenting as few streamers as possible.

4.2 Experimental Setup

The present Section describes the elements required to conduct the experimental campaign of this thesis work. Different setups layouts were designed depending on whether the tests were carried on in laboratory or under LHC-like conditions. The following parts detail the dedicated laboratory and irradiation setups in terms of the detector, gas system, and trigger system. The data acquisition and monitoring system sections cover how the data was acquired during tests and how the setup parameters were monitored. The analysis part describes the requirements and motivation for a dedicated framework to analyze data from the conducted campaign. The details on the implementation of the library are shown together with the explanation of the foremost parameters extracted from a run.

4.2.1 Laboratory setup

Several different detectors were used during tests. The detectors employed for tests conducted in laboratory conditions were all 2 mm, single-gap, High-Pressure Laminate Bakelite RPCs. The choice of the gap and size was dictated by the need to evaluate the performance for RPCs that resemble as close as possible to the majority of installed RPCs in LHC experiments. Table 4.1 reports the RPCs used together with their size and production site. It is worth noting that each detector has its own characteristics that may affect its intrinsic performance. As such, the operating conditions of each detector are different. For instance, the currents drawn for a detector with a higher resistivity are lower with respect to a detector with lower resistivity. Also, currents drawn by detectors with more extensive surfaces are higher than those with smaller ones. For this reason, it is often preferred to report some values normalized by the area of the RPC, such as the current density. Due to the different resistivity, it is sometimes preferred to report the parameters of a single chamber operated with different gas mixtures and compare the results to the performance obtained with the standard gas mixture.

Figure 4.4 shows a schematic layout of the setup used in the laboratory. The gas system consists of a mixing module, responsible for creating the desired gas mixture, and a humidifier module that adds a precise amount of water vapor into the gas mixture to keep the resistivity of the bakelite electrodes constant over time. The mixer allows the creation of a gas mixture with up to six different components provided from a main gas supply line or a gas bottle. Each gas is then sent to a pressure regulator to fix the downstream pressure.

RPC number	Production site	Year of production	Size [width x length]	Strip pitch
1	Pavia university	2010	80 cm x 100 cm	2.1 cm
2	General Tecnica	2016	70 cm x 100 cm	2.1 cm
4	General Tecnica	2016	70 cm x 100 cm	2.1 cm
7	Kodel university	2019	70 cm x 100 cm	2.1 cm
8	General Tecnica	2021	70 cm x 100 cm	2.5 cm
10	General Tecnica	2021	70 cm x 100 cm	2.5 cm

TABLE 4.1 – Details of the RPCs detector used to conduct tests.

The output of each pressure regulator is connected to a Bronkhorst Mass Flow Controller (MFC) that regulates the flow sent at the output. A small volume of 2 liters is installed after the MFCs to ensure the gas sent to the detector is adequately mixed. The output gas is then sent to a humidifier system: the gas is split into two lines, namely dry and wet. The wet line consists of a pipe installed into a 0.5 liters cylindrical tank filled with distilled water where the gas flows and returns humidified. The flow of the dry and wet lines is regulated using a Voegtlin flow rotameter. The gas from the wet and dry line is then joined into the main pipe, and the humidity is monitored using a Vaisala DMT 143 dew point analyzer.

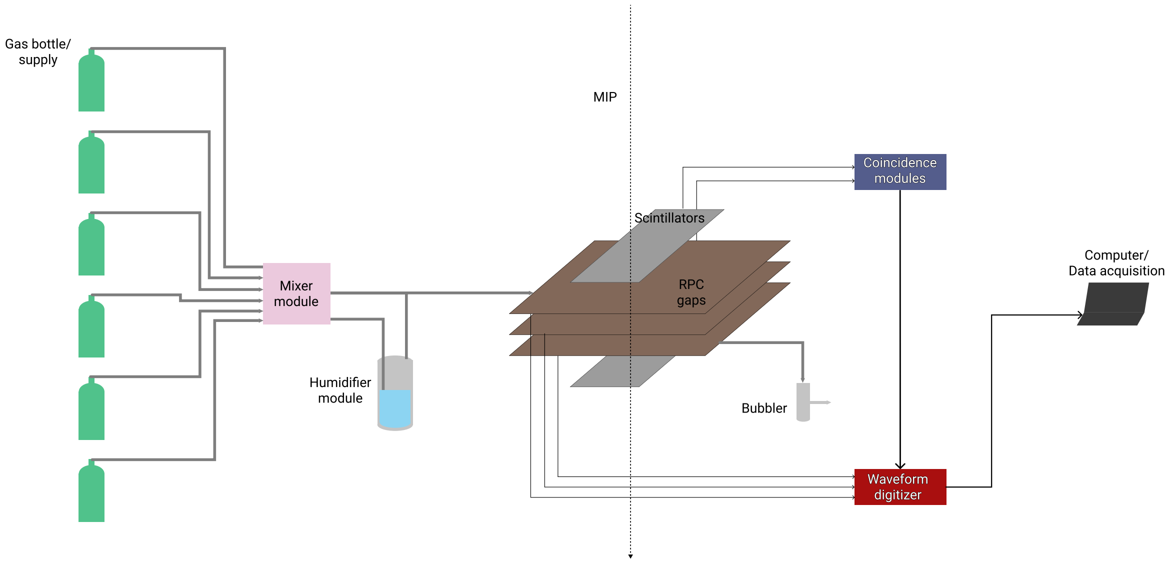

FIGURE 4.4 – Schema of the laboratory setup.

The gas is then sent to the RPCs connected in series. A bubbler with 1 cm of liquid Paraffin oil is placed at the output of the line to ensure the detectors are operating at a fixed gauge pressure of around one mbarg. The output of the bubbler is then collected to an extraction system to exhaust the gas outside the laboratory building. The RPCs are placed horizontally, stacked one on top of the other. Each detector is connected to a negative polarity board installed into a CAEN high voltage power supply that allows to set a voltage up to 16 kV and can read the currents drawn on the detector with a precision of 0.1 μA. The signal is read out using a set of seven 2.1-2.5 x 100 cm^2 copper strips installed between the RPC gap and its mechanical chassis. The strips are welded to a Lemo cable from one side and terminated with a resistance of 50 Ω on the opposite side. The lemo cables are directly connected to a CAEN digitizer, without any front-end electronics installed. At the top and the bottom, a

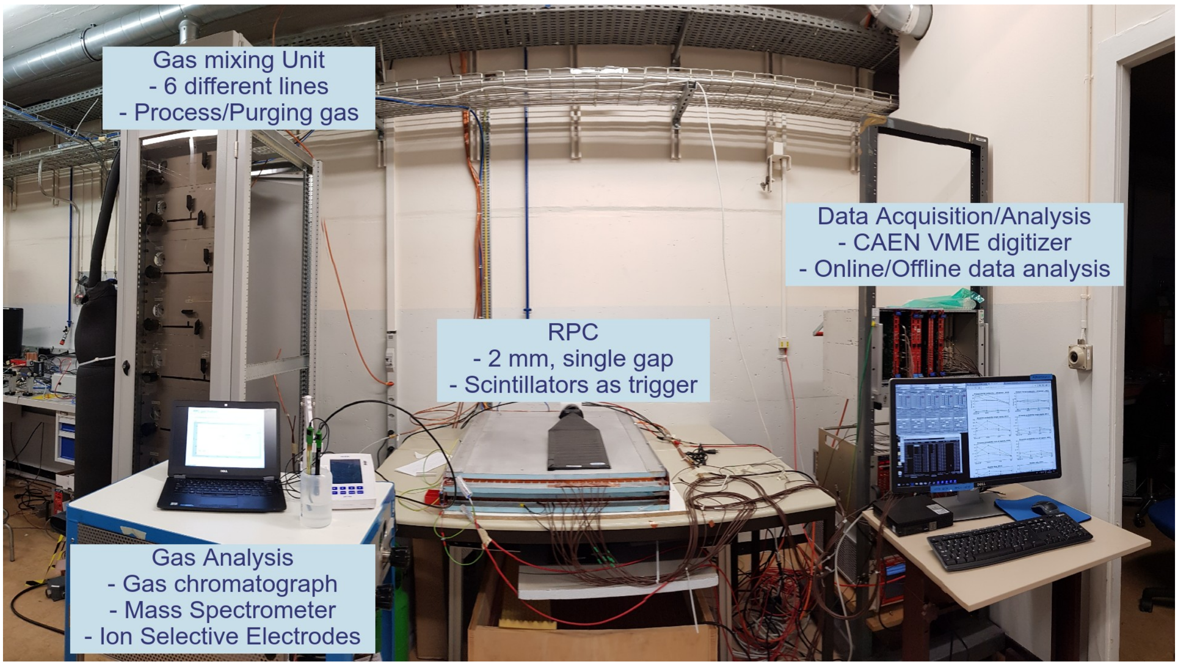

FIGURE 4.5 – Picture of the laboratory setup together with the main elements employed to conduct the experimental campaign.

Model	Type	Channels	Samping Rate	ADC resolution
V1730	VME	16	500 Ms/s	0.031 - 0.122 mv/ADC
DT5730	Desktop USB	8	500 Ms/s	0.031 - 0.122 mV/ADC
V1742	VME	32	5 Gs/s	0.244 mV/ADC

TABLE 4.2 – CAEN Waveform recording digitizer used for data acquisition.

set of two 20 x 40 cm^2 PMTs scintillators is installed. The width of the scintillators is chosen to be slightly narrower than the readout area to account for geometrical acceptance factors. The scintillators are used as an external trigger system for RPC signal recording. The trigger is generated by operating the scintillators at a fixed voltage and using an octal discriminator, coincidence module, and quad scaler to generate a NIM signal. The NIM signal is used as a trigger to record strips signals. The signal is stored as an ASCII waveform on a PC using a CAEN Digitizer. Different digitizer models were employed in the conducted campaign. A table showing the used digitizers and their main technical characteristics is reported in Table 4.2

V1730 and DT5730 digitizers were mainly used to conduct precise measurements of the charge of the signals, thanks to its adjustable dynamic range. V1742 has a higher sampling rate and was therefore employed for time resolution measurements.

4.2.2 LHC-like setup at GIF++

A second setup was built to evaluate both short and long-term performance of RPCs operated with different gas mixtures in conditions that aim to mimic the LHC experiments, i.e., gas recirculation and background irradiation. Similar to the laboratory setup, the main components are the detectors placed inside the irradiation area, the gas system, the power supply, and the electronic chain.

The Gamma Irradiation Facility

The Gamma Irradiation Facility (GIF++) is an experimental facility located at the CERN SPS North Area [52] along the H4 beamline. It consists of an irradiation zone called bunker where a ^{137}Cs source of 12.5 TBq is present. The gamma background of the Cesium source aims at providing a similar background to the neutron-induced gamma background in LHC [53]. The irradiation area is divided into two fields, namely upstream and downstream, as shown in Figure 4.6 A sophisticated set of lead filters allows controlling the intensity of the irradiation independently on both fields. The source itself is embedded between two Tungsten blocks, which assure the source OFF status when it is in the so-called garage position at the bottom of the support tube. The source can be moved on the top of the tube to bring the irradiator in the source ON status. An angular correction on the filters is applied to ensure a uniform photon distribution over the xy plane. With this correction, the irradiation mainly depends on the set of filters and the distance z from the irradiator.

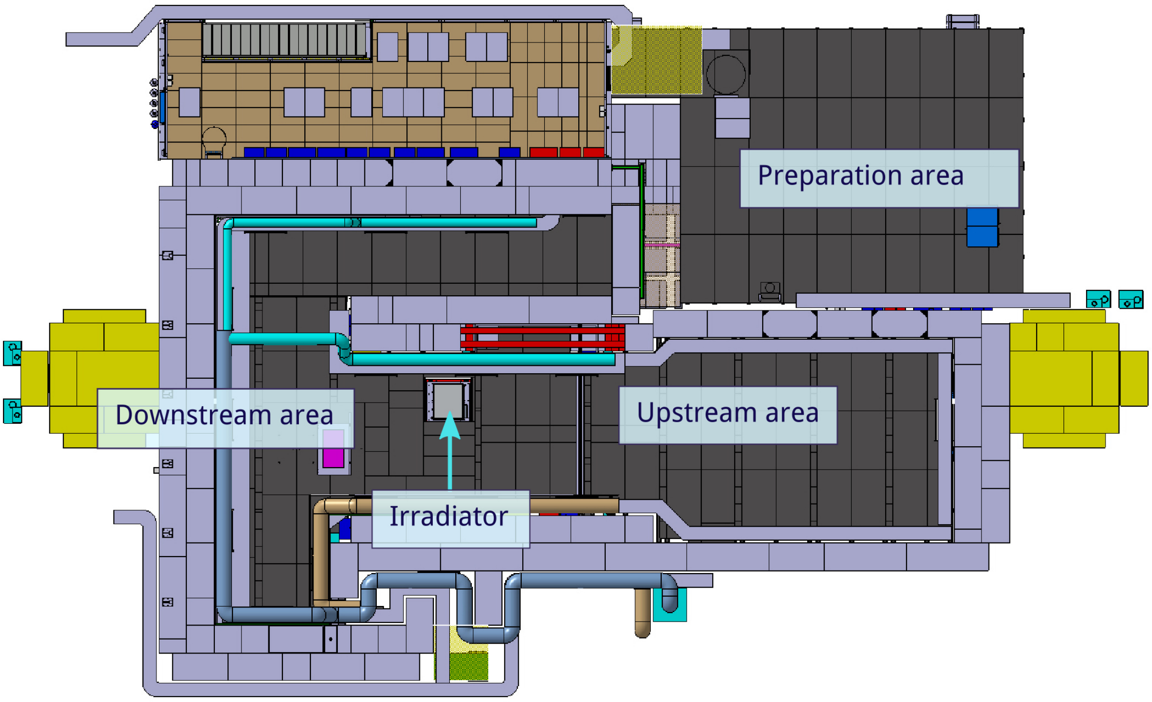

FIGURE 4.6 – Plan of the GIF++ experimental area [53].

A total source attenuation value between 1 and 46415 can be selected using an array of 3 filters, with nearly equidistant steps on a logarithmic scale. The filters can be arranged into 24 different nominal attenuations, as shown in Figure 4.7. It has, however, to be taken into account that the nominal attenuation factor of the filters is the attenuation of the 662 keV photons and that the effective attenuation of photons of lower energy can differ from these values. An indication of the difference between the nominal filters and the dose absorbed by an RDS-31ITX™ dosimeter at a fixed upstream position is reported in the plot shown in Figure 4.8

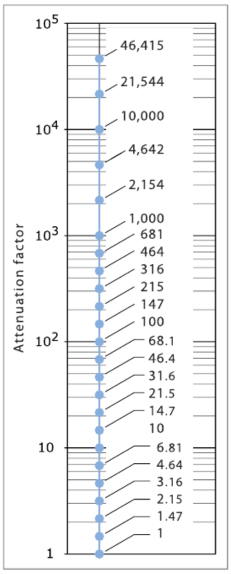

FIGURE 4.7 – Nominal attenuation factors [53].

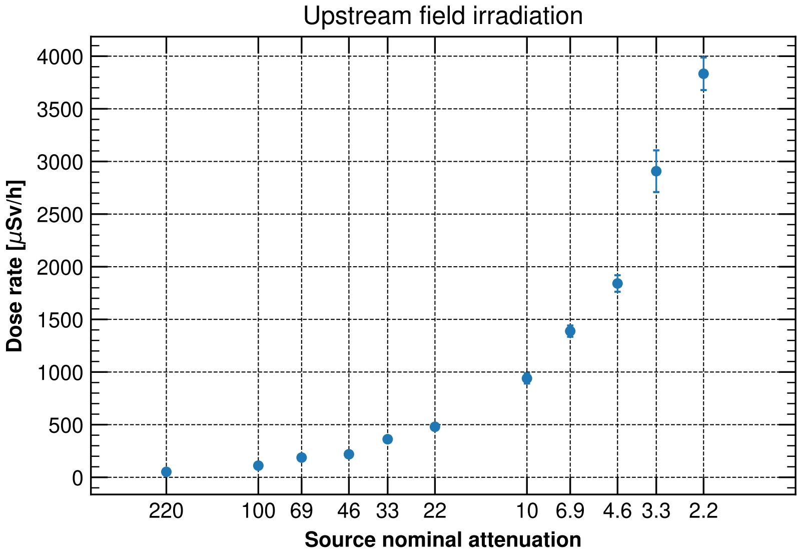

FIGURE 4.8 – Difference between the nominal upstream absorption filter and the effective dose attenuation measured by a Mirion RDS-31ITX™ dosimeter.

During SPS activity, the GIF++ can profit for few weeks per year of muon beam time from the T2/H4 line. The muon beam is generated by the decay of Pions and Kaons due to the primary SPS beam on a fixed target. The quality of the beam is ensured by a set of upstream magnets and mobile beam dumps (XTDV) [54]. The beam user can fine-tune collimator parameters to adjust the position of the beam and select the energy range of the beam particle, ranging from 10 GeV/c up to 400 GeV/c. The particles are coming following the SPS cycle of 30 seconds, with one or two spills per cycle lasting around 5 seconds. The beam distribution depends on several parameters. However, two-thirds of the muon beam are distributed around a 15 x 15 cm^2 area, while the remaining part can cover a surface of around 1 m^2.

Gas System

The gas system is installed at the GIF++ gas service area and it is a small replica of a LHC gas recirculation system [55]. It is made of two cabinet racks installed next to each other. The first rack is the gas mixing unit module. The second is the gas distribution and recirculation unit, which contains several modules similar to the LHC gas system. A detailed P&ID schema of the humidifier and gas recirculation system is reported in Figure 4.9. The gas is taken from the main supply line or gas bottles and is then mixed in a similar way to the mixer module used in the laboratory. The gas mixture is then sent to the second rack. The gas passes through a humidifier module where two Bronkhorst MFCs are present. The MFC on the wet line is kept with the valve open at 100%, while the MFC on the dry line is auto regulated using a LOGO! Programmable Logic Controller, where a Proportional-Integral controller sending a 4..20 mA signal to the wet MFC was used. The setpoint and the process variable are given by measuring a Vaisala DMT 143 dew point transmitter. The K_c and T_i parameters of the PI controller were tuned to allow the gas mixture to be humidified at a stable dew point level. The gas is then sent into the irradiation bunker, where gas patch panels are present. Each RPC of the setup has a dedicated gas line whose gas flow can be regulated using a Voegtlin flow rotameter.

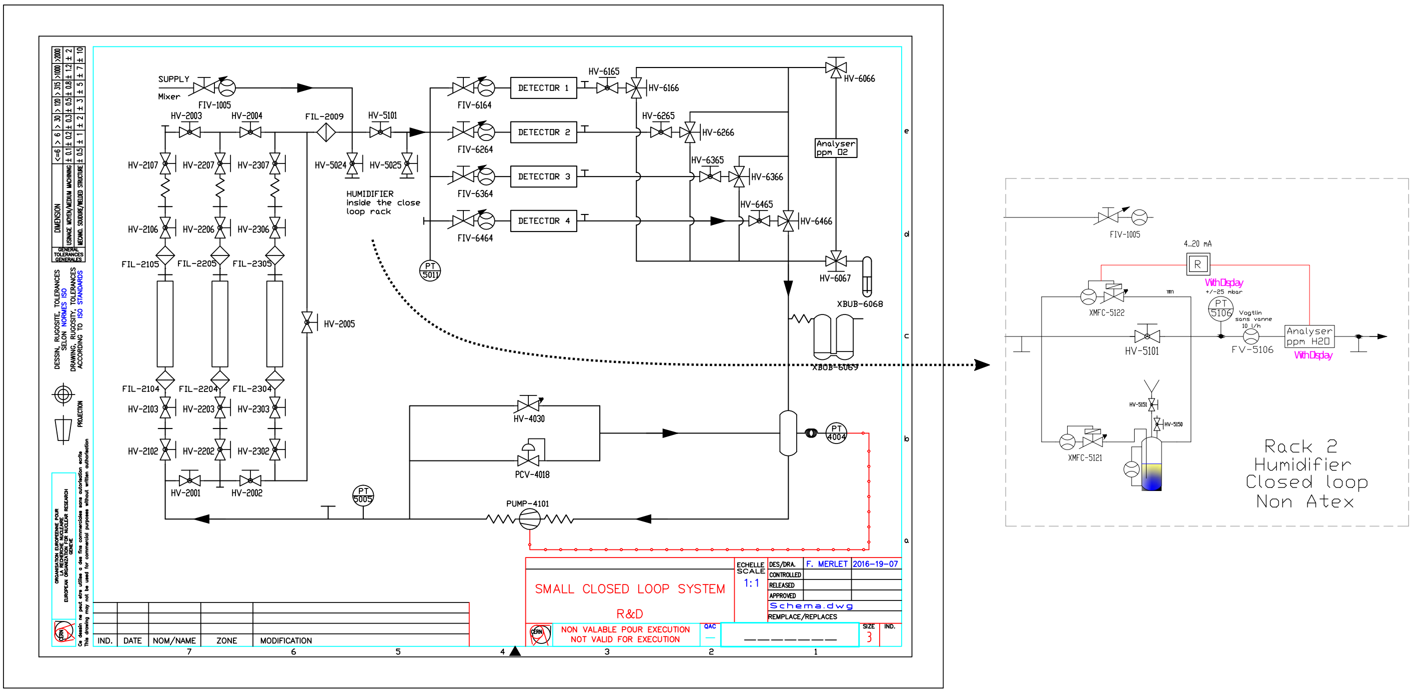

FIGURE 4.9 – P&ID drawings of the closed loop recirculation system designed to conduct R&D tests for RPC operated at GIF++ with eco-friendly gas mixtures [55].

The individual returning lines are then sent back to the gas recirculation unit. If the gas system is operated in open mode, the gas is exhausted through bubbler XBUB-6069. When operated in recirculation mode instead, PUMP-4101 is switched on. Since the pump operates at a considerably higher flow with respect to the required loop flow, a bypass is installed. The bypass has a pressure regulator that allows setting the amount of flow looping on the pump. The higher the flow circulating on the bypass, the lower the gas recirculated in the loop. The gas circulating in the loop passes through a set of 1 L purifier cartridges designed to remove H_2O and O_2 content from the gas mixture. The first cartridge is made of 5 Å Molecular Sieve material, mainly used to absorb water content (130 g H_2O / kg). The second purifier is made of a catalyst Ni-Al_2O_3, absorbing both O_2 and H_2O content from the gas (15/50 g (H_2O/O_2)/kg). The third cartridge is made of a mix of the two materials, and it is mainly used as a backup purifying unit when one or both other columns are saturated and need to be regenerated.

Detector installation

A mechanical trolley to support the RPC detectors was designed and installed in the irradiation area of the GIF++. The trolley allows installing up to three 80 cm x 100 cm detectors aligned on the xy plane as shown in Figure 4.10. The mechanical design also allows installing additional panel supports to fix PMTs scintillators on the top and the bottom of the RPCs, similarly to the laboratory conditions. The upper part of the trolley is designed to be rotated at an arbitrary angle with respect to the x-axis. This was done to allow it to operate the setup in a horizontal position, acquire data with cosmic muons during Source OFF periods, and operate the set up in the vertical position when the muon beam is present.

FIGURE 4.10 – RPCs trolley operated at different angles.

Trigger system

Similar to the set up in the laboratory, the trigger is given by the coincidence of a particle passing through two 20 x 40 cm^2 scintillators. The signal threshold discrimination and coincidence time window are set manually on the relative NIM modules. During muon beam time, the coincidence of the two scintillators installed on the mechanical trolley is combined in a logic AND with the coincidence provided by the GIF++ services. The coincidence provided is a NIM signal made by the coincidence of two 30 x 40 cm^2 scintillators installed on the upstream and downstream zones, aligned with the muon beam and outside the irradiation bunker.

4.3 The data acquisition and monitoring system

Due to both setups' common requirements, a dedicated data acquisition system (DAQ) was developed to be used both in the laboratory and at GIF++. The RPC installations in the laboratory and at GIF++ are equipped with a similar DAQs, and the environmental parameters are monitored using the same data access infrastructure. The DAQ is mainly targeted for performing HV scans, where several different voltages are applied to the RPC, and to read out the signals from the strips. The environmental, gas and HV parameters are monitored during run and standby times. The values are stored in a common time-series InfluxDB database. The data is then visualized using a Grafana-based web application, where several panels monitor each environmental parameter. Grafana also permits setting alerts when a condition on a time series is met; alerts are used for different purposes. In the first instance, they inform the user when an anomaly is occurring by sending an email or message notification on a predefined channel. They are also used as a software interlock system by sending an HTTP request on a web server that can control the high voltage of the detector. Such interlock is particularly useful when RPCs are switched on, but the irradiation conditions or the gas parameters do not meet the required conditions.

4.3.1 The data acquisition system

The DAQ consists of a Python program that interacts with different hardware components. In particular, the application was designed to perform HV scans: an HV scan is a sequence of voltages at which the RPC is set. For each voltage, the currents are measured, and the signal is read out at each trigger event. The detector's performance is evaluated for each trigger at each set voltage. When the run is over, the whole run data is analyzed. The program is distributed as a Python package, and it is hosted on the CERN GitLab repository[2]. Once installed together with its dependencies, it can be run as a Python script or module from the command line. The program accepts a string parameter indicating the path of the configuration file. The configuration file is structured as a JSON file containing different sections to adequately set the operating conditions of the detectors and readout system. All the possible accepted settings are described in the `models.py` module. The main settings include:

- **HVWrapper settings**: parameters and credentials to connect to the CAEN power supply;
- **Detector settings**: parameters related to the current limit to be set for the detectors, the time to let the detector stabilize when a voltage is reached and the time allowed to record the currents for the detector;
- **Noise settings**: if enabled, before starting the run, an auto-trigger acquisition of the signals from the strips of the detector is performed. A script detects the mean and standard deviation distributions of the acquired triggers signals, and if the values are above configurable thresholds, the run is stopped;
- **Readout settings**: parameters defining how many events should be recorded for each voltage and where to store the global run data;
- **WaveDump settings**: settings related to the digitizer and the path to its configuration file;
- **InfluxDB settings**: parameters related to the credentials to access the database to read data from;
- **HVPoint settings**: parameters representing the unit configuration for a voltage point. Each voltage point can be applied to a set of predefined channels. For a voltage point, the user can choose whether to record only the currents or also the signals from the trigger system. It is also possible to record an auto-trigger signal used to estimate the background rate;
- **Analysis settings**: these parameters relate to the `olefin` library settings. The specific details are reported later in Section 4.4;
- **Telegram settings**: settings used to send notification on the status of the run via the telegram messaging service[56];
- **Environmental settings**: settings related to the environmental parameters relevant for a run. In laboratory conditions, these parameters are mainly atmospheric pressure and

---

[2] `https://gitlab.cern.ch/grigolet/rpc-hvscan-256`

temperature. At the GIF++, the environmental parameters also include the irradiator status and filter positions during muon beam time;

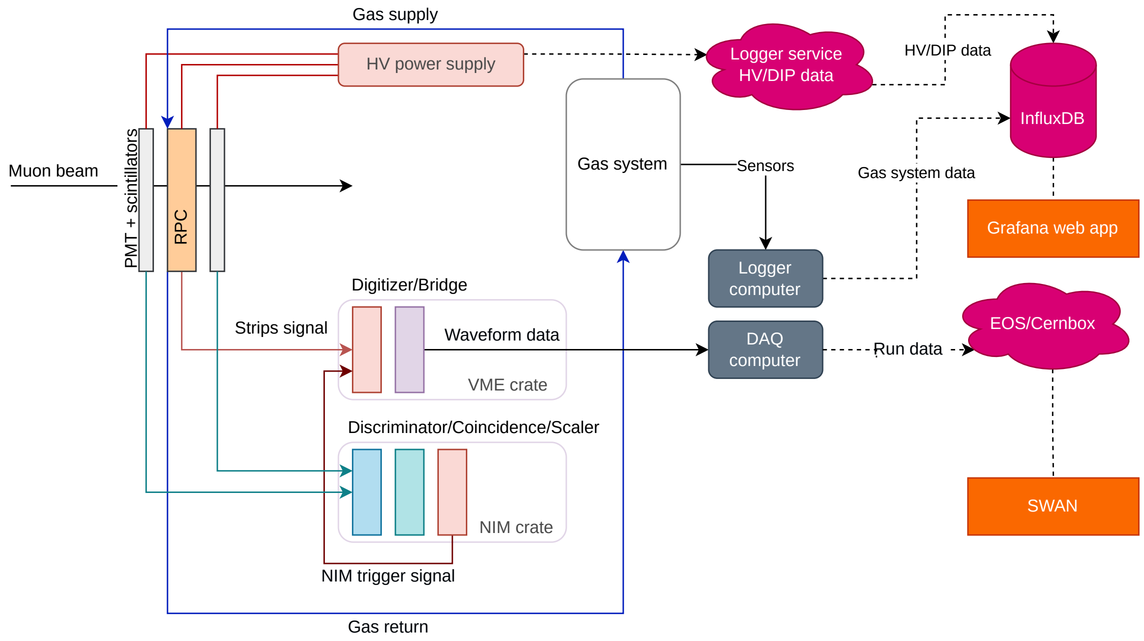

FIGURE 4.11 – Schema of the global DAQ and monitoring system for the GIF++ setup.

A library to monitor and control CAEN power supply

The DAQ program needs to communicate with the CAEN power supply and the CAEN digitizer to perform an HV scan. At the time of writing, no Python APIs are officially provided to interact with the CAEN power supply and digitizers. For this reason, a Python wrapper around the CAEN HVWrapper library was developed. The project is available on the CERN GitLab repository[3]. It provides a set of functions to interact with the power supply modules. The implementation is made by using python's `ctypes` package available in the standard library that provides a foreign function interface for calling compatible C DLL or shared libraries functions. The wrapper provides an object-oriented interface. For each module, an instance of the class `HVWrapper.HV` can be created with the proper IP address and credentials to connect to the module. Once the object is instantiated, it is possible to connect to the module using the method `HV.connect()` or disconnect with the `HV.disconnect()` parameter. As per CAEN HVWrapper documentation, the connection has a timeout of 30 seconds if no interaction with the power supply is performed. The main function to read parameters from a connected `HV` object is the `get_param(self, slot, channels, param, return_code=False)` where it is possible to define a list of channels for which the parameter should be retrieved and the name of the parameter. The `return_code` argument is used to return either a numeric code value or a string when the parameter requested is the module's status. The function call returns a dictionary where the keys are the channels, and the values are the actual values of the parameter requested. The list of available parameters is the one defined in the CAEN's HVWrapper documentation. Similarly, to set a parameter, the

---

[3] `https://gitlab.cern.ch/grigolet/pyhvwrapper/-/tree/packaging`

method `HV.set_param(self, slot, channels, param, value)` can be used. The parameter can be set for a list of channels at the same time. The result is an integer indicating the result from the HVWrapper function `CAENHV_SetChParam`.

Waveform recording software

Each digitizer is used with its waveform recording firmware. The CAEN's WaveDump library was used as a baseline to develop a custom Windows program that allows running acquisitions with the desired digitizer programmatically. The modified version of the library is available on the CERN GitLab repository[4]. The program is presented with a simple Command Line Interface (CLI). The syntax to run the program is: `WaveDump.exe <WaveDumpConfig.txt path> <output path> <Number of events> [Autotrigger]`. The first argument indicates the custom-built executable file's name or path. The parameter `<WaveDumpConfig.txt path>` indicates the path to a .ini like file containing the configuration necessary to operate the digitizer. The `WaveDumpConfig.txt` settings largely depend on the WaveDump version used. `<output path>` is a parameter indicating the path where the waveform files for each channel of the digitizer should be written. The path should already exist, or the program throws an I/O error on startup. `<Number of events>` indicates how many trigger events should be recorded. During the acquisition, the current recorded event over the total number of trigger events to record is displayed on the console. `[AutoTrigger]` is an optional flag parameter and, if present, runs the digitizer in auto-trigger mode, discarding the `WaveDumpConfig.txt` file trigger-related settings.

4.3.2 The data monitoring system

It is well known that the performance of a gaseous detector depends on environmental parameters such as temperature and pressure that affect the density of the gas, thus the effective Townsend coefficient and the gain in the multiplication region. Some other parameters, such as the quality of the gas mixture and the humidity of the gas, can also determine the detector's operating condition. In the first instance, the gas mixture composition is crucial, as a slight variation of one of its components may drastically change the performance in terms of working point, currents, streamer probability, mean prompt charge. Together with the gas mixture, the pressure and the flow at which the detectors are operated may affect long-term performances. When operating the gas system in closed-loop mode, the recirculation fraction may also affect the detector performance due to the possible accumulation of impurities if purifiers are saturated or not present. Monitoring all the parameters that could affect the detector's performance is hence fundamental. A dedicated monitoring system was designed and deployed to ensure all the relevant parameters could be monitored in the best possible way. The monitoring tools were chosen by taking into account different key factors:

- All the relevant parameters should be available under a single endpoint;
- It should be easy to arrange relevant parameters data into a dashboard;
- It should be easy to create, modify, delete the visualization for a time series of a parameter

---

[4] `https://gitlab.cern.ch/grigolet/wavedump-custom`

- Data should be stored in a database optimized for time series;

It should also be mentioned that different data comes from different sources. For example, MFCs data about flow and setpoint is available on a dedicated Bronkhorst Flow DDE software. The data relating to environmental sensors and transmitters is read using an Analog to Digital Converter Picolog ADC 24 data logger. The parameters that concern the GIF++ irradiator are instead availabe via DIP. In order to build a monitoring system with the requirements mentioned above, a logger application was built from scratch. The logger is a Python program that retrieves data from different devices and stores them into an InfluxDB database. The devices and APIs used by the script are:

- **Bronkhorst Mass Flow Controllers**: data is accessed by launching FlowDDE and using the `ctypes` library[5] to wrap the Windows Dynamic Data Exchange (DDE) library[6];
- **Closed-loop sensor transmitters** temperature sensors, mass flow meters, and dew point transmitters signals are read using a Picolog ADC-24 data logger. The data is then retrieved using the pico SDK python library[7];
- **Yoctopuce sensors**; Yoctopuce sensors are USB devices that act as electrical sensors for different purposes. The values read by these sensors are accessed using the dedicated Python APIs[8];

Data on the DIP network is accessed and stored using a separated logging script deployed on the CERN Openshift cluster. The reason is due to the incompatibility of the Windows operating system with the `cppyy` library used to access native DIP C++ APIs. The code can access an arbitrary DIP subscription and be configured to log the data on an arbitrary InfluxDB database [9]. Another separate script is responsible for retrieving CAEN power supply parameters and logging them into the InfluxDB database. The script was kept separated from the script running on the Windows computer in order to avoid any possible disruption of the logging activity due to a fault of the local machine. Like the `dip-to-influx` program, the script is deployed on the CERN Openshift cluster. The script's source code is hosted on the CERN GitLab repository[10].

The InfluxDB database

InfluxDB[57] was chosen as the primary storage to access data and from which the monitoring system was built. An InfluxDB instance was created and deployed using the CERN Database On-Demand service[11]. Each sensor data is stored as a time series into a single database entity but under different `measurements`. A measurement is an object in InfluxDB that can somehow be thought of as a table in a relational database. Each stored time-series point belongs to a single measurement. In addition, a series can have `tags` and `fields`. Tags are metadata that can be added to the data point. Fields are used to store the actual process value. An example of a data point is shown in Figure 4.12.

---

[5] https://gitlab.cern.ch/grigolet/simple-influxdb-data-logger/-/blob/master/dde.py

[6] https://docs.microsoft.com/en-us/windows/win32/dataxchg/about-dynamic-data-exchange

[7] https://github.com/picotech/picosdk-python-wrappers

[8] https://www.yoctopuce.com/EN/doc/reference/yoctolib-python-EN.html

[9] https://gitlab.cern.ch/grigolet/dip-to-influx

[10] https://gitlab.cern.ch/grigolet/pyhvlogger

[11] https://dbod.web.cern.ch/

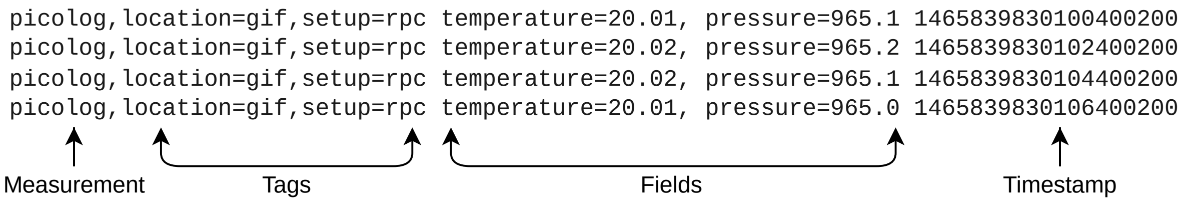

```
picolog,location=gif,setup=rpc temperature=20.01, pressure=965.1 1465839830100400200
picolog,location=gif,setup=rpc temperature=20.02, pressure=965.2 1465839830102400200
picolog,location=gif,setup=rpc temperature=20.02, pressure=965.1 1465839830104400200
picolog,location=gif,setup=rpc temperature=20.01, pressure=965.0 1465839830106400200
```

FIGURE 4.12 – Example of different data points. Each data point consists of a measurement, a set of key-value tags, a set of key-value fields and an epoch timestamp.

At the time of writing, data is stored under eight different measurements and 347 different time series with a rate of 160 000 points/hour.

Grafana monitoring dashboards

Grafana was chosen as a primary monitoring tool for the setups for several reasons:

- It is deployed as a web application, compatible with most modern browsers, thus being operating system independent;
- It integrates with the CERN authorization service as it supports the OpenID Connect protocol; It provides a flexible alert system that can send notifications over different channels such as email, webhooks, and messaging services;
- It has partial support from the CERN IT team. It is possible to deploy a Grafana instance on the CERN Openshift cluster by referring to the provided documentation[12]

Different dashboards were created for different areas or a different setup. Each dashboard consists of a web page. A set of panels are inserted and arranged within each dashboard as shown in Figure 4.13, with each panel displaying a subset of data from the InfluxDB data source.

Each panel can visualize data from one measurement, and the visualization can be arranged in different forms: time series, histograms, single values statistics, gauge, a heat map. For the setup at the GIF++, a dashboard was designed to display the following values:

- **Gas mixture composition**: these values are visualized as the percentage of every component and as a flow expressed in normal liters per hour;
- **Currents and voltage from the CAEN power supply module**: one panel is dedicated for the currents and one for the monitored voltage. Each panel shows `n` time series, where `n` is the number of RPCs used for the tests. Similarly, two panels were created to monitor the voltage and currents of the PMTs used for the trigger system;
- **Pressure on the gas system**: Pressures included the detector pressure PT4004, the loop pressure PT5005, and PT5011, the pressure of the humidifier PT5001, and pressure at the output of the mixer;
- **Gas humidity**: the value is monitored in terms of the dew point measured by the Vaisala DMT143 device;

---

[12] `https://grafana.docs.cern.ch/`

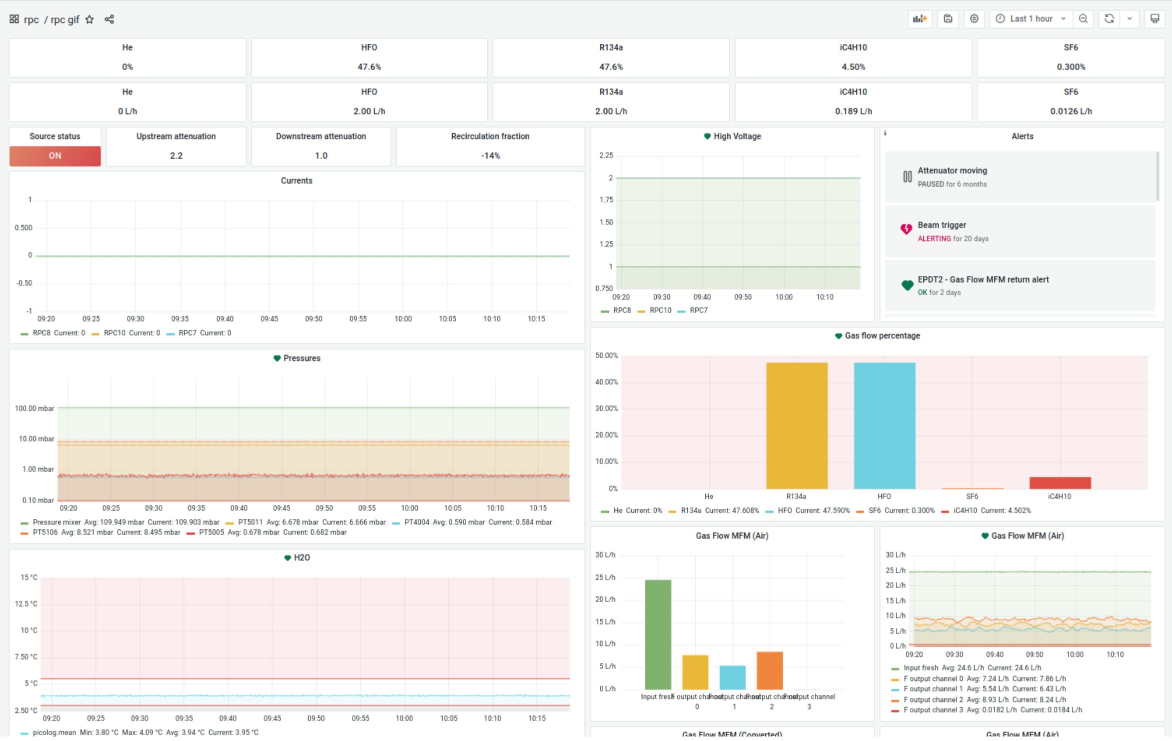

He 0%
HFO 47.6%
R134a 47.6%
iC4H10 4.50%
SF6 0.300%

He 0 L/h
HFO 2.00 L/h
R134a 2.00 L/h
iC4H10 0.189 L/h
SF6 0.0126 L/h

Source status ON
Upstream attenuation 2.2
Downstream attenuation 1.0
Recirculation fraction -14%

Alerts
Attenuator moving PAUSED for 6 months
Beam trigger ALERTING for 20 days
EPDT2 - Gas Flow MFM return alert OK for 2 days

FIGURE 4.13 – A Grafana dashboard displaying the relevant time series data for the GIF++ setup using different visualization toolkits.

- **Flows from MEMs Mass Flow Meters (MFMs)**: the flow sent from the mixer and the return flow is displayed as a time series and bar chart. The time series are plotted using a rolling average to smooth the signal, while the bar chart refers to the last available value on the database;
- **Pressure and temperature of the bunker**;
- **Oxygen level in the gas system**;
- **GIF++ irradiator status**: this mainly refers to the position of the source (On = 1 or Off = 0) and the upstream and downstream filters;

Each trend has an alert. An alert is an object in Grafana that periodically evaluates a predefined query on a time series and performs an action whether the condition on the series is met. An example of Grafana panel with a configured alert on the dew point is shown in Figure 4.14. For the GIF++ and laboratory setups, several alerts were configured. In particular, the flow of each gas component is monitored so that in case of a change of the mean flow over a period of a few seconds, an email is sent, allowing us to investigate the issue on the setup with a minimum delay. The status of the source panel is configured with an alert condition on the upstream filter: when the upstream filter is switched to 1 - which corresponds to a background radiation too high for the detectors - a web hook is generated and an HTTP request is sent to a dedicated server that switches off the high voltages of the detectors.

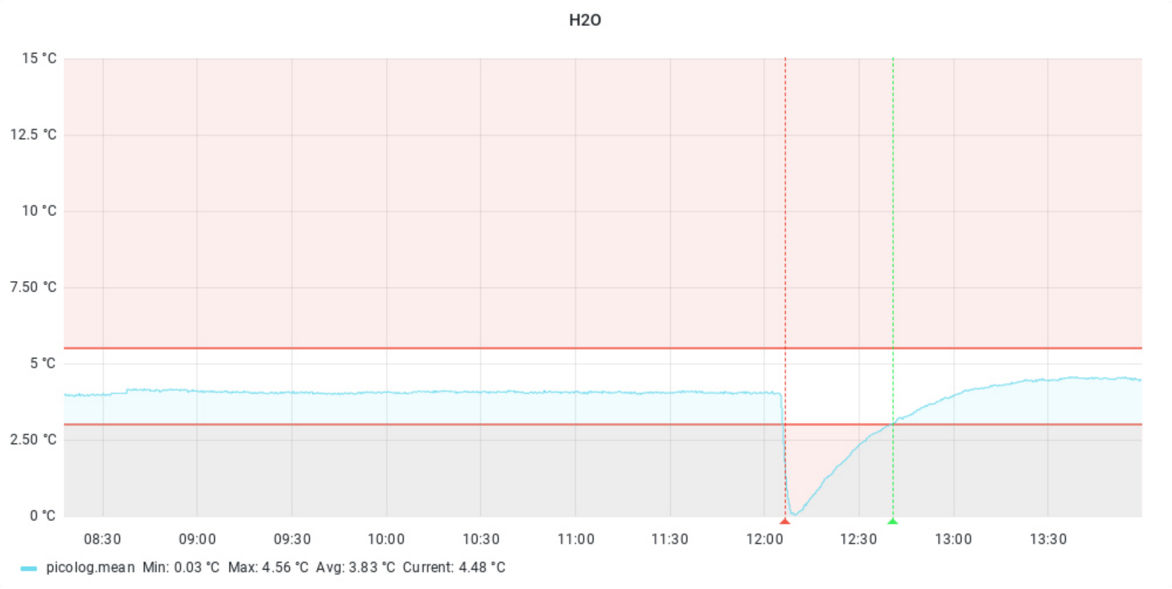

FIGURE 4.14 – A Grafana panel with configured thresholds for alert handling. When the value crosses one of the low or high thresholds a red vertical line is added to the graph and an email is sent. When the value comes back within threshold levels a green vertical line is added and an optional email informing the user could be sent.

4.4 Development of the `olefin` data analysis library

As described in Section4.3.1, the DAQ uses a CAEN waveform digitizer to record the signal collected by the RPC strips. The recording of the waveform for each strip allows one to deeply understand the characteristic of the signal formation inside the detector's gap. Information about the timing, charge, shape, type of the signal can be analyzed with different algorithms. Computed data such as the prompt charge, signal discrimination, time of the signals, detection efficiency depend primarily on the technical specification of the readout system and on the algorithms used to compute them. Some of such algorithms can depend on arbitrary parameters: for instance, a height threshold, expressed in millivolts, can be set to discriminate between noise and a signal of a particle. The threshold can assume different values depending on the signal-to-noise ratio of the digitizer employed for the data acquisition. In order to standardize the analysis algorithms and ensure a consistent analysis between different RPC and different gas mixtures, a custom analysis library was developed. The library, called `olefin`, is an open-source python package hosted on the CERN GitLab repository [58]. The library contains a set of functions and classes to analyze the data collected from a run with the DAQ system previously described. `olefin` was designed from the ground up by taking inspiration from existing analysis routines and by trying to fulfill the following requirements:

- The analysis itself should be performed separately at different levels: for example, the analysis should be performed on the single strip signal, on the collected strip signals from a trigger, on a fixed HV point with multiple triggers, or on a run where multiple HV points are scanned;
- The analysis of a run should allow the user to retrieve valuable information from the collected data in the order of seconds;

- The analysis should provide a configuration system where all the possible tunable parameters used in the algorithms can be adjusted;
- The analysis should be flexible enough to be extensible. Whenever required, a user of the library should be able to extend an analysis class and customize the implemented algorithms with the underlying data structures used by the framework;
- The library should be cross-platform compatible. In particular, the analysis should run on the Windows operating system where the local DAQ program is running, as well as on the CERN Service for Web-based Analysis (SWAN) cluster. This implication requires to discard CERN analysis libraries such as ROOT as its portability on the Python's Anaconda environment is not yet available[13].
- The library should provide unit tests that can be run against real detector data.

4.4.1 Architecture of the analysis classes

The olefin library consists of four main analysis classes. Each analysis class inherits from a public interface. As such, each class must implement two attributes and a method: `data`, `config` and `run()`. The `data` attribute is the data available after the analysis class has run its algorithms routines. The `config` attribute is a Python's `dict` representation of the parameter the analysis class needs to perform its analysis. The `run()` method refers to the actual computations performed by the analysis classes. A class's `data` attribute can be used as the input data of a class of a higher level. When calling the `run()` method on a class, the `data` attribute becomes available in the analysis object. To facilitate the data interchange between classes, the structure of the `data` is a data frame provided by the Pandas library[59]. A schema representing the interaction between the different classes is reported in Figure 4.15.

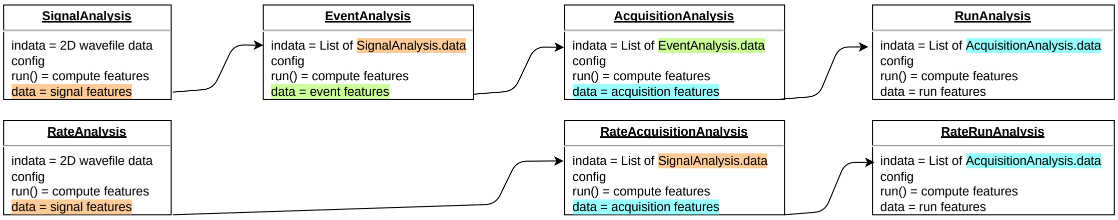

FIGURE 4.15 – Simplified schema of the `olefin` architecture. Each class inherits from the Analysis interface. An analysis class can be used as input of a higher level analysis class to aggregate computed results.

The library follows a hierarchical structure that can be read from a top-down or bottom-up approach: a run analysis is made by running several acquisition analyses for each HV point. Each acquisition analysis result is given by the events recorded for the specific HV point. Each event is the analysis result of the signals collected by the different strips of the detector.

---

[13] `https://root.cern/install/`

The `SignalAnalysis` class

The `SignalAnalysis` class is responsible for computing information about each signal present in a waveform file. A waveform file is an ASCII text file created by the CAEN digitizer through the DAQ system, containing a single column of integer or float values. Each value is a single sample recorded by the digitizer. Depending on the window length of the digitizer and on the number of events that the DAQ records, a file may contain more than one waveform. There are no explicit delimitations characters in the waveform file, meaning that the only way to analyze different waveforms is to know a priori the record length used by the digitizer. For example, suppose 1000 events are recorded, and the digitizer's record length is set to 520. In that case, the created text file for channel 1 in the digitizer will be named `wave1.txt` and contains 520 000 samples, with every 520 samples representing a different waveform. For convenience, the data is parsed into a 2-dimensional NumPy array. Each row index represents the trigger event, and each column index indicates the number of samples in the waveform. A set of features is computed for each row in the 2D array.

```
array([[8151, 8152, 8151, ..., 8140, 8140, 8146],
       [8147, 8154, 8149, ..., 8153, 8151, 8152],
       [8155, 8152, 8150, ..., 8152, 8154, 8154],
       ...,
       [8151, 8149, 8152, ..., 8150, 8153, 8143],
       [8150, 8151, 8154, ..., 8152, 8150, 8152],
       [8151, 8147, 8151, ..., 8149, 8152, 8145]])
```

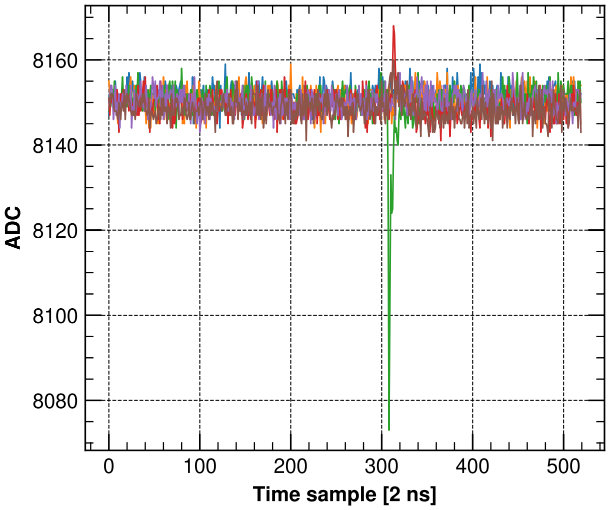

FIGURE 4.16 – Example of a WaveFile reshaped into a 2 dimensional array. Each row represents a different waveform with the samples expressed in ADC counts. The different waveforms can be visualized on the right plot.

Each feature is a boolean, integer, or floating value associated with the single waveform. When the `run()` method of the class is called, the following features are computed for each waveform:

- `baseline`: the baseline of the signal. The baseline is computed as the mean value of a configurable interval region of the waveform;
- `height`: the height in mV of the signal. Due to the negative pulse polarity, the height is computed by taking the difference between the baseline and the minimum value of the threshold. Hence, the height is expressed as a positive number;
- `inverse_height`: the height of the opposite polarity signal. This value is computed by taking the difference between the signal's maximum minus the baseline. It is used to detect undershoots or fake signals, as explained in the following part;

- `charge`: it is the sum of the samples for which the signal is above a certain configurable threshold. The sum of the sample is then divided by the digitizer's time resolution and multiplied for the resistance of the strip of the RPC. The value is expressed in pC;
- `heights_ratio`: it is the ratio between `height` and `inverse_height`. When the ratio is close to 1, most likely no charge is deposited, suggesting the signal could be noise interference or cross-talking;
- `time_peak`: it is the index of the sample at which the minimum of the waveform is found minus the index at which the falling edge of the trigger signal is found. The falling edge of the trigger signal is computed using a dedicated `TriggerAnalysis` class;
- `reflections_count`: the number of samples crossing a "negative" an opposite polarity threshold;
- `fired`: a boolean value indicating if `height` is above a configurable threshold;
- `isin_time_window`: a boolean value indicating if `time_peak` is present within a configurable sample interval range;
- `might_be_noise`: a boolean value indicating if `reflections_count` is higher than a configurable threshold;
- `is_signal`: a boolean value indicating if `fired` and `isin_time_window` are both true;
- `is_fat_signal`: a boolean value indicating if `is_signal` is true and `heights_ratio` is below a configurable threshold;
- `is_detected`: a boolean value indicating if `is_signal` is true and `is_fat_signal` is false;
- `type`: an integer, enumerable value indicating the type of signal: if the signal has `is_detected` set to false, the value is set to `olefin.SignalTypes.uncategorized`. If the flat `is_detected` is true, and the `charge` and `height` are above configurable thresholds, the signal is set to `olefin.SignalTypes.streamer`. For all the remaining cases, the signal is set to `olefin.SignalTypes.avalanche`

In order to perform accurate time resolution measurements, the NIM waveform signal is recorded in the first channel of the digitizer. This allows us to compute the times at which the falling edge of the NIM trigger signal is present and use it as a reference to calculate the difference between the time arrival of the particle with the timely arrival of the trigger. The trigger time is computed by setting a threshold in ADC samples. For each Trigger waveform, the falling edge crossing the threshold is found, and the two samples before and after the crossing are calculated. The time is computed as the line intersection between the y-value of the configurable threshold with the line passing through the two samples found. Using a linear interpolation to compute this result allows us to obtain time resolution results with higher precision than the digitizer's sampling rate[14].

---

[14] AN3251 - Time Measurements with CAEN Waveform Digitizers

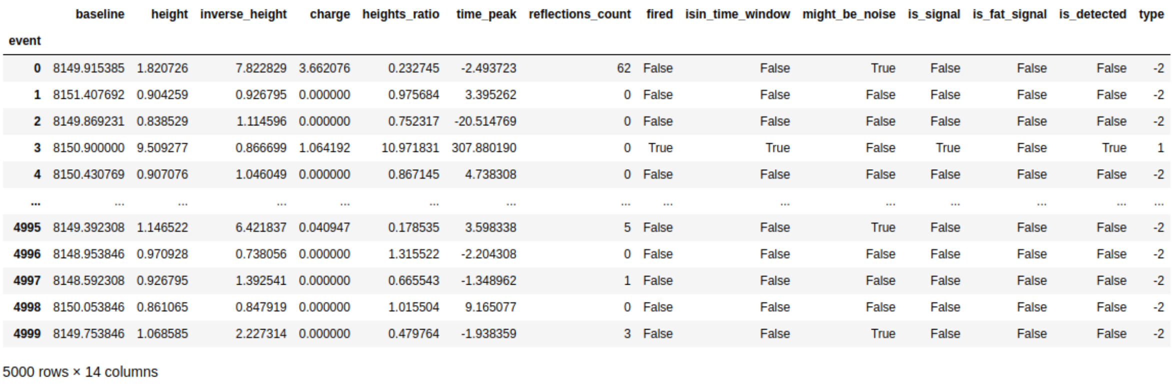

	baseline	height	inverse_height	charge	heights_ratio	time_peak	reflections_count	fired	isin_time_window	might_be_noise	is_signal	is_fat_signal	is_detected	type
event														
0	8149.915385	1.820726	7.822829	3.662076	0.232745	-2.493723	62	False	False	True	False	False	False	-2
1	8151.407692	0.904259	0.926795	0.000000	0.975684	3.395262	0	False	False	False	False	False	False	-2
2	8149.869231	0.838529	1.114596	0.000000	0.752317	-20.514769	0	False	False	False	False	False	False	-2
3	8150.900000	9.509277	0.866699	1.064192	10.971831	307.880190	0	True	True	False	True	False	True	1
4	8150.430769	0.907076	1.046049	0.000000	0.867145	4.738308	0	False	False	False	False	False	False	-2
...	...	...	...	...	...	...	...	...	...	...	...	...	...	...
4995	8149.392308	1.146522	6.421837	0.040947	0.178535	3.598338	5	False	False	True	False	False	False	-2
4996	8148.953846	0.970928	0.738056	0.000000	1.315522	-2.204308	0	False	False	False	False	False	False	-2
4997	8148.592308	0.926795	1.392541	0.000000	0.665543	-1.348962	1	False	False	False	False	False	False	-2
4998	8150.053846	0.861065	0.847919	0.000000	1.015504	9.165077	0	False	False	False	False	False	False	-2
4999	8149.753846	1.068585	2.227314	0.000000	0.479764	-1.938359	3	False	False	True	False	False	False	-2

5000 rows × 14 columns

FIGURE 4.17 – Example of data computed from the SignalAnalysis class. For each waveform a set of features is computed and displayed as columns in a pandas dataframe object.

The `EventAnalysis` class

The `EventAnalysis` class is responsible for computing trigger-related features for a set of waveforms. For instance, the total collected charge of a trigger event is the sum of the charge collected by each strip of the same detector. Similarly, the cluster size, defined as the maximum number of contiguous strips that detect a signal, requires the signal features information for multiple channels coming from the same trigger event. The `EventAnalysis` class provides a factory function `from_folder()` that instantiates a `SignalAnalysis` class for each wave file in a folder and aggregates the result into a pandas DataFrame object. Each row of the DataFrame is uniquely identified by the name of the wave file (i.e., the channel of the digitizer) and the number of the trigger event. Once the data is aggregated, each row of the data frame is assigned the RPC and the event number. The mapping between waveform files and strip number of an RPC is defined in the configuration file. A set of features is then computed, grouping the data frame by the tuple (RPC, event). Each group is a DataFrame containing the signal features for different channels sharing the same RPC and trigger event. The main computed event features are:

- `event_charge`: the sum of charges over all the channels;
- `cluster_size`: the maximum number of contiguous strips for which the `is_detected` condition is true;
- `is_detected`: a boolean value set to true if any of the signals has `is_detected` set to true;
- `time_peak`: the mean value of the time peaks for which the `is_detected` of the signals is true;
- `event_type`: the maximum value among the `event_type` of the signals. The signals are ordered so that an event considered as noise has a lower integer value with respect to an avalanche signal that has a lower value with respect to a streamer signal. Figure 4.19 highlights the difference between `signal_type` and `event_type`;

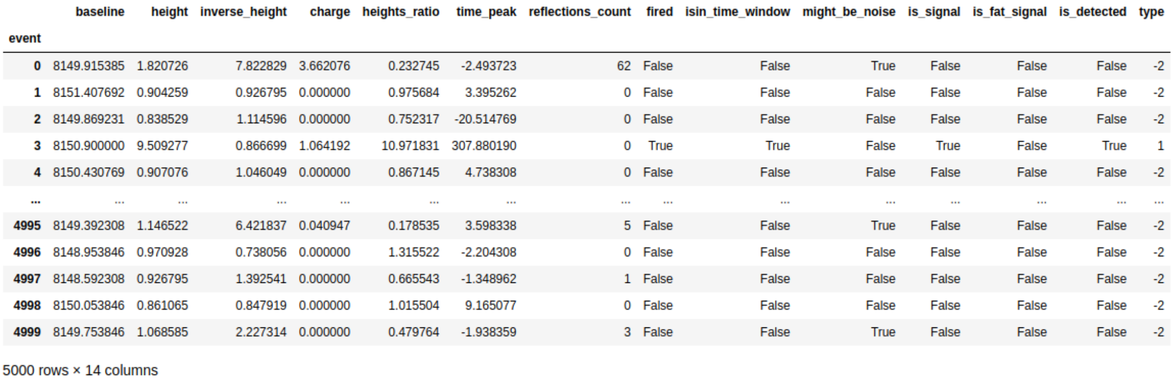

	baseline	height	inverse_height	charge	heights_ratio	time_peak	reflections_count	fired	isin_time_window	might_be_noise	is_signal	is_fat_signal	is_detected	type
event														
0	8149.915385	1.820726	7.822829	3.662076	0.232745	-2.493723	62	False	False	True	False	False	False	-2
1	8151.407692	0.904259	0.926795	0.000000	0.975684	3.395262	0	False	False	False	False	False	False	-2
2	8149.869231	0.838529	1.114596	0.000000	0.752317	-20.514769	0	False	False	False	False	False	False	-2
3	8150.900000	9.509277	0.866699	1.064192	10.971831	307.880190	0	True	True	False	True	False	True	1
4	8150.430769	0.907076	1.046049	0.000000	0.867145	4.738308	0	False	False	False	False	False	False	-2
...	...	...	...	...	...	...	...	...	...	...	...	...	...	...
4995	8149.392308	1.146522	6.421837	0.040947	0.178535	3.598338	5	False	False	True	False	False	False	-2
4996	8148.953846	0.970928	0.738056	0.000000	1.315522	-2.204308	0	False	False	False	False	False	False	-2
4997	8148.592308	0.926795	1.392541	0.000000	0.665543	-1.348962	1	False	False	False	False	False	False	-2
4998	8150.053846	0.861065	0.847919	0.000000	1.015504	9.165077	0	False	False	False	False	False	False	-2
4999	8149.753846	1.068585	2.227314	0.000000	0.479764	-1.938359	3	False	False	True	False	False	False	-2

5000 rows × 14 columns

FIGURE 4.18 – Example of data computed from the EventAnalysis class. Each row of the table represents one trigger signal, while the columns represent the computed statistics from different strips.

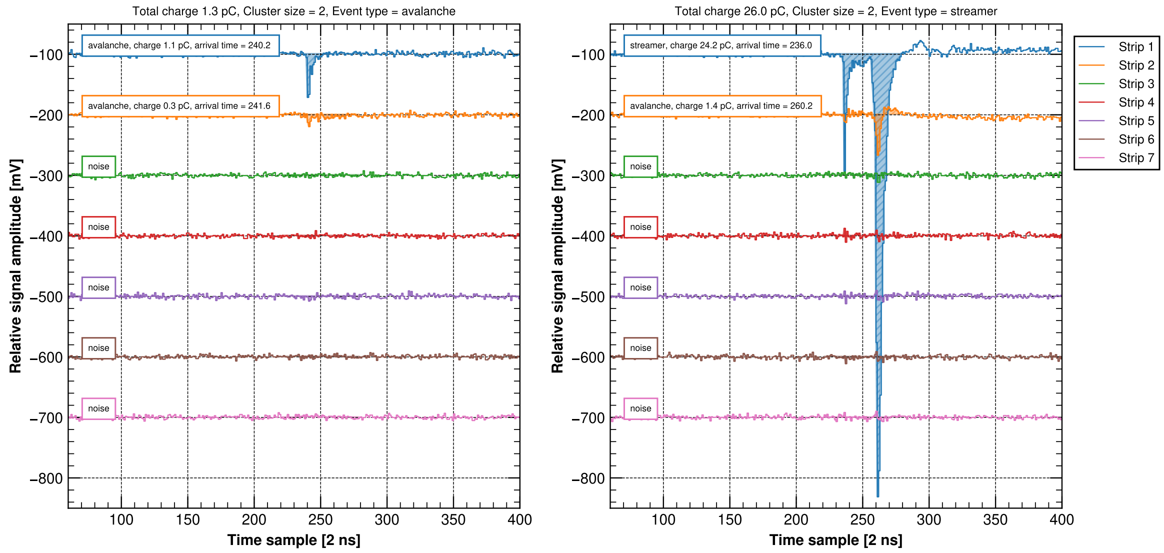

FIGURE 4.19 – On the left, an example of an avalanche classified event. Waveforms from a single trigger event collected on seven different strips. For each strip, signal-level features such as type, charge, arrival time are computed. The corresponding event-level features are then displayed in the title of the subplot. On the right, an example of streamer classified event.

The `AcquisitionAnalysis` class

The `AcquisitionAnalysis` class computes a set of features dependent on the voltage of the detector. To compute such features, the `EventAnalysis` class is instantiated and the analysed data is used as input data for the `AcquisitionAnalysis` class. Similar to the `EventAnalysis` class, the input data frame is grouped by RPC. The set of computed features is:

- `efficiency`: the efficiency is computed as the number of events for which `is_detected` is true over the total number of events. The error on the efficiency is computed as:

$$\sigma_\epsilon = \sqrt{\frac{\epsilon(1-\epsilon)}{n_{events}}} \tag{4.15}$$

- `streamer_probability`: the streamer probability is computed as the number of events for which `is_detected` is true and `event_type` is `olefin.SignalTypes.streamer` over the total number of events for which `is_detected` is true. Similarly to the efficiency, the error on the streamer probability is calculated as:

$$\sigma_{st.prob} = \sqrt{\frac{st.prob(1-st.prob)}{n_{events}}} \tag{4.16}$$

- `avalanche`: it is defined as the mean value of the events for which `is_detected` is true and event type is equal to `olefin.SignalTypes.avalanche`. The error on the mean of the distribution is computed as the standard deviation of the distribution divided by the square root of the number of avalanche events.
- `streamer`: Similar to avalanche, it is the mean on the detected events for which the event type is set to `olefin.SignalTypes.streamer`. The error is defined as the same way of the avalanche feature;
- `prompt_charge`: it is defined as the mean of all the events for which `is_detected` is true. The error is defined in a similar way to the avalanche feature;
- `cluster_size`: it is defined as the mean value of the cluster size distribution for all the events for which `is_detected` is true. The error is defined as the standard deviation of the distribution divided by the square root of the number of detected events;
- `time_res`: it is the time resolution. The feature is computed by fitting the distribution of all the event times for which `is_detected` is true with a gaussian function. The σ from the fit, together with the estimated error σ_{σ_t} and the reduced χ^2 square is returned from the fit;

An example of the resulting data frame structure is shown in Figure 4.20

The `RateAnalysis` classes

A dedicated family of analysis classes was developed to compute the hit rate of gamma particles in the presence of background radiation. When the DAQ system records long-windowed auto-trigger waveforms, the `RateSignalAnalysis` class computes the number of peaks in the signal using the SciPy's `find_peaks()` function[60]. The parameters used to

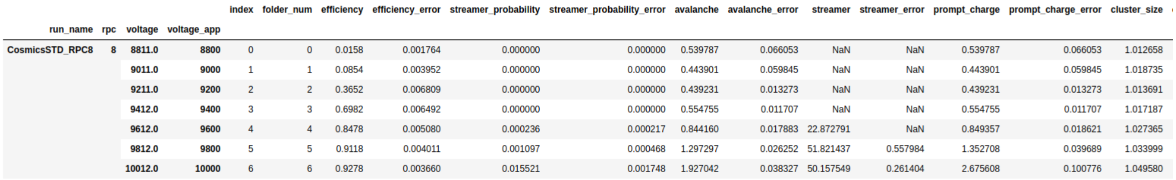

				index	folder_num	efficiency	efficiency_error	streamer_probability	streamer_probability_error	avalanche	avalanche_error	streamer	streamer_error	prompt_charge	prompt_charge_error	cluster_size
run_name	**rpc**	**voltage**	**voltage_app**													
CosmicsSTD_RPC8	**8**	**8811.0**	**8800**	0	0	0.0158	0.001764	0.000000	0.000000	0.539787	0.066053	NaN	NaN	0.539787	0.066053	1.012658
		9011.0	**9000**	1	1	0.0854	0.003952	0.000000	0.000000	0.443901	0.059845	NaN	NaN	0.443901	0.059845	1.018735
		9211.0	**9200**	2	2	0.3652	0.006809	0.000000	0.000000	0.439231	0.013273	NaN	NaN	0.439231	0.013273	1.013691
		9412.0	**9400**	3	3	0.6982	0.006492	0.000000	0.000000	0.554755	0.011707	NaN	NaN	0.554755	0.011707	1.017187
		9612.0	**9600**	4	4	0.8478	0.005080	0.000236	0.000217	0.844160	0.017883	22.872791	NaN	0.849357	0.018621	1.027365
		9812.0	**9800**	5	5	0.9118	0.004011	0.001097	0.000468	1.297297	0.026252	51.821437	0.557984	1.352708	0.039689	1.033999
		10012.0	**10000**	6	6	0.9278	0.003660	0.015521	0.001748	1.927042	0.038327	50.157549	0.261404	2.675608	0.100776	1.049580

FIGURE 4.20 – Example of data computed by the AcquisitionAnalysis class. Each row in the table represents an HV point for which several triggers were collected. For each HV point features like the efficiency, streamer probability, time resolution, etc. are computed.

detect peaks can be set from the configuration file. Once the number of peaks is computed for each waveform, the `RateAcquisitionAnalysis` class performs a rate estimation by dividing the number of the peaks found for the time interval of the waveform over the strips' covered area. The error is estimated considering the peak times counts from a Poissonian distribution. Hence, the error is computed as the square root of the rate value.

The `RunAnalysis` class

The `RunAnalysis` class represents the top level class used to analyse a single run. It computes features that are dependent on the whole data acquired by the DAQ system when a run is performed. The class takes a list of `AcquisitionAnalysis` objects for each voltage point scanned in the run. The data is aggregated into a dataframe and grouped by RPC. Each group contains the information about the voltage, RPC and the computed features by the `AcquisitionAnalysis` object. For each group, a fit on the voltage-efficiency curve is calculated. The fit function used is a sigmoid with three free parameters:

$$\epsilon = \frac{\epsilon_{max}}{1 + e^{-\lambda(HV_{eff} - HV_{50})}} \tag{4.17}$$

The fit has three parameters: ϵ_max, HV_50 and γ. ϵ_max represents the maximum reached efficiency. HV_50 indicates the voltage at which the efficiency is half of the maximum efficiency. γ is a parameter that defines the slope of the sigmoid curve. The initial guess on the parameters used to fit the function can be defined from the configuration file. After the fit is performed, the following features are computed for each RPC-related group:

- `efficiency_knee`: it is the voltage at which the efficiency reaches 95% of the ϵ_max value;
- `working_point`: defined as the sum of the `efficiency_knee` with an arbitrary voltage value. The value is usually chosen to be 150 V as the CMS-RPC community sometimes uses it for RPCs installed in the barrel[61].
- `streamer_probability`: it is the interpolation at the working point of the computed streamer probability points from the different `AcquisitionAnalysis` objects. The interpolation is usually performed by choosing the sigmoid model used for the efficiency fit. The error is computed by interpolating the streamer probability error in a similar way
- `avalanche`, `streamer`, `prompt_charge`, and `cluster_size`: similarly to

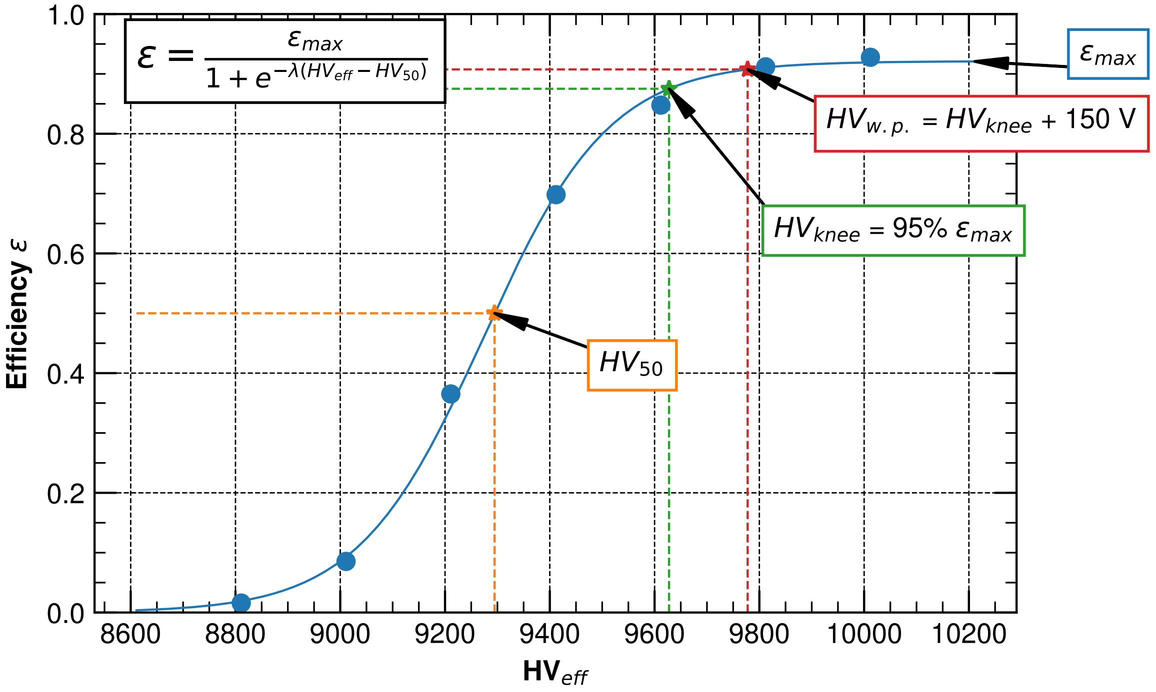

FIGURE 4.21 – Efficiency versus effective High Voltage for a single RPC run. The fit is drawn using Formula4.17 where the fitted parameters give information about the position of the curve, its slope and its maximum value. From these parameters, the efficiency knee and working point can be easily calculated.

streamer_probability, they are defined as the interpolated values at the working point;

In addition to the `AcquisitionAnalysis` computed values, some special features are computed from other run-related data:

- `currents_standard_mean`: the value interpolated at the working point of the RPC currents data recorded by the DAQ system. For each voltage point, the DAQ system records the mean value of the currents and stores them in a plain file on the same folder of the run;
- `currents_standard_std`: similarly to `currents_standard_mean`, it is the standard deviation value of the RPCs currents interpolated at working point;
- `currents_standard_beam`: when a run is performed in the presence of a muon beam, the currents of the beam during a spill are recorded by the DAQ system;
- `rate`: when a run is performed in the presence of background radiation and the DAQ system acquires auto-trigger data, the rate is obtained using the rate analysis classes defined in the previous section. The rate and its error are then interpolated at the working point;

Each `RunAnalysis` can optionally store all the information related to its lower-level classes in a convenient pandas DataFrame form. It is then possible to access each computed signal, event, and acquisition feature from a `RunAnalysis` object as shown in Figure 4.22.

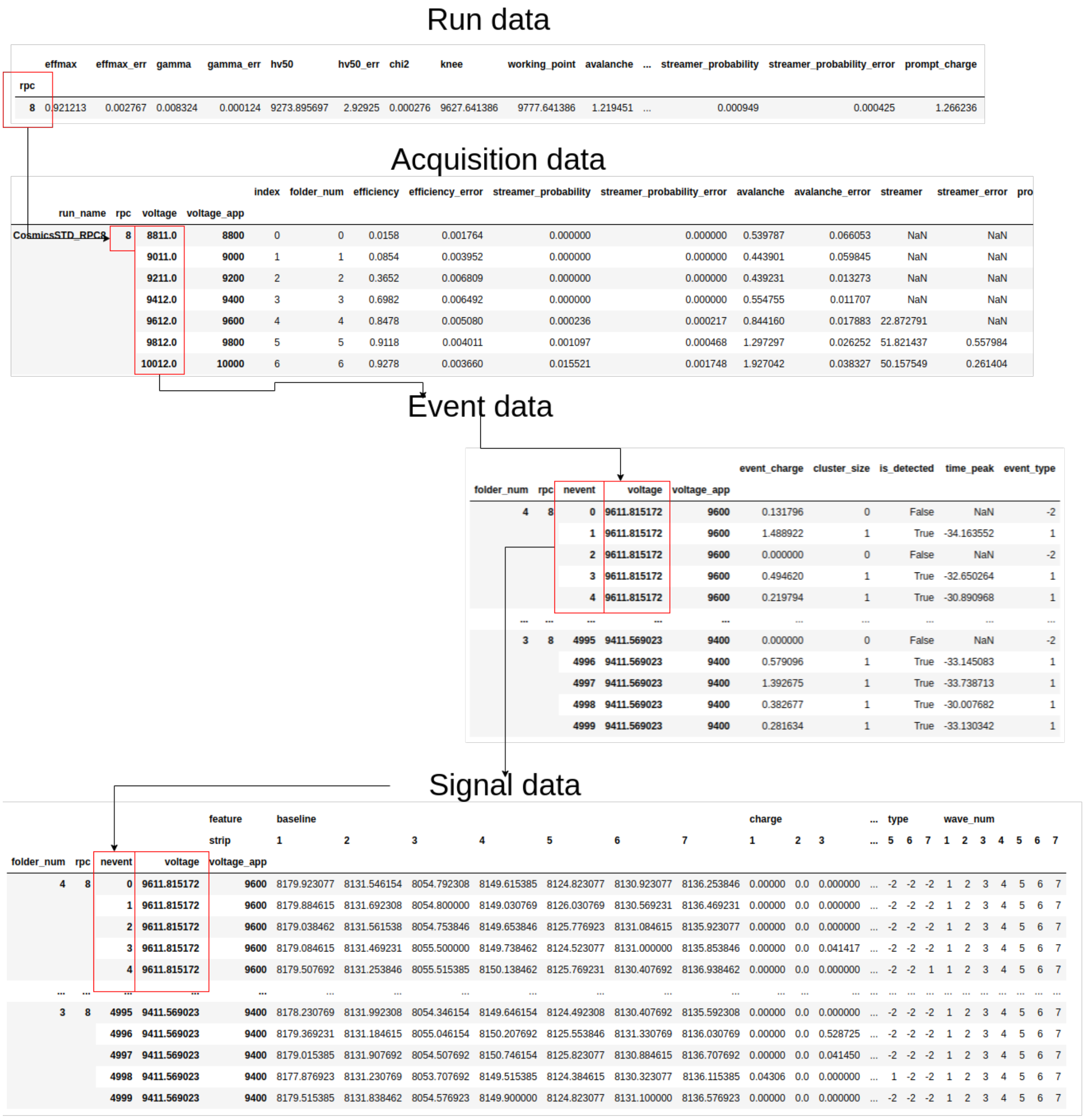

	effmax	effmax_err	gamma	gamma_err	hv50	hv50_err	chi2	knee	working_point	avalanche	...	streamer_probability	streamer_probability_error	prompt_charge
rpc														
8	0.921213	0.002767	0.008324	0.000124	9273.895697	2.92925	0.000276	9627.641386	9777.641386	1.219451	...	0.000949	0.000425	1.266236

				index	folder_num	efficiency	efficiency_error	streamer_probability	streamer_probability_error	avalanche	avalanche_error	streamer	streamer_error	pro
run_name	**rpc**	**voltage**	**voltage_app**											
CosmicsSTD_RPC8	**8**	**8811.0**	**8800**	0	0	0.0158	0.001764	0.000000	0.000000	0.539787	0.066053	NaN	NaN	
		9011.0	**9000**	1	1	0.0854	0.003952	0.000000	0.000000	0.443901	0.059845	NaN	NaN	
		9211.0	**9200**	2	2	0.3652	0.006809	0.000000	0.000000	0.439231	0.013273	NaN	NaN	
		9412.0	**9400**	3	3	0.6982	0.006492	0.000000	0.000000	0.554755	0.011707	NaN	NaN	
		9612.0	**9600**	4	4	0.8478	0.005080	0.000236	0.000217	0.844160	0.017883	22.872791	NaN	
		9812.0	**9800**	5	5	0.9118	0.004011	0.001097	0.000468	1.297297	0.026252	51.821437	0.557984	
		10012.0	**10000**	6	6	0.9278	0.003660	0.015521	0.001748	1.927042	0.038327	50.157549	0.261404	

					event_charge	cluster_size	is_detected	time_peak	event_type
folder_num	**rpc**	**nevent**	**voltage**	**voltage_app**					
4	**8**	**0**	**9611.815172**	**9600**	0.131796	0	False	NaN	-2
		1	**9611.815172**	**9600**	1.488922	1	True	-34.163552	1
		2	**9611.815172**	**9600**	0.000000	0	False	NaN	-2
		3	**9611.815172**	**9600**	0.494620	1	True	-32.650264	1
		4	**9611.815172**	**9600**	0.219794	1	True	-30.890968	1
...	**...**	**...**	**...**	**...**	...	...	...	...	...
3	**8**	**4995**	**9411.569023**	**9400**	0.000000	0	False	NaN	-2
		4996	**9411.569023**	**9400**	0.579096	1	True	-33.145083	1
		4997	**9411.569023**	**9400**	1.392675	1	True	-33.738713	1
		4998	**9411.569023**	**9400**	0.382677	1	True	-30.007682	1
		4999	**9411.569023**	**9400**	0.281634	1	True	-33.130342	1

				feature	baseline							charge			...	type			wave_num						
				strip	**1**	**2**	**3**	**4**	**5**	**6**	**7**	**1**	**2**	**3**	**...**	**5**	**6**	**7**	**1**	**2**	**3**	**4**	**5**	**6**	**7**
folder_num	**rpc**	**nevent**	**voltage**	**voltage_app**																					
4	**8**	**0**	**9611.815172**	**9600**	8179.923077	8131.546154	8054.792308	8149.615385	8124.823077	8130.923077	8136.253846	0.00000	0.0	0.000000	...	-2	-2	-2	1	2	3	4	5	6	7
		1	**9611.815172**	**9600**	8179.884615	8131.692308	8054.800000	8149.030769	8126.030769	8130.569231	8136.469231	0.00000	0.0	0.000000	...	-2	-2	-2	1	2	3	4	5	6	7
		2	**9611.815172**	**9600**	8179.038462	8131.561538	8054.753846	8149.653846	8125.776923	8131.084615	8135.923077	0.00000	0.0	0.000000	...	-2	-2	-2	1	2	3	4	5	6	7
		3	**9611.815172**	**9600**	8179.084615	8131.469231	8055.500000	8149.738462	8124.523077	8131.000000	8135.853846	0.00000	0.0	0.041417	...	-2	-2	-2	1	2	3	4	5	6	7
		4	**9611.815172**	**9600**	8179.507692	8131.253846	8055.515385	8150.138462	8125.769231	8130.407692	8136.938462	0.00000	0.0	0.000000	...	-2	-2	1	1	2	3	4	5	6	7
...	**...**	**...**	**...**	**...**	...	...	...	...	...	...	...	...	...	...	...	...	...	...	...	...	...	...	...	...	...
3	**8**	**4995**	**9411.569023**	**9400**	8178.230769	8131.992308	8054.346154	8149.646154	8124.492308	8130.407692	8135.592308	0.00000	0.0	0.000000	...	-2	-2	-2	1	2	3	4	5	6	7
		4996	**9411.569023**	**9400**	8179.369231	8131.184615	8055.046154	8150.207692	8125.553846	8131.330769	8136.030769	0.00000	0.0	0.528725	...	-2	-2	-2	1	2	3	4	5	6	7
		4997	**9411.569023**	**9400**	8179.015385	8131.907692	8054.507692	8150.746154	8125.823077	8130.884615	8136.707692	0.00000	0.0	0.041450	...	-2	-2	-2	1	2	3	4	5	6	7
		4998	**9411.569023**	**9400**	8177.876923	8131.230769	8053.707692	8149.515385	8124.384615	8130.323077	8136.115385	0.04306	0.0	0.000000	...	1	-2	-2	1	2	3	4	5	6	7
		4999	**9411.569023**	**9400**	8179.515385	8131.838462	8054.576923	8149.900000	8124.823077	8131.100000	8136.576923	0.00000	0.0	0.000000	...	-2	-2	-2	1	2	3	4	5	6	7

FIGURE 4.22 – Data frames stored into a RunAnalysis object. Each data frame is linked to its lower level dataframe, providing information about features calculated for each Analysis class.

4.4.2 Commissioning of the `olefin` library

The olefin library provides many configuration options and flexibility thanks to its modular design. However, the large number of parameters that can be set requires proper commissioning for the library to analyze the data correctly. The commissioning phase was done first by setting up a unit test suite with mock-up data against which the library can be run. The test suite is integrated with the source code, using the pytest [62] framework to build unit tests. Each unit test aims to check the correct execution of the library's functionalities to prevent the addition of unwanted regressions when new features are added. The test suite includes small-sized real data from the DAQ system to evaluate the correct behavior of the analysis algorithms. The coverage of the source code for the 1.0.1 version is 95%. Once the test suite was defined, the library was run against real data acquired from the DAQ system. In order to set the proper thresholds, several tests were performed using the CMS RPC gas mixture (from here on referred to as standard gas mixture for simplicity) as a reference since its main properties were well defined [63].

Time region for signal detection

In order to detect only muon particles and discard background noise, it is important to set the correct time window for signal detection. The window is arbitrarily chosen depending on the electronics used to generate the trigger signal and the length of the cables connected to the RPC strip. The configuration parameters used are expressed in digitizer samples units. The configuration variables in the library are `config.signal.time_min` and `config.signal.time_max`. The setting of the proper window is done by switching on the detector with the standard gas mixture at the working point together with the external trigger system and using the CAEN's WaveDump program to detect at what time the strips are detecting a particle signal.

Height detection threshold

As explained in the previous paragraph, the `fired` variable for a signal is set to true when the signal's peak is above a certain threshold. The threshold is expressed in mV, and its value is usually set to discard the noise of the readout system. Several runs with different thresholds were performed to evaluate the effects on efficiency drops and working point change. It was found out that a threshold of 1-2 mV is suitable for the currently used readout systems and the working point is comparable with the working point used by the ALICE, ATLAS, and CMS experiments for RPC operated the standard gas mixture (9400-9800 V).

Figure 4.23 shows that when the threshold is set to very small values, the efficiency drops as the time of the peak of the first sample crossing the threshold is used as a reference. If the time trigger lies outside the detection window, the signal is considered noise, and the efficiency drops. When raising the height threshold, fewer signals are considered noise until a plateau condition is reached. When increasing the height threshold, the efficiency drops again as the smaller avalanche signals start to be discarded.

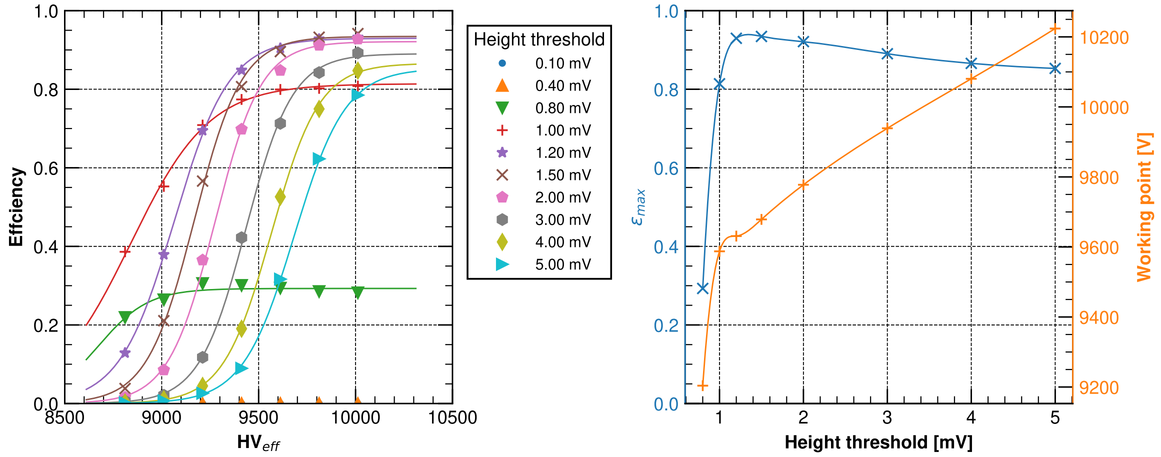

FIGURE 4.23 – On the left, efficiency curves for different values of height detection thresholds. On the right, computed ϵ_{max} and working point against height thresholds.

Signal discrimination threshold

The parameter `config.signal.charge_thresh_av` discriminates between an avalanche and a streamer signal. The choice of a threshold is not trivial as the separation of the avalanche signals from the streamer signals may depend on the gas mixture. A value of 10^8 electrons (16 pC) was chosen to be used as it corresponds to the Rather limit [50].

Rate analysis related parameters

The count of peaks to estimate the background rate is done using SciPy's `signal.find_peaks()` function. The waveform is first smoothed using a Savitzky–Golay filter [64] to avoid any spurious noise signal in the count of rate. The choice of the window and the polynomial order to smooth the signal was made by manually comparing the smoothed signals against the original one and checking for the quality of the smoothed one. The `find_peaks()` function was tuned using `config.rate.height`, `config.rate.distance` and `config.rate.prominence` using appropriate parameters for distance and considering the estimated impinging gamma rate on the detector.

4.5 Environmentally friendly gas mixtures studies in laboratory conditions

The following section is dedicated to the study the RPC performance when operated in laboratory conditions with cosmic muons and different gas mixtures. First, the detector's performance was characterized by the standard gas mixture. Later, an addition or a change of a component in a gas mixture was studied in detail to understand its effects.

4.5.1 Characterization of the standard gas mixture

The RPC performance with the standard gas mixture was widely studied in the past for the commissioning phase of the muon systems for LHC experiments [63, 65, 13] . The present

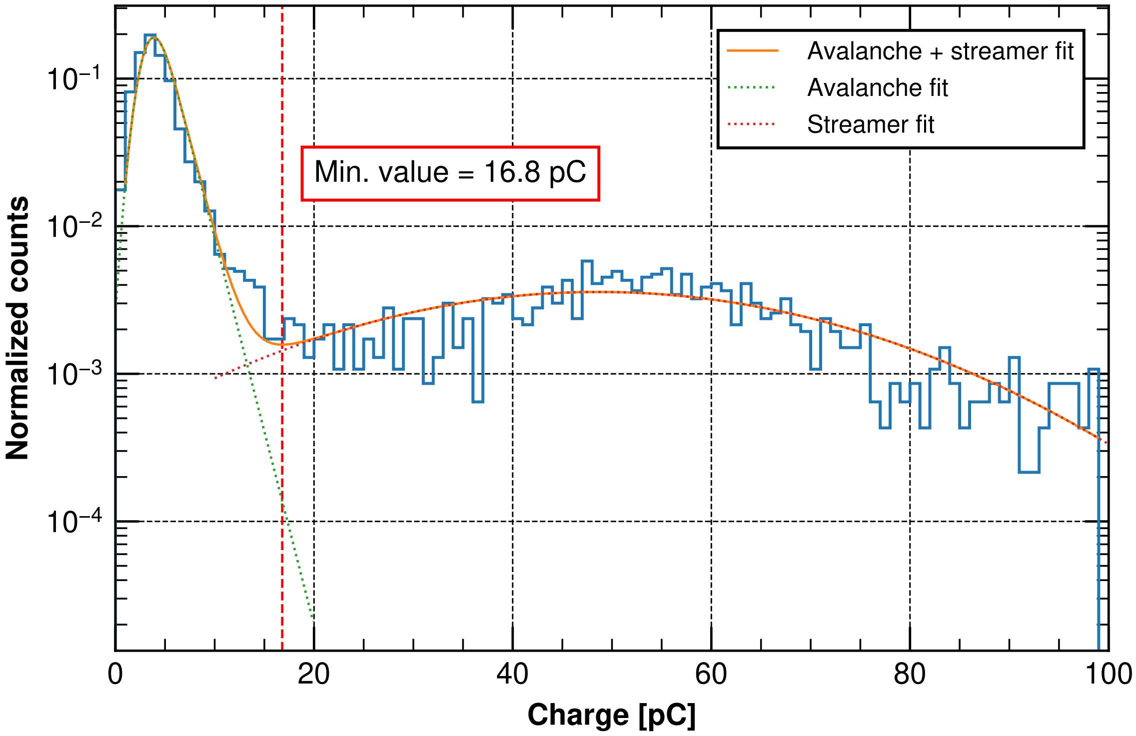

FIGURE 4.24 – Charge distribution at working point for a 2 mm RPC operated with the standard gas mixture. The avalanche and streamer curves are fitted and the minimum of the distribution is used to confirm the separation thresholds correspond to the Raether limit of 10^8 electrons.

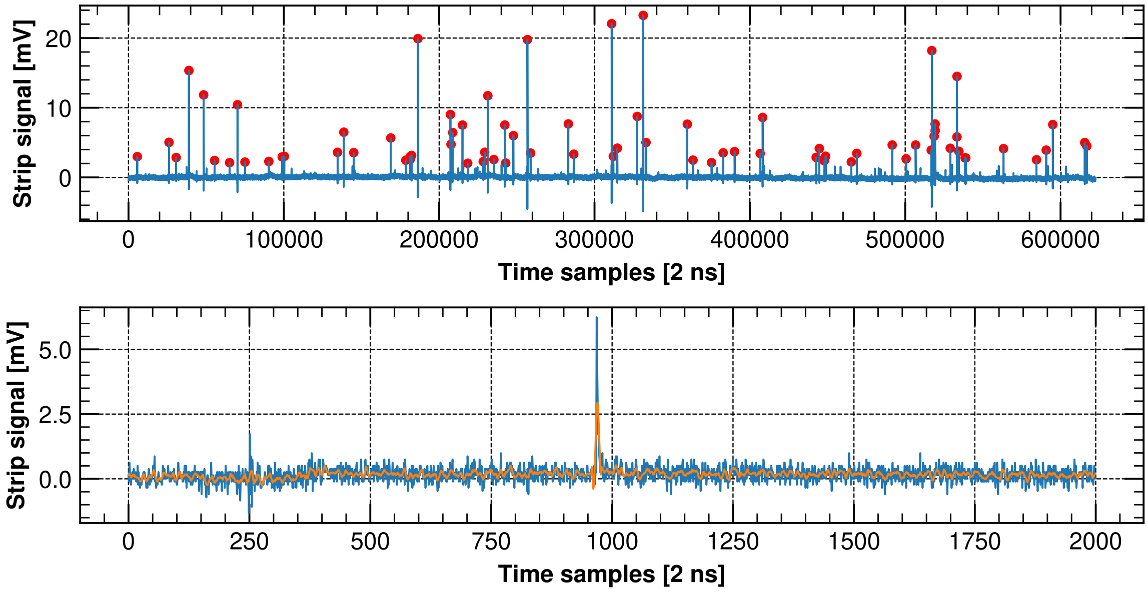

FIGURE 4.25 – On the top, an example of a long, single recorded window with the peaks detected by the olefin library. On the bottom, a zoomed region of the window showing the raw signal in blue and the smoothed signal in orange.

standard gas mixture refers to the currently used gas mixture for the CMS RPC sub-detector. It is composed of a large fraction of 95.2% of R-134a, followed by 4.5% of i-C_4H_{10} and 0.3% of SF_6. Each gas component in the mixtures has a specific role: R-134a provides a high density of primary ion-electron clusters, ensuring a high detection efficiency. Furthermore, its electronegativity allows it to reduce the transversal spatial charge spread. Isobutane is used for its quenching properties: being a hydrocarbon with a high number of roto-vibrational states, it absorbs a significant fraction of photons and reduces the photon feedback effects. A maximum amount of 4.5-5% was chosen for the ATLAS and CMS experiments as it is the upper limit for which the gas mixture remains non-flammable. An amount of 0.3% of SF_6 is added to the mixture as it further helps charge localization and streamer suppression, being itself strongly electronegative. Figure 4.26 shows the efficiency and streamer probability against the effective voltage for a single gap RPC operated with the standard gas mixture. The working point of the detector is found to be around 9400-9800 V, depending on the detector itself. It can be noticed that the streamer probability at the working point is less than 1%. It can also be observed that the difference between the working point and the voltage at which the streamer probability is 10% is around 500-550 V. These characteristics are fundamental as the streamer contamination gives valuable information about the rate capability of the detector. The higher the streamers fraction, the higher the prompt charge developed inside detectors with a consequent drop of voltage within the gas, thus decreasing efficiency. This effect is crucial for the detector's operation in high rate environments such as LHC experiments. Thus, a desirable feature for a gas mixture would be to have the streamer probability similar or less than the standard gas mixture's.

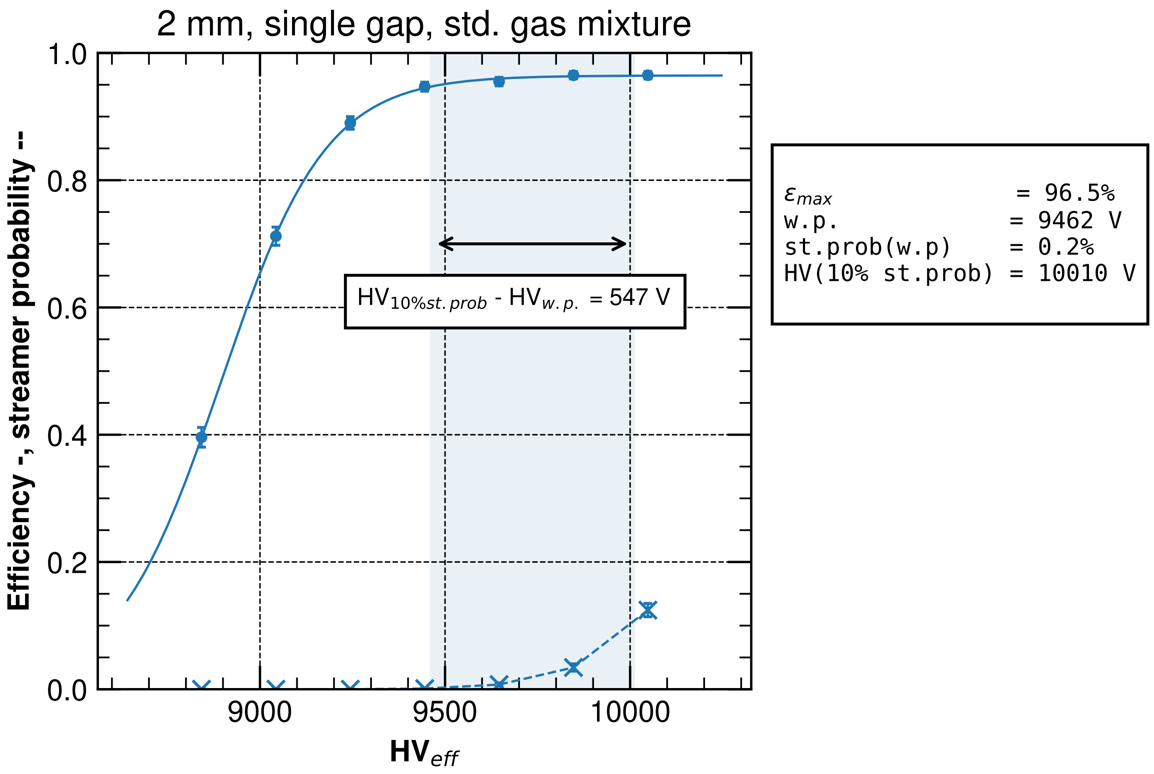

FIGURE 4.26 – Efficiency and streamer probability curves for the standard gas mixture.

The currents drawn on the detector depend both on the active surface of the detector and its resistivity, and it might be affected by aging effects. Figure 4.27 shows the currents for detectors of different productions and different resistivities operated with the standard gas mixture. Currents play a crucial role in the performance of the detector: they provide information about the charge per count developing in the gap, hence the behavior of the detector in high rate environments: the actual field inside the gap depends on the applied voltage on the detector minus the voltage across the resistive electrodes as shown in Formula4.18. Increasing currents corresponds to a more significant voltage drop across the resistive electrodes. The voltage drop across the electrodes decreases the effective electric field inside the gap, leading to a smaller efficiency of the detector.

$$HV_{gap} = HV_{applied} - R_{electrodes} I_{gap} \tag{4.18}$$

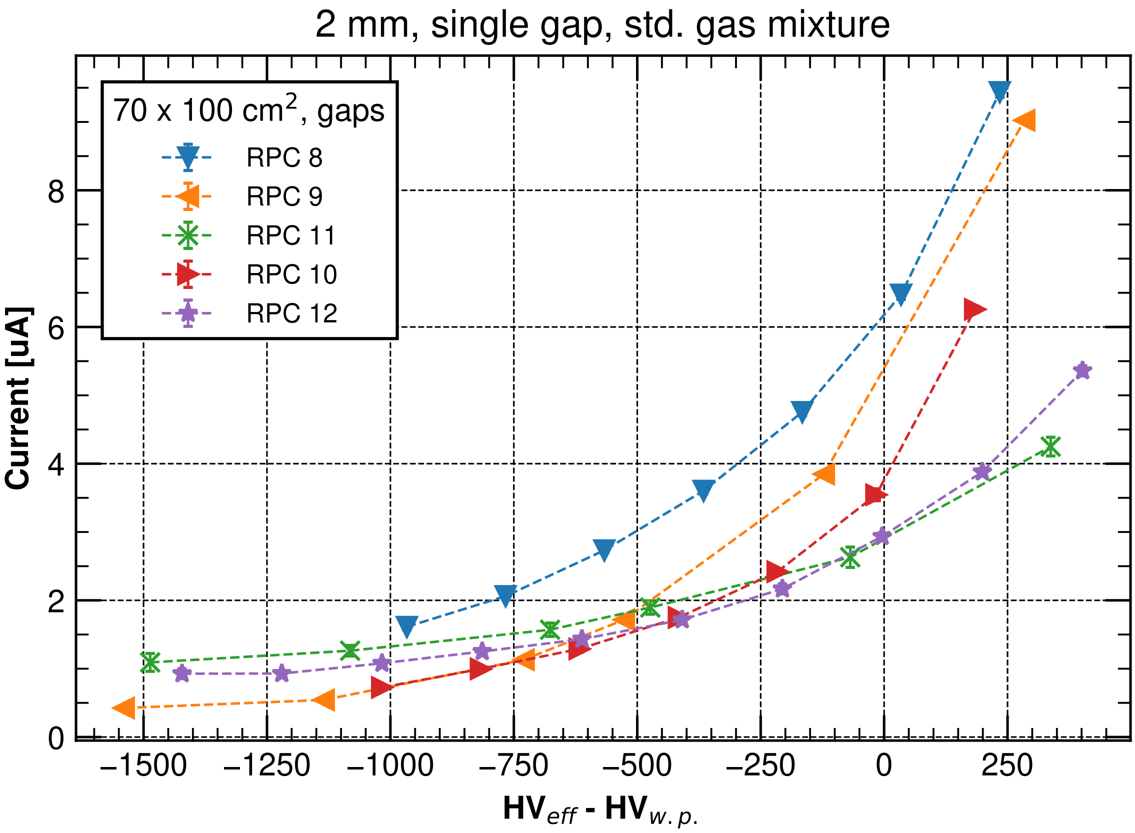

FIGURE 4.27 – Currents plotted against the applied voltage minus the working point.

It is also known that when operating RPC in a background environment, some undesired gas pollutants are produced due to the fluorinated molecules breaking into different products. It is was shown that the production of such pollutants is proportional to the currents [66, 67]. Thus, Freon-based gas mixtures with higher currents than the standard one might indicate a possible increased production of fluoride impurities with a possible increased aging effect.

The charge distribution of the standard gas mixture is shown in Figure 4.28. It can be noticed that for voltages less than the detector working point, the majority of signals have a prompt charge less than 10^8 electrons, indicating the avalanche operation mode of the RPC. When further increasing the electric field within the gap, a separate streamer population starts to be visible for charge values above 15-20 pC.

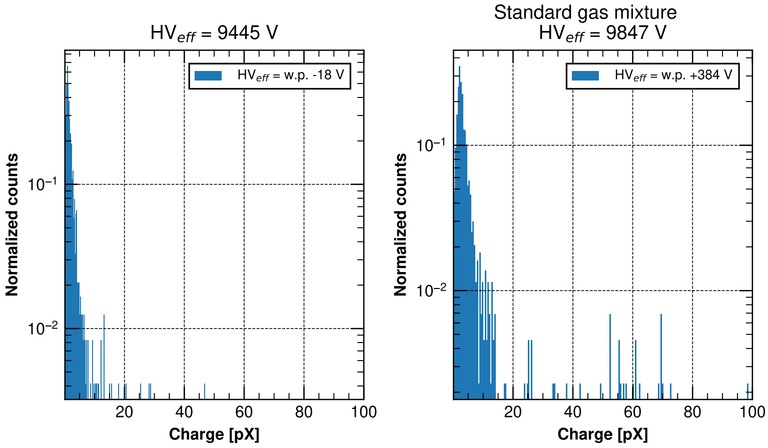

FIGURE 4.28 – Charge distribution for increasing applied voltages for the standard gas mixture.

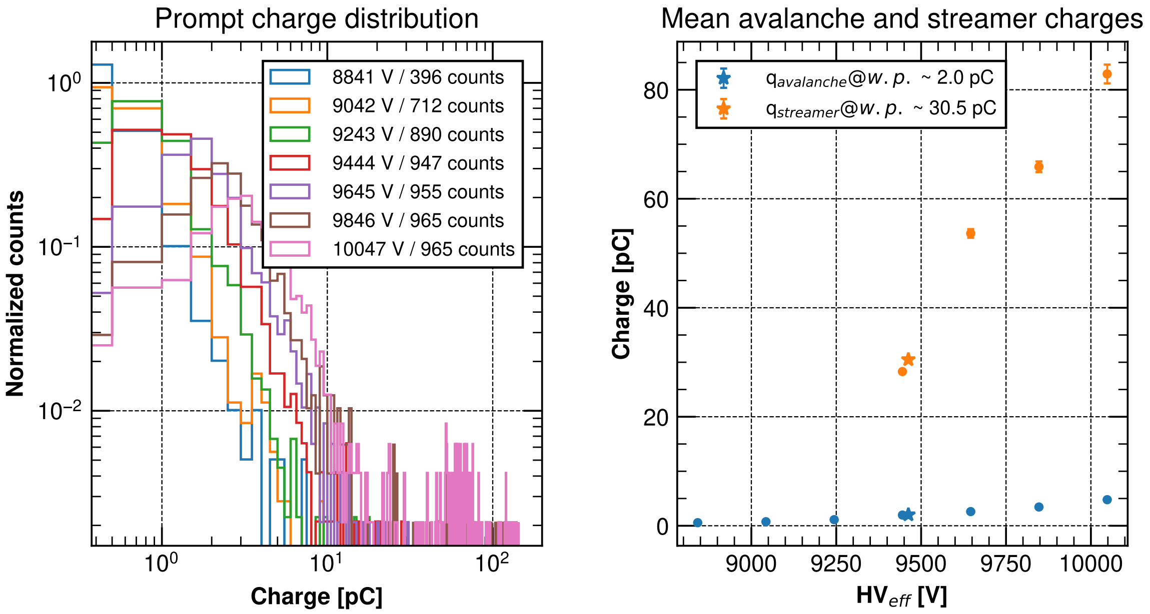

FIGURE 4.29 – On the left, charge distributions for different voltages. On the right, mean avalanche and streamer prompt charges against effective high voltage. Measurements obtained with the standard gas mixture.

The spatial distribution of the charge can be investigated by looking at the cluster size distribution. Figure 4.30 shows the cluster size distribution for an RPC with a strip pitch of 2.5 cm. A smaller cluster size improves the charge localization, and an increased tracking precision can be accomplished by calculating the centroid of the charge collected by neighboring strips. When applying an increasing electric field, the mean cluster size increases. The reason could be investigated in the increasing number of large signals such as streamers and in

Working point	9400-9800 V
Efficiency	>95 %
Streamer probability	<= 1%
Cluster size	1-2 strips (2-2.5 cm pitch)
Time resolution	1-2 ns
Mean avalanche charge	2 pC

TABLE 4.3 – Foremost parameters of RPC operated with the standard gas mixture.

the increasing predominance of spatial charge effects for which the number of transversal side discharges increases.

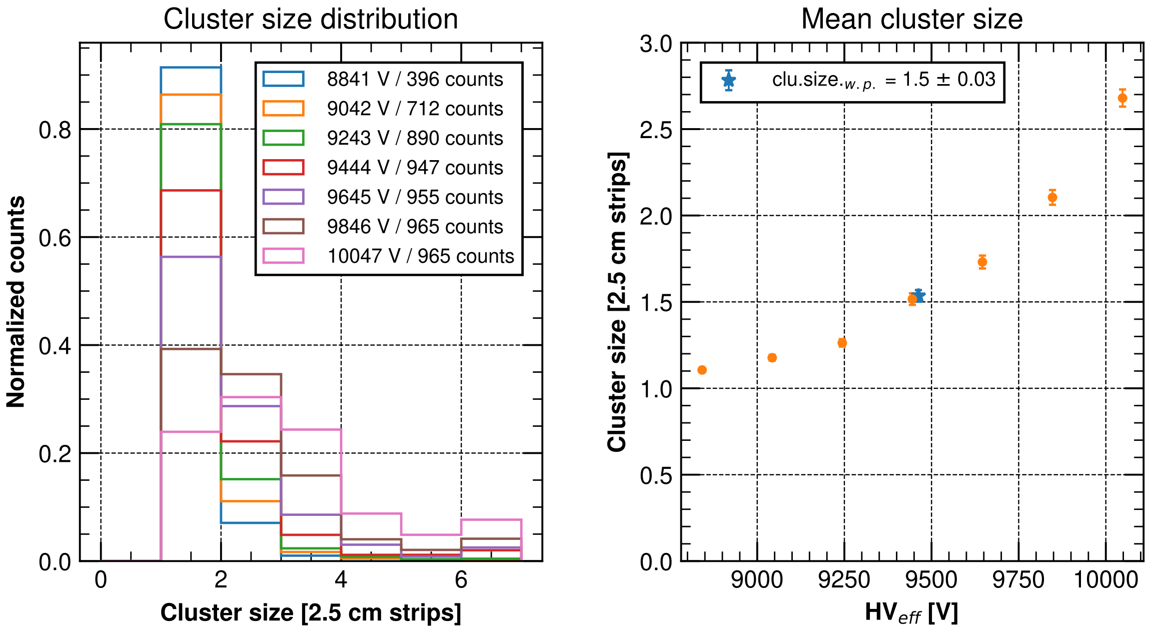

FIGURE 4.30 – On the left, cluster size distribution for different voltages. On the right, mean cluster size against effective voltage.

The time resolution of the detector operated with the standard gas mixture is reported in Figure 4.31. It is worth mentioning that the intrinsic time resolution for a single gap RPC depends on a first approximation on the drift velocity and the Townsend coefficient. The estimated value for the standard gas mixture is around 1 ns. The front-end electronics or readout system could add an additional time jitter to the measurements [63, 47]. It can be observed that the time resolution increases when the applied voltage increases. The reason is due to the fact the charge development is proportional to the drift velocity, which increases when the electric field increases [68].

The time resolution obtained with the present readout system and RPC setup is around 2 ns, compatible with the time detector intrinsic limit of 1 ns and in agreement with reported performance in the technical design reports of the CMS and ATLAS muon systems[63, 65]. A summary of the foremost parameters of RPCs operated with the standard gas mixtures is reported in Table 4.3

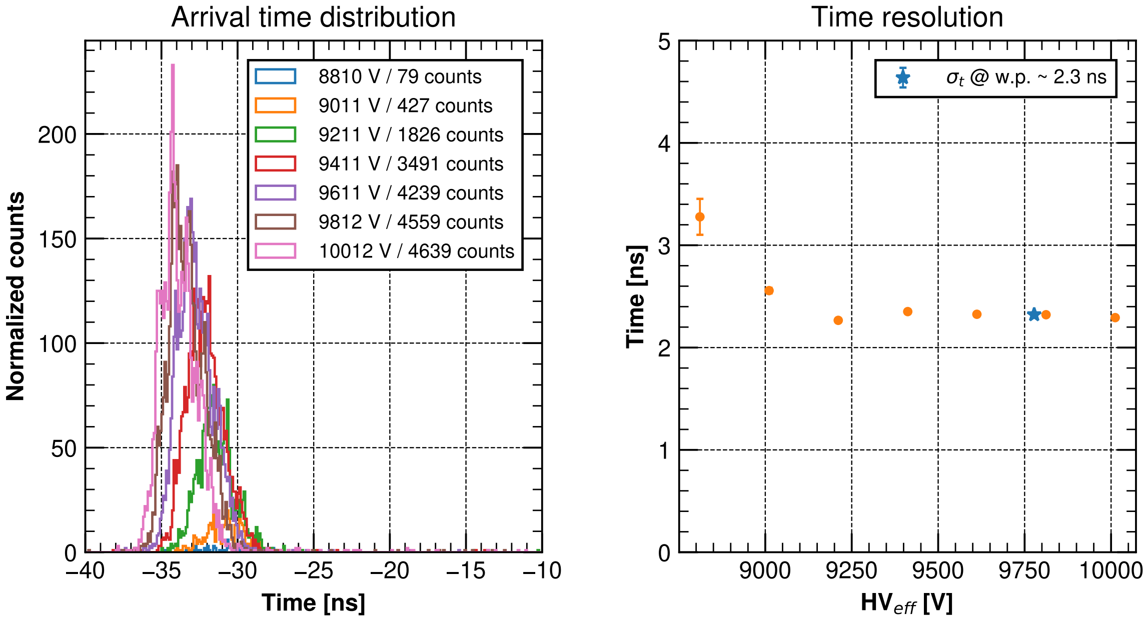

FIGURE 4.31 – On the left, the time arrival distribution computed for different voltages. On the right, σ computed from a gaussian fit for each time arrival distribution against the effective voltage.

4.5.2 Characterization of He and CO_2 based gas mixtures

The search for lower GWP gas mixtures was done by attempting to replace R-134a with a new generation of low-GWP refrigerant gas in the family of Hydro-Fluoro-Olefin gases. In particular, the refrigerant industry identified two gases, R-1234ze and R-1234yf, as possible candidates to substitute R-134a thanks to their similar thermodynamic properties, GWP_{100} of 7, and atmospheric lifetime of 7 days. However, the direct replacement of R-134a with R-1234ze in a 2 mm RPC is not possible due to the higher electronegativity of the gas [69, 70]: the working point is well beyond 12 kV, which represents the maximum sustainable voltage for the RPC power supply systems at LHC. An additional component in the gas mixture is therefore required to lower the working point. Several different gas mixtures were tested with a combination of He [71] and CO_2 [72]. In the present work, an experimental campaign was set up to understand the effects of the addition of He or CO_2 to the detector. A precise amount of one of the two components was added to the standard gas mixture at increasing steps of 10%, removing the corresponding amount of R-134a. Figure 4.32 reports the efficiency and streamer probability curves for different concentrations of He and CO_2, while Figure 4.33 shows that the variation of 10% of He roughly corresponds to a shift of working point of 600 V, while the addition of 10% of CO_2 produces a smaller shift of around 190 V. When compared with He-based gas mixtures, the addition of CO_2 seems to change the high-efficiency region of the detector: the plateau appears to be smoother and decreases the useful region for the detector to work without the presence of streamers. It is worth noting that when the two gases are added with concentrations higher than 30-40%, the streamer contamination increases significantly. One explanation could be related to the total electronegativity of the gas: when the amount of He or CO_2 increases up to 30%, the gas still has a sufficient electron affinity to suppress streamer formation and contain space charge effects. When the amount is further increased, the transversal charge development due to an ionizing particle starts to dominate the development of the signal due to the lower electronegativity of the gas, increasing the streamer contamination.

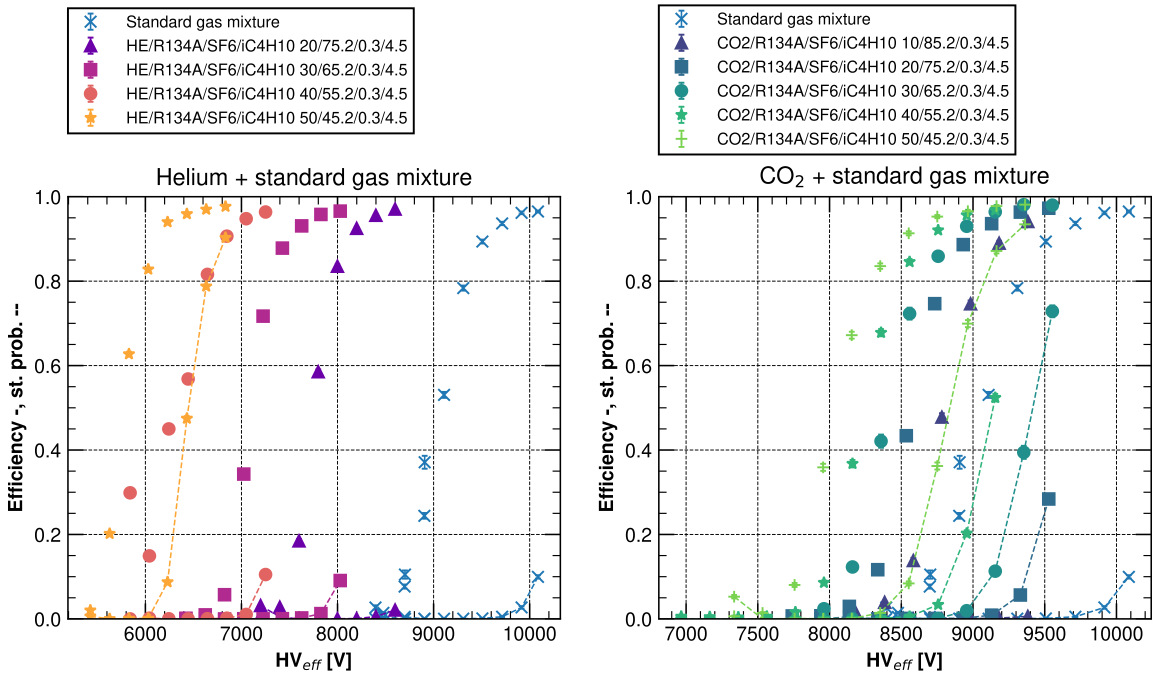

FIGURE 4.32 – Efficiency and streamer probability curves for different values of He and CO_2 addition. On the left, the addition of He to the standard gas mixture shows a decrease of the working point of the detector. The streamer probability shows a significant increase then adding 50% of He. On the right, the same efficiency curves for the addition of CO_2. It can be observed that the shift in working point is lower with respect to He, while the streamer probability shows a significant increase when used with concentrations above 30%.

The operation with a lower applied electric field can be exploited to fine-tune the gas mixture by adding a higher fraction of high-electronegative components. This can result in increased usage of SF_6 or its alternatives, keeping the R-134a usage lower than the standard gas mixture and reducing the net GWP of the gas mixture. The performance related to the addition of He at 30-40% is appealing from a detector point of view as the working point is around 2.5 kV lower. However, the usage of He in LHC experimental caverns is still a matter of concern due to the presence of Photomultiplier Tubes (PMTs), whose performance is sensitive to the presence of few ppms of He, a value that may be present in the UX cavern if one takes into account the current RPC leaks. Investigation to qualify and quantify the performance and aging effects of the He presence in PMTs is currently undergoing. For the mentioned reason, CO_2 was often used together with R-1234ze when studying the performance of HFO-based gas mixtures.

4.5.3 Characterization of R-1234ze-based gas mixtures

1,3,3,3-Tetrafluoropropene or R-1234ze is a recently engineered gas in the family of Hydro-Fluoro-Olefins. Its formula is $C_3H_2F_4$, classifying it as an Alkene molecule with a double carbon bond. The gas was initially developed by Honeywell™[73] as a replacement of R-134a that could supply with the European Union regulatory requirements for reducing the

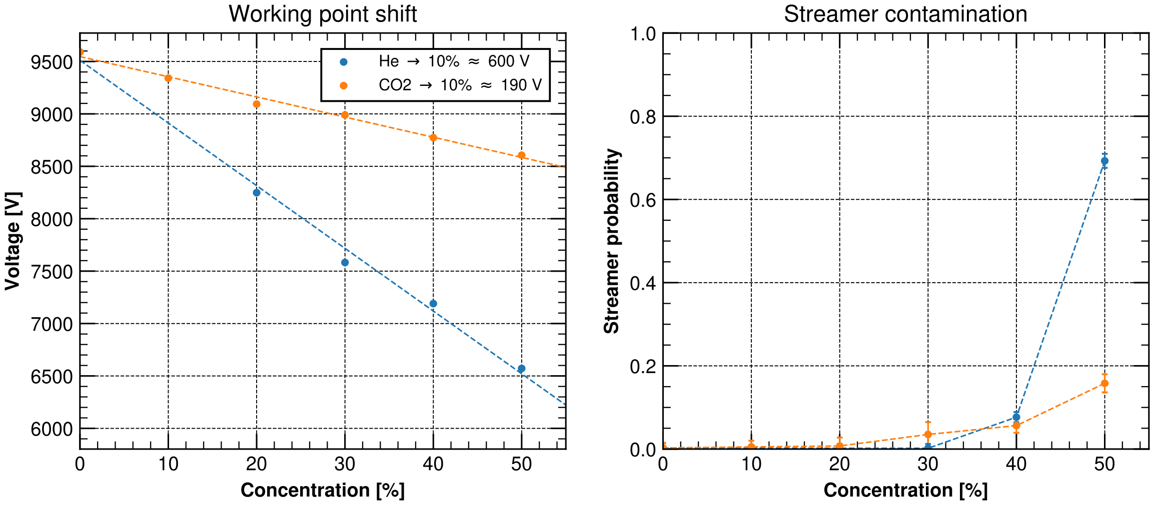

FIGURE 4.33 – Effects of adding CO_2 or He in different concentrations to the standard gas mixture. On the left, the change of detector's working point is reported. On the right, the streamer probability calculated at working point is shown,

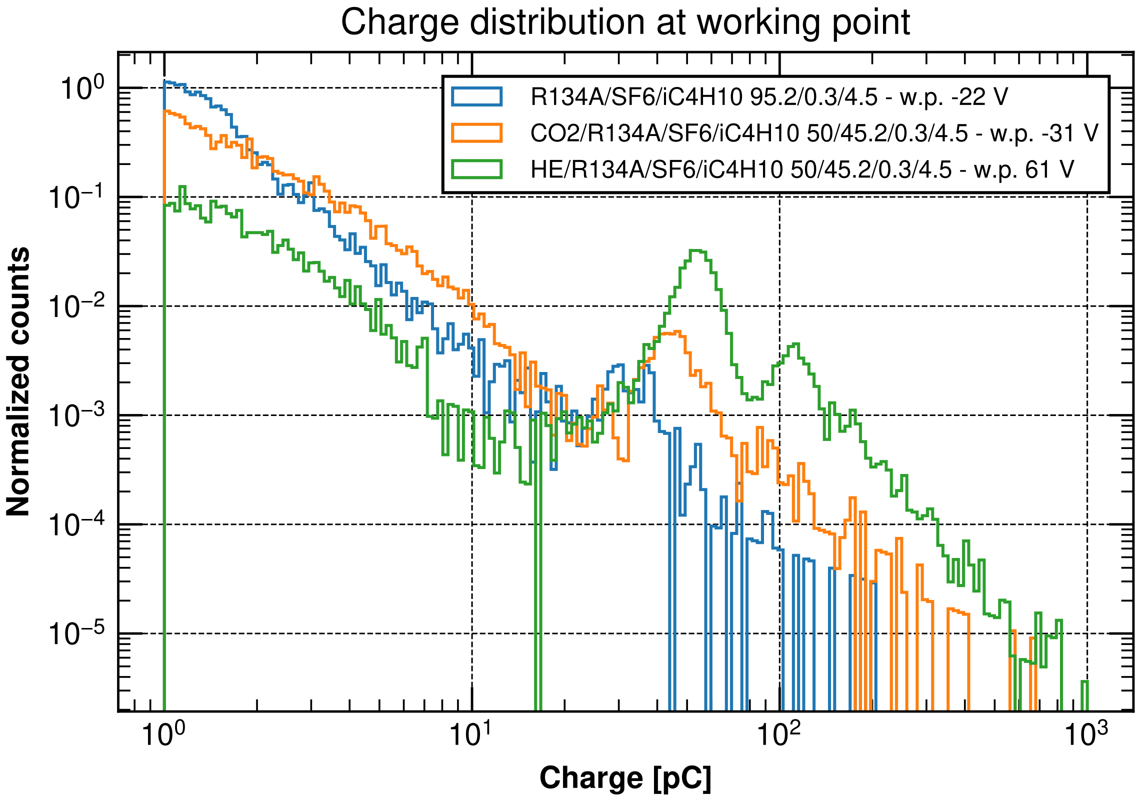

FIGURE 4.34 – Charge distribution for RPC operated close to the working point for the standard gas mixture, 50% CO_2 gas mixture and 50% He gas mixture. The contamination of streamers is particularly visible for the He-based gas mixture, where two populations at 50 and 100 pC are visible.

use of high-GWP substances. The gas has a zero ozone-depletion potential, and a GWP_{100} estimated to be between 1 and 7. The boiling point of the gas is -19 °C, with a vapor pressure of around 4 bars at ambient temperature, making it suitable to be used in current LHC-gas supply installations. The gas meets the LHC safety requirements, as it is not flammable at room temperature and has a very low toxicity value (LC_{50}(rat)[15] > 207000 ppm). The performance study of RPCs operated with cosmic muons, and R-1234ze based gas mixture can be found in several works [70, 72, 71, 69, 74, 75]. RPC performance operated with HFO-based gas mixtures with muon beam and with background radiation were recently studied by the CERN gas group in [76, 77, 78]. New performance studies were recently conducted, for which the work will be discussed in the following sections. Studies on the aging effects of RPCs operated with gamma background radiation were started. Results were published by the RPC ECOGAS collaboration in [79]. In the present work, the RPCs were operated with several HFO-based gas mixtures by always comparing the foremost parameters with the standard gas mixture. In particular, four components R-1234ze/CO_2 gas mixtures were studied in [80], where i-C_4H_{10} and SF_6 were kept fixed at 5% and 1% respectively, and the ratio of R-1234ze/CO_2 was varied. It was shown that a change of 10% of R-1234ze resulted in a shift of working point of around 800 V. Figure 4.35 shows the performance of an RPC operated with two gas mixtures at different HFO concentrations. The gas mixtures are well suitable for cosmic muons experiments as the RPCs reach full efficiency with a high charge per count value. The working point of the HFO-based gas mixtures is considerably higher with respect to the standard gas mixture. The streamer probability at the working point of the detector is also higher. Investigation of the causes is undergoing. An explanation could be related to the high presence of CO_2 and the higher chemical reactivity of R-1234ze due to its double carbon bond.

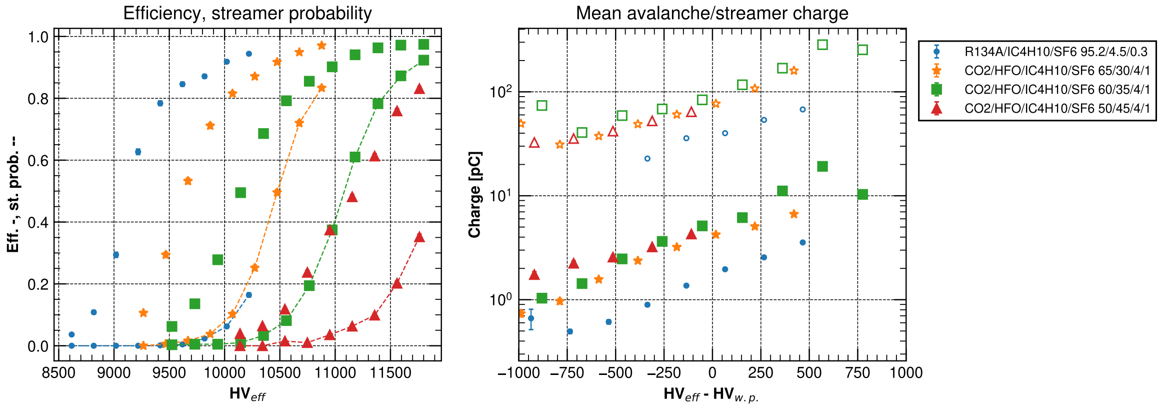

FIGURE 4.35 – Foremost parameters of R-1234ze/CO_2 based gas mixtures. On the left, efficiency and streamer probability values. HFO gas mixtures present a shift towards higher voltages, due to the R-1234ze electronegativity. Also, it can be noticed a higher streamer probability at the working point of the selected gas mixture is higher with respect to the standard one. On the right, mean avalanche (filled marker) and mean streamer (empty marker) against the voltage relative to the working point. Both avalanche and streamer charges for HFO gas mixtures at the working point present a factor two higher, with weak dependence on the ratio HFO/CO_2 used in the mixture.

---

[15] LC_{50} is defined as the concentrations of the chemical in air that kills 50% of the test animals during the observation period.

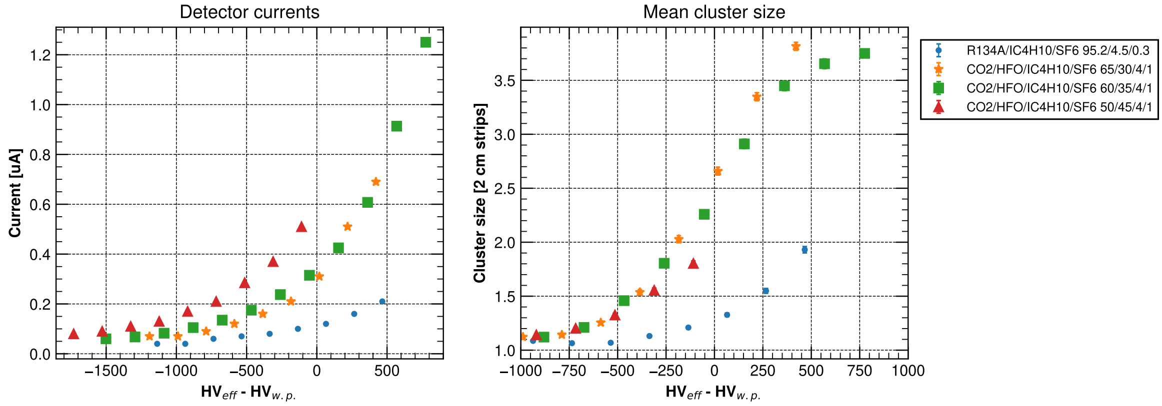

FIGURE 4.36 – Foremost parameters of HFO/CO_2-based gas mixtures. On the left, the currents drawn by the detector. It can be observed that increasing HFO in the mixture leads to an increase of currents at working point. On the right, mean cluster size. Similarly to the prompt avalanche and streamer charges, the cluster size is around 80% higher for the HFO-based gas mixtures, with no big dependency on the amount of R-1234ze used.

However, in the presence of gamma background radiation, the high streamer contamination and higher charge per count might affect the detector's performance as voltages higher than the current limits may be required to operate the detector at desired efficiency. The detector performance was then studied by requiring the addition of some amount of R-134a to the gas mixture. In particular, the R-134a/R-1234ze ratio was kept equal, and the amount of CO_2 was varied between 40% and 50%.

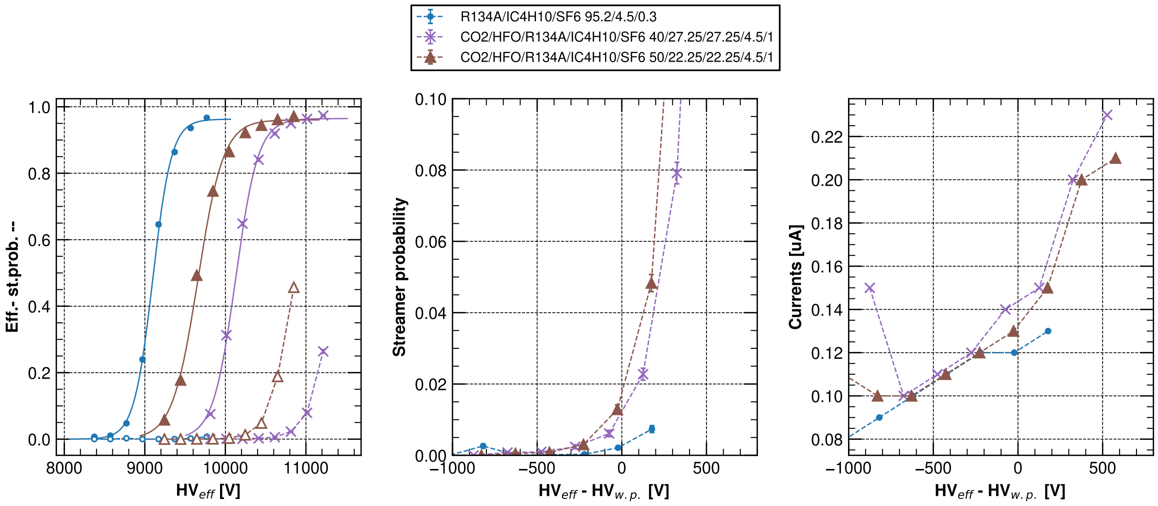

FIGURE 4.37 – R-134/R-1234ze/CO_2 based gas mixtures. a) efficiency and streamer probability curves. b) Streamer probability against relative voltage. c) Currents against relative voltage.

Results, shown in Figure 4.37 and Figure 4.38, indicate that although the working point remains higher than the standard gas mixture, the streamer contamination tends to be lower than HFO only gas mixtures. The mean prompt avalanche and streamer charges show similar values to the standard gas mixture, with the 40% CO_2 gas mixture having slightly higher values for the mean avalanche prompt charge. When evaluating the currents, it can be noticed that the gas mixture with 40% of CO_2 has higher values at the working point, while the mixture with 50% of CO_2 results in a detector current similar to the standard gas mixture. The reason could be explained by the higher mean avalanche prompt charge in the 40% CO_2 gas mixture. No significant differences were observed in terms of cluster size for the two gas mixtures.

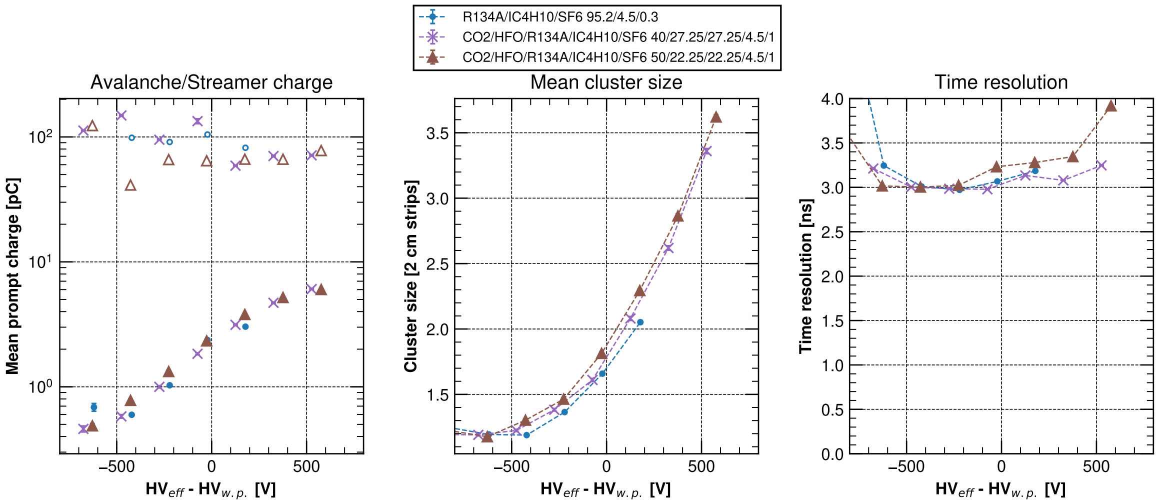

FIGURE 4.38 – R-134/R-1234ze/CO_2 based gas mixtures. a) Mean prompt avalanche charge (filled marker) and mean streamer prompt charge (empty marker) against relative voltage. b) Mean cluster size against relative voltage. c) Time resolution against relative voltage.

In order to better understand the effects of the combination R-1234ze/CO_2, the performance of a gas mixture R-1234ze/CO_2/i-C_4H_{10}-/SF_6 25/69/5/1 was compared with a gas mixture R-134a/CO_2/i-C_4H_{10}-/SF_6 25/69/5/1. The results are shown in Figure 4.39 and Figure 4.40 The working point of the detector is higher for the HFO-based gas mixtures, while for the R-134a/CO_2, the working point is around 1 kV less than the standard gas mixture, suggesting that the shift of working point for 10% variation of R-134a/CO_2 is around 150 V, a value slightly lower than the one estimated in Figure 4.33. The streamer probability at the working point is around 15% for both gas mixtures, much higher than the standard gas mixture. It is worth noting that no significant difference is observed in terms of streamers' contamination between the two CO_2-based gas mixtures. This may indicate that the photon-feedback suppression mechanisms are somehow inhibited with the lack of R-134a or the addition of CO_2, and they do not depend on the electronegativity of the gas components. The currents for the HFO-based gas at the working point are significantly higher than the other two gas mixtures. For both CO_2 gas mixtures, exponential growth for voltages higher than the working point can be observed, indicating the increasing presence of streamers.

Figure 4.40 shows that the mean avalanche prompt charge for the CO_2-based gas mixtures is higher with respect to the standard gas mixture. The increased size of the avalanche charges and the higher streamer fraction could explain the higher currents. It is also interesting to note that the R-134a/CO_2 gas mixture has slightly higher currents with respect to the HFO/CO_2 one. The increased charge size might be due to CO_2 itself, while the presence of HFO instead of R-134a slightly decreases the mean prompt charge. The transverse size

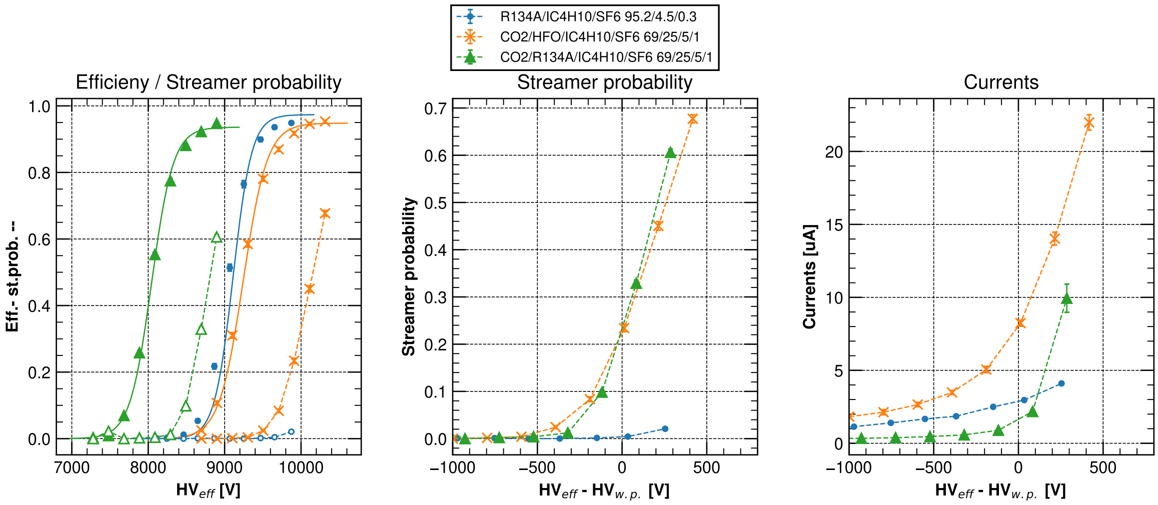

FIGURE 4.39 – Comparison of R-134a/CO_2 versus R-1234ze/CO_2 gas mixtures. From the left: a) efficiency and streamer probability curves for the three selected gas mixtures. b) Streamer probability against relative effective voltage. c) Currents against relative effective voltage.

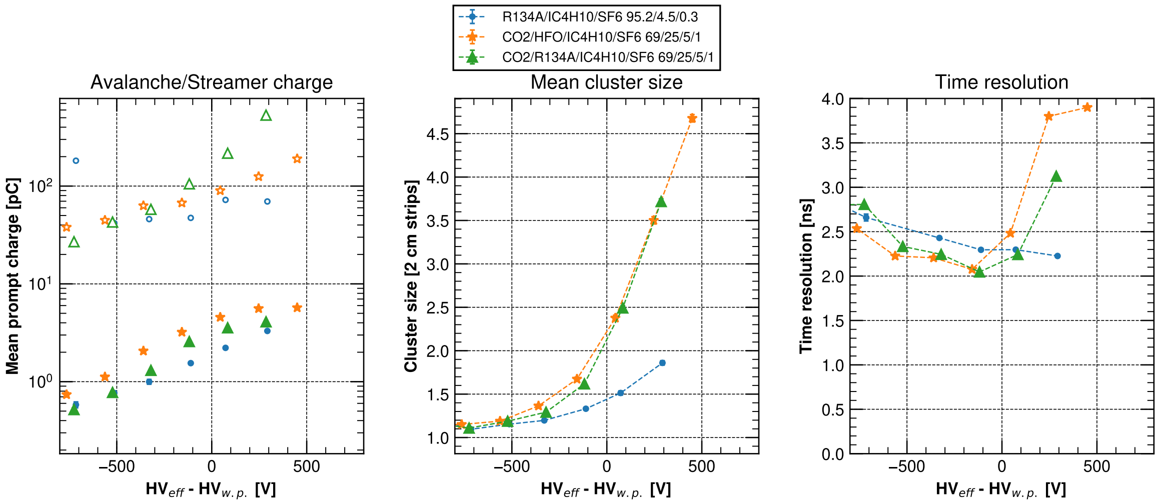

FIGURE 4.40 – Comparison of R-134a/CO_2 versus R-1234ze/CO_2 gas mixtures.From the left: a) Mean prompt avalanche and streamer charges. b) Cluster size against relative voltage. c) Time resolution against relative voltage

of discharge can be observed by looking at the cluster size, which is about 40% higher in the two CO_2-based gas mixtures, with no significant difference between the R-134a and the R-1234ze one. The time resolution for the three gas mixtures is roughly the same, with a mean value of around 2 ns. However, more minor differences may be observed when using a higher precision readout system.

The use of CO_2 in RPCs gas mixtures helps lower the working point but presents some concerns about performance, especially in terms of tracking and rate capability of the detector. Few gas mixtures with R-134/R-1234ze and He were tested. Results are reported in Figure 4.41 and Figure 4.42.

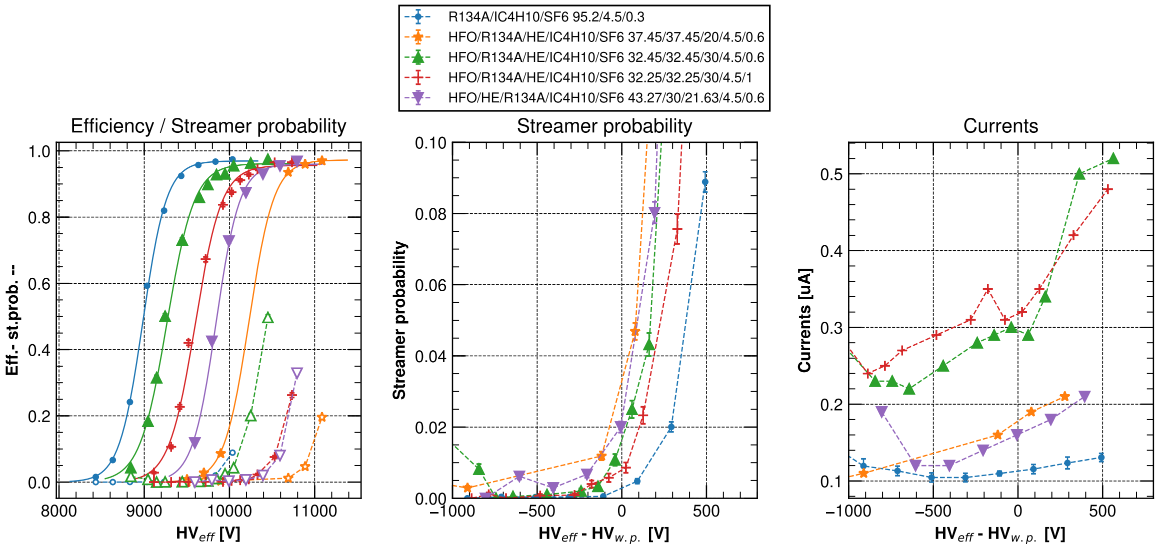

FIGURE 4.41 – He-based gas mixtures. From the left: a) efficiency and streamer probability curves for He and R-134a/R-1234ze based gas mixtures compare with the standard one. b) Streamer probability against relative effective voltage. c) Currents against relative effective voltage.

The working point is lowered using a smaller fraction of He to CO_2-based gas mixtures, although the working points for the tested gas mixtures are a few hundred to 1.6 kV higher with respect to the standard gas mixture. Streamer probability values are similar to the R-134a/R-1234ze/CO_2-based gas mixtures, ranging around a few percentage points at the working point and slightly higher than the standard gas mixtures ones. It is worth noting that the streamer probability is significantly lower than HFO-only gas mixtures, indicating that R-134a may absors enough free electrons to reduce streamers while keeping a lower ionization energy, thus a lower detector working point, when compared to R-1234ze. The currents drawn by the detector at the working point are noticeably higher in the HFO-based gas mixtures. The explanation could be related to the slightly higher avalanche charge and the higher presence of streamers. The charge localization in terms of cluster size shows no significant difference concerning the standard gas mixture, while the time resolution is 0.5-1 ns higher.

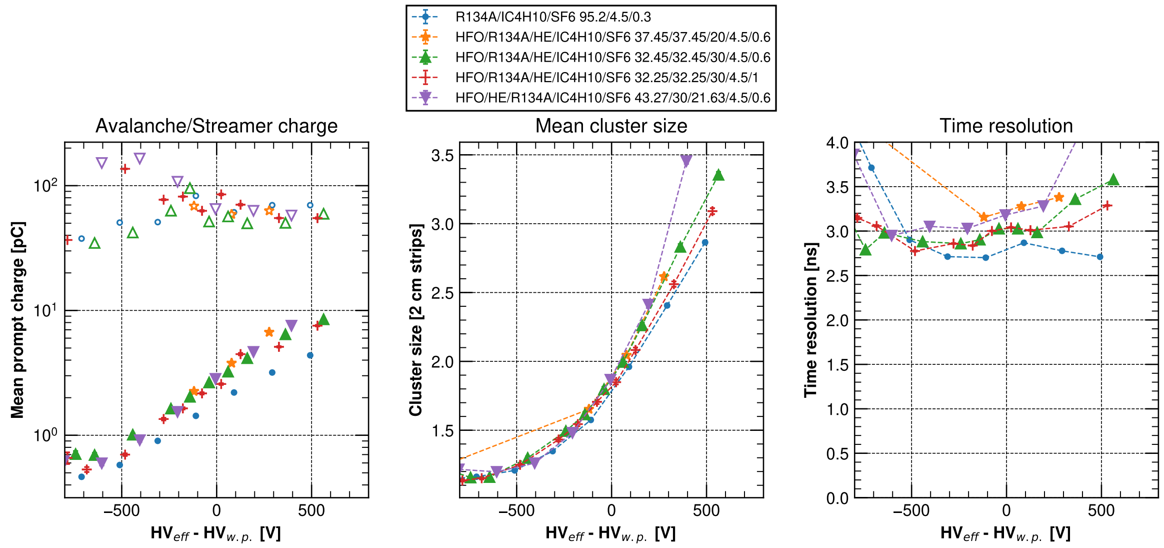

FIGURE 4.42 – He-based gas mixtures. From the left: a) efficiency and streamer probability curves for the three selected gas mixtures. b) Streamer probability against relative effective voltage. c) Currents against relative effective voltage.

Gas	GWP	Lifetime	Boiling point	Toxic
SF6	22800	3200 years	-51 °C	No
C4F8O	12000	>3000 years	1-2 °C	No
CF3I	0.4	<30 days	-22 °C	Yes, intermediate mutagenix toxicity
Novec 5110	<1	15 days	26.8 °C	No
Novec 4710	2100	30 years	-5 °C	No
Amolea 1224yd	<1	20 days	15 °C	No

TABLE 4.4 – Main SF_6 alternative gases and their relevant properties.

4.5.4 Characterization of SF_6 alternative gases

SF_6 is a gas that finds a large employment in medium and high-voltage applications. It is widely used in gas-insulated switch-gear (GIS) systems thanks to its electronegative properties and low boiling point [81]. However, it has the highest known GWP_{100} with a value 22800 times higher than the CO_2 one, and a lifetime of more than 3200 years. Several attempts to substitute SF_6 are currently being made by companies such as ABB™and 3M™. Several eco-friendly replacements were created, such as perfluorinated ketones $C_5F_{10}O$ and fluoronitrile C_4F_7N, commercially known as Novec™ 5110 and Novec™ 4710 respectively [82]. Some other gases that are found to be suitable alternatives include Trifluoroiodomethane (CF_3I) and other perfluorinated ketones (C_4F_8O, $C_6F_{12}O$). An experimental campaign was conducted to characterize the performance of SF_6 alternative gases by using the standard gas mixture as a reference and replacing the SF_6 with the gas to test. For each gas candidate, several different concentrations were tested by keeping the amount of i-C_4H_{10} constant and adjusting the amount of R-134a. In particular, five gases were tested as SF_6 replacement. A table of the tested gases with their main physical and environmental properties is reported in Table 4.4

The performances were evaluated by comparing the foremost parameters at different concentrations of the gas under test. The results, evaluated at working point, are shown in Figure 4.43, while Table 4.5 reports a summary of the obtained numerical values of the foremost parameters.

C_4F_8O was firstly tested. When used in a concentration of 0.3%, the streamer probability appears to be higher than the standard gas mixture. The lowest streamer probability was reached at a concentration of 1.5% of C_4F_8O. However, the net contribution to the GWP of the mixture is considerably higher than the SF_6, making the gas not suitable from the environmental point of view. In addition, the working point at 1.5% is around 400 V higher than the standard gas mixture.

CF_3I was then tested in concentrations ranging from 0.1% to 1.5%. Results show that an amount of 0.3-0.5% could achieve the same capability of the standard gas mixture in terms of streamer probability. However, the mean prompt streamer charge and cluster size result to be higher. The causes of these effects are currently under investigation. Unfortunately, CF_3I has specific mutagenic toxicity, making its usage unsuitable for operation in LHC experiments.

Two gases in the family of Novec produced by the 3M company were tested. Novec™ 5110 is a gas with very low GWP_{100} and zero toxicity. The boiling point of the gas is considerably higher than SF_6 and comparable with the standard laboratory temperature (26.8 °C), making its usage in the gas phase relatively tricky. For this reason, only a few tests were conducted. It was observed that when used in concentrations of 0.3%, the streamer probability is substantially higher than the standard gas mixture. When used in amounts of 2%, the streamer probability decreases, although still higher than the standard gas mixture, but the working point of the gas mixture resulted in a shift of 1 kV, making the gas challenging to be used as an SF_6 alternative.

Novec 4710 has a relatively higher GWP compared to Novec 5110, but it also has a higher boiling point, making the gas suitable to be used in arbitrary concentrations. The gas was tested in concentrations ranging from 0.1% to 0.7%. Results indicate that a tiny amount is required to match the SF_6 performance. In fact, a concentration of 0.1% has comparable streamer probability and pulse charge for avalanche and streamer signals. Concerns arise when Novec 4710 should be used together with gas mixtures with environmental humidity levels. Preliminary reports suggest that it may react with water by forming an amide[16], which can lead to the formation of undesired solid particles.

Finally, a new gas in the family of Hydro-Chloro-Fluoro-Olefins, Amolea™1224yd, was tested. The gas, whose formula is (Z)-CF3-CF=CHCl, was engineered by the AGC chemicals company and has extremely GWP values < 1. The gas also has a low toxicity value, making it suitable for LHC operation. The tested concentration ranged from 0.1% to 0.5%. Results showed that when used in concentrations of 0.3%, the performance in terms of streamer probability, currents, and cluster size matched the standard gas mixture ones, making the gas suitable to be tested in LHC-like conditions.

---

[16] `http://iba-dynamitron-lifesf6free.com/sites/default/files/ressources/SF6-Technical%20Report%202.pdf`

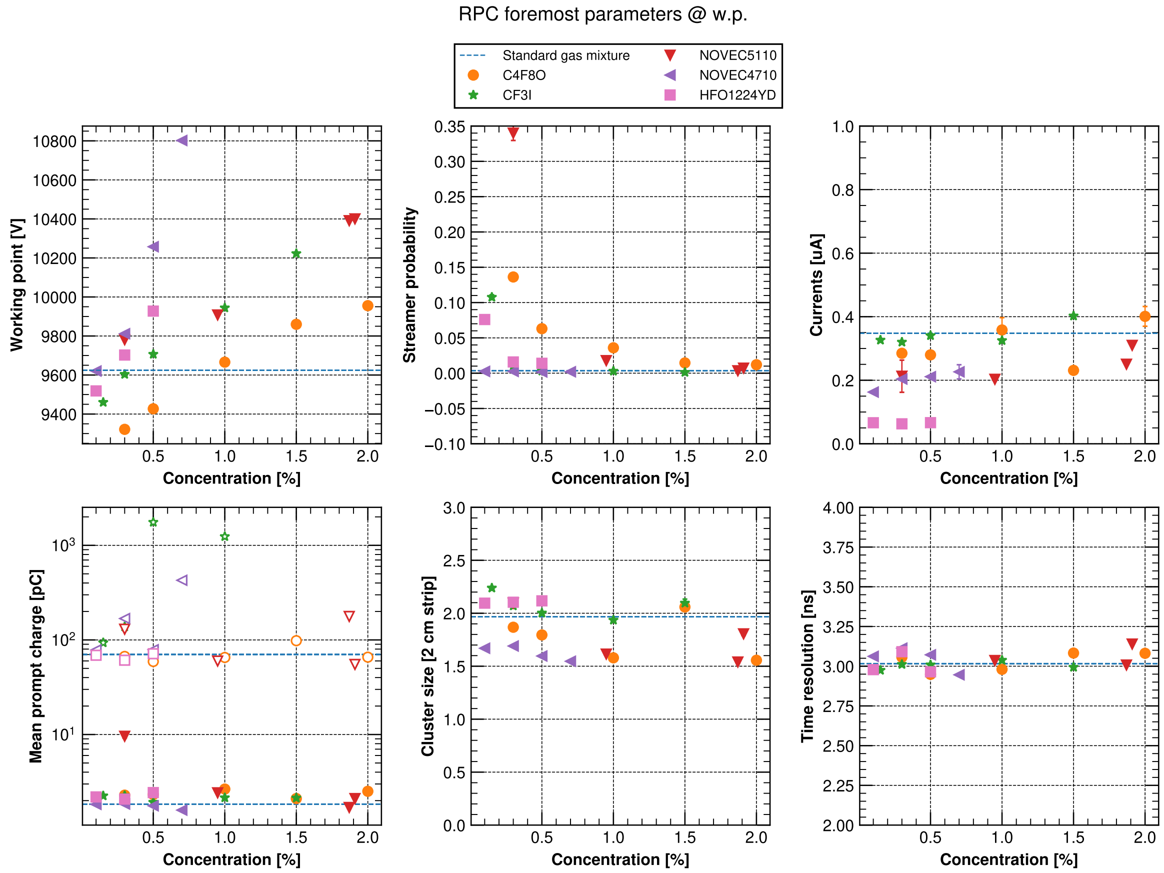

FIGURE 4.43 – Foremost parameters of RPCs operated with SF_6 alternative gases at working point and different concentrations.

Gas	GWP	GWP [moles equivalent]	GWP x concentration	Working Point	Streamer Probability	Currents	Mean avalanche charge	Mean streamer charge	Cluster size	Time resolution
SF6	0.3 %	75690	22710	9624 V	0.4%	0.3 uA	1.8 pC	70.2 pC	2.0 / 2.1 cm	3.0 ns
C4F8O	0.3 %	39270	11780	9322 V	13.6%	0.3 uA	2.3 pC	66.9 pC	1.9 / 2.1 cm	3.1 ns
	0.5 %	39270	19640	9426 V	6.1%	0.3 uA	2.2 pC	58.8 pC	1.8 / 2.1 cm	2.9 ns
	1.0 %	39270	39270	9633 V	2.5%	0.3 uA	2.7 pC	62.2 pC	1.6 / 2.1 cm	3.0 ns
	1.5 %	39270	58910	9860 V	1.8%	0.2 uA	2.2 pC	74.8 pC	2.1 / 2.1 cm	3.1 ns
	2.0 %	39270	78550	9912 V	1.6%	0.4 uA	3.0 pC	61.5 pC	1.6 / 2.1 cm	3.1 ns
NOVEC5110	0.3 %	0	0	9781 V	67.3%	0.3 uA	23.2 pC	249.4 pC	2.1 / 2.1 cm	19.7 ns
	0.9 %	0	0	9908 V	1.8%	0.2 uA	2.4 pC	59.8 pC	1.6 / 2.1 cm	3.0 ns
	1.8 %	0	0	10391 V	0.3%	0.3 uA	1.7 pC	177.2 pC	1.5 / 2.1 cm	3.0 ns
	1.9 %	0	0	10400 V	0.7%	0.3 uA	2.1 pC	55.1 pC	1.8 / 2.1 cm	3.1 ns
NOVEC4710	0.1 %	31020	3100	9621 V	0.2%	0.2 uA	1.8 pC	82.5 pC	1.7 / 2.1 cm	3.1 ns
	0.2 %	31020	6200	9958 V	0.2%	0.2 uA	1.8 pC	101.1 pC	1.7 / 2.1 cm	3.0 ns
	0.3 %	31020	9310	9812 V	0.3%	0.2 uA	1.8 pC	168.4 pC	1.7 / 2.1 cm	3.1 ns
	0.5 %	31020	15510	10258 V	0.2%	0.2 uA	1.8 pC	78.8 pC	1.6 / 2.1 cm	3.1 ns
	0.7 %	31020	21720	10802 V	0.2%	0.2 uA	1.5 pC	783.3 pC	1.5 / 2.1 cm	2.9 ns
CF3I	0.1 %	0	0	9460 V	10.8%	0.3 uA	2.2 pC	93.5 pC	2.2 / 2.1 cm	3.0 ns
	0.3 %	0	0	9604 V	1.0%	0.3 uA	2.3 pC	137.7 pC	2.1 / 2.1 cm	3.0 ns
	0.5 %	0	0	9707 V	0.3%	0.3 uA	1.9 pC	1756.0 pC	2.0 / 2.1 cm	3.0 ns
	1.0 %	0	0	9944 V	0.3%	0.3 uA	2.1 pC	1239.5 pC	1.9 / 2.1 cm	3.0 ns
	1.5 %	0	0	10223 V	0.1%	0.4 uA	2.1 pC	nan pC	2.1 / 2.1 cm	3.0 ns
HFO1224YD	0.1 %	0	0	9519 V	7.6%	0.1 uA	2.2 pC	68.9 pC	2.1 / 2.1 cm	3.0 ns
	0.3 %	0	0	9702 V	1.6%	0.1 uA	2.1 pC	61.0 pC	2.1 / 2.1 cm	3.1 ns
	0.5 %	0	0	9928 V	1.4%	0.1 uA	2.4 pC	71.5 pC	2.1 / 2.1 cm	3.0 ns

TABLE 4.5 – Summary of the performance with SF6 alternative gases. For each gas, the tested concentrations are reported. Note that the GWP is normalized to the normal liters (i.e. the number of moles) to allow a more useful comparison since concentrations in gas mixtures are volumetrics.

4.6 Performance studies of RPC operated with alternative gas mixtures in LHC-like conditions

The RPC set up described in 4.2.2 was operated with several gas mixtures at GIF++ during muon beam time, allowing to characterize the performance of RPCs under LHC-like conditions, thanks to the beam itself and the gamma background of the irradiator. Several HV scans were performed operating RPCs with a fixed gas mixture but under different irradiation conditions. For each HV point, a rate scan was performed using an acquisition window of a few milliseconds and counting the number of peaks for each strip. The performance of the gas mixture under irradiation was compared with the standard gas mixture by interpolating the gamma counting rates, currents, efficiency, cluster size, and time resolution at the working point. The foremost parameters of each gas mixture were first evaluated with muon beam and Source Off condition. Later, depending on the performance of the gas mixture, the parameters were evaluated with Source On and different filters. The tests were conducted with background rates up to 500-600 Hz/cm^2, corresponding to the foreseen background hit rates for most of the current 2 mm RPCs installed at the ATLAS and CMS experiments with a safety factor 1-3 [83, 84].

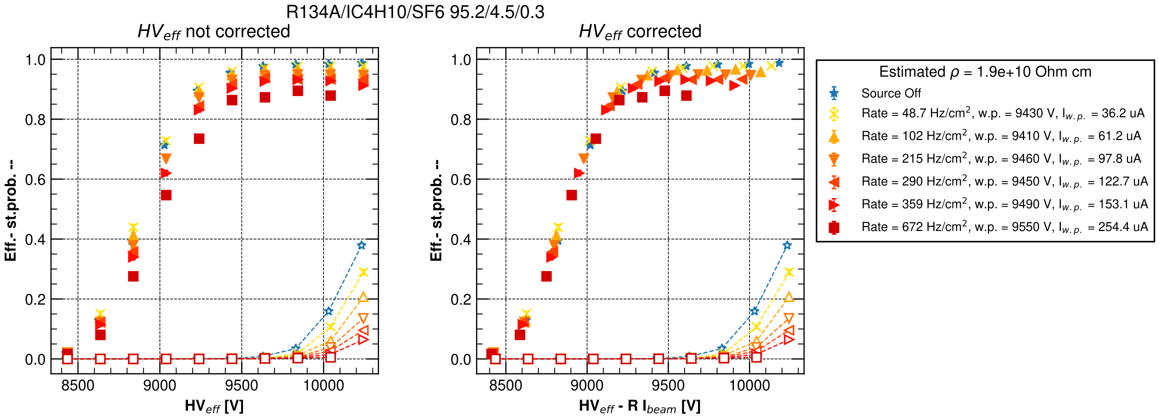

FIGURE 4.44 – Characterization of the standard gas mixture with muon beam and gamma source. On the left: efficiency and streamer probability curves for the standard gas mixture with source off and source on with different filters. On the right: the same efficiency curves plotted against the effective voltage within the gas gap.

Figure 4.44 shows efficiency curves of an RPCs operated with the standard gas mixture under background conditions against the effective voltage corrected for temperature and pressure. At higher intensities of the background radiation, the efficiency curves shift to higher voltages. This known effect is due to the drop of effective voltage within the gas gap due to the resistivity of the electrode. The effective voltage of the gas gap can be estimated if the resistivity of the electrodes is known according to Formula 4.18. It should also be noted that a rough estimation of the resistivity can be extracted from the efficiency curves by rewriting Formula 4.18 as

$$HV_{gas} - HV_{applied} = R_{electrode} * I_{gap} \tag{4.19}$$

And solving the minimization problem for R by imposing $HV_{gas} - HV_{applied} = 0$. A simple estimate by manual tuning of R gives a resistivity value of 1.9 10^{10} Ω cm, in agreement with the resistivity value of 1.93 10^{10} Ω cm measured by means of Argon scans. From the right plot of Figure 4.44 it can be observed that the correction holds well for efficiency values up to the knee. Once reaching maximum efficiency values, the efficiency values for different background rates do not overlap perfectly. The reason for this effect is under investigation. One possible explanation could be related to the internal analysis mechanism for which the baseline of the waveform tends to be overestimated due to the presence of gamma signals in the acquisition window.

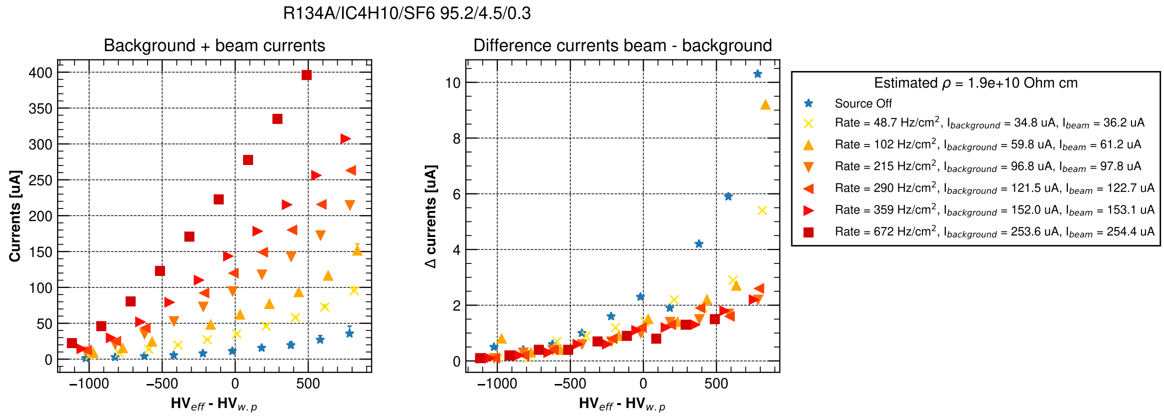

FIGURE 4.45 – Characterization of the standard gas mixture with muon beam and gamma source. On the left: Currents against relative voltage for source off and different background rates. On the right: difference between the currents measured in the presence of beam and the background only.

Figure 4.45 reports the currents measured for each HV point with source off and different source on filters. The contribution of the muon beam to the current is noticeable for low irradiation conditions, as shown in Figure 4.45b. When increasing the background rate, the currents induced by the muon particles start to be neglectable compared to the ones produced by the electrons produced by gamma interactions with the cathode. This phenomenon can be explained in terms of impinging area if we consider that most of the beam is focused on a 10 x 10 cm^2 square while the gamma source irradiates all the 70 x 100 cm^2 detector surface.

The cluster size and time resolution for different rates are shown in Figure 4.46. No significant differences can be noticed in the presence of gamma background, indicating that the dynamics of the charge development depends only on the muon particle locally developing an avalanche signal.

4.6.1 Characterization of He and CO_2 based gas mixtures

He and CO_2 were added to the standard gas mixture in amounts of 30% to characterize better the performance of the standard gas mixture with a reduced amount of R-134a. The SF_6 concentration was adjusted to 1% to stabilize the performance and suppress streamer contamination. Figure 4.47 shows the performance of the He and CO_2 gas mixtures compared with the standard one against the rate.

It can be observed that the CO_2-based gas mixtures have roughly the same working point as the standard gas mixture due to the increased amount of SF_6 with respect to the gas

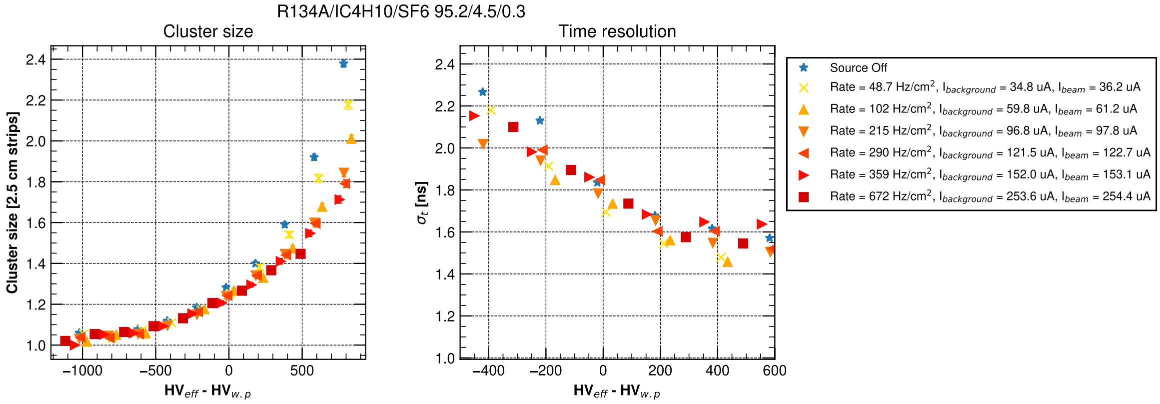

FIGURE 4.46 – Characterization of the standard gas mixture with muon beam and gamma source. On the left: Cluster size against relative voltage for source off and different source on filters. On the right, the time resolution against the relative voltage for the same irradiation conditions.

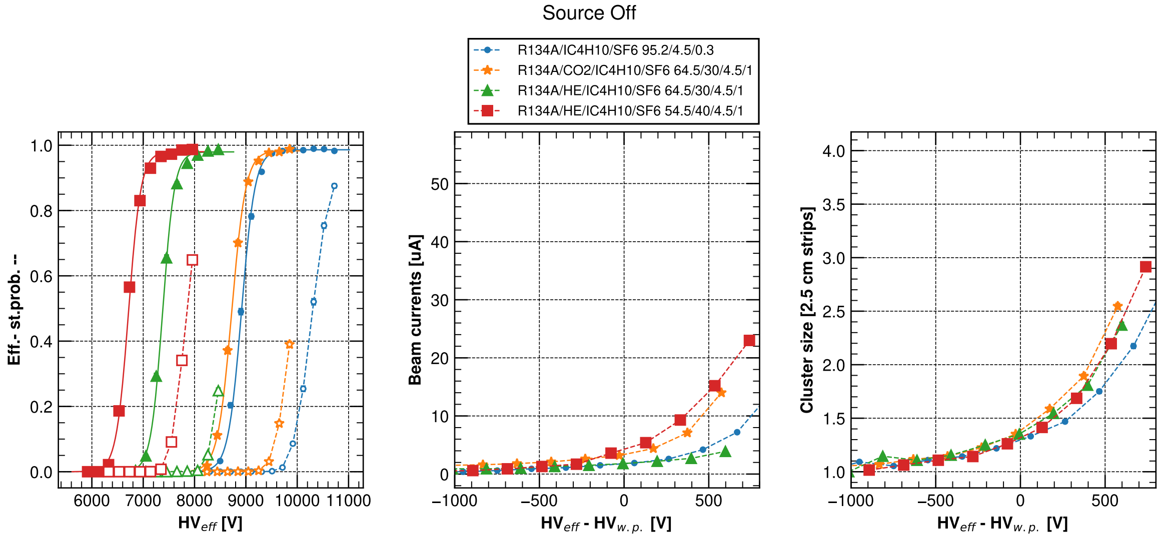

FIGURE 4.47 – Characterization of R-134a with the addition CO_2, He with muon beam and gamma source. From the left: a) Efficiency and streamer probability curves with muon beam and source off conditions. b) Currents recorded during beam spill against the voltage relative to the working point. c) Mean cluster size against the voltage relative to the working point

mixtures. The He-based gas mixtures instead show a significant decrease of working point, reducing to 2 to 3 kV, respectively for 30% and 40% of He.

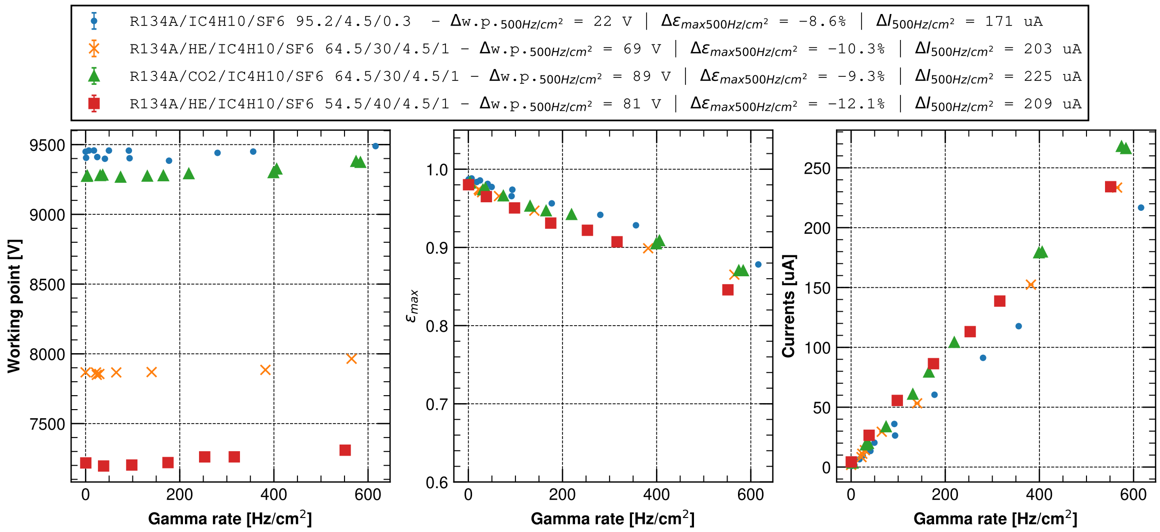

FIGURE 4.48 – Characterization of R-134a with the addition CO_2, He with muon beam and gamma source. From the left: a) Working point at different background conditions. b) Maximum reached efficiency at different background conditions. c) Drawn currents versus gamma rate

The three different tested gas mixtures show a 70-90 V drop when evaluated at a gamma hit rate of 500 Hz/cm^2 (Figure 4.48). The drop of efficiency ranges from 10-12%, which is slightly higher than the standard gas mixture drop. The recorded currents seem to be around 20% higher than the standard gas mixture. Figure 4.47 shows the cluster size at different gamma rates. No significant differences can be observed at different rates and between different gas mixtures. The standard and the 40% He gas mixture show a stable performance against the rate when looking at the time resolution. The gas mixtures with 30% of He and 30% of CO_2 instead show an increase of about 2 ns at 500 Hz/cm^2 of gamma hit rate. The reasons for the phenomena are currently under investigation.

4.6.2 Characterization of R-1234ze based gas mixtures

Performance with gas mixtures based on R-1234ze and R-134a/R-1234ze were characterized and compared with the standard gas mixture. In particular, the gas mixture CO_2/R-1234ze/R-134a/i-C_4H_{10}/SF_6 50/22.25/22.25/4.5/1 was initially tested and compared with a similar gas mixture CO_2/R-1234ze/i-C_4H_{10}/SF_6 69/25/5/1, having a similar amount of R-1234ze but with R-134a replaced with CO_2. The foremost parameters, evaluated at the working point for different background rates, are shown in Figure 4.50. The working point for the R-134a/R-1234ze gas mixture is around 1 kV higher than the standard one. In contrast, the R-1234ze only gas mixture has a shift of 300 V. The currents for the R-1234ze only gas mixture evaluated at 500 Hz/cm^2 appear to be 80% higher than the standard gas mixture.

The R-1234ze/R-134a gas mixture increases the currents by around 55% with respect to the standard gas mixture. Consequently, the drop in efficiency is also reflected with similar

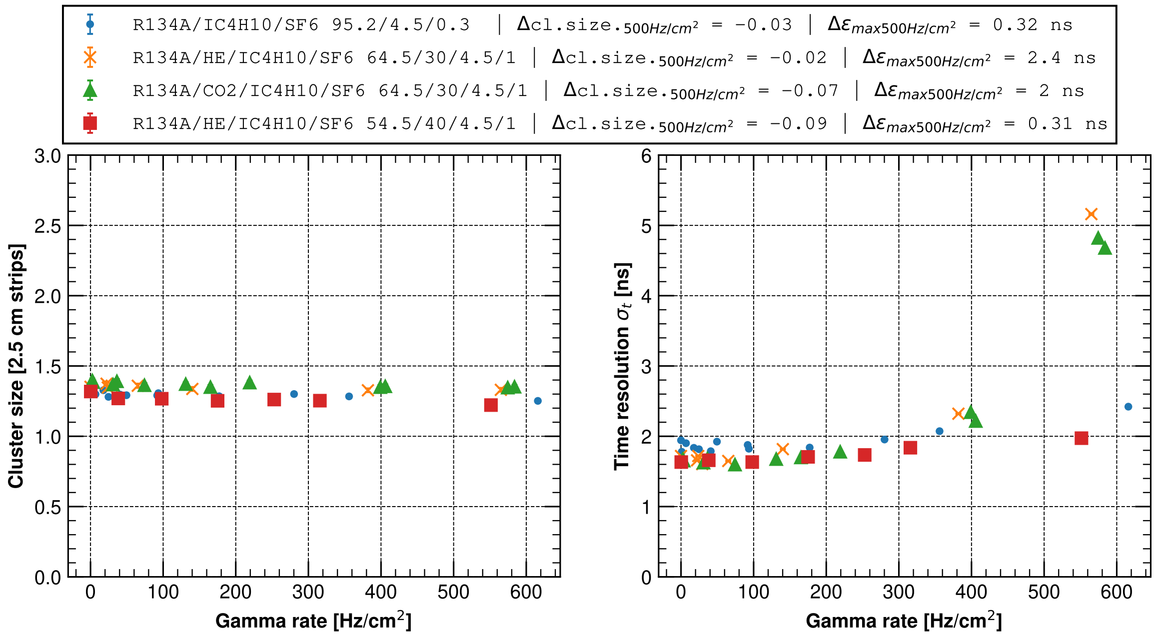

FIGURE 4.49 – Characterization of R-134a-based gas mixtures with the addition CO_2 or He, with muon beam and gamma source. On the left: mean cluster size evaluated at working point for different gamma rates and gas mixtures. On the right: time resolution of the different gas mixtures evaluated at working point for different gas mixtures.

percentages when comparing the two gas R-1234ze mixtures with the standard one. The results may suggest that some amount of R-134a in an R-1234ze/CO_2 gas mixture helps minimize the efficiency drop, enhancing the trigger performance and reducing possible currents-related aging effects.

Figure 4.51 shows instead the cluster size and time resolution for the three gas mixtures. No significant differences can be observed, indicating good time trigger and space tracking capabilities for the tested gas mixtures.

A gas mixture with R-134a/R-1234ze and He was tested and compared with the R-134a/R-1234ze/CO_2 gas mixture. The amount of SF_6 in the He gas mixture was adjusted from 1% to 0.6% to reduce the working point shift.

The results reported in Figure 4.52 show a shift of 200 V for the He gas mixture and a similar efficiency drop to the R134a/R-1234ze/CO_2 gas mixture. The currents evaluated at the working point are slightly lower than the CO_2-based gas mixture but still 48% higher than the standard one.

Figure 4.53 shows no significant differences in terms of cluster size, while the time resolution for the He-based gas mixture shows an increasing trend: evaluated at 500 Hz/cm^2, the time resolution increases by 1.8 ns, which is significantly higher with the 0.5 and 0.2 ns increases of the standard and CO_2-based gas mixture respectively.

The tested HFO-based gas mixtures show an overall good trigger performance at low background rates. When the background conditions start to be similar to the HL-LHC expected ones, the tested gas mixtures show higher currents and a higher efficiency drop with respect

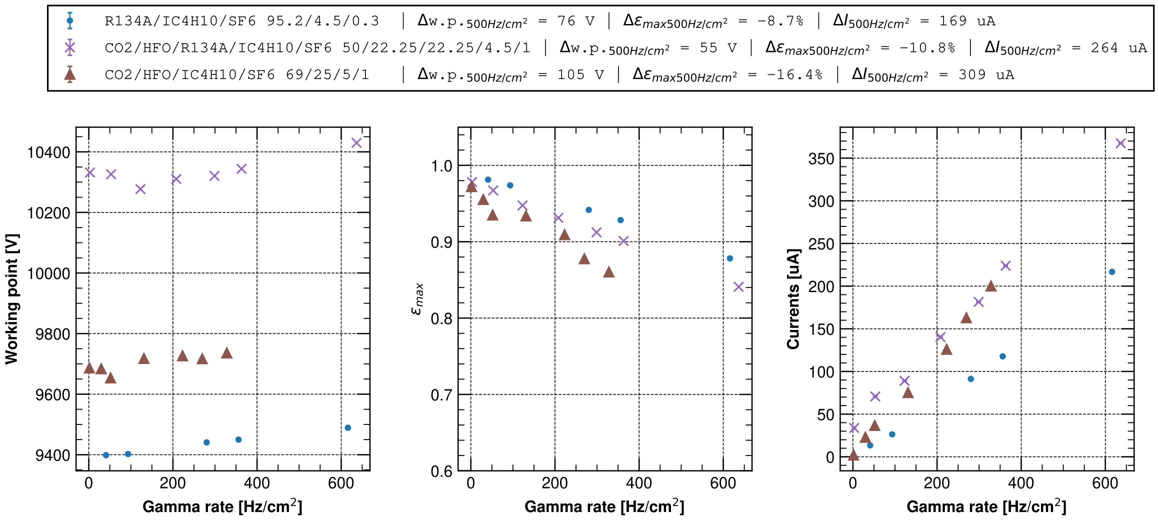

FIGURE 4.50 – Characterization of R-1234ze and CO_2 based gas mixtures. From the left: a) Working point at different background conditions. b) Maximum reached efficiency at different background conditions. c) Drawn currents versus gamma rate.

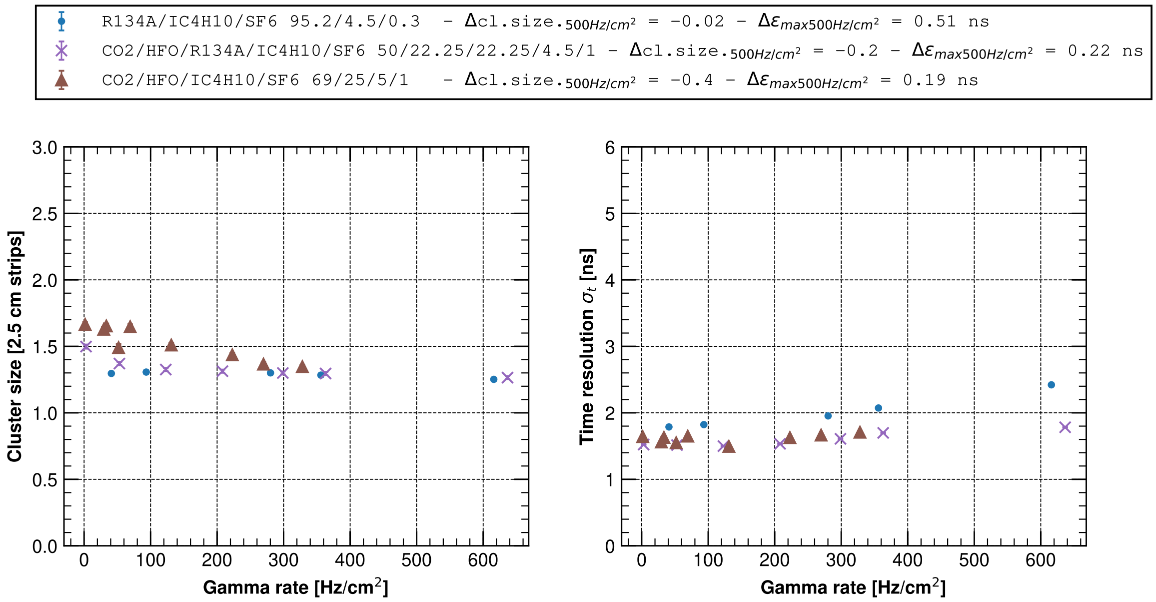

FIGURE 4.51 – Characterization of R-1234ze and CO_2 based gas mixtures. On the left: Cluster size against relative voltage for source off and different source on filters. On the right, the time resolution against the relative voltage for the same irradiation conditions.

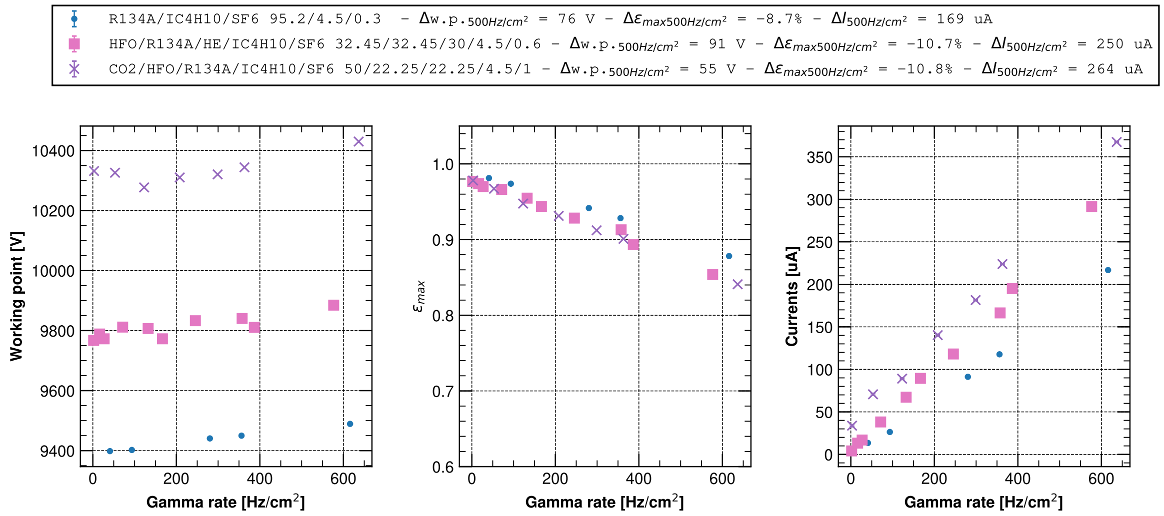

FIGURE 4.52 – Comparison of R-1234ze/CO_2 with R-1234ze/He gas mixtures. From the left: a) Working point at different background conditions. b) Maximum reached efficiency at different background conditions. c) Drawn currents versus gamma rate.

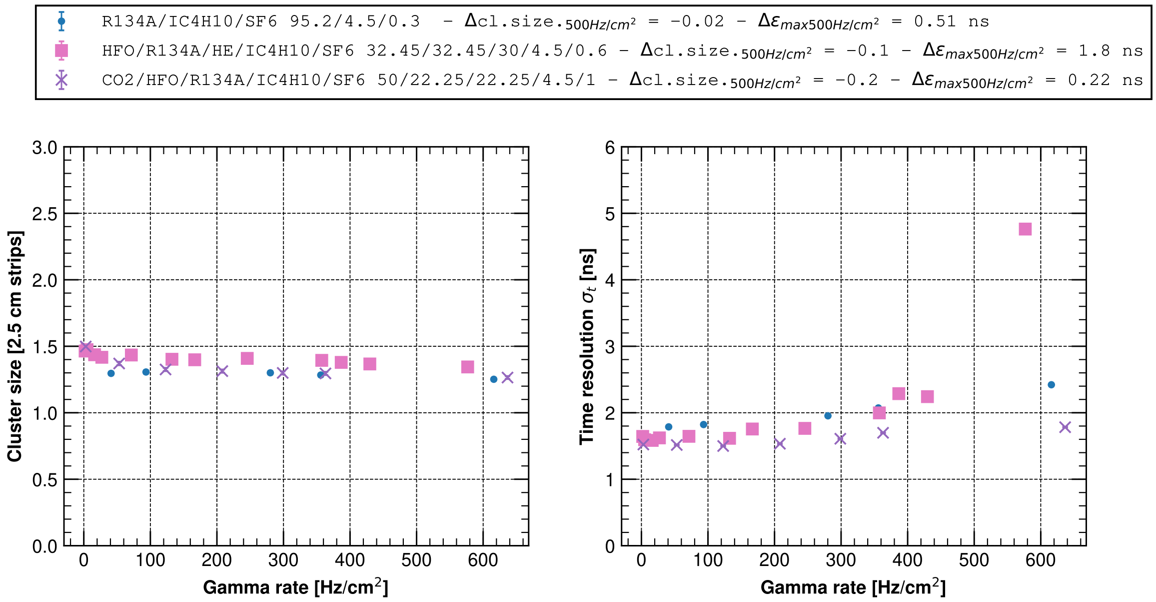

FIGURE 4.53 – Comparison of R-1234ze/CO_2 with R-1234ze/He gas mixtures. On the left: Cluster size against relative voltage for source off and different source on filters. On the right, the time resolution against the relative voltage for the same irradiation conditions.

to the standard gas mixture. Also, the tested gas HFO-based gas mixtures have a higher working point when compared to the standard one. The long-term performance of the studied gas mixtures is currently being investigated. It is worth mentioning that an increased applied electric field together with an increased current may also induce higher electrical stress between the graphite coatings and the insulation layer separating the electrodes from the detector's frame. Both the R-134a/He and R-134a/R-1234ze/He gas mixture seems to perform slightly better than the equivalent CO_2 gas mixtures, except for the time resolution. However, the usage of He in LHC caverns is still being investigated, making the He-based gas mixtures somewhat less appealing from the LHC operation point of view.

4.6.3 Characterization of Novec™ 4710 gas mixtures

Novec 4710 was tested as an SF_6 alternative in the standard gas mixture with concentrations of 0.1% and 0.3%. Figure 4.54 shows the efficiencies, streamer probability, currents and cluster size value for muon beam without gamma background.

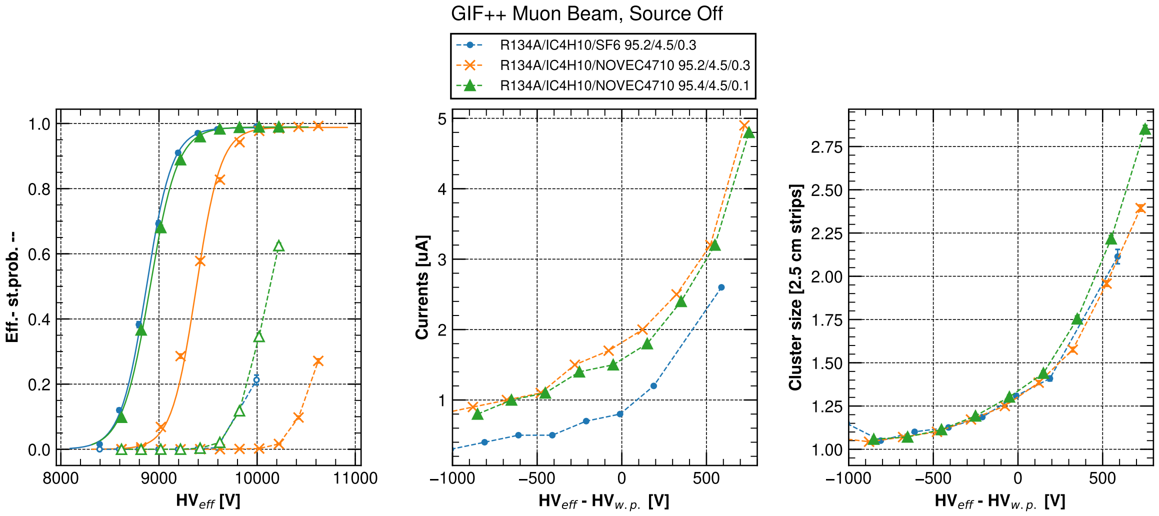

FIGURE 4.54 – Characterization of Novec™ 4710-based gas mixtures with muon beam and source off. From the left: a) Efficiency and streamer probability curves with muon beam and source off conditions. b) Currents recorded during beam spill against the voltage relative to the working point. c) Mean cluster size against the voltage relative to the working point

First, the performances were evaluated with muon beam and without gamma source. When used in 0.3% the working point is 500 V higher than the standard gas mixture, indicating an extremely high electron attachment coefficient for the gas. To reach the same working point as the standard gas mixture, only 0.1% of Novec™ 4710 is necessary. Although the efficiency and streamer probability values are similar to the standard gas mixture, the currents are almost two times higher for the Novec™ 4710 based gas mixtures. Reasons are currently being investigated. One hypothesis could be related to the bigger prompt charge as shown in Figure 4.55.

However, the increased avalanche prompt charge was observed only for the gas mixture with 0.3% of Novec™ 4710, while no apparent differences were found for the 0.1% one. One other hypothesis involves the operating conditions in terms of beam quality, related to the presence of pions in the muon beam, and the beam intensity, related to the number of

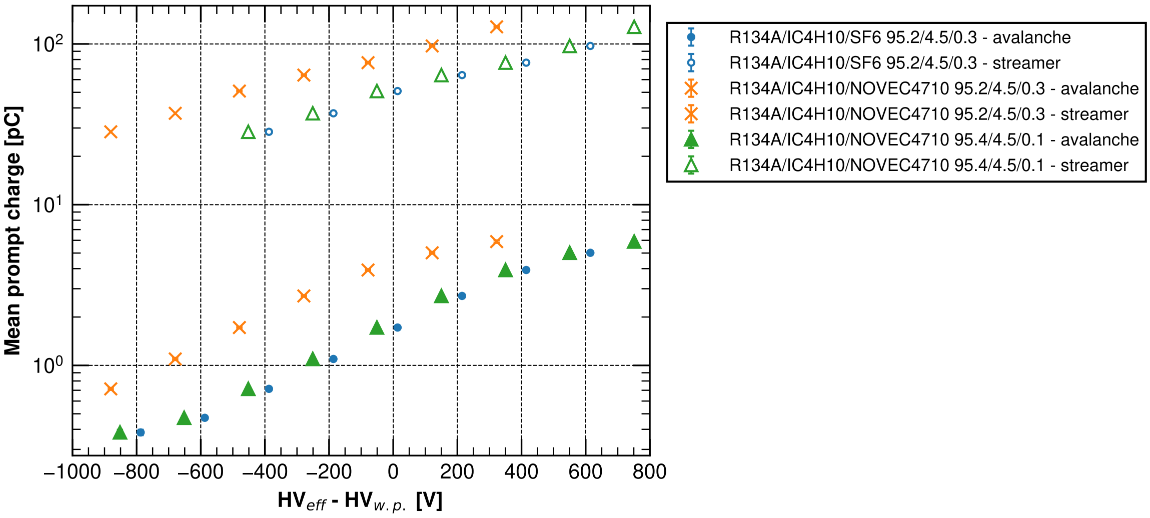

FIGURE 4.55 – Mean avalanche and streamer prompt charge for Novec™ 4710-based gas mixtures in comparison with the standard gas mixture, plotted against the applied HV substracted by the working point.

ionizing particles per spill. No significant differences were instead observed for the cluster size.

When operated under the presence of gamma background as in Figure 4.56, the shift in working point at 500 Hz/cm^2 for the mixture is 0.1% of Novec™ 4710 is equal to the standard gas mixture's one. The increase of currents at 500 Hz/cm^2 in the gas mixture with 0.3% is about 18% higher than the increase of the standard gas mixture, in agreement with the observed higher currents and higher prompt charge with muon beam only. Currents are slightly smaller for the gas mixture with 0.1% compared to the 0.3% one. The reason could be due to the increasing space charge effects that become more important than the electron attachment coefficient of the gas when with a sufficiently high electric field in the gas. This could suggest that the performances of the gas mixture with 0.3% of Novec 4710 are somewhat "saturated", and less amount is required to operate the detector in optimal conditions. No significant differences from the standard gas mixture were observed in terms of cluster size and time resolution for the Novec 4710-based gas mixtures.

4.6.4 Characterization of Amolea™ 1224yd gas mixtures

The Amolea™ 1224yd HCFO gas was tested as a replacement for SF_6 and i-C_4H_{10}. When replaced to SF_6, amounts of 0.3% and 0.5% were tested. When used in place of i-C_4H_{10}, the addition of CO_2 or He was required to lower the working point. The efficiency curves shown in Figure 4.57 at Source Off for 0.3% of Amolea™ 1224yd almost match the standard gas mixture, indicating that gas may have the same electronegativity of SF_6. However, the streamer contamination appears to be higher for the Amolea gas mixtures, both when used in 0.3% and in 0.5%.

When the standard-like gas mixtures with 0.3% and 0.5% of Amolea™ 1224yd were operated under gamma background radiation as shown in Figure 4.58 and Figure 4.59, the gas mixture with 0.3% of Amolea showed a shift in the working point of around 50 V. In comparison, the 0.5% showed a shift of 250 V, suggesting that the change of 0.1% Amolea™ 1224yd

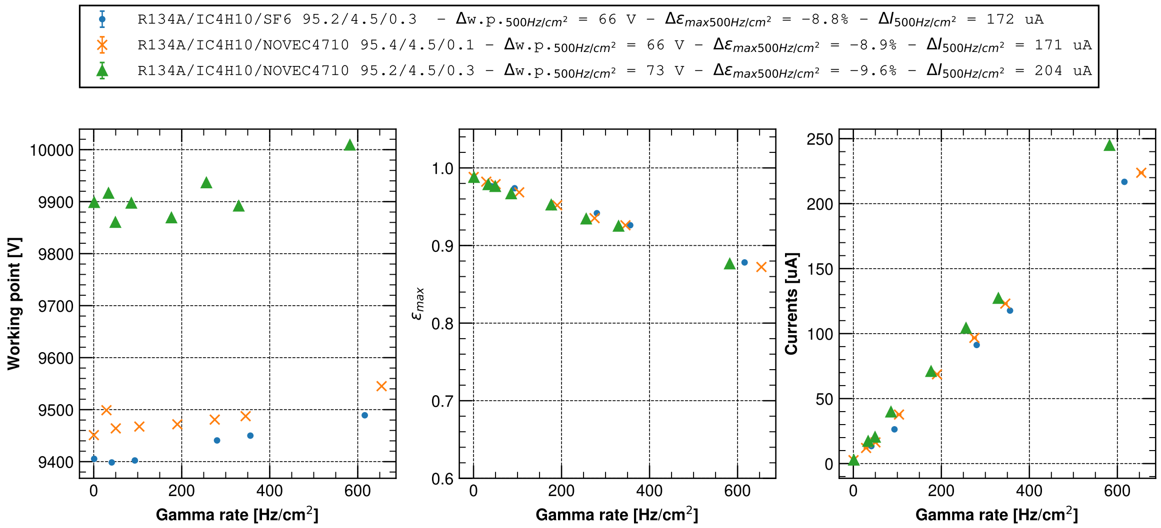

FIGURE 4.56 – From the left: a) Working point at different background conditions. b) Maximum reached efficiency at different background conditions. c) Drawn currents versus gamma rate.

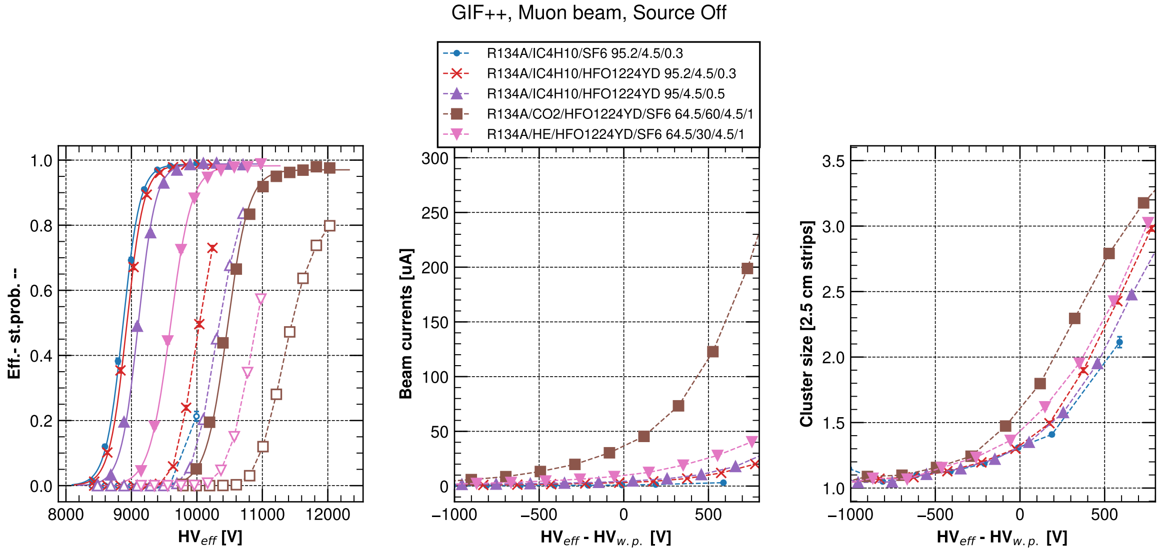

FIGURE 4.57 – Characterization of Amolea™ 1224yd-based gas mixtures with muon beam and source off. a) Efficiency and streamer probability curves with muon beam and source off conditions. b) Currents recorded during beam spill against the voltage relative to the working point. c) Mean cluster size against the voltage relative to the working point

in the gas mixture moves the working point of the detector of 100 V. No main differences in terms of efficiency drop, currents, cluster size and time resolution were observed, possibly indicating Amolea™ 1224yd as a good SF_6 alternative.

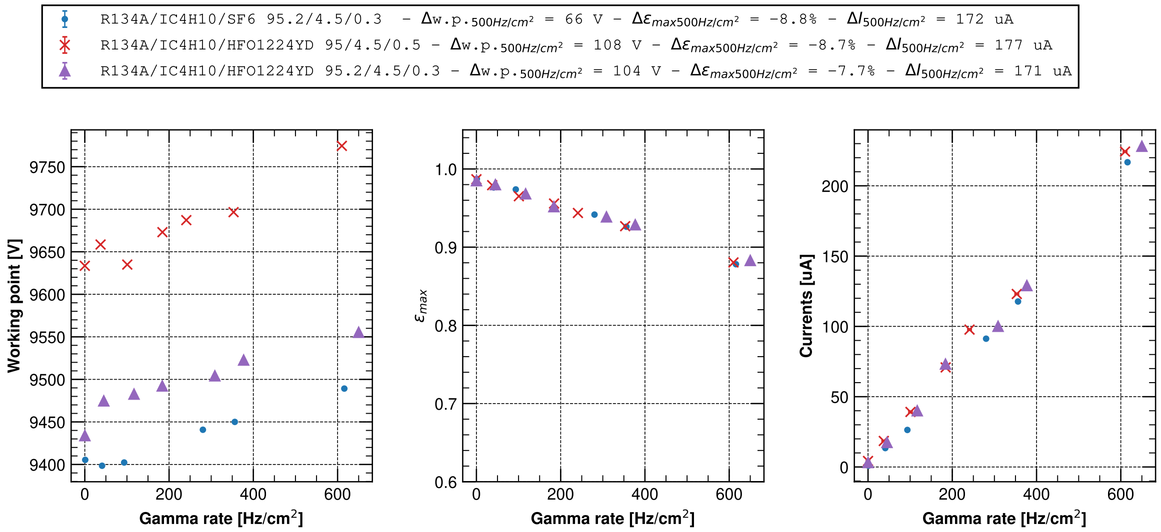

FIGURE 4.58 – Characterization of Amolea™ 1224yd-based gas mixtures in the presence of muon beam and gamma source. a) Working point at different background conditions. b) Maximum reached efficiency at different background conditions. c) Drawn currents versus gamma rate.

The gas was also tested as a quencher by adding it in place of i-C_4H_{10} in the standard gas mixture. However, the working point of the gas mixture was higher than 12 kV. For this reason, two gas mixtures, one with the addition of CO_2 and one with the addition of He, were tested. The amount of He added was such that the resulting gas mixture could be compared with the same gas mixture whose results were reported in Figure 4.48. The CO_2/Amolea™ 1224yd gas mixture could not be operated at rates higher than 350 Hz/cm^2 due to the elevated value of the currents. The performances are then extrapolated at 500 Hz/cm^2 using a cubic polynomial fit.

Preliminary results reported in Figure 4.60 shows a higher working point and suggest that Amolea 1224yd may not be a good substitute of i-C_4H_{10}: the voltage drop is around 2 times higher, the efficiency drop shows a significant loss for rates higher than 350 Hz/cm^2, and currents increase of factor two. It can be clearly seen that when comparing the two gas mixtures with He, the one with i-C_4H_{10} shows much similar performance compared to the Amolea™ 1224yd-based one.

No significant changes in cluster size and time resolution were instead observed for the Amolea based gas mixtures.

Table 4.6 reports a summary of the tested gas mixtures in LHC-like conditions. The foremost parameters are reported at their nominal values with source off, together with their change when the RPCs are operated at a background hit rate of 500 Hz/cm^2.

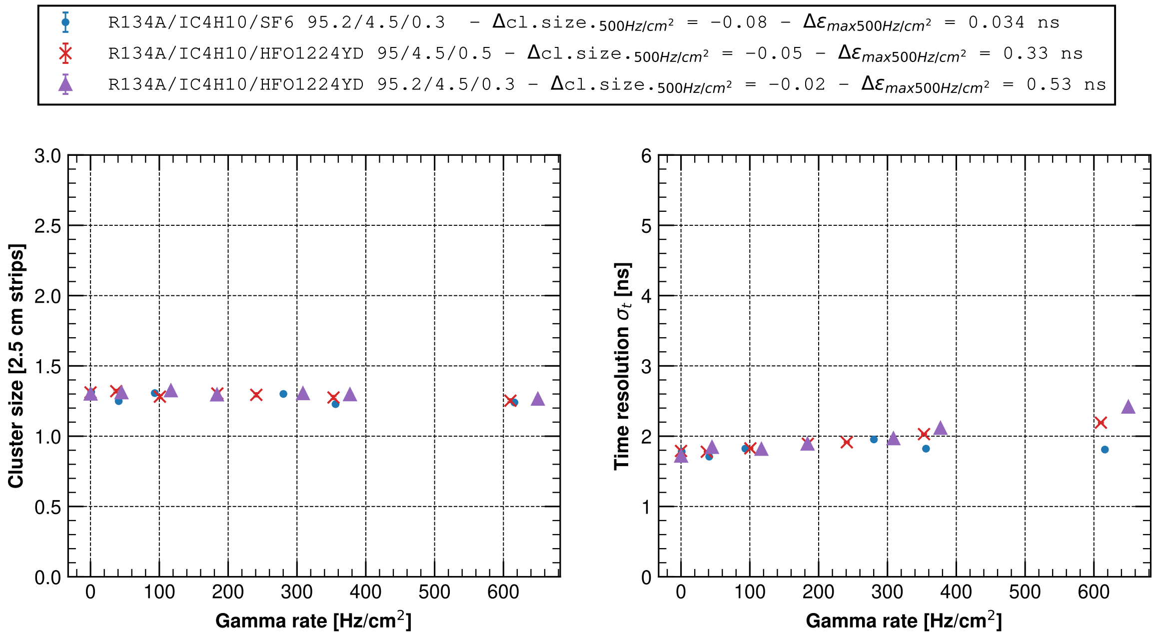

FIGURE 4.59 – Characterization of Amolea™ 1224yd-based gas mixtures in the presence of muon beam and gamma source. From the left: Cluster size against relative voltage for source off and different source on filters. On the right, the time resolution against the relative voltage for the same irradiation conditions.

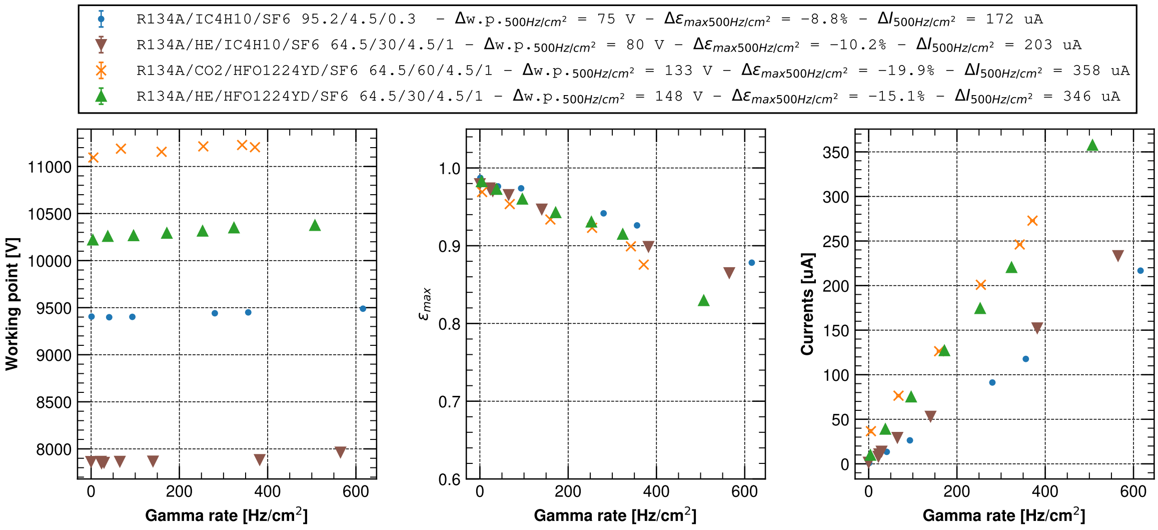

FIGURE 4.60 – Characterization of Amolea™ 1224yd as a quencher in place of i-C_4H_{10}. a) Working point at different background conditions. b) Maximum reached efficiency at different background conditions. c) Drawn currents versus gamma rate.

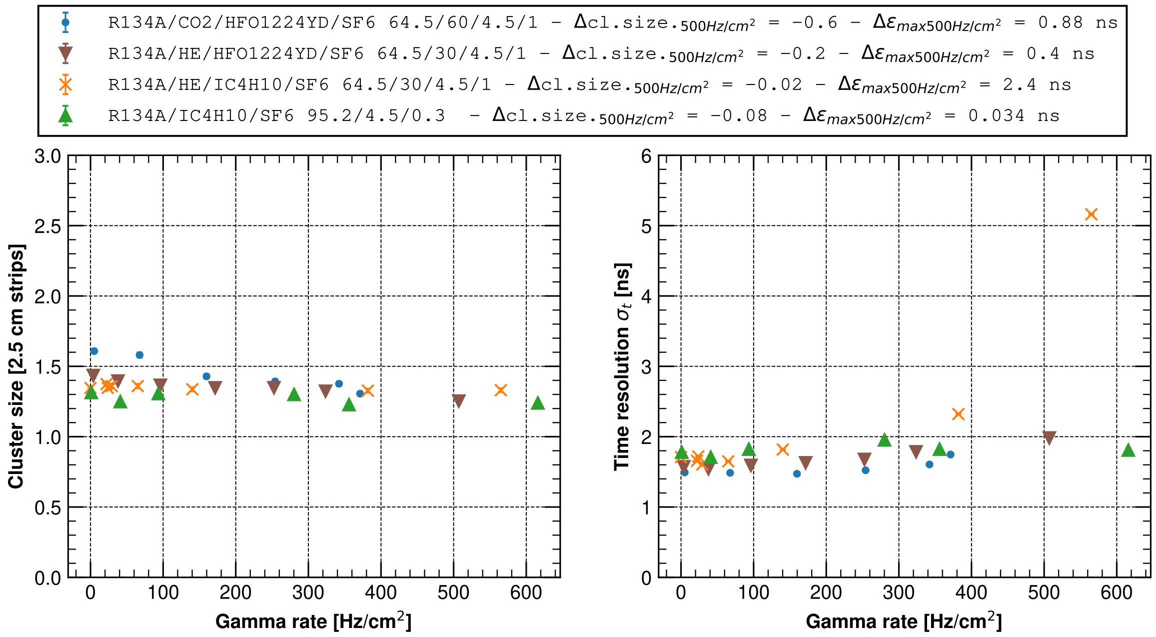

FIGURE 4.61 – Characterization of Amolea™ 1224yd as a quencher in place of i-C_4H_{10}. From the left: Cluster size against relative voltage for source off and different source on filters. On the right, the time resolution against the relative voltage for the same irradiation conditions.

	GWP		Working point		Maximum efficiency		Currents		Cluster size		Time resolution	
Standard gas mixture												
R134A/IC4H10/SF6 95.2/4.5/0.3	3380		9410 V	+79 V	98.7%	-8.9%	0.9 uA	+182 uA	1.3 / 2.5 cm	-0.1 / 2.5 cm	1.8 ns	+0.5 ns
Standard gas mixture + CO2/He												
R134A/HE/IC4H10/SF6 64.5/30/4.5/1	2900	(-14%)	7860 V	+61 V	98.0%	-10.3%	1.8 uA	+202 uA	1.4 / 2.5 cm	-0.0 / 2.5 cm	1.7 ns	+2.1 ns
R134A/CO2/IC4H10/SF6 65.2/30/4.5/0.3	2390	(-29%)	8930 V	+72 V	98.0%	-8.4%	11.8 uA	+185 uA	1.3 / 2.5 cm	-0.1 / 2.5 cm	1.7 ns	+0.2 ns
R134A/CO2/IC4H10/SF6 64.5/30/4.5/1	2900	(-14%)	9270 V	+69 V	98.3%	-9.4%	3.5 uA	+223 uA	1.4 / 2.5 cm	-0.0 / 2.5 cm	1.7 ns	+1.7 ns
R-1234ze-based gas mixtures												
CO2/HFO/IC4H10/SF6 69/25/5/1	760	(-78%)	9690 V	+42 V	97.2%	-32.6%	2.0 uA	+387 uA	1.7 / 2.5 cm	-0.4 / 2.5 cm	1.6 ns	+0.1 ns
CO2/HFO/R134A/IC4H10/SF6 50/22.25/22.25/4.5/1	1500	(-56%)	10330 V	+67 V	97.8%	-10.5%	33.8 uA	+261 uA	1.5 / 2.5 cm	-0.2 / 2.5 cm	1.5 ns	+0.3 ns
HFO/R134A/HE/IC4H10/SF6 32.45/32.45/30/4.5/0.6	1540	(-54%)	9780 V	+74 V	97.9%	-10.3%	4.5 uA	+240 uA	1.5 / 2.5 cm	-0.1 / 2.5 cm	1.6 ns	+1.7 ns
SF6 alternatives												
R134A/IC4H10/NOVEC4710 95.4/4.5/0.1	3190	(-6%)	9460 V	+47 V	98.9%	-8.9%	2.6 uA	+173 uA	1.3 / 2.5 cm	-0.0 / 2.5 cm	1.8 ns	+0.4 ns
R134A/IC4H10/NOVEC4710 95.2/4.5/0.3	3250	(-4%)	9900 V	+71 V	98.8%	-9.4%	2.7 uA	+198 uA	1.3 / 2.5 cm	-0.0 / 2.5 cm	1.8 ns	+0.4 ns
R134A/IC4H10/HFO1224YD 95.2/4.5/0.3	3160	(-7%)	9450 V	+81 V	98.6%	-7.6%	3.3 uA	+165 uA	1.3 / 2.5 cm	-0.0 / 2.5 cm	1.8 ns	+0.5 ns
R134A/IC4H10/HFO1224YD 95/4.5/0.5	3150	(-7%)	9640 V	+100 V	98.8%	-8.5%	4.4 uA	+173 uA	1.3 / 2.5 cm	-0.0 / 2.5 cm	1.8 ns	+0.4 ns
i-C4H10 alternatives												
R134A/HE/HFO1224YD/SF6 64.5/30/4.5/1	2900	(-14%)	10220 V	+155 V	98.3%	-14.8%	9.7 uA	+342 uA	1.4 / 2.5 cm	-0.2 / 2.5 cm	1.6 ns	+0.4 ns
R134A/CO2/HFO1224YD/SF6 64.5/30/4.5/1	2900	(-14%)	11110 V	+625 V	97.0%	-17.5%	36.6 uA	+301 uA	1.6 / 2.5 cm	-0.4 / 2.5 cm	1.5 ns	+0.8 ns

TABLE 4.6 – Foremost parameters evaluated at source off and at 500 Hz/cm^2 for the tested gas mixtures.

4.6.5 Studies on fluoride production for RPCs operated under high gamma background radiation

RPCs at LHC are expected to be operated for the whole HL-LHC program, possibly up to 2040. Hence, it is critical to understand the long-term effects of eco-friendly gas mixtures when used in RPCs operated under LHC-like conditions. During the LHC run phase, the detectors are operated with a constant presence of neutrons and neutron-induced gamma background. It is known that the effect of the electric field together with ionizing particles leads to the breaking of the R-134a molecule into several compounds [85, 67]. Among others, the F- radicals are created. The presence of water vapor in the gas mixtures allows the radicals to form hydrogen fluoride (HF). HF is a highly-reactive compound that can interact with the surface of the electrode and the spacers, altering the performance of the detector [86, 87, 88, 89, 90]. It was shown that linseed oil could mitigate the degradation of the inner electrode surface by trapping the HF molecule. However, some imperfections on the coating and the electrodes were observed. In [86], a decrease in the resistivity of the bakelite was observed when the electrodes' inner surfaces were flushed with some amount of HF vapor. The same work, together with [89] and [91], showed that the usage of Argon could partially detach the fluorine impurities attached to the surface of the electrodes. The rate of HF production was shown to be linearly correlated with the currents drawn by the detector [67]. The amount of fluoride ions and impurities works as an indicator of the rate of the breakdown of fluorinated compounds happening inside the gas gap in the presence of an electric field and ionizing radiation. An experimental campaign was then conducted to quantify the amount of HF production for an RPC gap operated with two different gas mixtures, at working point (calculated from muon beam tests) and with gamma background. The test was conducted at GIF++ using a 2 mm, 80 x 100 cm^2, single gap RPC flushed with a fixed flow rate of 1 gap volume per hour. The output of the detector was then sent into a capillary pipe immersed at the height of 1 cm into a 15 ml water and 15 ml Total Ionic Strength Adjustment Buffer (TISAB II) solution. The detectors and the GIF++ irradiator were then switched on simultaneously, and the chamber was irradiated for around 3-4 hours. After the irradiation period, the detector was switched off, and the solution was removed from the gas output line. A previously calibrated Ion-Selective Electrode (ISE) probe was then used to measure the concentration of dissolved HF into the solution. Figure 4.63 shows the rate of HF production at different HVs and background rates for a R-1234ze/R-134a/CO_2/i-C_4H_{10}/SF_6 27.25/27.25/40/4.5/1 gas mixture.

Figure 4.64 shows that the HFO-based gas mixture produces around four times more HF than the standard gas mixture at a background rate of 100 Hz/cm^2. By assuming that:

- HF is mainly produced by the breaking of R-134a and R-1234ze molecules;
- the amount of HF is proportional to the relative concentration of the Freon molecules in the gas mixtures;
- the breaking of Freon molecules is due to the impinging gamma particles;

It is possible to estimate that the R-1234ze has an HF production rate 13 times higher than the R-134a molecule. The reasons should be investigated in the atmospheric chemistry of the R-1234ze molecule, as the molecule has an atmospheric lifetime of 7-14 days, which is about 300 times less than the 13 years of the atmospheric lifetime of R-134a, suggesting that

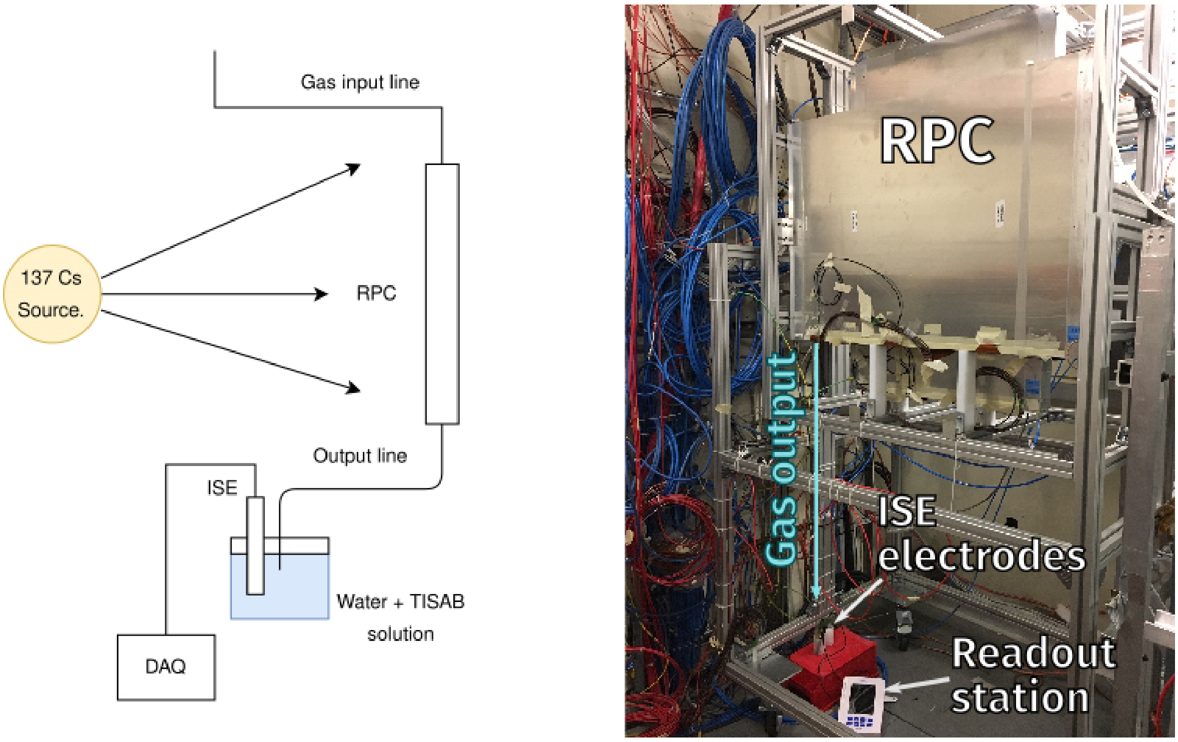

FIGURE 4.62 – On the left, simplified schema of ISE sampling setup. On the right, picture of the setup installed at GIF++

the reactivity of the gas to UV radiation and OH^- radicals is much higher and indicating a possibly higher rate of degradation into fluorinated compounds [92].

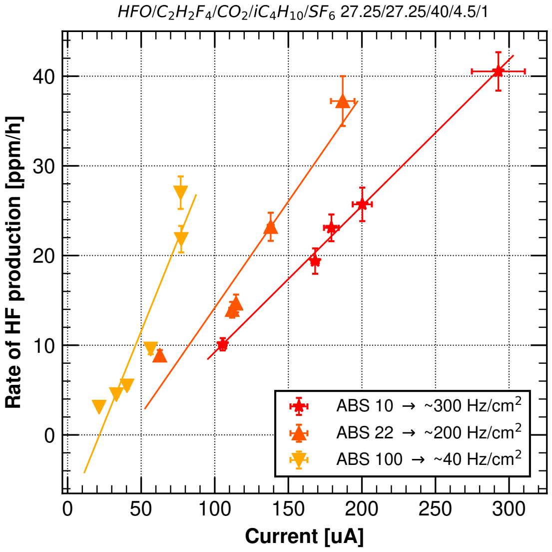

FIGURE 4.63 – Rate of HF production against the current drawn by the detectors at different background rates. The relationship between the two quantities seems to be linear and the slope depends on the background rate. In particular, at higher gamma rates the increase of the rate of HF production is lower.

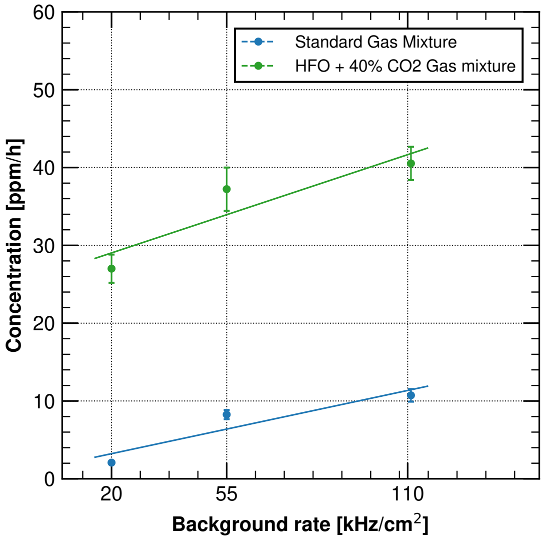

FIGURE 4.64 – Rate of HF production against the gamma rate for the standard and HFO-based gas mixture. The detector was operated at a working point. At higher gamma rates the HF production for the HFO-based gas mixture is about four times higher than the standard gas mixture.

Conclusions

Muon detection at CERN experiments is a fundamental activity for the LHC physics program. Gas systems ensure the correct operation for gaseous detectors in terms of gas quality, purity, flow, and pressure. Few of the employed gases, namely R-134a, CF_4, and SF_6, are known to be Greenhouse Gases (GHG)s subjected to phase-out policy. CERN identified four main strategies to reduce GHG emissions from particle detectors of LHC experiments. The present thesis focused on two main research branches.

The first research line consisted of optimizing the current gas systems technologies. Gas systems are built using a modular design to minimize costs and ease operation. During the LS2 period of LHC, several upgrades were performed to improve their performance and reduce GHG emissions. A web-based monitoring service was designed to help both gas experts and detector users to monitor the status of critical gas systems data with minimal effort. The service was implemented by creating an instance of an InfluxDB time-series database. A Python application was developed to retrieve gas systems data from the CERN's DIP protocol and store it into the InfluxDB instance. A Grafana web application was provisioned, and different dashboards were designed based on the needs of detector users and gas experts.

To improve the navigation and usability of the available SCADA tools, a Human Machine Interface (HMI) panel prototype was built. The panel consisted of a schematic representation of the gas system with the essential values displayed in one place. The HMI panel was designed to display a weekly maximum and minimum statistic for each declared device value. The simple weekly-aggregated statistics allowed the operators to quickly inspect the gas systems and spot possible anomalies without opening the trend tools for each device. A prototype was built for the ATLAS MDT gas system, and it is currently undergoing the last review phase before being deployed to other LHC gas systems.

Data analysis pipelines were developed using CERN's Service for Web-Based ANalysis (SWAN) that provided a python Jupyter notebook to connect to the NeXt Cern Accelerator Logging Service (NXCALS) cluster, where gas systems data is stored. Together with online monitoring tools, offline data analyses were performed to evaluate the performance of gas systems during LHC run activity and investigate possible issues. In particular, few analyses were conducted on the flow cells data of the ATLAS RPC gas systems during Run 2 and the initial period of LS2. A change point detection algorithm was run for each flow cell time-series data to identify the dates of possible leak creations and to understand possible correlations between leak development and gas system operation. No leading, evident dates were found, suggesting a relatively homogeneous leak development over time.

During the LS2 period, several gas systems underwent a parameter tuning campaign to improve their startup phase and run operation. The main parameters tuned are related to the Proportional, Integral, Derivative (PID) controller used to regulate control valves using pressure sensors as a feedback tracking device. The main controllers tuned were present in the Distribution Racks and the Pump module. The PID gains tuned were the proportional K_c and the integral T_i.

The ATLAS MDT distribution PID gains were set to improve the startup phase of the system and reduce the pressure overshoot and undershoot observed after LS2 upgrades. The newfound PID gains reduced the overshoot from 20-30 mbar to about 2-3 mbar for most distribution racks.

The ALICE TOF gas system PID gains were tuned to allow a proper startup phase without generating full stop interlocks. The PID integral and proportional gains were tuned in the two distribution racks and the pump module. Tests were conducted by stopping the gas system, applying a set of PID gains, and restarting the system. The performances were evaluated by monitoring the evolution of the system status and the eventual presence of interlocks during the startup phase. The tested PID gains were mainly chosen by human expertise since modeling the system was quite tricky due to its non-linear behavior in the startup phase.

A second main research line treated in this work to reduce GHG emissions consisted of the performance studies of Resistive Plate Chamber (RPC) detectors operated with new environmentally friendly gas mixtures in the presence of an LHC-like environment. RPCs account for most GHG emissions due to their leaks at detector level and their gas mixture made of around 95% of R-134a, a fluorinated compound with a Global Warming Potential (GWP_{100}) of 1430. The work aimed to find new gas mixtures that had similar performances to the standard ATLAS and CMS one and required no change in the current RPC systems, meaning no change in front-end electronics, power supply systems, and gas systems.

A dedicated Data Acquisition system (DAQ) was developed. The DAQ consisted of a program allowing to control the HV of the RPCs, perform waveform recording using a CAEN digitizer, store data into CERN EOS file system and analyze real-time detector data to give insightful information about the detector status.

A data analysis library, namely `olefin`, was specifically developed to analyze data collected by the RPCs operated with alternative gases. The framework was organized in four different hierarchical analysis layers, from the lowest level, regarding the analysis of the signal waveform signal, to the highest concerning the whole HV scan run. The analysis was intensively used in the present work to compare the performance of RPCs operated in different environments and with different gas mixtures.

2 mm, single-gap, bakelite RPCs performances were evaluated in laboratory conditions with cosmic muons. First, the RPCs were characterized by operating them with the standard CMS gas mixture. The addition of Helium and CO_2 to the standard gas mixture was studied to understand the effect of a relatively inert gas and its possible use for more complex gas mixtures. Results showed that 30-40% of CO_2 or Helium might reduce GWP_{100} by 30-40% and lower the RPC working point while maintaining a stable performance level. R-1234ze based

gas mixtures were then evaluated. Some R-134a was kept, and SF_6 concentration was adjusted to stabilize streamer contamination performance. Some five-component gas mixtures based on R-1234ze/R-134a/i-C_4H_{10}/SF_6 and CO_2 or He were identified as suitable alternatives for the standard gas mixture. Results suggest that some amount of R-134a should be kept to stabilize performance in terms of currents and streamer contamination. He-based gas mixtures proved to be good alternatives to the standard gas mixture, although they may not be entirely compatible with operation in LHC caverns.

SF_6 alternatives gases were also studied by replacing SF_6 in the standard gas mixture with the selected candidate. Novec™ 5110 was found to have discrete performance when used in concentrations of around 2%. However, the fluid phase is liquid at room temperature, making it difficult to operate in its gas form. Novec™ 4710, was also tested: the gas showed excellent performances when used in concentrations of 0.1% to 0.3%. Primary concerns for Novec™ 4710 arose due to its reaction with water vapor present in bakelite RPC gas mixture, that is currently being investigated. C_4F_8O was later tested, showing discrete performance when used in concentrations higher than 2%. However, its GWP_{100} of 8000 makes its effective GWP_{100} contribution higher than the SF_6 one. Concerning CF_3I, results showed good performance when used in concentrations similar to SF_6. Regardless, CF_3I was found to have a high mutagenic toxicity level, making the gas unsuitable for LHC operation. Lastly, a gas in the family of Hydro-Chloro-Fluoro-Olefins, namely Amolea™ 1224yd, was tested. Results showed good performance when operated in concentrations of 0.3% to 0.5%, making it a possible SF_6 candidate.

Once a few selected gas mixtures were thoroughly characterized with cosmic muons in the laboratory environment, the RPCs performance was studied with muon beam and LHC-like background at the GIF++ facility. The performance of RPCs was evaluated by analyzing the foremost parameters with the detectors operated at working points and different gamma background rates. Preliminary results showed excellent performance for standard gas mixture with 30% of Helium or CO_2. R-1234ze based gas mixtures showed hundreds of volts higher working points and increased streamer contaminations. The usage of R-1234ze with CO_2 showed a noticeable efficiency drop of a few percentage points at background rates of 500 Hz/cm^2. R-1234ze/R-134a/He/i-C_4H_{10}/SF_6 gas mixtures showed similar performances to the standard gas mixtures and a GWP_{100} of 600, making them suitable, eco-friendly alternatives. However, the use of Helium may be critical for PMTs operation in the experiments and it requires further investigation.

Studies on the impurities production of RPCs operated with R-1234ze based gas mixture were started. The RPCs were operated at working point and different background rates. The production of HydroFluoric acid was measured by analyzing the gas at the detector's output with Ion Selective Electrodes. The HF was measured initially for the standard gas mixtures and later for the R-1234ze/R-134a/CO_2/i-C_4H_{10}/SF_6 27.25/27.25/40/4.5/1 gas mixture. The production of HF in the HFO-based gas mixture was observed to be around four times higher than the standard gas mixture, indicating that the HFO molecule may produce around an order of magnitude more fluorine ions than R-134a.

Bibliography

[1] O. Aberle et al. *High-Luminosity Large Hadron Collider (HL-LHC): Technical design report*. CERN Yellow Reports: Monographs. Geneva: CERN, 2020. DOI: `10.23731/CYRM-2020-0010`. URL: `https://cds.cern.ch/record/2749422`.

[2] Esma Mobs. "The CERN accelerator complex - 2019. Complexe des accélérateurs du CERN - 2019". In: (July 2019). General Photo. URL: `http://cds.cern.ch/record/2684277`.

[3] Thomas Schörner-Sadenius, ed. *The Large Hadron Collider: Harvest of Run 1*. Berlin: Springer, 2015. ISBN: 978-3-319-15001-7. DOI: `10.1007/978-3-319-15001-7`.

[4] The ALICE Collaboration. "The ALICE experiment at the CERN LHC". In: *Journal of Instrumentation* 3.08 (Aug. 2008), S08002–S08002. DOI: `10.1088/1748-0221/3/08/s08002`. URL: `https://doi.org/10.1088/1748-0221/3/08/s08002`.

[5] The ATLAS Collaboration. "The ATLAS Experiment at the CERN Large Hadron Collider". In: *Journal of Instrumentation* 3.08 (Aug. 2008), S08003–S08003. DOI: `10.1088/1748-0221/3/08/s08003`. URL: `https://doi.org/10.1088/1748-0221/3/08/s08003`.

[6] The CMS Collaboration. "The CMS experiment at the CERN LHC". In: *Journal of Instrumentation* 3.08 (Aug. 2008), S08004–S08004. DOI: `10.1088/1748-0221/3/08/s08004`. URL: `https://doi.org/10.1088/1748-0221/3/08/s08004`.

[7] The LHCb Collaboration. "The LHCb Detector at the LHC". In: *Journal of Instrumentation* 3.08 (Aug. 2008), S08005–S08005. DOI: `10.1088/1748-0221/3/08/s08005`. URL: `https://doi.org/10.1088/1748-0221/3/08/s08005`.

[8] L Rossi and O Brüning. "Introduction to the HL-LHC Project". In: *Adv. Ser. Dir. High Energy Phys.* 24 (2015), pp. 1–17. DOI: `10.1142/9789814675475_0001`. URL: `http://cds.cern.ch/record/2130736`.

[9] "ALICE upgrade physics performance studies for 2018 Report on HL/HE-LHC physics". In: (Feb. 2019). URL: `https://cds.cern.ch/record/2661798`.

[10] Susanne Kuehn. *Impact of the HL-LHC detector upgrades on the physics program of the ATLAS and CMS experiments*. Tech. rep. Geneva: CERN, May 2021. URL: `https://cds.cern.ch/record/2770467`.

[11] CMS Collaboration. *The Phase-2 Upgrade of the CMS Data Acquisition and High Level Trigger*. Tech. rep. This is a temporary submission, just to get the LHCC reference number, to be used in this and other CMS documents. Geneva: CERN, Mar. 2021. URL: `https://cds.cern.ch/record/2759072`.

[12] LHCb collaboration. *Framework TDR for the LHCb Upgrade: Technical Design Report*. Tech. rep. Apr. 2012. URL: `http://cds.cern.ch/record/1443882`.

[13] Gines Martinez. "The Muon spectrometer of the ALICE experiment". In: *Nucl. Phys. A* 749 (2005). Ed. by D. Damova, A. Kugler, and P. Tlusty, pp. 313–319. DOI: `10.1016/j.nuclphysa.2004.12.059`. arXiv: `hep-ex/0410061`.

[14] L Pontecorvo. "The ATLAS Muon Spectrometer". In: (June 2003). revised version number 1 submitted on 2003-07-27 16:31:16. DOI: `10.1140/epjcd/s2004-04-013-y`. URL: `https://cds.cern.ch/record/676896`.

[15] Vincenzo Izzo. *ATLAS Upgrades*. Tech. rep. Geneva: CERN, Sept. 2020. DOI: `10.22323/1.382.0094`. URL: `https://cds.cern.ch/record/2732959`.

[16] C. Battilana. "Performance of the CMS muon system in LHC Run-2". In: *Nuclear Instruments and Methods in Physics Research Section A: Accelerators, Spectrometers, Detectors and Associated Equipment* 936 (2019). Frontier Detectors for Frontier Physics: 14th Pisa Meeting on Advanced Detectors, pp. 472–473. ISSN: 0168-9002. DOI: `https://doi.org/10.1016/j.nima.2018.09.006`. URL: `https://www.sciencedirect.com/science/article/pii/S016890021831088X`.

[17] M. Bianco. "Upgrade of the CMS Muon Spectrometer in the forward region with the GEM technology". In: *Journal of Instrumentation* 15.09 (Sept. 2020), pp. C09045–C09045. DOI: `10.1088/1748-0221/15/09/c09045`. URL: `https://doi.org/10.1088/1748-0221/15/09/c09045`.

[18] A Cardini. "The LHCb Muon Upgrade". In: *Journal of Instrumentation* 9.02 (Feb. 2014), pp. C02014–C02014. DOI: `10.1088/1748-0221/9/02/c02014`. URL: `https://doi.org/10.1088/1748-0221/9/02/c02014`.

[19] LHCb collarboation. "LHCb Detector Performance". In: *Int. J. Mod. Phys. A* 30 (Dec. 2014), 1530022. 73 p. DOI: `10.1142/S0217751X15300227`. arXiv: `1412.6352`. URL: `https://cds.cern.ch/record/1978280`.

[20] R Guida, M Capeans, and B Mandelli. "Gas Systems for Particle Detectors at the LHC Experiments: Overview and Perspectives". In: *Springer Proc. Phys.* 212 (2018), 91–96. 6 p. DOI: `10.1007/978-981-13-1313-4_19`. URL: `https://cds.cern.ch/record/2649531`.

[21] M Capeans, Roberto Guida, and Beatrice Mandelli. "Gas Mixture Monitoring Techniques for the LHC Detector Muon Systems". In: *Springer Proc. Phys.* 212 (2018), 97–101. 5 p. DOI: `10.1007/978-981-13-1313-4_20`. URL: `https://cds.cern.ch/record/2643547`.

[22] *CERN UNICOS framework*. URL: `https://unicos.web.cern.ch/`.

[23] Intergovernmental Panel on Climate Change. *Fourth Assessment Report: Climate Change 2007: The AR4 Synthesis Report*. Geneva: IPCC, 2007. URL: `http://www.ipcc.ch/ipccreports/ar4-wg1.htm`.

[24] M Schulz and D Kourkoulas. "Regulation (EU) No 517/2014 of The European Parliament and of the council of 16 April 2014 on fluorinated greenhouse gases and repealing Regulation (EC) No 842/2006". In: *Off. J. Eur. Union* 2014.517 (2014), p. L150.

[25] *2020 Update of the European Strategy for Particle Physics (Brochure)*. Tech. rep. Geneva, 2020. DOI: `10.17181/CERN.JSC6.W89E`. URL: `https://cds.cern.ch/record/2721370`.

[26] *CERN. Environment Report*. Geneva: CERN. URL: `https://cds.cern.ch/record/2737239`.

[27] Mara Corbetta. "Development of Gas Systems for Gaseous Detector Operation at HL-LHC. Développement de systèmes de gaz pour le fonctionnement des détecteurs gazeux au HL-LHC". Presented 30 Apr 2021. Feb. 2021. URL: `https://cds.cern.ch/record/2765846`.

[28] Jakub Wozniak and Chris Roderick. "NXCALS - Architecture and Challenges of the Next CERN Accelerator Logging Service". In: (2019), WEPHA163. 5 p. DOI: `10.18429/JACoW-ICALEPCS2019-WEPHA163`. URL: `https://cds.cern.ch/record/2778529`.

[29] Raogo Kabore et al. "Review of Anomaly Detection Systems in Industrial Control Systems Using Deep Feature Learning Approach". In: *Engineering* 13.01 (2021), pp. 30–44. DOI: `10.4236/eng.2021.131003`. URL: `https://doi.org/10.4236/eng.2021.131003`.

[30] Tanmoy Kanti Das, Sridhar Adepu, and Jianying Zhou. "Anomaly detection in Industrial Control Systems using Logical Analysis of Data". In: *Computers & Security* 96 (Sept. 2020), p. 101935. DOI: `10.1016/j.cose.2020.101935`. URL: `https://doi.org/10.1016/j.cose.2020.101935`.

[31] Chao Wang et al. "Anomaly Detection for Industrial Control System Based on Autoencoder Neural Network". In: *Wireless Communications and Mobile Computing* 2020 (Aug. 2020), pp. 1–10. DOI: `10.1155/2020/8897926`. URL: `https://doi.org/10.1155/2020/8897926`.

[32] Gauthama Raman M. R., Chuadhry Mujeeb Ahmed, and Aditya Mathur. "Machine learning for intrusion detection in industrial control systems: challenges and lessons from experimental evaluation". In: *Cybersecurity* 4.1 (Aug. 2021). DOI: `10.1186/s42400-021-00095-5`. URL: `https://doi.org/10.1186/s42400-021-00095-5`.

[33] Cheng Feng, Tingting Li, and Deeph Chana. "Multi-level Anomaly Detection in Industrial Control Systems via Package Signatures and LSTM Networks". In: *2017 47th Annual IEEE/IFIP International Conference on Dependable Systems and Networks (DSN)*. IEEE, June 2017. DOI: `10.1109/dsn.2017.34`. URL: `https://doi.org/10.1109/dsn.2017.34`.

[34] Charles Truong, Laurent Oudre, and Nicolas Vayatis. "Selective review of offline change point detection methods". In: *Signal Processing* 167 (2020), p. 107299. ISSN: 0165-1684. DOI: `https://doi.org/10.1016/j.sigpro.2019.107299`. URL: `https://www.sciencedirect.com/science/article/pii/S0165168419303494`.

[35] R. Killick, P. Fearnhead, and I. A. Eckley. "Optimal Detection of Changepoints With a Linear Computational Cost". In: *Journal of the American Statistical Association* 107.500 (Oct. 2012), pp. 1590–1598. ISSN: 1537-274X. DOI: `10.1080/01621459.2012.737745`. URL: `http://dx.doi.org/10.1080/01621459.2012.737745`.

[36] Jushan Bai. "Least Absolute Deviation Estimation of a Shift". In: *Econometric Theory* 11.3 (1995), pp. 403–436. DOI: `10.1017/S026646660000935X`.

[37] Lucas Hermann Negri and Christophe Vestri. *lucashn/peakutils: v1.1.0*. Version v1.1.0. Sept. 2017. DOI: `10.5281/zenodo.887917`. URL: `https://doi.org/10.5281/zenodo.887917`.

[38] Rakesh P. Borase et al. "A review of PID control, tuning methods and applications". In: *International Journal of Dynamics and Control* 9.2 (2020), pp. 818–827. DOI: `10.1007/s40435-020-00665-4`.

[39] Lorenzo Massa. *The BIS78 Resistive Plate Chambers upgrade of the ATLAS Muon Spectrometer for the LHC Run-3*. Tech. rep. Geneva: CERN, Apr. 2020. URL: `https://cds.cern.ch/record/2716039`.

[40] Yu N Pestov. "Development of spark counters for particle identification". In: (July 1990), 15 p. URL: `https://cds.cern.ch/record/213602`.

[41] R. Santonico and R. Cardarelli. "Development of resistive plate counters". In: *Nuclear Instruments and Methods in Physics Research* 187.2 (1981), pp. 377–380. ISSN: 0167-5087.

DOI: https://doi.org/10.1016/0029-554X(81)90363-3. URL: https://www.sciencedirect.com/science/article/pii/0029554X81903633.

[42] P. Camarri et al. “Streamer suppression with SF-6 in RPCs operated in avalanche mode”. In: *Nucl. Instrum. Meth. A* 414 (1998), pp. 317–324. DOI: 10.1016/S0168-9002(98)00576-2.

[43] I. Duerdoth et al. “The transition from proportional to streamer mode in a resistive plate chamber”. In: *Nuclear Instruments and Methods in Physics Research Section A: Accelerators, Spectrometers, Detectors and Associated Equipment* 348.2 (1994), pp. 303–306. ISSN: 0168-9002. DOI: https://doi.org/10.1016/0168-9002(94)90751-X. URL: https://www.sciencedirect.com/science/article/pii/016890029490751X.

[44] I. Crotty et al. “Investigation of resistive parallel plate chambers”. In: *Nuclear Instruments and Methods in Physics Research Section A: Accelerators, Spectrometers, Detectors and Associated Equipment* 329.1 (1993), pp. 133–139. ISSN: 0168-9002. DOI: https://doi.org/10.1016/0168-9002(93)90928-B. URL: https://www.sciencedirect.com/science/article/pii/016890029390928B.

[45] D.F. Anderson, S. Kwan, and V. Peskov. “High counting rate resistive-plate chamber”. In: *Nuclear Instruments and Methods in Physics Research Section A: Accelerators, Spectrometers, Detectors and Associated Equipment* 348.2 (1994), pp. 324–328. ISSN: 0168-9002. DOI: https://doi.org/10.1016/0168-9002(94)90755-2. URL: https://www.sciencedirect.com/science/article/pii/0168900294907552.

[46] G. Carboni et al. “A model for RPC detectors operating at high rate”. In: *Nuclear Instruments and Methods in Physics Research Section A: Accelerators, Spectrometers, Detectors and Associated Equipment* 498.1 (2003), pp. 135–142. ISSN: 0168-9002. DOI: https://doi.org/10.1016/S0168-9002(02)02082-X. URL: https://www.sciencedirect.com/science/article/pii/S016890020202082X.

[47] Marcello Abbrescia, Vladimir Peskov, and Paulo Fonte. *Resistive Gaseous Detectors*. Wiley-VCH Verlag GmbH & Co. KGaA, Apr. 2018. DOI: 10.1002/9783527698691. URL: https://doi.org/10.1002/9783527698691.

[48] M. Abbrescia et al. “Progresses in the simulation of resistive plate chambers in avalanche mode”. In: *Nuclear Physics B - Proceedings Supplements* 78.1 (1999). Advanced Technology and Particle Physics, pp. 459–464. ISSN: 0920-5632. DOI: https://doi.org/10.1016/S0920-5632(99)00587-3. URL: https://www.sciencedirect.com/science/article/pii/S0920563299005873.

[49] M Abbrescia et al. “The resistive plate chambers for CMS and their simulation”. In: *Nuclear Instruments and Methods in Physics Research Section A: Accelerators, Spectrometers, Detectors and Associated Equipment* 471.1 (2001). Imaging 2000, pp. 55–59. ISSN: 0168-9002. DOI: https://doi.org/10.1016/S0168-9002(01)00915-9. URL: https://www.sciencedirect.com/science/article/pii/S0168900201009159.

[50] H. Raether. *Electron Avalanches and Breakdown in Gases*. Butterworths advanced physics series. Butterworths, 1964. ISBN: 9780598450210. URL: https://books.google.fr/books?id=2nSCvEq6AFcC.

[51] R Cardarelli, V Makeev, and R Santonico. “Avalanche and streamer mode operation of resistive plate chambers”. In: *Nuclear Instruments and Methods in Physics Research Section A: Accelerators, Spectrometers, Detectors and Associated Equipment* 382.3 (1996), pp. 470–474. ISSN: 0168-9002. DOI: https://doi.org/10.1016/S0168-9002(96)00811-X. URL: https://www.sciencedirect.com/science/article/pii/S016890029600811X.

[52] R. Guida. "GIF++: The new CERN Irradiation Facility to test large-area detectors for HL-LHC". In: *2015 IEEE Nuclear Science Symposium and Medical Imaging Conference (NSS/MIC)*. 2015, pp. 1–4. DOI: `10.1109/NSSMIC.2015.7581874`.

[53] Dorothea Pfeiffer et al. "The radiation field in the Gamma Irradiation Facility GIF++ at CERN". In: *Nuclear Instruments and Methods in Physics Research Section A: Accelerators, Spectrometers, Detectors and Associated Equipment* 866 (2017), pp. 91–103. ISSN: 0168-9002. DOI: `https://doi.org/10.1016/j.nima.2017.05.045`. URL: `https://www.sciencedirect.com/science/article/pii/S0168900217306113`.

[54] Rachel Margraf and Nikolaos Charitonidis. "Muon Beam Studies in the H4 beam line and the Gamma Irradiation Facility (GIF++)". In: (Mar. 2018). URL: `https://cds.cern.ch/record/2310593`.

[55] R. Guida and B. Mandelli. "A portable gas recirculation unit for gaseous detectors". In: *JINST* 12.10 (2017), T10002. DOI: `10.1088/1748-0221/12/10/T10002`.

[56] Telegram FZ LLC and Telegram Messenger Inc. *Telegram*. Version Windows: 1.8.5. Sept. 5, 2019. URL: `https://telegram.org`.

[57] InfluxData. *InfluxDB*. URL: `https://www.influxdata.com/products/influxdb/`.

[58] Gianluca Rigoletti. *The olefin analysis library*. Version 1.0.1. https://gitlab.cern.ch/grigolet/olefin/-/tree/v1.0 .1. Jan. 2022. DOI: `10.5281/zenodo.5816688`. URL: `https://doi.org/10.5281/zenodo.5816688`.

[59] Wes McKinney et al. "Data structures for statistical computing in python". In: *Proceedings of the 9th Python in Science Conference*. Vol. 445. Austin, TX. 2010, pp. 51–56.

[60] Pauli Virtanen et al. "SciPy 1.0: Fundamental Algorithms for Scientific Computing in Python". In: *Nature Methods* 17 (2020), pp. 261–272. DOI: `10.1038/s41592-019-0686-2`.

[61] P Paolucci et al. "CMS Resistive Plate Chamber overview, from the present system to the upgrade phase I". In: *Journal of Instrumentation* 8.04 (Apr. 2013), P04005–P04005. DOI: `10.1088/1748-0221/8/04/p04005`. URL: `https://doi.org/10.1088/1748-0221/8/04/p04005`.

[62] Holger Krekel et al. *pytest 6.2*. 2004. URL: `https://github.com/pytest-dev/pytest`.

[63] J. G. Layter. *The CMS muon project: Technical Design Report*. Technical design report. CMS. Geneva: CERN, 1997. URL: `http://cds.cern.ch/record/343814`.

[64] Abraham. Savitzky and M. J. E. Golay. "Smoothing and Differentiation of Data by Simplified Least Squares Procedures." In: *Analytical Chemistry* 36.8 (1964), pp. 1627–1639. DOI: `10.1021/ac60214a047`. eprint: `https://doi.org/10.1021/ac60214a047`. URL: `https://doi.org/10.1021/ac60214a047`.

[65] *ATLAS muon spectrometer: Technical Design Report*. Technical design report. ATLAS. Geneva: CERN, 1997. URL: `https://cds.cern.ch/record/331068`.

[66] B. Mandelli et al. "Gas mixture quality monitoring for the RPC detectors at the LHC experiments". In: *Journal of Instrumentation* 14.09 (Sept. 2019), pp. C09006–C09006. DOI: `10.1088/1748-0221/14/09/c09006`. URL: `https://doi.org/10.1088/1748-0221/14/09/c09006`.

[67] M. Abbrescia et al. "Results about HF production and bakelite analysis for the CMS Resistive Plate Chambers". In: *Nuclear Instruments and Methods in Physics Research Section A: Accelerators, Spectrometers, Detectors and Associated Equipment* 594.2 (2008), pp. 140–147. ISSN: 0168-9002. DOI: `https://doi.org/10.1016/j.nima.2008.06.009`. URL: `https://www.sciencedirect.com/science/article/pii/S0168900208008504`.

[68] A Colucci et al. *Measurement of drift velocity and amplification coefficient in C2H2F4-Isobutane mixtures for avalanche operated Resistive Plate Counters*. Tech. rep. Geneva: CERN, Nov. 1998. URL: `http://cds.cern.ch/record/683763`.

[69] R. Guida, M. Capeans, and B. Mandelli. "Characterization of RPC operation with new environmental friendly mixtures for LHC application and beyond". In: *Journal of Instrumentation* 11.07 (July 2016), pp. C07016–C07016. DOI: `10.1088/1748-0221/11/07/c07016`. URL: `https://doi.org/10.1088/1748-0221/11/07/c07016`.

[70] B. Liberti et al. "Further gas mixtures with low environment impact". In: *Journal of Instrumentation* 11.09 (Sept. 2016), pp. C09012–C09012. DOI: `10.1088/1748-0221/11/09/c09012`. URL: `https://doi.org/10.1088/1748-0221/11/09/c09012`.

[71] M. Abbrescia et al. "Eco-friendly gas mixtures for Resistive Plate Chambers based on tetrafluoropropene and Helium". In: *Journal of Instrumentation* 11.08 (Aug. 2016), P08019–P08019. DOI: `10.1088/1748-0221/11/08/p08019`. URL: `https://doi.org/10.1088/1748-0221/11/08/p08019`.

[72] L. Benussi et al. *A study of HFO-1234ze (1,3,3,3-Tetrafluoropropene) as an eco-friendly replacement in RPC detectors*. Tech. rep. 15 pages, 20 figures. May 2015. arXiv: `1505.01648`. URL: `https://cds.cern.ch/record/2014841`.

[73] www.honeywell.com. *HONEYWELL STARTS FULL-SCALE PRODUCTION OF LOW-GLOBAL-WARMING PROPELLANT, INSULATING AGENT, AND REFRIGERANT*. 2015. URL: `https://www.honeywell.com/content/honeywell/us/en/newsroom/pressreleases/2015/01/honeywell-starts-full-scale-production-of-low-global-warming-propellant-insulating-agent-and-refrigerant`.

[74] G. Saviano et al. "Properties of potential eco-friendly gas replacements for particle detectors in high-energy physics". In: *Journal of Instrumentation* 13.03 (Mar. 2018), P03012–P03012. DOI: `10.1088/1748-0221/13/03/p03012`. URL: `https://doi.org/10.1088/1748-0221/13/03/p03012`.

[75] A. Bianchi et al. "Characterization of tetrafluoropropene-based gas mixtures for the Resistive Plate Chambers of the ALICE muon spectrometer". In: *Journal of Instrumentation* 14.11 (Nov. 2019), P11014–P11014. DOI: `10.1088/1748-0221/14/11/p11014`. URL: `https://doi.org/10.1088/1748-0221/14/11/p11014`.

[76] R. Guida, B. Mandelli, and G. Rigoletti. "Performance studies of RPC detectors with new environmentally friendly gas mixtures in presence of LHC-like radiation background". In: *Nuclear Instruments and Methods in Physics Research Section A: Accelerators, Spectrometers, Detectors and Associated Equipment* 958 (Apr. 2020), p. 162073. DOI: `10.1016/j.nima.2019.04.027`. URL: `https://doi.org/10.1016/j.nima.2019.04.027`.

[77] G. Rigoletti, B. Mandelli, and R. Guida. "Performance studies of RPC detectors with new environmentally friendly gas mixtures in presence of LHC-like radiation background". In: *Journal of Instrumentation* 15.05 (May 2020), pp. C05004–C05004. DOI: `10.1088/1748-0221/15/05/c05004`. URL: `https://doi.org/10.1088/1748-0221/15/05/c05004`.

[78] G. Rigoletti, B. Mandelli, and R. Guida. "Characterization of RPC detectors with LHC-like background radiation and new eco-friendly gas mixtures". In: *JINST* 15.11 (2020). Ed. by Barbara Liberti, Alessandro Paoloni, and Paolo Camarri, p. C11003. DOI: `10.1088/1748-0221/15/11/C11003`.

[79] Gianluca Rigoletti et al. "Studies of RPC detector operation with eco-friendly gas mixtures under irradiation at the CERN Gamma Irradiation Facility". In: *Proceedings of*

European Physical Society Conference on High Energy Physics — PoS(EPS-HEP2019). Sissa Medialab, Oct. 2020. DOI: 10.22323/1.364.0164. URL: https://doi.org/10.22323/1.364.0164.

[80] G. Proto et al. “Characterization of new eco friendly gas mixtures based on HFO for RPCs”. In: *JINST* 16.02 (2021). Ed. by Barbara Liberti, Alessandro Paoloni, and Paolo Camarri, p. C02001. DOI: 10.1088/1748-0221/16/02/C02001. arXiv: 2006.00331 [physics.ins-det].

[81] Boya Zhang et al. “Fundamental physicochemical properties of SF6-alternative gases: a review of recent progress”. In: *Journal of Physics D: Applied Physics* 53.17 (Feb. 2020), p. 173001. DOI: 10.1088/1361-6463/ab6ea1. URL: https://doi.org/10.1088/1361-6463/ab6ea1.

[82] Ang Xiao et al. “Environmentally Friendly Insulating Gases as SF<inf>6</inf> Alternatives for Power Utilities”. In: *2019 2nd International Conference on Electrical Materials and Power Equipment (ICEMPE)*. 2019, pp. 42–48. DOI: 10.1109/ICEMPE.2019.8727308.

[83] *The Phase-2 Upgrade of the CMS Muon Detectors*. Tech. rep. This is the final version, approved by the LHCC. Geneva: CERN, Sept. 2017. URL: https://cds.cern.ch/record/2283189.

[84] *Technical Design Report for the Phase-II Upgrade of the ATLAS Muon Spectrometer*. Tech. rep. Geneva: CERN, Sept. 2017. URL: https://cds.cern.ch/record/2285580.

[85] M. Abbrescia et al. “HF production in CMS-Resistive Plate Chambers”. In: *Nuclear Physics B - Proceedings Supplements* 158 (2006). Proceedings of the 8th International Workshop on Resistive Plate Chambers and Related Detectors, pp. 30–34. ISSN: 0920-5632. DOI: https://doi.org/10.1016/j.nuclphysbps.2006.07.002. URL: https://www.sciencedirect.com/science/article/pii/S092056320600421X.

[86] Changguo Lu. “RPC electrode material study”. In: *Nucl. Instrum. Meth. A* 602 (2009). Ed. by Naba K. Mondal, Sergio P. Ratti, and Rinaldo Santonico, pp. 761–765. DOI: 10.1016/j.nima.2008.12.225.

[87] R. Santonico. “RPC understanding and future perspectives”. In: *Nuclear Instruments and Methods in Physics Research Section A: Accelerators, Spectrometers, Detectors and Associated Equipment* 533.1-2 (Nov. 2004), pp. 1–6. DOI: 10.1016/j.nima.2004.06.160. URL: https://doi.org/10.1016/j.nima.2004.06.160.

[88] H.R. Band et al. “Study of HF production in BaBar Resistive Plate Chambers”. In: *Nuclear Instruments and Methods in Physics Research Section A: Accelerators, Spectrometers, Detectors and Associated Equipment* 594.1 (Aug. 2008), pp. 33–38. DOI: 10.1016/j.nima.2008.06.007. URL: https://doi.org/10.1016/j.nima.2008.06.007.

[89] L. Quaglia et al. “Performance and aging studies for the ALICE muon RPCs”. In: *Journal of Instrumentation* 16.04 (Apr. 2021), p. C04002. DOI: 10.1088/1748-0221/16/04/c04002. URL: https://doi.org/10.1088/1748-0221/16/04/c04002.

[90] Andrea Gelmi et al. “Fluoride production in CMS Resistive Plate Chambers and aging study”. In: *PoS* EPS-HEP2019 (2020), p. 108. DOI: 10.22323/1.364.0108.

[91] G. Aielli et al. “Fluoride production in RPCs operated with F-compound gases”. In: *Nucl. Phys. B Proc. Suppl.* 158 (2006). Ed. by S. K. Park, S. P. Ratti, and R. Santonico, pp. 143–148. DOI: 10.1016/j.nuclphysbps.2006.07.025.

[92] Vassileios C. Papadimitriou et al. “CF3CFCH2and (Z)-CF3CFCHF: temperature dependent OH rate coefficients and global warming potentials”. In: *Phys. Chem. Chem.*

Phys. 10.6 (2008), pp. 808–820. DOI: `10.1039/b714382f`. URL: `https://doi.org/10.1039/b714382f`.